MECHANISMS OF IMINE-BASED INHIBITORS OF DAHP SYNTHASE.

MECHANISMS OF IMINE-BASED INHIBITORS OF DAHP SYNTHASE, AN ANTIMICROBIAL TARGET.

By

MAREN HEIMHALT

A Thesis

Submitted to the School of Graduate Studies

in Partial Fulfillment of the Requirements

for the Degree

Doctor of Philosophy

McMaster University

DOCTOR OF PHILOSOPHY
(Chemistry Graduate Program)

McMaster University
Hamilton, Ontario

TITLE: MECHANISMS OF IMINE-BASED INHIBITORS OF DAHP SYNTHASE, AN ANTIMICROBIAL TARGET.

AUTHOR: Maren Heimhalt, Dipl. Pharm.

SUPERVISOR: Dr. Paul J. Berti

NUMBER OF PAGES: xx, 198

Lay abstract

Antibiotic resistance is imposing a growing disease burden on society that the United Nations calls "…a global crisis that we cannot ignore". Many traditional antibiotics have now lost their efficacy as bacteria increasingly develop mechanisms of resistance. The development of new treatment options is therefore crucial. The first step towards this goal is the characterization of new antimicrobial targets. DAHPS is an enzyme that is exclusively expressed by bacteria, fungi and plants. Its absence in mammalian cells is expected to reduce side effects in humans. DAHPS inhibitors have previously been developed, but none of them has shown sufficient effectiveness in bacterial cell culture. Possible reasons for this failure were, among others, reduced inhibition in the presence of metal ions, low cell membrane penetration and incomplete enzyme inhibition. This thesis examines DAHPS's properties and provides solutions on how to successfully inhibit this enzyme, to fight antibiotic resistance with new treatment options.

Abstract

Bacterial 3-deoxy-D-*arabino*heptulosonate 7-phosphate synthase (DAHPS) is an antimicrobial target. A transition state (TS) mimic inhibitor of DAHPS, DAHP oxime, was developed in our lab, with K_i = 1.5 μM. Despite being a potent inhibitor, some of DAHP oxime's properties could hinder its efficacy in blocking bacterial growth.

One problem was that DAHP oxime bound competitively with respect to the metal cofactor, Mn^{2+}. Identifying the origin of this competition was crucial for *in vivo* success of DAHPS inhibitors, as the abundance of metal ions in living cells could hinder DAHP oxime's effectiveness. Mutant enzymes and fragment-based inhibitors demonstrated that the competition originated in interactions involving the O4 hydroxyl of DAHP oxime and residues Asp326, and Cys61. This suggested improved inhibitor designs to avoid metal competition.

Another drawback was the highly negatively charged nature of DAHP oxime and other DAHPS inhibitors. The charge hindered cell membrane penetration, and therefore its effectiveness in cells. Truncating DAHP oxime to a fragment reduced its hydrophilicity and charge, while the introduction of fluorine in the oxime's α-position increased potency. DAHPS-specific bacterial growth inhibition was obtained with this fragment.

DAHPS inhibition by high DAHP oxime concentrations resulted in a 15% residual activity. This residual activity would be sufficient for bacterial survival, so two derivatives, DAHP hydrazone and DAHP *O*-(2-fluoroethyl) oxime that

showed complete inhibition were characterized. DAHP hydrazone was successfully co-crystallized with DAHPS. Its 100-fold higher potency relative to DAHP oxime was attributed to an extra water bound in the active site. The inhibitor bound in all four of the enzyme's subunits. However, the observed subunit asymmetry showed that the subunits communicate with each other and that there is a significant energetic penalty to enforcing full subunit symmetry.

Acknowledgements

I would like to thank Dr. Berti for the opportunity to work in his lab. Thank you for all the time you invested supporting this project, for teaching me patience and confidence and for your open ear, advice, and understanding at all times.

Thank you to my committee members, Dr. Russell Bishop and Dr. Paul Harrison for your advice and guidance over the last years.

This project would not have been possible without collaborators. I would like to thank Dr. Murray Junop, Ryan Grainger and Chris Brown (Western University) for their work and support on the protein crystallography structures, Dr. José Carlos Bozelli Junior and Dr. Richard Epand (Laboratory of Membrane Biophysics, McMaster University) for the extensive help and advice with the ITC experiments, and Dr. James Dzandzi and Dr. Valliant (McMaster University) for the assistance during parts of the synthesis of DAHP *O*-(2-fluoroethyl) oxime.

Thank you to the great people in the Berti lab that spent parts of this journey with me: Dr. Simanga Gama, Dr. Vincent Azhikannickal, Dr. Naresh Balachandran, Rasa Bakhtiari, Lisset Llano, Alvin Niu, Shahbano Syed, Christopher McChesney, Sabih Jamil and Victoria Brown, Funing Lin, Shivneet Gill, Jacob Pierscianowski, Wayne Law, Reem Aziz, Jennifer Wild, Kelvin Tsao, and Elizabeth Curiel-Tejeda. I am thankful for all the great memories.

I would like to thank Twyla and Brian for encouraging me to apply at McMaster University and giving me a home during my first months in Hamilton.

To Patrick for his endless support, selflessness, and love. Thank you for making sure I had a life outside of the lab, for sharing my love to nature, giving me the possibility to disconnect from everything occasionally and allowing me to be myself.

Für meine Familie, die mir über die letzten Jahre sehr gefehlt hat. Danke, dass ihr all meine Entscheidungen bedingungslos unterstützt habt, auch wenn es für euch nicht immer leicht war, und dass wir uns über die Entfernung so nah geblieben sind. Danke für den Halt und die Sicherheit, die ihr mir jeden Tag gebt und die es mir ermöglicht hat, diesen Weg zu gehen. Ich habe euch sehr lieb.

Table of Contents

List of Figures

List of Tables

List of Abbreviations

C61A	Cys61 to Ala mutant of $DAHPS_{H6}$
D326A	Asp326 to Ala mutant of $DAHPS_{H6}$
DAHP	deoxy-D-*arabino*-heptulosonate-7-phosphate
DAHPS	DAHP synthase
$DAHPS_G$	*E. coli* DAHPS(Phe) with an *N*-terminal Gly residue
$DAHPS_{H6}$	*E. coli* DAHPS(Phe) with an *N*-terminal His_6-tag
DTT	DL-dithiothreitol
E. coli	*Escherichia coli*
E4P	erythrose 4-phosphate
EDTA	ethylenediaminetetraacetic acid
EPSP	5-enoylpyruvyl shikimate phosphate synthase
Ero4P	erythritol 4-phosphate
FBDD	fragment-based drug discovery
FDG	2-deoxy-2-fluoroglucose
Gro3P	glycerol 3-phosphate
H268A	His268 to Ala mutant of $DAHPS_{H6}$
HDX	hydrogen/deuterium exchange
HEPES	4-(2-hydroxyethyl)-1-piperazineethansulfonic acid
IPTG	isopropyl β-D-1-thiogalactopyranoside
ITC	isothermal titration calorimetry
KDO8P	3-deoxy-D-*manno*-octulosonate-8-phosphate
KDO8PS	KDO8P synthase
K_i	equilibrium dissociation constant for inhibitor binding
K_D	equilibrium dissociation constant
K_M	Michaelis constant
LB	lysogeny broth
LDH	lactate dehydrogenase
LFER	linear free energy relationship
LPS	lipopolysaccharides
ManNAc	*N*-acetylmannosamine
MJ6341	DAHPS·DAHP $hydrazone_4$ crystal
mPDA	*m*-phenylenediamine
NeuB	bacterial sialic acid synthase
NeuNAc	*N*-acetylneuraminic acid
PEP	phosphoenolpyruvate
P_i	inorganic phosphate
PMSF	phenylmethane sulfonyl fluoride
pPDA	*p*-phenylenediamine
ppsA	phosphoenolpyruvate synthetase
rmsd	root-mean-square deviation
TCEP	tris(2-carboxyethyl)phosphine

TEV	tobacco etch virus
TFP	3,3,3-trifluoropyruvate
TFPOX	$DAHPS_G$·TFP $oxime_3$ crystal
TFPSC	$DAHPS_G$·TFP $semicarbazone_4$ crystal
THI	tetrahedral intermediate
TIM	triose phosphate isomerase
t_R	residence time
Tris	tris(hydroxymethyl)amino methane
TS	transition state
wt	wildtype

Standard amino acid nomenclature:

A	Ala	Alanine
C	Cys	Cysteine
D	Asp	Aspartic acid
E	Glu	Glutamic acid
F	Phe	Phenylalanine
G	Gly	Glycine
H	His	Histidine
I	Ile	Isoleucine
K	Lys	Lysine
L	Leu	Leucine
M	Met	Methionine
N	Asn	Asparagine
P	Pro	Proline
Q	Gln	Glutamine
R	Arg	Arginine
S	Ser	Serine
T	Thr	Threonine
V	Val	Valine
W	Trp	Tryptophan
Y	Tyr	Tyrosine

Declaration of academic achievement

All work described in this thesis has been performed by the author, with the following exceptions: Kinetic parameters for $DAHPS_{H6}$ at pH 7 as well as the DAHP oxime's K_i at pH 7 have been obtained by Dr. Naresh Balachandran. Raw data for $DAHPS_{H6}$'s inhibition by pyruvate oxime + G3P has been obtained by Shan Jiang. Protein diffraction data were collected by Dr. Murray Junop, data processing was performed by Ryan Grainger, and the refinement was performed by the author, Dr. Paul J. Berti, Dr. Murray Junop, and Ryan Grainger. The method for DAHP hydrazone synthesis has been developed by Jenny Zheng and Jennifer Wild.

Chapter 1. Introduction

1.1. Overview

In times of an increasing health threat due to antibiotic resistance, the characterization of new targets for antibiotics is indispensable. This thesis reports the in-depth characterization of imine-based inhibitors of DAHPS (deoxy-D-*arabino*-heptulosonate-7-phosphate synthase), the first enzyme of the shikimate pathway. DAHPS is a target for antibiotics as there is no mammalian counterpart. Nonetheless, the inhibition of this enzyme has previously faced obstacles. DAHP oxime, a transition state mimic inhibitor that was previously designed in our lab, showed metal-competitive binding, low bacterial growth inhibition and there was residual activity even at high inhibitor concentrations. This thesis deepens the understanding of the causes by characterizing inhibitory mechanisms and outlines ideas of how to effectively inhibit DAHPS to make it a reliable target for antibiotics.

1.2. Antibiotic resistance

The discovery of penicillin by Fleming in 1928[1] and its first clinical use in the early 1940's[2] were significant steps in the development of antibacterials. Sulfonamides, synthetic compounds available prior to penicillins,[3] had reduced efficacy and serious side effects.[4,5] Penicillin quickly captured the market due to

its excellent safety profile and high efficacy.[4] Inspired by the success with penicillin, other antibacterial substances such as streptomycin and chloramphenicol were discovered soon after.[6] Like penicillin, which was isolated from the *Penicillium* mold,[1] they were isolated from microbial sources.[7,8] In the following years, the availability of antibiotics led to major advances in medicine. Not only did they treat infectious diseases, but they enabled improved medical care with regard to surgeries, cancer treatment and organ transplantations.[9] However, the success of antibiotics was quickly impaired by resistance.[10,11] Resistance to penicillin derivatives was observed as early as 1944,[10] and the first multi-drug resistance bacteria strains were reported in the middle of the 1950's.[11] Today, we are faced with a group of Gram-positive and Gram-negative multi-drug resistant strains, particularly the ESKAPE organisms (*Enterococcus faecium*, *Staphylococcus aureus*, *Klebsiella pneumoniae*, *Acinetobacter baumanni*, *Pseudomonas aeruginosa*, and *Enterobacter species*) that are no longer susceptible to the treatment with antibiotics.[12] While resistant bacteria were first discovered in hospitals, these bacteria are now increasingly detected in community-acquired infections.[13] The routine use of antibiotics in hospitals and in the community poses a constant selective pressure for bacteria, making the development of resistance inevitable.[14,15] Therefore, as the increased use of antibiotics correlates with an elevated emergence of infections with resistant bacteria,[16] strict policies must be developed and applied for the administration of antibiotics in hospitals, for community-acquired infections, and in livestock.[17–19]

At the same time, the development of new antibiotics is indispensable.[20] Current antibiotics act on a small selection of targets, such as the cell wall, protein and DNA synthesis.[21] In recent years, new targets have rarely been identified, but rather the design of derivatives and an increased drug stability against the mechanisms of resistance have been in the center of development.[20] Broadening the spectrum of antibiotic targets would be an important step towards conquering antibacterial resistance. In contrast, over the last few decades, the development of new antibiotics declined drastically.[22] Pharmaceutical companies are not investing in antibiotic development.[23–25] The low commitment to antibiotic development is based on high costs vs. low success rates of new compounds in clinical trials. Additionally, in the light of antibiotic resistance, new antibiotics that successfully entered the clinic, are often held in reserve until front-line antibiotics failed. The following course of treatment is short, which makes it difficult to create profitable new antibiotics. Thus, the development of new antibiotics is both a technical and financial challenge. Nonetheless, the emergence of resistances in bacteria against antibiotics will continue to grow, and the development of new antibiotics with new mechanisms of action is therefore urgently needed.

1.3. Shikimate pathway as a target for antimicrobial therapy

The first step in drug development is identifying a suitable therapeutic target. At this stage, the consideration of potential side effects caused by the treatment is indispensable. To minimize side effects during antimicrobial therapy,

it is advisable to choose a therapeutic target which is specific to the pathogen while absent in the human host. Enzymes of the shikimate pathway satisfy this requirement as this pathway only exists in bacteria, fungi and plants, while there is no mammalian counterpart.[26] The shikimate pathway leads to the biosynthesis of the aromatic and, for humans, essential amino acids phenylalanine, tyrosine, and tryptophan, and other aromatic and pre-aromatic compounds.[27] The irreversible condensation of phosphoenolpyruvate (PEP) and erythrose 4-phosphate (E4P) to form deoxy-*arabino*-heptulosonate-7-phosphate (DAHP) is the first step along this pathway.[28] Six more enzymatic reactions result in chorismate, a branch point in the synthesis of the aromatic amino acids (Figure 1.1).[29] For Phe and Tyr biosynthesis, chorismate is then converted by chorismate mutase to prephenate, while anthranilate serves as the intermediate on the metabolic pathway to Trp (Figure 1.2).[30] In bacteria, the aromatic amino acids account for the majority of the aromatic compound biosynthesis.[31] Higher organisms use the products of the shikimate pathway to synthesize more complex compounds over a plethora of branches from the main synthetic sequence.[27,29] Vitamin K, siderophores, ubiquinone and folic acid are examples of products which result from metabolic processes that branch off the main trunk of the shikimate pathway (Figure 1.2).[29]

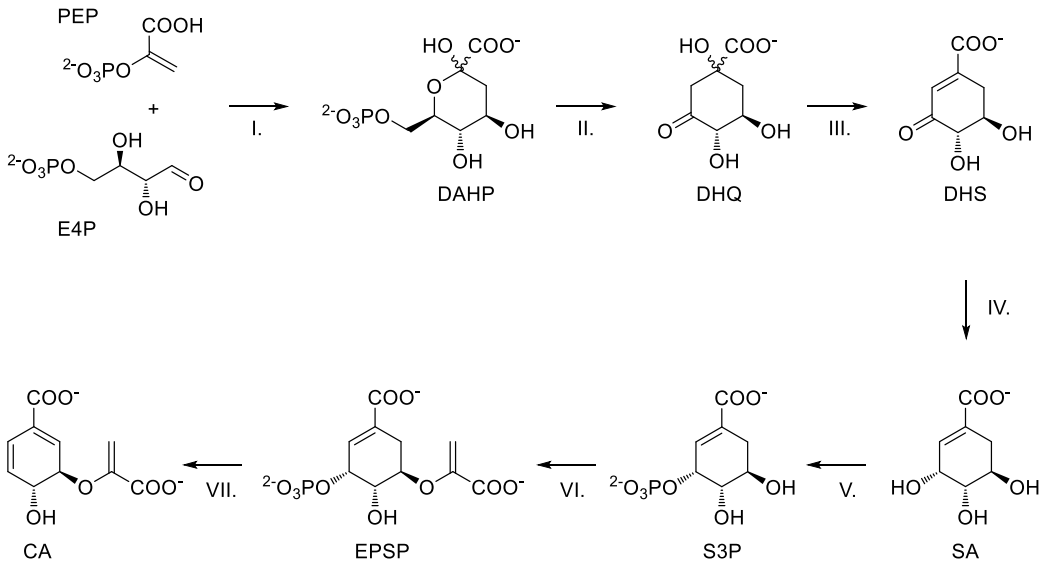

Enzymes:

I. DAHP synthase
II. 5-dehydroquinate synthetase
III. 3-dehydroquinate dehydratase
IV. shikimate dehydrogenase
V. shikimate kinase
VI. 5-enolpyruvylshikimate 3-phosphate synthase
VII. chorismate synthase

Substrates

DAHP 3-deoxy-D-*arabino* heptulosate 7-phosphate
DHQ 5-dehydroquinate
DHS 5-dehydroshikimate
SA shikimate
S3P shikimate 3-phosphate
EPSP 5-enolpyruvylshikimate 3-phosphate
CA chorismate

Figure 1.1 The common steps of the shikimate pathway.

Seven enzymes catalyze a series of reactions resulting in chorismate, a branch point on the biosynthetic pathway to the aromatic amino acids Phe, Tyr and Trp.

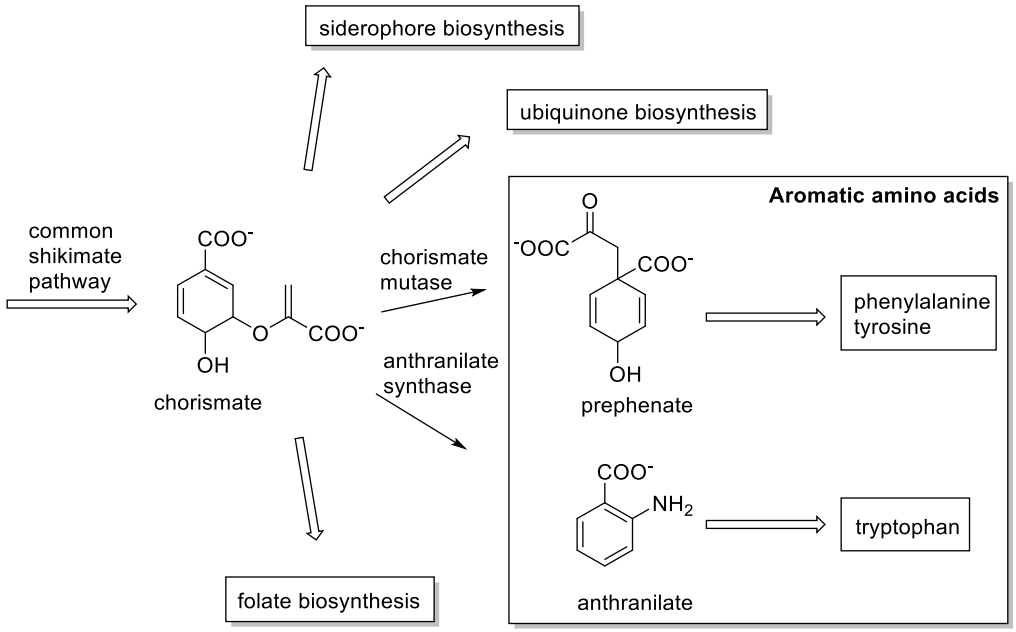

Figure 1.2 Branching of the shikimate pathway.

Adapted from Light *et al*., 2013.[32]

Numerous knockout and mutation experiments have demonstrated that bacteria lacking enzymes of the shikimate pathway are no longer viable and/or virulent.[33–38] This confirms that this pathway is essential for bacterial growth/pathogenicity, and validates the shikimate pathway enzymes as suitable targets for pharmacotherapy. Furthermore, bacteria which were attenuated due to an interruption of the shikimate pathway, have been proposed for the preparation of vaccines.[39,40] Indeed, the shikimate pathway has been a target for enzyme inhibitors for 46 years, when the herbicide glyphosate was first discovered.[41] Glyphosate is an 5-enoylpyruvyl shikimate phosphate (EPSP) synthase inhibitor, and its binding is competitive with respect to PEP.[42–44] More recently, other enzymes along the pathway have been in focus of research.[26,45–47] Shikimate

kinase inhibitors, for example, have shown *in vitro* activity against *Mycobacterium tuberculosis*,[45] and 3-dehydroquinate dehydratase, has recently been inhibited by flavonoids, which inhibited *Enterococcus faecalis* growth in cell culture.[46] Despite these and other recent studies, there is no enzyme inhibitor of the shikimate pathway in clinical use.

1.4. DAHPS

DAHPS is the first enzyme in the shikimate pathway, and was first purified in 1959.[48] DAHPS regulation is well-developed, presumably due to its position at the beginning of the shikimate pathway, controlling the downstream output.[32,49] Two DAHPS classes have been identified.[32,50] Class I DAHPSs are primarily microbial enzymes with a subunit molecular weight of 39 kDa, while class II DAHPSs originate mainly, but not exclusively, from plants, and possess a monomeric molecular weight of 54 kDa.[51,52] The class I DAHPSs can be further divided into subclasses Iα and Iβ, which are distinguished by their regulatory mechanisms.[32] Class Iα enzymes are commonly found in Gram-negative bacteria and are feedback regulated by different aromatic amino acids.[53] Class Iβ enzymes are either unregulated, or Phe/Tyr, or chorismate/prephenate regulated.[32]

There is a multiplicity of combinations and patterns of DAHPS isoenzymes simultaneously occurring in single microorganisms.[32] The types of isoenzymes in an organism depends on its metabolic needs, mainly based on whether it relies on external sources of aromatic compounds, or if it is fully

prototrophic, producing all of its own aromatic compounds.[29] The Gram-negative bacterium *Escherichia coli*, like some other Enterobacteriaceae, possesses three DAHPS class Iα isoenzymes.[54] DAHPS(Tyr), DAHPS(Phe) and DAHPS(Trp) are each feedback regulated by their eponymous aromatic amino acid,[55] and are encoded by the structural genes *aroF*, *aroG* and *aroH*, respectively.[56] Besides end-product feedback inhibition, gene expression of all three isoenzymes is under transcriptional control by the repressor protein TrpR.[57] In *E. coli*, DAHPS(Phe) is responsible for 80% of DAHPS activity in the cells, while DAHPS(Tyr) contributes to 20%, and DAHPS(Trp) accounts for 1%.[58] DAHPS(Phe) is a homotetrameric enzyme, while the two other are homodimers.[29] Feedback inhibition of DAHPS(Phe) and DAHPS(Tyr) by their respective amino acid leads to 95% reduction in activity, while DAHPS(Trp)'s activity is only reduced to 60%.[57] This residual activity ensures a supply of DAHP for the biosynthesis of other compounds, like vitamins, which are synthesized via side branches of the shikimate pathway.

1.5. The α-carboxyketose synthase superfamily

DAHPS is part of the α-carboxyketose synthase superfamily, together with 3-deoxy-D-*manno*-octulosonate-8-phosphate synthase (KDO8PS) and sialic acid synthase (NeuB).[59] These enzymes form 3-deoxy-2-keto sugars with differing chain lengths by a stereoselective condensation of PEP and an aldose (Figure 1.3).[48,60,61] The aldoses utilized by KDO8PS and NeuB are 3-deoxy-D-*manno*-

octulosonate-8-phosphate and *N*-acetylmannosamine, respectively. In all three enzymes, the phosphate group of PEP is lost through C-O bond cleavage, releasing inorganic phosphate (P_i).[62–64] Despite low sequence identity, the tertiary structures of the family members are surprisingly similar.[62,65] All of them are oligomeric enzymes possessing a triose phosphate isomerase (TIM) barrel fold.[62,65,66] Similar positioning of active site residues for KDO8PS and DAHPS was observed.[65] The three family members differ in their metal requirements: NeuB, DAHPS, and some KDO8PSs are metalloenzymes, while some KDO8PSs are metal-independent.[67,68] In metal-dependent KDO8PSs, the metal ion was described to be of structural relevance,[69] in DAHPS and NeuB a catalytic role is hypothesized.[62,70] All three enzymes are involved in crucial metabolic processes in bacteria (Figure 1.3),[48,60,71] and no mammalian counterparts exist. This qualifies them as great targets for antibiotics.

Enzyme	Aldose	Product	Biological function
DAHPS	C4	DAHP	biosynthesis of aromatic amino acids
KDO8PS	C5	KDO8P	lipopolysaccharide envelope of bacteria
NeuB	C6	NeuNAc	cellular and molecular recognition

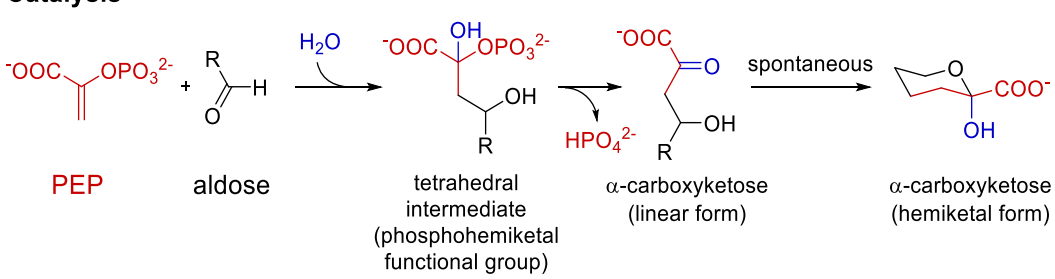

Figure 1.3 The α-carboxyketose synthase superfamily enzymes at a glance.

DAHP spontaneously cyclizes to form the hemiketal after dissociation from DAHPS.

1.5.1. NeuB

NeuB synthesizes *N*-acetylneuraminic acid (NeuNAc), the predominant sialic acid in nature.[60] Sialic acids are a family of nine carbon monosaccharides that typically occur in vertebrates and higher invertebrates and have an important function for cell recognition and adhesion.[72] Bacteria, especially pathogens in the mucus of the lower respiratory tract, use sialic acid to disguise themselves as host cells and hide from the immune system.[73] Some bacteria scavenge sialic acids from host cells to decorate their surface.[74] Others, like *E. coli* K1, *Neisseria meningitidis* and *Campylobacter jejuni* synthesize sialic acid *de novo*. The NeuNAc biosynthetic pathway in bacteria and humans are distinct, making bacterial NeuB a suitable drug target (Figure 1.4).[75] Bacterial sialic acid synthase (NeuB) performs a condensation reaction of PEP and *N*-acetylmannosamine (ManNAc), while the human orthologous enzyme NeuNAc 9-phosphate synthase utilizes a phosphorylated ManNAc derivative, ManNAc-6-phosphate. The resulting product then undergoes a dephosphorylation before the subsequent reactions.[75]

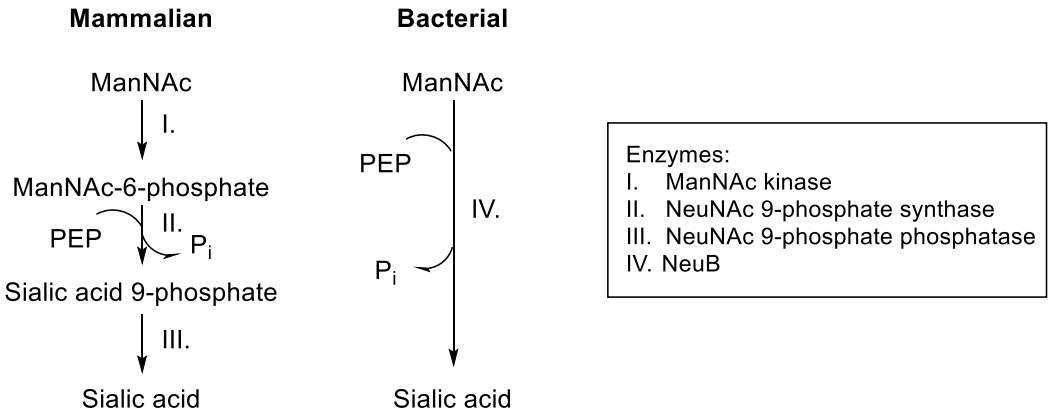

Figure 1.4 The biosynthesis of sialic acid in mammals and bacteria is distinct.

The X-ray crystallographic structure of NeuB suggests that the enzyme is structured as a domain-swapped homodimer.[62,76] The *N*-terminal domain has a TIM barrel fold that is homologous to other α-carboxyketose synthases. This domain is connected by a linker with the *C*-terminal domain that resembles the fish type III antifreeze protein.[62,77] The *C*-terminal domain from one subunit interacts with the *N*-terminal domain from the other subunit. The active site is located at the dimer interface.[62] The metal-binding site and most of the active site residues are contributed by the *N*-terminal domain, but some residues of the *C*-terminal domain also interact with the substrates (Figure 1.5). Despite less than 10% sequence identity with DAHPS, its *N*-terminal domain has a surprisingly similar tertiary structures.[62]

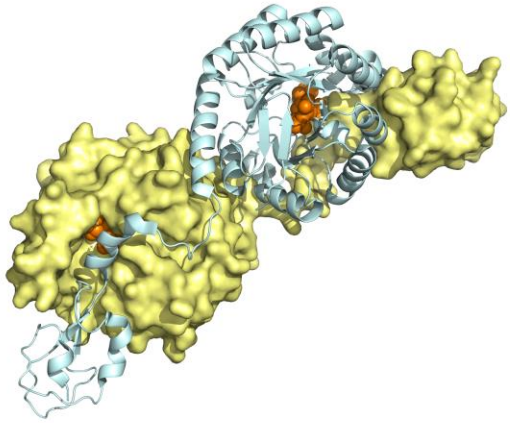

Figure 1.5 NeuB structure.

NeuB structure 1XUZ[62] showing domain structure and the ligands *N*-acetylmannositol and PEP (orange spheres). The crystal structure consisted of one subunit per asymmetric unit. The dimer was visualized by adding the monomer's symmetry partner. One subunit is shown as a cartoon, the second one is presented as the surface.

1.5.2. KDO8PS

KDO8PS catalyses the reaction of arabinose 5-phosphate and PEP (Figure 1.6).[61] The product, KDO8P, is a precursor for KDO, an important component of lipopolysaccharides (LPSs) in Gram-negative bacteria.[78] LPSs are crucial for the integrity of the outer membrane. They stabilize the membrane by adding negative charges bridged by divalent cations to provide a permeability barrier to hydrophobic antibiotics and detergents, protect the cell; they also activate the immune response in the host.[79] KDO acts as the linker between lipid A, LPS's anchor in the outer membrane, and its core oligosaccharide moiety which can be connected to an O-antigen polysaccharide (Figure 1.6A).[80,81] KDO is synthesized

from KDO8P by dephosphorylation and is subsequently converted to CMP-KDO, the activated form of KDO, for transglycosylation and incorporation into LPS (Figure 1.6B).[71] Bacteria lacking KDO8PS are severely growth-inhibited, which makes KDO8PS to a suitable target for antibiotics.[82,83]

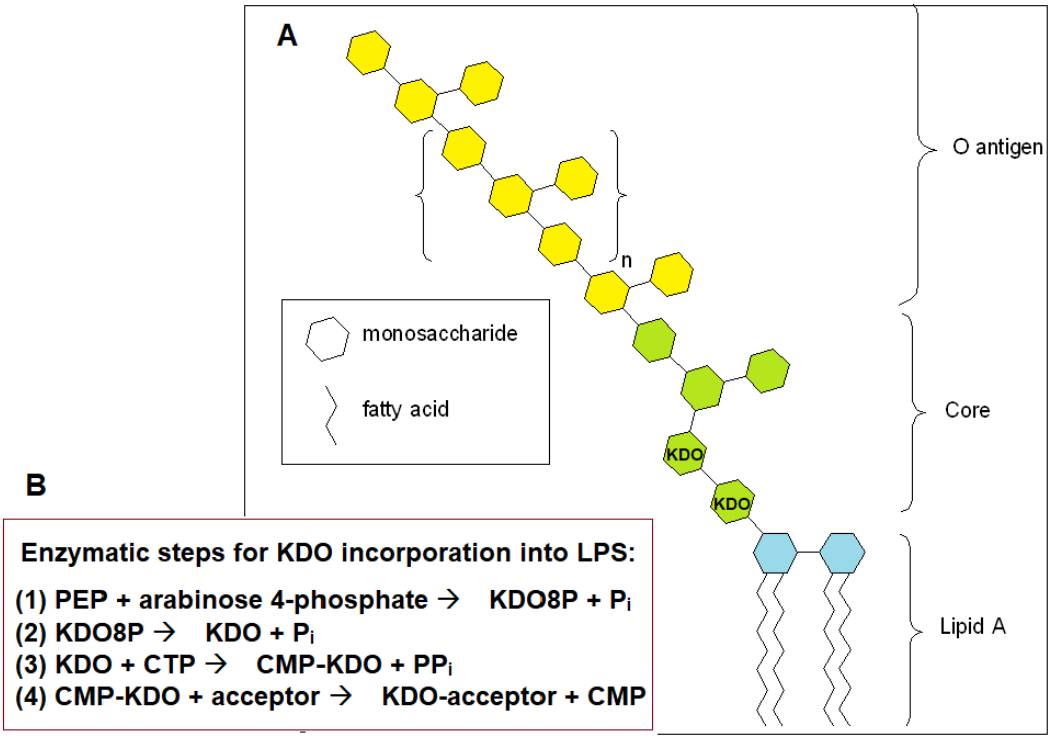

Figure 1.6 KDO8PS function in cells.

(A) General structure of LPS. Adapted from Wang et al. (2006).[84] (B) The enzymatic steps leading to KDO incorporation into LPS.

Evolutionarily, KDO8PS likely evolved from a simple unregulated DAHPS as a common ancestor with DAHPS.[50] While DAHPS Iα enzymes developed complex mechanisms of regulation, KDO8PS and some DAHPS Iβ remained unregulated.[50] KDO8PS catalyses a similar reaction to DAHPS, but mechanistic differences regarding the involvement of the metal cofactor and

aldose orientation in the active site were observed.[85] This is consistent with the observation that for some KDO8PS the metal ion is dispensable for catalysis, while all DAHPS are strictly metal-dependent.[50,67,86] In metal-dependent KDO8PS, the four metal binding residues, Cys11, His185, Glu222 and Asp333 (*Aquifex aeolicus* KDO8PS numbering), are conserved.[67] In metal-independent enzymes, Cys11 is not conserved, but replaced by Asn.[87] Shulami *et al*. showed that the metal requirement of KDO8PS is dependent on the presence of Cys11, as mutating it to Asn eliminated metal dependence from metal-dependent KDO8PS and vice versa.[69] Several studies of this type were reported in literature where metal activation or metal dependence of KDO8PS could be controlled by up to quadruple mutations of residues around the active site.[88–90]

1.6. Catalytic mechanism of α-carboxyketose synthases

The α-carboxyketose synthase superfamily enzymes catalyze an aldol-like, stereoselective condensation of PEP and an aldose.[48,60,61] The reaction follows an addition/elimination pathway in which PEP adds to the aldose to form a tetrahedral intermediate (THI) containing a phosphohemiketal functional group (Figure 1.3).[62,91,92] The THI then breaks down through a phosphate elimination step to form the linear α-carboxyketose product. After release from the active site, the product then spontaneously cyclizes to the cyclic hemiketal form. The THI has been observed mass spectrometrically in the KDO8PS reaction.[93] In addition, [2-^{18}O]PEP, i.e., PEP labelled with ^{18}O in the phosphate group's bridging oxygen

position yielded [^{18}O]-P_i as a product in the DAHPS,[63] KDO8PS,[64]and NeuB[62] reactions. This demonstrated that PEP's C2-O2 bond is cleaved during the reaction, and the only plausible way this can happen is through THI formation.

In DAHPS and KDO8PS, the *si* face of PEP attacks the *re* face of the aldose.[94–96] In contrast, in NeuB, the *si* face of PEP attacks the *si* face of ManNAc.[62] It was previously shown that DAHPS and KDO8PS follow a sequential ordered bi bi kinetic mechanism, with PEP binding first, then the aldose.[97–99] Product release is also ordered, with P_i dissociating first, then the α-carboxyketose. Previously, the essential metal ion was not considered in the kinetic mechanism; kinetics were run under high [metal] conditions, and it was assumed that the enzyme was saturated with the metal ion. However, in light of the fact that an inhibitor developed by our lab, DAHP oxime, was a competitive inhibitor with respect to the metal ion, in addition to PEP and E4P, it was necessary to determine *E. coli* DAHPS(Phe)'s complete kinetic mechanism, including metal ion binding.[100] The kinetic mechanism was shown to be rapid equilibrium sequential ordered ter ter. That is, each substrate binding step was rapid compared to catalysis, with Mn^{2+} binding first, followed by PEP, then E4P. More recently, our lab also showed that KDO8PS also follows a rapid equilibrium sequential ordered ter ter kinetic mechanism, with Mn^{2+} binding first, followed by PEP, then A5P.[101] For NeuB, no kinetic mechanism has been established to date.

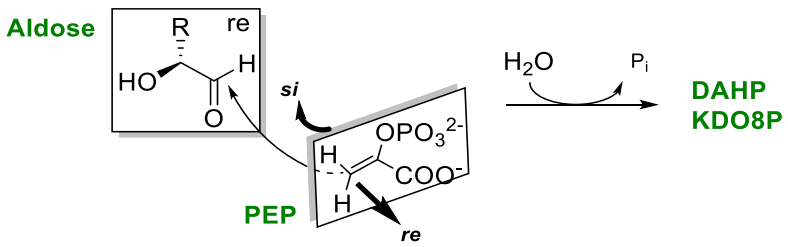

Figure 1.7 Stereoselective condensation reaction in DAHPS and KDO8PS.

The *si* face of PEP is coupling with the *re* face of the aldose, leading to the formation of DAHP and KDO8P.

Controversy surrounds the exact details of the mechanism of THI formation. Two pathways have been proposed (Figure 1.8). In mechanism A, the "cationic mechanism", the reaction is initiated by nucleophilic attack of PEP's C3 on the carbonyl carbon of E4P, leading to an oxacarbenium ion intermediate.[70,96] In DAHPS and NeuB, this nucleophilic attack would be facilitated by a Lewis acid activation of E4P's aldehyde by the metal cofactor.[70,76] Subsequently, nucleophilic attack of water on PEP's C2 gives rise to the THI. Alternatively, in pathway B, the "anionic mechanism", nucleophilic attack by water or hydroxide on PEP's C2, forming a carboanion intermediate, occurs before PEP's C3 attacking C1 of E4P.[92,102,103] It has been shown that nucleophilic attack on C2 of an unactivated enolpyruvyl groups is essentially impossible, making the anionic mechanism unlikely.[104] Pathways A and B represent the stepwise extremes of possible mechanisms; concerted mechanisms for THI formation are also possible.[102] THI breakdown in either pathway involves C-O bond cleavage to release P_i and formation of the ketone's double bond.[62–64] Phosphate departure is catalyzed by protonation of the bridging oxygen before C-O bond cleavage.[105]

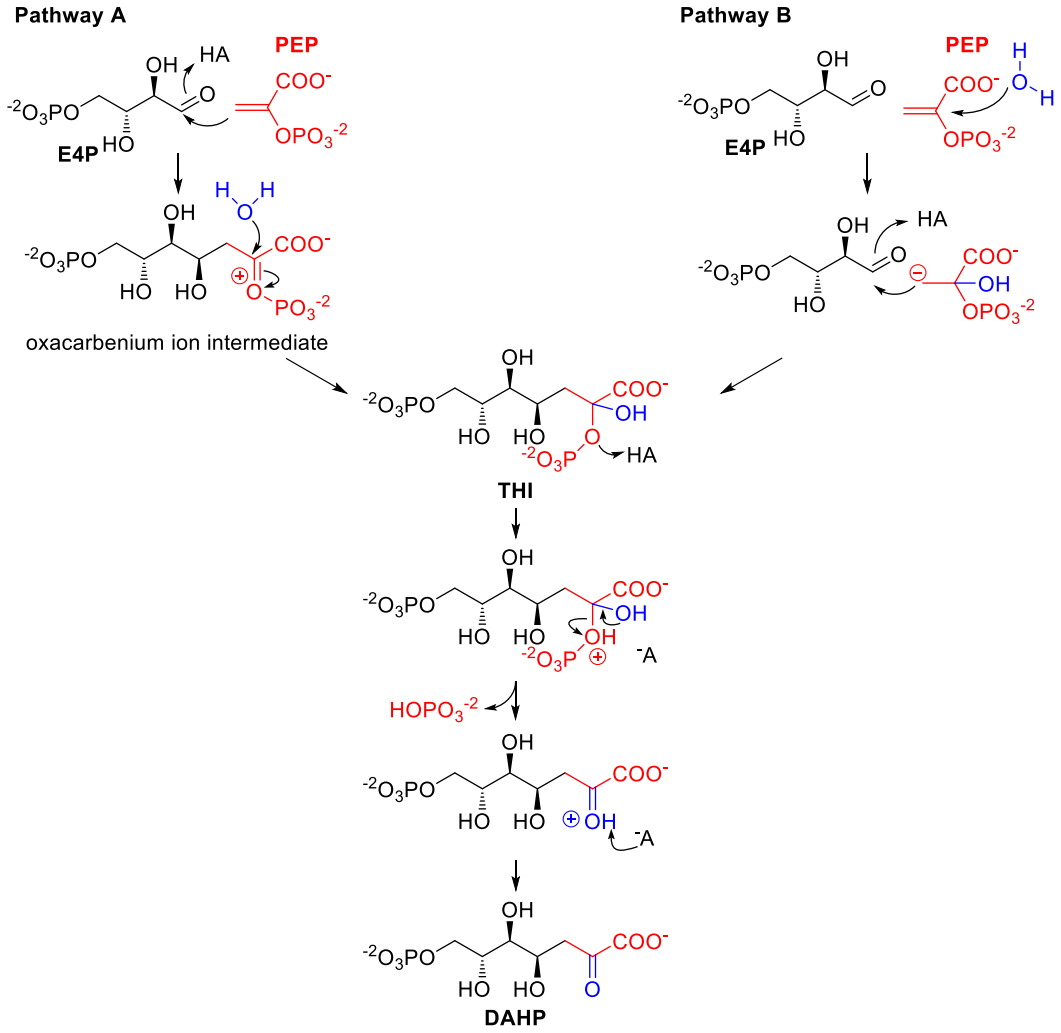

Figure 1.8 The catalytic mechanism of DAHPS.

Two pathways for THI formation have been proposed, pathway A, the cationic mechanism, and pathway B, the anionic mechanism. Concerted steps in THI formation are also possible. THI breakdown will involve protonation of the phosphate's bridging oxygen atom and P_i departure to form the linear form of the product, DAHP.

While KDO8PS shows high substrate selectivity, DAHPS tolerates a wider range of substrates: D-threose 4-phosphate, 2-deoxy-D-erythrose 4-phosphate and A5P are all catalytically converted by the enzyme.[85] Additionally, mutations of DAHPS active site residues directly involved in catalysis had modest

effects on k_{cat} ($\leq$ 100-fold), suggesting that the enzyme's main catalytic strategy is entropy compensation; i.e., using substrate binding energy to bring the reactive groups into proximity in the correct orientation.[106] The chemical steps then proceed in a relatively facile manner.

1.7. Structure and dynamics of *E. coli* DAHPS(Phe)

E. coli DAHPS(Phe) is a homotetramer in solution.[107] X-ray crystallography structures reveal that it has a dimer-of-dimers structure.[58,100,108,109] Monomers in the tight dimer (Figure 1.9A, subunits A/ B and C/D) interact through a multiplicity of van der Waals interactions and hydrogen bonding, as well as two antiparallel β-sheets comprised of two β-strands of one monomer and a third from the other (Figure 1.9B).[58] The weaker dimer-dimer interface consists primarily of electrostatic interactions and hydrogen bonds. The isoenzymes DAHPS(Tyr) and DAHPS(Trp) are both dimeric in solution.[98,110] Interestingly, they differ from DAHPS(Phe) in the amino acid residues that form the dimer-dimer interactions.[58]

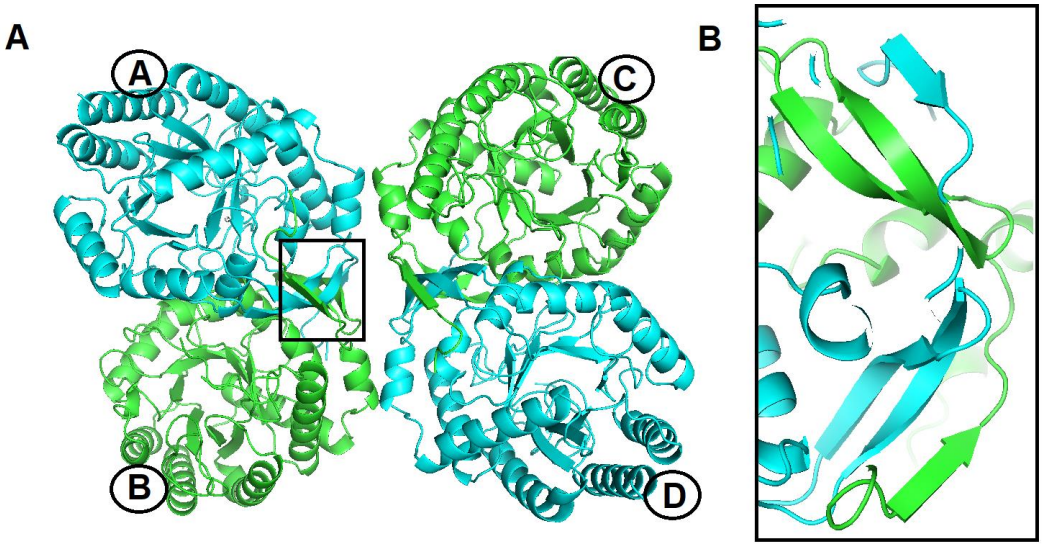

Figure 1.9 Structure of *E. coli* DAHPS(Phe).

(A) The $DAHPS_G$ (pdb ID: 5CKS[100]) homotetramer is structured as a tight dimer (A/B and C/D) and a dimer of dimers (AB/CD). (B) Zoomed in view of the tight dimer interface: two antiparallel three-stranded beta sheets, colored by subunit.

The individual subunits are built on a TIM barrel.[58] TIM barrels are common supersecondary structures, also called $(\alpha/\beta)_8$-folds, composed of eight parallel β-strands and eight α-helices surrounding the β-barrel.[111] This overall structure offers the possibility of incorporating structural elements for advanced functionalities by extending the loops that connect the α-helices and β-strands.[66] This is observed in DAHPS, as this extremely well-regulated enzyme possesses a TIM barrel which is extended by additional secondary structure elements at the protein's *N*-terminus and in α-β connecting loops (Figure 1.10).[66,109] The β-strands and α-helices of the TIM barrel are of differing lengths and consist of 4 – 7 and 7 – 19 residues, respectively.[58] The α-β connecting loops are located at the *N*-terminal side of the TIM barrel, and are generally shorter than the β-α

connecting loops at the *C*-terminal side. The *C*-terminal side of the barrel is furthermore the location of the active site,[58] a common phenomenon for $(\alpha/\beta)_8$-folds.[112] The binding site for the allosteric regulator is situated at the outskirts of the TIM barrel, at the *N*-terminal side of the barrel.[108] The cavity serving as Phe's binding site is formed by residues from both subunits of the tight dimer (Figure 1.10).

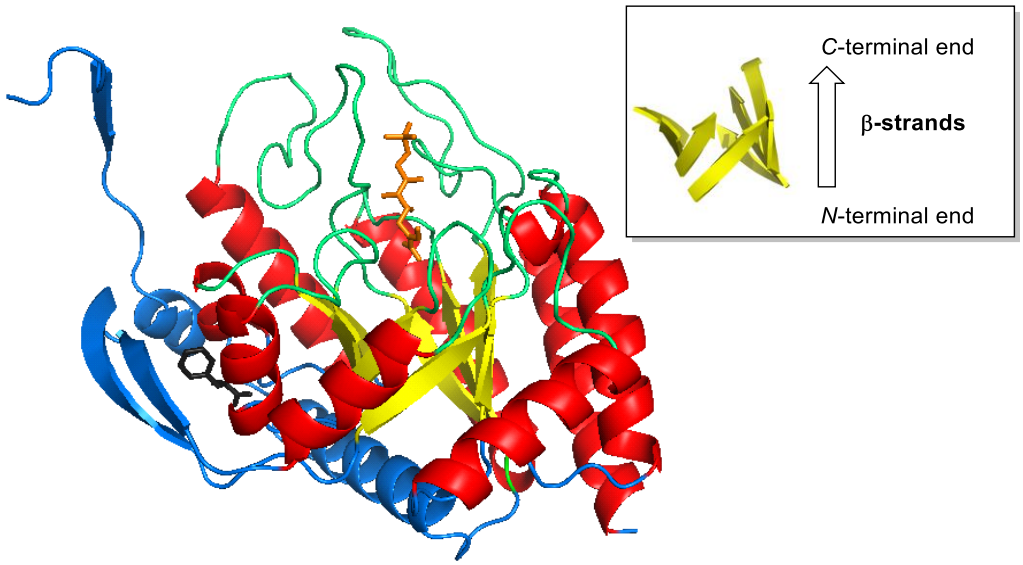

Figure 1.10 Subunit structure of DAHPS.

The β-strands, α-helices and loops are represented in yellow and red, respectively. The *C*-terminal side of the barrel (green) is the location of the active site, which is indicated by the bound DAHP derivative (orange). The allosteric Phe binding site is located at the *N*-terminal side (blue) of the TIM barrel. It is in contact with the anti-parallel β-sheet formed by β-strands from two subunits. Phe is represented in grey. Created from pdb ID: 5CKS[100] and 1KFL[108].

The active site consists mainly of positively charged amino acid residues to accommodate the two highly negatively charged substrates.[58,70,100] As many as five cationic residues form the PEP binding pocket (Arg92, Lys97, Arg165,

Lys186, and Arg234).[58] The metal binding pocket is more diverse; the divalent ion is coordinated by four amino acid residues (Cys61, His268, Glu302, and Asp326) and a water molecule (Figure 1.11A).[103] There is no interaction between PEP and the metal ion.[70] No crystal structure of DAHPS in complex with E4P has been obtained to date. However, a crystal structure with bound metal ion, PEP and the E4P analogue glycerol 3-phosphate (Gro3P) was solved to predict E4P's binding.[70] In comparison to E4P, Gro3P is lacking the C1 carbonyl functionality. The positioning of the E4P analogue in the structure by König *et al.* aligns well with the E4P derived moiety of the DAHP-based inhibitor DAHP oxime (Chapter 1.11.) which was co-crystallized with $DAHPS_G$ in our lab.[70,100] Both models suggest that E4P's phosphate moiety interacts with Arg99 and Thr100. The C2 and C3 hydroxyl groups seem well coordinated, with hydrogen bridges to residues Asp326 and Pro98. The aldehyde is predicted to coordinate to the metal ion as well as Lys97 (Figure 1.11B).[70,100] The residue Lys97 therefore plays an important role for catalysis by coordinating both substrates, orienting them properly for the enzymatic reaction and potentially transferring the proton to form a hydroxyl group in place of E4P's carbonyl group.[70] This is supported by the observation that a K97A mutant was reported as inactive.[70] Nonetheless, the kinetic data of this study was not shown and it was not investigated if the protein was correctly folded.

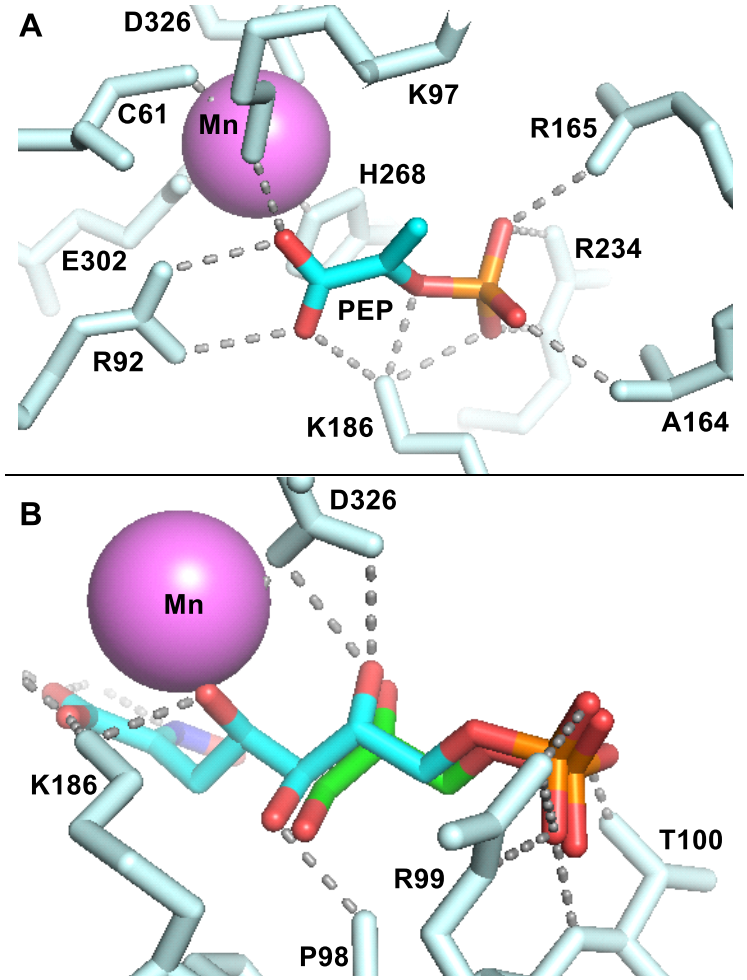

Figure 1.11 Crystal structure of DAHPS's substrates and mimics coordinated in the active site.

(A) Metal ion and PEP coordination in DAHPS's active site (pdb ID: 1N8F[109]) (B) Binding of Gro3P (green carbon backbone) and DAHP oxime (cyan carbon backbone) were analyzed to simulate E4P binding in the DAHPS binding pocket (pdb ID: 5CKS[100] and 1OF8[70])

It was demonstrated by a global hydrogen/deuterium exchange (HDX) experiment that the ligand-free DAHPS possesses an exceptionally high degree of flexibility, which is diminished upon substrate binding.[100] Spatially resolved HDX showed that the unbound protein is highly flexible even in sequences that form

secondary structure elements like α-helices in the substrate-bound state of the enzyme.[108,113] A similar observation was made by protein X-ray crystallography, where the structuring of loops responsible for ligand binding was observed for DAHPS·Co^{2+}·PEP or DAHPS·Co^{2+}·PEP·G3P in comparison to ligand-free DAHPS.[70] This further showed that substrate binding significantly reduces protein flexibility and leads to an ordering of structural elements.

1.8. DAHPS's metal requirement and metal coordination

All DAHPSs require a divalent metal co-factor.[50] The identity of the metal ion under physiological conditions is not known. Iron(II),[110,114,115] cobalt(II),[116,117] and copper(II)[118] have been proposed as endogenous cofactors. Various metal ions have been tested *in vitro*, with the observed activities being Mn^{2+} > Cd^{2+} > Fe^{2+} > Co^{2+} > Ni^{2+} > Cu^{2+} > Zn^{2+} > Ca^{2+}.[114] The identity of the metal ion can also affect the rate of product release.[102] Additionally, various metal ions showed differing residence times on the enzyme: while Fe^{2+}, Co^{2+} and Zn^{2+} were not easily displaced from the binding site, and could serve for more than one catalytic cycle, Mn^{2+}, Cu^{2+} and Ca^{2+} dissociated quickly.[114] The apparent degree of occupancy of DAHPS's active site was dependent on metal identity: DAHPS with Mn^{2+} reached only 30% occupancy, 52% with Zn^{2+} and 88% with Cu^{2+}.[102]

Metal ion coordination in the active site, as revealed by X-ray crystallography, is trigonal bipyramidal, independent of the metal's identity.[70] The four residues which constitute the metal binding site, Cys61, His268, Glu302 and

Asp326, are conserved in all DAHPSs.[50] A water molecule forming a bridge to Lys97 is commonly observed as the fifth ligand in structures containing metal ion plus PEP or a PEP analog.[58,103] Nonetheless, during enzymatic turnover, this water molecule is likely to be displaced by E4P. Studies by König *et al*. and our group suggest that E4P's carbonyl oxygen coordinates directly with the metal ion and Lys97 (Figure 1.11B) and is localized at an identical position as the water molecule.[70,100] The direct coordination of E4P's carbonyl functionality by the metal ion would lead to the activation of E4P's C1 for nucleophilic attack by PEP's C3. The hypothesis of a direct interaction between the metal ion and E4P is further strengthened by the observation that $K_{M,E4P}$ is dependent on metal identity.[114] There has been a long-term debate of whether the metal ion plays a catalytic or a structural role in DAHPS.[70,103,114] The assumption that E4P's carbonyl functionality is directly activated by metal coordination suggests that the metal cofactor in DAHPS is involved in catalysis.[70,114] Nevertheless, this does not exclude a structural function of the metal ion. Indeed, it has been previously observed that the addition of divalent metal ions leads to structural changes and stabilization of the enzyme.[119,120]

DAHPS structures coordinating Pb^{2+}, Mn^{2+}, Co^{2+}, and Cd^{2+} have been reported (pdb ID: 1OF8,[70] 1KFL,[108] 1N8F,[109] 1QR7,[58] 1RZM[91]). Depending on the characteristics of the metal ions, coordination distances to active site residues vary. Using the HSAB (hard and soft (Lewis) acids and bases) concept, metal ions can be characterized by their softness and hardness, which also reflects their

preference for the interaction with soft or hard ligands.[121] Mn^{2+}, the metal ion leading to the highest activation in DAHPS, is a hard Lewis acid, preferring interactions with oxygen donors (such as Glu302 and Asp326), while it does not strongly coordinate to nitrogen or thiol groups (such as Cys61 and His268).[102] Other metal ions, like Fe^{2+}, Co^{2+} and Zn^{2+}, which showed extended residence times for binding, are borderline metals and are more likely to interact with the imidazole and thiol functionalities. Considering metal preferences for ligand coordination, the function and properties of the metal binding site ligands are not clear. Cys61 was found to be important for catalysis and metal binding.[119] Furthermore, it has previously been observed that $K_{M,Mn2+}$ and $K_{M,E4P}$ collectively increased for the C61A mutant (16-fold and 440-fold, respectively).[106] At the same time, interaction of the thiol group and Mn^{2+} is weak.[122] If the sole function of C61 was to coordinate the metal ion, only modest differences would have been expected in the $K_{M,Mn}$, and especially in the $K_{M,E4P.}$ Therefore, besides metal coordination, a structural role for this residue is suspected.[120]

1.9. DAHPS inhibitors

Multiple DAHPS inhibitors have been characterized, and both inhibition of the isolated enzyme,[100,123–126] and bacterial growth inhibition[127] have previously been studied. In none of the bacterial growth inhibition studies DAHPS has been confirmed as the target of inhibition. To date, no DAHPS inhibitor has entered clinical trials. Nonetheless, these reported inhibitors are of great importance, as

they probe what kinds of inhibitor design are possible and serve as mechanistic tools to allow a deeper insight into DAHPS catalysis. A common design strategy is to mimic DAHPS's substrates, intermediates, or the presumed transition states (TSs). Mimicking intermediates assists to confirm proposed catalytic pathways and gives indications of the intermediate's stereochemistry. DAHPS's substrates are highly negatively charged, which has been reflected in the inhibitor design: To date, there are no small neutral inhibitors of DAHPS, even though a negative charge commonly hinders cell membrane penetration and *in vivo* effectiveness. In addition, comparing the reported potencies of the inhibitors is very difficult, as the authors utilize differing equations for K_i determination. The kinetic properties of the enzyme, such as ordered substrate binding and product release for the K_M determination, as well as the mode of inhibition of the small molecules, are often not examined or are not considered in the choice of the equations.

1.9.1. Oxacarbenium ion mimics

In the cationic mechanism of THI formation (Figure 1.8), an oxacarbenium ion intermediate is formed. Multiple DAHPS inhibitors have attempted to mimic this putative intermediate (Figure 1.12). Compound **1** mimics the positive charge at the carbon atom of the oxacarbenium ion intermediate with an aminophosphonate functionality.[125] Its structure is based on an inhibitor previously designed for KDO8PS.[128] This dual site inhibitor was created to interact with both the PEP and distal phosphate binding site corresponding to

E4P's phosphate binding site. Compound **1** and the corresponding analogue of KDO8P exhibit slow-binding inhibition.[125] Compound **2** was designed based on the assumption that the phosphate's C-O bond has a partial double bond character in the oxacarbenium intermediate, which introduces planarity to the molecule.[124] This planarity is imitated by the vinyl phosphonate. Adding a trifluoromethyl group did not enhance the inhibitory efficiency. Inhibitor **3** was based on the same pharmacophore, but extended to capture binding energy from E4P phosphate's binding site.[126]

Oxacarbenium ion intermediate mimic

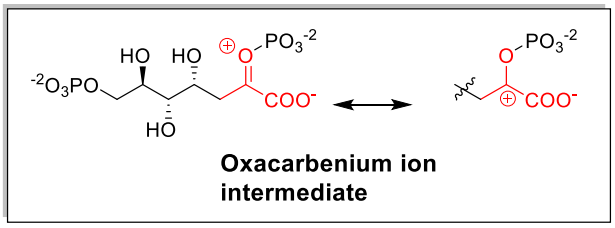

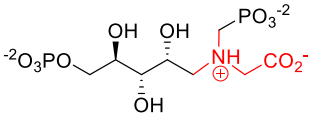

1

IC_{50} = 6.6 μM

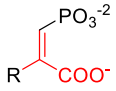

2

R=CH_3: K_i = 4.7 μM

R=CF_3: K_i = 8.8 μM

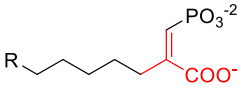

3

R=OPO_3^{-2}: K_i = 5.3 μM

R=Br :K_i = 3.6 μM

Figure 1.12 Inhibitors based on the oxacarbenium ion intermediate.

IC_{50} or K_i values were determined with *E. coli* DAHPS(Phe).

1.9.2. Tetrahedral intermediate mimics

Several inhibitors are based on the THI (Figure 1.13). To capture the tetrahedral geometry and increase the compound's stability, the THI's phosphate was replaced by a phosphonate group. The resulting compounds **4a** (seven carbon backbone, based on DAHP) and **4b** (eight carbon backbone, based on KDO8P) inhibited growth of several Gram-negative bacteria, including *E. coli*.[127] The phospholactate enantiomers, **5**, were designed as THI mimics, and inhibited DAHPS competitively with respect to PEP.[124] The (*R*)-enantiomer was >10-fold more potent than the (*S*)-enantiomer. The inhibitors with the lowest K_i values reported to date are the enantiomers of the bisphosphate, **6**, (K_i = 360 nM and 620 nM).[123] Their design was based on **5**, extended to serve as a dual binding site inhibitor.

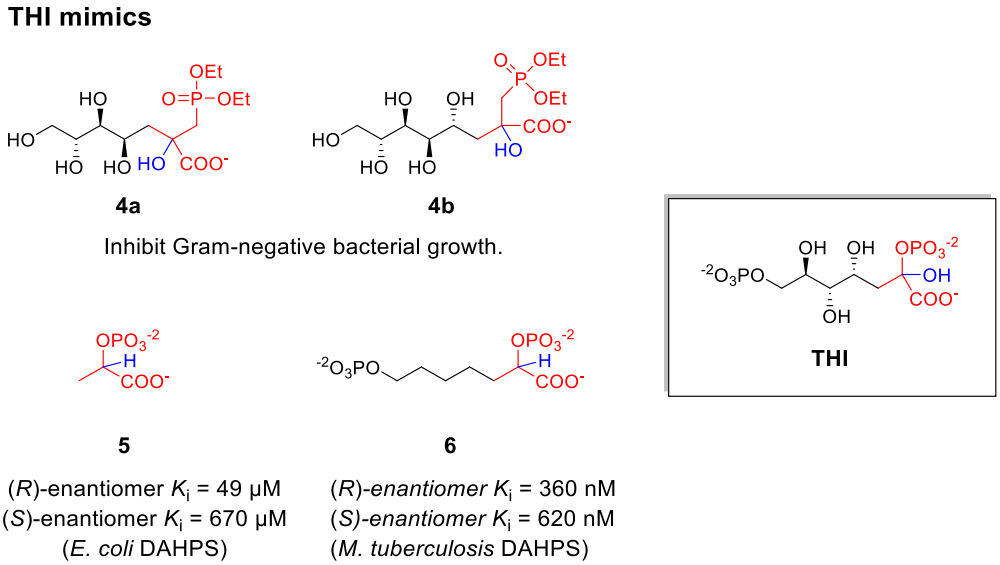

Figure 1.13 THI mimics as DAHPS inhibitors.

The THI and the mimicking structural elements are coloured.

1.9.3. Substrate mimics

Few E4P mimics have been reported (Figure 1.14). Fosmidomycin, a 1-deoxy-D-xylulose 5-phosphate reductoisomerase inhibitor, was tested for DAHPS inhibition.[124] Due to its structure and binding mode to DXP reductoisomerase, it was expected to interact with E4P's binding pocket and coordinate the metal ion. Inhibition was observed, but it was competitive with respect to PEP and uncompetitive with E4P, implying that it bound in the PEP binding site. Fosmidomycin's inhibition of DAHPS had slow onset, and the extent of inhibition depended on the identity of the metal ion.[124]

PEP mimics have been designed for the inhibition and characterization of a plethora of PEP-utilizing enzymes and metabolic pathways.[129–131] Some have been tested on DAHPS. Replacing PEP's phosphate group with a bioisosteric sulphate group did not result in an DAHPS inhibitor.[124] The allylic phosphonate, **7**, was designed with the intention that the absence of the phosphate's bridging oxygen would hinder P_i release and interrupt catalysis (Figure 1.14).[124] The success of this strategy initiated the development of the dual site inhibitor **8**.[126]

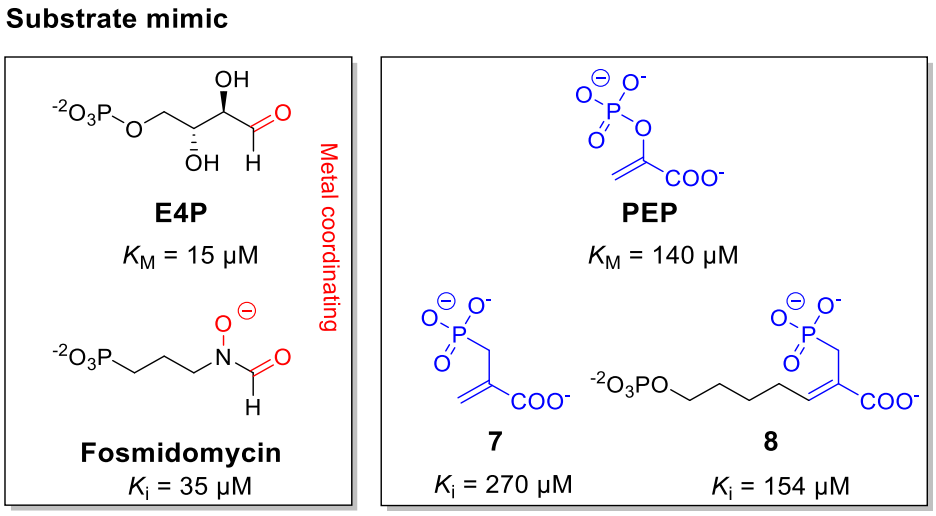

Figure 1.14 Substrate mimics imitating E4P and/or PEP binding.

1.10. Other α-carboxyketose synthase inhibitors

The catalytic similarities among α-carboxyketose synthase superfamily members implies that inhibition of all enzymes of this family might be achievable by comparable strategies. Therefore, it is indispensable to be informed about inhibitors of KDO8PS and NeuB (Figure 1.15). Several KDO8PS inhibitors have been described, including the oxacarbenium ion intermediate mimic, **9a**, that later served as basic structure for the DAHPS inhibitor **1** (Chapter 1.9.1).[128] This bisubstrate inhibitor exhibited slow-binding inhibition. Despite its high efficacy, no bacterial growth inhibition by this inhibitor or its phosphonate derivative, **9b,** were observed, most likely due to cell membrane impermeability.[132] The acyclic product analogue, **10**, inhibited KDO8PS.[128,133] For NeuB, the potent THI mimic inhibitor, **11**, with slow binding behaviour has been reported. X-ray

crystallography showed that only the (2*R*)-isomer of the racemic inhibitor mixture was bound, indicative of the THI's stereochemistry in NeuB.[76]

KDO8PS inhibitors

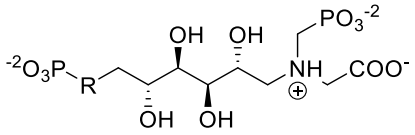

9a

R = O
oxacarbenium ion mimic
K_i = 3.3 μM; K_i* =0.4 μM

9b

R = CH_2
oxacarbenium ion mimic
K_i = 50 μM

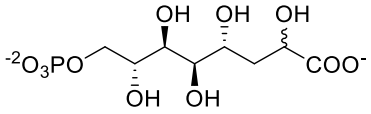

10

acyclic product mimic
K_i = 500 μM

NeuB inhibitors

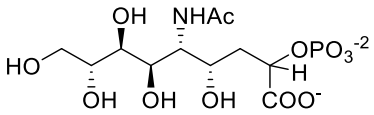

11

THI mimic
K_i = 3.1 μM

Figure 1.15 Inhibitors of KDO8PS and NeuB.

In **9a**, K_i* represents the slow binding inhibition constant.

1.11. DAHP oxime

DAHP oxime is a potent, slow-binding DAHPS inhibitor (Figure 1.16A).[100,106] Its design was based on experiences in our laboratory with NeuNAc oxime, a slow and tight-binding inhibitor of NeuB (K_i* = 1.6 pM).[134,135] DAHP oxime is prepared in a simple one-step synthesis from DAHP, with the 2-keto group reacting with hydroxylamine to form an oxime. It inhibits DAHPS with

K_i = 1.5 µM.[100] Similar to NeuNAc oxime and several other reported inhibitors of the α-carboxyketose synthase superfamily enzymes,[76,124,125,128] DAHP oxime shows slow-binding inhibition with a residence time, t_R, of 83 min, where $t_R = 1/k_{off}$. Competitive binding behavior with respect to both substrates and the metal cofactor was demonstrated.[100] X-ray crystallography showed that DAHP oxime occupies both the PEP and E4P binding sites. The metal binding site was vacant, and isothermal titration calorimetry (ITC) experiments demonstrated that DAHP oxime was unable to bind to the DAHPS·Mn^{2+} complex, demonstrating competitive binding behaviour of the metal ion and DAHP oxime (Chapter 2.3.6).[100] Crystal structures revealed that the inhibitor binds to only two of the four subunits of the homotetrameric enzyme, leaving one subunit per tight dimer empty. These unoccupied subunits explain the 15% residual activity even at high DAHP oxime concentrations.[100] The coordination of the DAHP moiety of the inhibitor occurs with the same residues which are responsible for PEP and E4P binding, while the oxime functionality, in combination with two crystallographic waters, captures some of the interactions of the THI's phosphate group in the binding pocket, suggesting that the oxime acts as a phosphate group mimic in DAHPS (Figure 1.16B and C).[100]

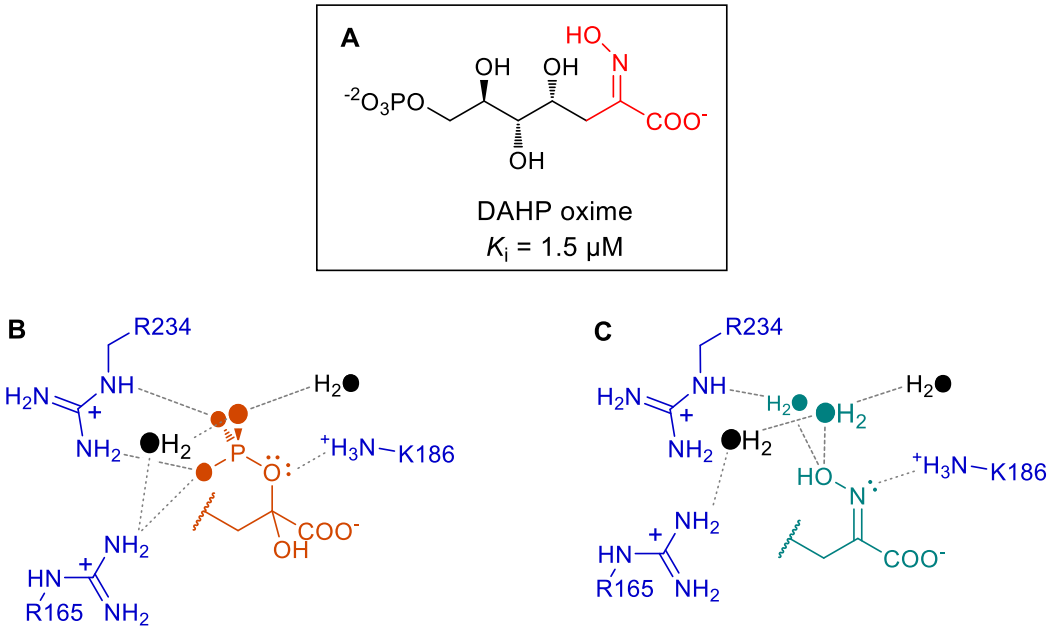

Figure 1.16 (A) The structure of DAHP oxime and a comparison of the active site interactions of (B) the THI and (C) DAHP oxime.

Figure from Balachandran *et al.* (2017).[106]

Phosphate is abundant in all living organisms. It is a building block of our DNA and RNA; it is involved in intracellular energy transfer in the form of ATP; it is part of lipids that form biomembranes; and many metabolic intermediates contain phosphate groups.[136] The development of phosphate mimics is therefore a major concern in medicinal chemistry. Nevertheless, their design remains challenging because of the phosphate group's negative charge and hydrolytic susceptibility *in vivo*.[137] Most bioisosteric phosphate replacements are either charged, which hinders cell membrane penetration, or bulky, which could interfere with binding in some phosphate binding sites.[138] Similar issues have been described for the previously proposed inhibitors of α-carboxyketose synthase

enzymes (Chapter 1.9 and 1.10). The molecules are highly charged and fail to inhibit bacterial cell growth.[127,132] The oxime functional group, when acting as a phosphate mimic, has the advantages of being uncharged and small, which helps cell membrane penetration and makes it applicable to a wide range of targets.[100]

A linear free energy relationship (LFER) analysis with seven DAHPS mutant enzymes showed that the inhibitor does not only mimic phosphate structurally but also functions as a TS mimic of THI breakdown.[106] Enzymes catalyze chemical processes by stabilizing the TS of the reaction, and thereby lowering its activation energy (Figure 1.17A). During this process, the enzyme binds the TS many times more tightly than the substrates or products, which results in dissociation constants for transition states between 10^{-14} to 10^{-23} M.[139] TS analogues, that is, compounds that mimic the TS, can be potent inhibitors with high selectivity towards their target.[140] LFER analysis of enzyme inhibitors involves examining the relationship between k_{cat}/K_M and K_i. The specificity constant, k_{cat}/K_M, reflects the free energy difference between free enzyme and substrate in solution (E + S), and the transition state for the first irreversible step of the reaction ($E \cdot S^{\ddagger}$). The specificity constant therefore describes the quality of the TS stabilization (Figure 1.17A). The K_i expresses inhibitor binding as the equilibrium constant between enzyme and inhibitor free in solution (E + I), and the enzyme·inhibitor complex (E·I). If an inhibitor is interacting with active site residues in the same manner as the TS, k_{cat}/K_M and K_i should exhibit a log linear

relationship to each other when the enzymatic function is perturbed by modifying either the enzyme or parallel modifications of the substrate and inhibitor. For this LFER analysis, seven DAHPS mutants were generated. Because DAHPS has three substrates, the three substrate specificity constant $k_{cat}/(K_{M,Mn},K_{M,PEP},K_{M,E4P})$ was examined in relation to K_i, and a linear relationship was found (Figure 1.17B).[106] This LFER analysis therefore demonstrated that DAHP oxime is a TS mimic. For the THI breakdown and phosphate departure, a protonation step at the phosphate's bridging oxygen is crucial.[105] In DAHPS, Lys186 is the presumed general acid catalyst for this step. DAHP oxime mimics this interaction with Lys186, and therefore mimics the TS of the THI breakdown.[106]

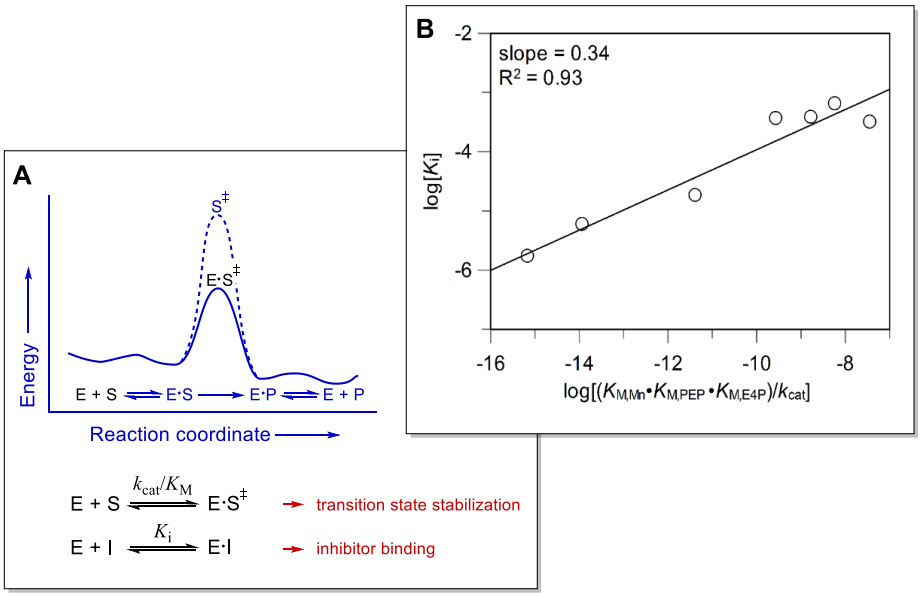

Figure 1.17 A linear free energy relationship analysis for DAHP oxime.

(A) Basics of enzymatic function. The enzymatic stabilization of the TS during the catalytic turnover lowers the activation energy. (**B**) LFER analysis with DAHP oxime using seven mutant enzymes of DAHPS. A linear relationship between $\log((K_{M,Mn},K_{M,PEP},K_{M,E4P}/k_{cat})$ and $\log(K_i)$ was observed. Figure from Balachandran *et al.* (2017).[106]

1.12. Research objective

DAHP oxime is a TS mimic inhibitor of DAHPS (K_i = 1.5 µM) and shows slow-binding behavior. Nevertheless, the inhibitor has three drawbacks that were addressed in independent projects:

Chapter 2 discusses the competitive mode of binding by DAHP oxime with respect to Mn^{2+}. Metal identity and concentrations in living cells are highly variable, so the efficacy of a metal-competitive inhibitor becomes unpredictable. We found that DAHP oxime is no longer metal-competitive at basic pH. With mutant enzymes of DAHPS, we identified active site residues that influence the mode of binding and used fragment-based inhibitor design to establish an inhibitor design strategy which prevents the metal/ inhibitor competition in DAHPS.

Chapter 3 addresses the high hydrophilicity which prevents DAHP oxime from penetrating into cells. The metal noncompetitive fragment introduced in Chapter 2 has been optimized by the addition of fluorine to the pyruvate moiety to increase potency and by esterification of the carboxylate to decrease the hydrophilicity. Also, different imine derivatives have been synthesized and characterized. Based on these modifications, bacterial growth inhibition was observed, and inhibition was relieved by the DAHPS overexpression, suggesting that the inhibitor is indeed targeting the enzyme in cells. This showed us for the first time that DAHPS is a suitable target for small molecule inhibitors to stop bacterial growth.

Chapter 4 discusses the residual activity that is observed even at high DAHP oxime concentrations. DAHP hydrazone and DAHP *O*-(2-fluoroethyl) oxime, which are structurally closely related to DAHP oxime, do not show residual activity. DAHP hydrazone furthermore possesses increased potency in comparison to the oxime derivative. X-ray crystallographic study was performed to analyze differences of the DAHP derivatives' binding in the active site and their influence on enzyme conformations.

Chapter 2. The mode of inhibition by DAHP oxime is pH dependent

2.1. Introduction

Recently, DAHP oxime binding to DAHPS was found to be competitive with the metal co-factor under physiological conditions, even though inhibitor and metal do not occupy the same physical space.[100] The origin of metal/ inhibitor competition remains unknown. Understanding this competition is critical for *in vivo* success of DAHPS inhibitors because the abundance of metal ions in living cells could hinder the effectiveness of DAHPS inhibitors. Furthermore, it has been demonstrated that some metal ions show exceptionally tight binding to DAHPS and are not readily displaced from the active site.[114] Competition between these metal ions and the inhibitor is therefore undesirable. Most DAHPS inhibitors in literature, including DAHP oxime, resemble substrates, intermediates or the presumed transition states of DAHPS's catalytic mechanism (Chapter 1.9), and many of them mimic the THI.[123,124,127] Based on our experience with DAHP oxime, these inhibitors could potentially exhibit metal competition, as they were designed based on a similar strategy. Indeed, it has previously been observed that the quality of Fosmidomycin's inhibition (Chapter 1.9.3) was dependent on the metal ion's identity.[124] To successfully inhibit DAHPS and to make this enzyme accessible as a reliable target for antibiotics, it is crucial to understand the nature of the competition between metal and inhibitor binding. While investigating the pH profile of inhibition for DAHP oxime, an apparently lowered K_i under basic conditions was observed. This initiated a closer investigation of DAHP oxime's

binding at high pH to take advantage of the inhibitor's supposedly enhanced potency. But instead of tighter binding, it became evident that the mode of inhibition for DAHP oxime changes at high pH, with metal ion and DAHP oxime binding no longer being competitive. Mutant enzymes, as well as inhibitor fragments, were designed to explore the origin of this competition. The project aimed for the identification of active site residues as well as structural elements of the inhibitor that are responsible for the competition. An optimized inhibitor design to avoid metal competitive binding is suggested.

2.2. Materials and Methods

2.2.1. General

After it was demonstrated that $DAHPS_{H6}$ showed equivalent kinetic properties to the His-tag cleaved $DAHPS_G$,[100] *N*-terminally His_6-tagged DAHPS ($DAHPS_{H6}$) was used for all steady state kinetic experiments. Purification for both enzymes followed previous established methods.[100] Mutant enzymes were generated by N. Balachandran.[141] Kinetic experiments were performed using the colorimetric Malachite Green/ammonium molybdate assay for inorganic phosphate (P_i) released over time due to the enzymatic turnover.[142] The substrate E4P was synthesized following an adapted protocol,[141] which was based on the established method reported by Sieben *et al*.[143] All solutions, with the exception of the enzyme and $MnCl_2$ were treated with Chelex 100 to remove contaminating

metal ions. All enzymatic reactions were performed at 25 °C. All reagents were purchased from Sigma-Aldrich or Bioshop (Burlington, ON), unless otherwise stated.

2.2.2. DAHPS$_G$ kinetic parameters

All experiments were performed by varying one substrate concentration, while keeping the other two at 250 µM in kinetics buffer (50 mM K-HEPES, pH 7.0, 100 mM KCl, 0.1 mM TCEP). The $MnCl_2$ concentration was varied from 0 to 0.075 mM; PEP was varied from 0 to 1 mM, and E4P was varied from 0 to 1 mM. A premix was prepared containing all substrates, and the reaction was started by adding 25 nM DAHPS$_G$. The kinetic parameters were fitted using eq. **2.1** for the rapid equilibrium sequential ordered ter ter kinetic mechanism:[144]

$$\frac{v_0}{[E]_0} = \frac{\dfrac{k_{cat}[Mn][PEP][E4P]}{K_{Mn}K_{PEP}K_{E4P}}}{1+\dfrac{[Mn]}{K_{Mn}}+\dfrac{[Mn][PEP]}{K_{Mn}K_{PEP}}+\dfrac{[Mn][PEP][E4P]}{K_{Mn}K_{PEP}K_{E4P}}} \quad (2.1)$$

For the calculation of the individual K_M of all three substrates, as well as for $k_{cat}/(K_{M,Mn}K_{M,PEP}K_{M,E4P})$, the equation was restructured to fit $k_{cat}/(K_{M,Mn}K_{M,PEP}K_{M,E4P})$ as a single parameter (eq. **2.2**) which resulted in lower standard errors:

$$\frac{v_0}{[\mathrm{E}]_0} = \frac{\left(\frac{k_{\mathrm{cat}}}{K_{\mathrm{M,Mn}} K_{\mathrm{M,PEP}} K_{\mathrm{M,E4P}}}\right)[\mathrm{Mn}][\mathrm{PEP}][\mathrm{E4P}]}{1 + \frac{[\mathrm{Mn}]}{K_{\mathrm{M,Mn}}} + \frac{[\mathrm{Mn}][\mathrm{PEP}]}{K_{\mathrm{M,Mn}} K_{\mathrm{M,PEP}}} + \frac{[\mathrm{Mn}][\mathrm{PEP}][\mathrm{E4P}]}{K_{\mathrm{M,Mn}} K_{\mathrm{M,PEP}} K_{\mathrm{M,E4P}}}} \quad (2.2)$$

2.2.3. pH profile of the K_M's and $k_{cat}/(K_{M,Mn},K_{M,PEP},K_{M,E4P})$ of $DAHPS_{H6}$

The Michaelis constants (K_M) and k_{cat} were determined for $DAHPS_{H6}$ at the individual pH values tested. Two substrate concentrations were kept constant (Table 2.1), while the third was varied. PEP varied from 0 to 8 mM, E4P from 0 to 2 mM and $MnCl_2$ from 0 to 1 mM. A substrate premix containing PEP, E4P and $MnCl_2$, as well as 0.1 mM TCEP, was prepared and each kinetic experiment was initiated by adding the enzyme. The reaction was quenched at 10 s time intervals, with an overall duration of the experiment of 1 min. Under basic conditions, Mn^{2+} stability in solution was impaired due to the formation of manganese hydroxide. To avoid precipitation, the $MnCl_2$ concentration was reduced at basic pH and Mn^{2+} was added into the reaction mix at the same time as the enzyme to reduce the exposure time to the basic environment. The kinetic parameters were calculated based on eq. **2.1** and **2.2**.

Table 2.1 Conditions for the k_{cat}, K_M and $k_{cat}/(K_{M,Mn},K_{M,PEP},K_{M,E4P})$ determination at varying pH.

pH	buffer [a]	[$MnCl_2$] (μM)	[PEP] (mM)	[E4P] (mM)	[$DAHPS_{H6}$] (nM)	Enzyme preincubation with Mn^{2+}?
7 [b]	50 mM K-HEPES	2	0.1	0.1	25	No
8	50 mM K-HEPES	10	0.5	0.25	100	No
8 - 9	50 mM K-CHES	10	0.5	0.25	100	No
10	50 mM K-CAPS	10	2.5	0.25	100	Yes
10.5	50 mM K-CAPS	1	5	0.5	100	Yes

[a] Kinetics buffers also contained 100 mM KCl, and 0.1 mM TCEP.
[b] Data collected by N. Balachandran.[141]

The pH profile for $K_{M,Mn}$ was fitted to yield a single pK_a for the basic limb with eq. **2.3**:

$$K_{M,Mn} = Limit \times \frac{10^{3\times(pK_a - pH)}}{10^{3\times(pK_a - pH)}+1} \quad (2.3),$$

where *Limit* is the upper limit for $K_{M,Mn}$ at acidic pH.

The pH profile of $K_{M,PEP}$ showed a single pK_a for the acidic limb and was fitted to eq. **2.4**:

$$K_{M,PEP} = Limit\left(1 - \frac{10^{(pK_a - pH)}}{10^{(pK_a - pH)}+1}\right) \quad (2.4)$$

where *Limit* was the upper limit for $K_{M,PEP}$ at basic pH.

The pH profile for $K_{M,E4P}$ was fitted to a bell-shaped curve (eq. **2.5**), as two ionizing groups were observed:

$$K_{M,E4P} = Limit \times \frac{10^{pH-pK_{a1}}}{10^{2\times pH - pK_{a1} - pK_{a2}} + 10^{pH-pK_{a1}} + 1} \quad (2.5)$$

where *Limit* was the upper limit of the $K_{M,E4P}$ values, and pK_{a1} and pK_{a2} were the pK_a values of the acidic and basic limb, respectively. Similarly, the pH profile of $k_{cat}/(K_{M,Mn},K_{M,PEP},K_{M,E4P})$ was fitted to eq. **2.5**.

2.2.4. pH profile of K_i

All substrate concentrations were kept constant (Table 2.1) while the DAHP oxime concentration was varied from 0 to 800 µM. The reactions were initiated by the addition of 100 nM $DAHPS_{H6}$ and the reaction progress was monitored over 1 min. The fast binding inhibition data were initially fitted on the assumption that inhibitor binding was competitive with respect to all three substrates (eq. **2.6**).[144]

$$\frac{v_0}{V_{max}} = \frac{\dfrac{k_{cat}[Mn][PEP][E4P]}{K_{M,Mn}K_{M,PEP}K_{M,E4P}}}{1+\dfrac{[Mn]}{K_{M,Mn}}+\dfrac{[Mn][PEP]}{K_{M,Mn}K_{M,PEP}}+\dfrac{[Mn][PEP][E4P]}{K_{M,Mn}K_{M,PEP}K_{M,E4P}}+\dfrac{[I]}{K_i}} + offset \qquad (2.5)$$

The pH profile of K_i was fitted to yield a single pK_a for the basic limb (eq. **2.7**):

$$K_i = \frac{limit1 + limit2 \times 10^{3\times(pH-pK_a)}}{1+10^{3\times(pH-pK_a)}} \qquad (2.6),$$

where limit1 and limit2 are the K_i values at low and high pH, respectively.

2.2.5. Kinetic constants for C61A at pH 10

Determining the $K_{M,Mn}$ and K_i values for the C61A mutant required determining all the substrates' K_M values at basic pH so they could be used to calculate the kinetic parameters based on eq. **2.1** and **2.2** for a rapid equilibrium ordered sequential ter ter kinetic mechanism. K_M values were determined by varying one substrate while the other two were kept constant at 10 mM PEP, 4.5 mM E4P and 0.3 µM $MnCl_2$. The experiment was performed in 50 mM CAPS, pH 10, 100 mM KCl and 0.1 mM TCEP, with 4.5 µM $DAHPS_{H6}$. A substrate premix was prepared, and the reaction was initiated with the addition of enzyme and $MnCl_2$. P_i production was monitored by the Malachite Green/ammonium molybdate assay in 5 min intervals over 30 min. C61A inhibition by DAHP oxime was investigated at pH 10 using an identical method, but keeping substrate concentrations at 10 mM PEP, 4.5 mM E4P, and 305 µM $MnCl_2$. The kinetic parameters, as well as K_i for DAHP oxime were fitted to eq. **2.1**, **2.2** and **2.6**.

2.2.6. DAHP O-methyloxime – synthesis and inhibitory properties at pH 7 and 10

DAHP was synthesized by incubating 0.021 mmol PEP, 0.02 mmol E4P, 0.05 µmol $MnCl_2$, and 2 nmol DAHPS(Phe) in 5 mL buffer (10 mM K-HEPES, pH 7.0) at room temperature for 3h. After the reaction was completed, an Amicon Ultra 0.5 mL centrifugal filter was used to remove the enzyme. To the crude DAHP reaction mix containing 3.75 mM DAHP, 25 mM methoxyamine

hydrochloride was added, and the pH was adjusted to 5.5. The reaction progress was confirmed by HPLC and ^{1}H NMR and the product quantified by ^{1}H NMR.

Inhibition at pH 7 was determined in 50 mM K-HEPES, pH 7, 100 mM KCl and 0.1 mM TCEP. A substrate premix was prepared with 9 µM $MnCl_2$, 0.5 mM PEP and 0.25 mM E4P, and the reaction was started with 100 nM DAHPS.

The inhibition experiment at pH 10 was performed in 50 mM K-CAPS, pH 10, 100 mM KCl and 0.1 mM TCEP. The substrates were kept at a constant concentration of 2.5 mM PEP, 0.25 mM E4P, and 9 µM $MnCl_2$. To avoid metal precipitation, the enzyme and Mn^{2+} were added into the premix of substrates simultaneously to initiate the reaction.

2.2.7. DAHP oxime mode of inhibition at pH 7 and 9 by ITC titration

Isothermal titration calorimetry (ITC) was performed using a NanoITC calorimeter (TA Instruments, Delaware, MD), with the kind permission of Prof. Richard Epand and the advice of Dr. José Bozelli. Purification of $DAHPS_{H6}$ was performed as described previously.[100] After elution from the Ni^{2+}-loaded Hightrap Chelating-Sepharose column (GE Healthcare), the enzyme was kept in the elution buffer (50 mM Tris-Cl, pH 7.0, 100 mM KCl, 400 mM imidazole), and 10% glycerol, 0.1 mM TCEP and 1 mM EDTA were added, followed by a two-day incubation to remove bound metal ions. The enzyme solution was then dialyzed against 3 ×1 L of 20 mM K-HEPES, pH 7.0, and 0.1 mM TCEP to

remove the EDTA. The enzyme was concentrated to 185 µM using a Amicon Ultra 4 mL centrifugation filter (EMD Millipore Corporation).

DAHP oxime was synthesized and purified as described previously.[141] After the anion exchange purification on a Q-Sepharose column (GE Healthcare), the sample was lyophilized repeatedly to remove residual ammonium formate. This was done to minimize the background signal due to NH_4^+'s heat of dilution during the ITC experiment. An aliquot of the inhibitor was then dried and dissolved to 400 µM in the ultrafiltrate from the enzyme's concentration step. Similarly, a 400 µM $MnCl_2$ solution was prepared with the ultrafiltrate. All solutions were degassed in a vacuum chamber under stirring for 15 min at 15°C, then the calorimeter's reference cell was filled with 170 µL of ultrafiltrate. The reaction cell was filled with 170 µL of the $DAHPS_{H6}$ or $DAHPS_{H6}{\cdot}Mn^{2+}$ solution, and blank titrations were performed with buffer in the reaction cell. The titrant ($MnCl_2$ or DAHP oxime) was loaded into the 50 µL injection needle. All solutions were equilibrated under constant stirring (300 rpm) to 20°C. A total of 19 injections was performed, the first with a volume of 0.48 µL and all subsequent ones with a volume of 2.5 µL.

For the K_d determination at pH 9, the enzyme was buffer exchanged by centrifugal ultrafiltration immediately before the experiment into 20 mM K-CHES, pH 9.0, and 0.1 mM TCEP, then concentrated to 100 µM. A solution of 400 µM DAHP oxime and a stock solution of $MnCl_2$ were prepared using the

ultrafiltrate. After degassing all solutions for 15 min, $MnCl_2$ was added to the DAHPS solution to a final concentration of 400 μM $MnCl_2$.

K_d values were calculated using the NanoAnalyze software (TA Instruments). The areas of the single injection peaks were plotted as a function of injection number. The calculations take into consideration the fact that the working volume of solution in the titration cell (V_o) is held constant at 170 μL, with the added volume of titrant (ΔV) resulting in an equal volume of titration mixture moving into the inactive tube. Thus, the initial enzyme concentration ($M°_t$) in the working volume (V_o) decreases through the course of the titration. The enzyme concentration at point *t*, M_t, can be expressed with eq. **2.8**:

$$M_t = M_t^\circ \left(\frac{1 - \frac{\Delta V}{2 \times V_\circ}}{1 + \frac{\Delta V}{2 \times V_\circ}} \right) \tag{2.7}$$

A similar assumption must be made for the actual bulk concentration of the ligand (X_t) in relationship to the hypothetical bulk concentration $X°_t$ (eq. **2.9**):

$$X_t = X_t^\circ \left(1 - \frac{\Delta V}{2 \times V_\circ} \right) \tag{2.8}$$

For independent binding to identical binding sites, equations eq. **2.10** and **2.11** apply:

$$K_d = \frac{\theta}{(1 - \theta) \times [X]} \tag{2.9}$$

$X_t = [X] + n\theta M_t$ (2.10),

where K_d is the dissociation equilibrium constant, θ is the fraction of binding sites occupied by ligand *X*, [*X*] is the free ligand concentration, and *n* is the number of binding sites. Combining eq. **2.10** and **2.11** leads to the quadratic equation (eq. **2.12**):

$$\theta^2 - \theta\left[1 + \left(\frac{X_t}{nM_t}\right) + \left(\frac{1}{nK_d M_t}\right)\right] + \frac{X_t}{nM_t} = 0 \quad (2.11)$$

The total heat, *Q*, in V_o at a specific θ value can be expressed as eq. **2.13**:

$Q = n\theta M_t \Delta H V_o$ (2.12),

where ΔH is the enthalpy of ligand binding.

Combining eq. **2.12** and **2.13** finally leads to equation **2.14**, which enables the calculation of *Q* after the i^{th} injection:

$$Q = \frac{nM_t \Delta H V_o}{2}\left[1 + \left(\frac{X_t}{nM_t}\right) + \left(\frac{1}{nK_d M_t}\right) - \sqrt{\left(1 + \frac{X_t}{nM_t} + \frac{1}{nK_d M_t}\right)^2 - \frac{4X_t}{nM_t}}\right] \quad (2.13)$$

Fitting the equation requires initial guesses for *n*, K_d, and ΔH.[145]

2.2.8. DAHP oxime's mode of inhibition at pH 9 by fast binding initial velocity experiments

Initial velocities were measured in buffer containing 50 mM K-CHES, pH 9.0, 100 mM KCl and 0.1 mM TCEP, with two constant substrate concentrations of 0.25 mM each of PEP and E4P, and 10 μM $MnCl_2$, while the third was varied. The inhibitor concentration was kept constant at 50 μM DAHP oxime. Both, the PEP and the $MnCl_2$ concentration were varied up to 1 mM. All reactions were initiated with 25 nM $DAHPS_{H6}$.

2.2.9. K_i values for pH dependent mode of inhibition

The mode of inhibition, i.e., competitive vs. noncompetitive vs. uncompetitive, affects how K_i values are calculated. When the mode of inhibition changes as a function of pH, then K_i calculations must consider the fraction of inhibition that is metal competitive vs. not metal competitive at each pH. These fractions are determined by the pH and the pK_a, and can be calculated with the Henderson-Hasselbalch equation (eq. **2.15**).

$$\mathrm{pH} = \mathrm{p}K_a + \log\left(\frac{[\mathrm{A}^-]}{[\mathrm{HA}]}\right) \tag{2.14}$$

The rapid equilibrium sequential ordered ter ter kinetic mechanism equation that assumes competition between inhibitor and metal binding (eq. **2.6**) applies to lower pH, while at higher pH, equation **2.16**[144] applies, which assumes

noncompetitive inhibition with respect to the metal ion, but competitive inhibition with respect to the other two substrates.

$$\frac{v_0}{[\mathrm{E}]_0} = \frac{k_{\mathrm{cat}} \dfrac{[\mathrm{Mn}][\mathrm{PEP}][\mathrm{E4P}]}{K_{\mathrm{M,Mn}} K_{\mathrm{M,PEP}} K_{\mathrm{M,E4P}}}}{\left(1+\dfrac{[\mathrm{I}]}{K_{\mathrm{i}}}\right)\left(1+\dfrac{[\mathrm{Mn}]}{K_{\mathrm{M,Mn}}}\right)+\dfrac{[\mathrm{Mn}][\mathrm{PEP}]}{K_{\mathrm{M,Mn}} K_{\mathrm{M,PEP}}}+\dfrac{[\mathrm{Mn}][\mathrm{PEP}][\mathrm{E4P}]}{K_{\mathrm{M,Mn}} K_{\mathrm{M,PEP}} K_{\mathrm{M,E4P}}}} \qquad (2.15)$$

Initial velocities in the overall equation (eq. **2.17**) for the pH dependent mode of inhibition are the sum of the two terms representing inhibition which is competitive (eq. **2.18**) and noncompetitive (eq. **2.19**) with respect to Mn^{2+}:

$$\frac{v_0}{[\mathrm{E}]_0} = \left(1-\frac{10^{\mathrm{pH}-\mathrm{p}Ka}}{10^{\mathrm{pH}-\mathrm{p}Ka}+1}\right)\times competitive + \left(\frac{10^{\mathrm{pH}-\mathrm{p}Ka}}{10^{\mathrm{pH}-\mathrm{p}Ka}+1}\right)\times noncompetitive + offset \qquad (2.16),$$

where:

$$competitive = \frac{\dfrac{k_{\mathrm{cat}}[\mathrm{Mn}][\mathrm{PEP}][\mathrm{E4P}]}{K_{\mathrm{M,Mn}} K_{\mathrm{M,PEP}} K_{\mathrm{M,E4P}}}}{1+\dfrac{[\mathrm{Mn}]}{K_{\mathrm{M,Mn}}}+\dfrac{[\mathrm{Mn}][\mathrm{PEP}]}{K_{\mathrm{M,Mn}} K_{\mathrm{M,PEP}}}+\dfrac{[\mathrm{Mn}][\mathrm{PEP}][\mathrm{E4P}]}{K_{\mathrm{M,Mn}} K_{\mathrm{M,PEP}} K_{\mathrm{M,E4P}}}+\dfrac{[\mathrm{I}]}{K_{\mathrm{i,comp}}}} \qquad (2.17)$$

$$noncompetitive = \frac{\frac{k_{cat}[Mn][PEP][E4P]}{K_{M,Mn}K_{M,PEP}K_{M,E4P}}}{\left(1+\frac{[I]}{K_{i,noncomp}}\right)\left(1+\frac{[Mn]}{K_{M,Mn}}\right)+\frac{[Mn][PEP]}{K_{M,Mn}K_{M,PEP}}+\frac{[Mn][PEP][E4P]}{K_{M,Mn}K_{M,PEP}K_{M,E4P}}} \quad (2.18)$$

The equation was fitted for $K_{i,comp}$, the competitive inhibition constant, $K_{i,noncomp}$, the noncompetitive inhibition constant, the pK_a for the change in mode of inhibition, and *offset*, the residual activity at high inhibitor concentrations. The other kinetic parameters were set as constants, using the fitted values from eq. **2.1** and **2.2**.

2.2.10. DAHP O-methyloxime's mode of inhibition

Rate assays to probe competition between DAHP *O*-methyloxime and Mn^{2+} were performed at pH 7 with 0.1 mM PEP and E4P, 1.5 mM DAHP *O*-methyloxime, and $MnCl_2$ concentrations from 5 µM to 5 mM. At pH 9, the substrate concentrations were kept at 0.25 mM PEP and E4P, with 1.5 mM DAHP *O*-methyloxime, and $MnCl_2$ concentrations from 2 µM to 2 mM.

2.2.11. Mutant enzymes' mode of inhibition over the pH range

The fast binding inhibition experiments and the Eadie-Hofstee plot to determine the mode of inhibition for the DAHPS mutants C61A, D326A and H268A were performed in 50 mM K-HEPES, pH 7.0, 100 mM KCl and 0.1 mM TCEP, using individually adapted substrate and enzyme concentrations (Table

2.2), and varying $MnCl_2$ concentrations ranging from 5 µM to 10 mM. The reactions were initiated by the addition of the enzyme and P_i production was followed in individually adapted time intervals (Table 2.2).

Table 2.2 Fast binding reaction conditions for the DAHPS mutant enzymes.

	[PEP] (mM)	[E4P] (mM)	[DAHP oxime] (mM)	[DAHPS] (nM)	time interval [a] (min)
C61A	0.6	1	0.25, 1, 4	1975	10
D326A	0.5	1	0.25	825	2
H268A	0.5	0.05	0.04, 0.2, 1	400	3

[a] Time interval between aliquots in initial velocity measurements. There were typically six aliquots per v_0 measurement.

ITC titrations for D326A to determine the competitiveness of DAHP oxime and Mn^{2+} binding were performed as for $DAHPS_{H6}$, but with 120 µM $DAHPS_{H6}$ in 20 mM Tris-Cl, pH 7.0, 0.1 mM TCEP, and 800 µM $MnCl_2$, being titrated with 800 µM DAHP oxime.

2.2.12. Fragment-based inhibitors' mode of inhibition

Pyruvate oxime and glyoxylate oxime were synthesized as previously described.[146] The K_i values for both, in combination with glycerol 3-phosphate (Gro3P), have previously been determined, but were re-calculated based on eq. **2.16**. The K_i for glyoxylate oxime and erythritol 4-phosphate (Ero4P) was determined in kinetic buffer with 250 µM PEP, 125 µM E4P, 50 µM $MnCl_2$, 8 mM Ero4P and varying glyoxylate oxime concentrations. The reactions were initiated by adding 50 nM $DAHPS_{H6}$. The K_i value was fitted using eq. **2.6**. Using the same conditions, an Eadie-Hofstee plot for glyoxylate oxime and Ero4P was

generated. Here, the inhibitor concentration was fixed at 5, 16.7, 50, or 65 mM while the $MnCl_2$ concentration was varied from 50 to 1000 µM. The competitiveness of binding between the metal ion and pyruvate oxime plus Gro3P was further tested using an Eadie-Hofstee plot. The substrate premix was prepared in 50 mM K-HEPES, pH 7.0, 100 mM KCl, and 0.1 mM TCEP, with 0.1 mM each of PEP and E4P. The $MnCl_2$ concentration was varied from 2 to 1000 µM. The Gro3P concentration was constant at 4 mM, and the pyruvate oxime concentration was set to 0.78, 3, or 12.5 mM. The reactions were initiated by adding 25 nM $DAHPS_{H6}$ and aliquots were taken at 30 s time intervals.

2.3. Results

2.3.1. Kinetic parameters for $DAHPS_G$

The kinetic properties of $DAHPS_G$ and $DAHPS_{H6}$ calculated by the rapid equilibrium sequential ordered ter ter kinetic mechanism equation (eq. **2.1** and **2.2**) did not differ significantly from each other (Table 2.3). The largest difference was in the values of $K_{M,PEP}$, which were 2.5-fold higher in $DAHPS_G$. This corresponds to a free energy difference of 0.5 kcal/mol, equivalent to about one-fifth of a good hydrogen bond. While the differences in the $K_{M,PEP}$ values could be readily measured, they were not functionally significant. The K_M's of E4P and Mn^{2+} were very similar between $DAHPS_{H6}$ and $DAHPS_G$.

Table 2.3 A comparison of the steady state kinetic parameters for $DAHPS_{H6}$ and $DAHPS_G$.

	Substrate		
	Mn^{2+}	PEP	E4P
		$DAHPS_{H6}$ [a]	
k_{cat} (s^{-1}) [b]		16.4 ± 0.6	
K_M (μM) [c]	5.5 ± 0.7	140 ± 20	15 ± 2
$k_{cat}/(K_{Mn}K_{PEP}K_{E4P})$ [c] ($M^{-3}s^{-1}$)		$(1.5\pm 0.2) \times 10^{15}$	
		$DAHPS_G$	
k_{cat} (s^{-1}) [b]		12.1 ± 0.4	
K_M (μM) [c]	5.0 ± 0.8	370 ± 70	13 ± 3
$k_{cat}/(K_{Mn}K_{PEP}K_{E4P})$ [c] ($M^{-3}s^{-1}$)		$(5 \pm 0.7) \times 10^{14}$	

[a] Data collected by N. Balachandran.[100]
[b] Fitted to eq. **2.1.**
[c] Fitted to eq. **2.2.**

2.3.2. pH profile of K_M's and $k_{cat}/(K_{M,Mn},K_{M,PEP},K_{M,E4P})$

The pH profile of $DAHPS_{H6}$'s steady state kinetic parameters were examined. Each substrate's Michaelis constant, determined by the rapid equilibrium sequential ordered ter ter kinetic mechanism equations (**eq. 2.1** and **2.2**), exhibited a characteristic pH profile (Figure 2.1). The pH profiles for $K_{M,Mn}$, $K_{M,PEP}$ and $K_{M,E4P}$ were fitted to the **eq. 2.3**, **2.4**, and **2.5**, respectively. $K_{M,Mn}$ showed a significant (21-fold) decrease towards basic pH, with the basic limb pK_a = 8.2. In contrast, $K_{M,PEP}$ increased over the same pH range, while $K_{M,E4P}$ displayed a bell-shaped pH dependence.

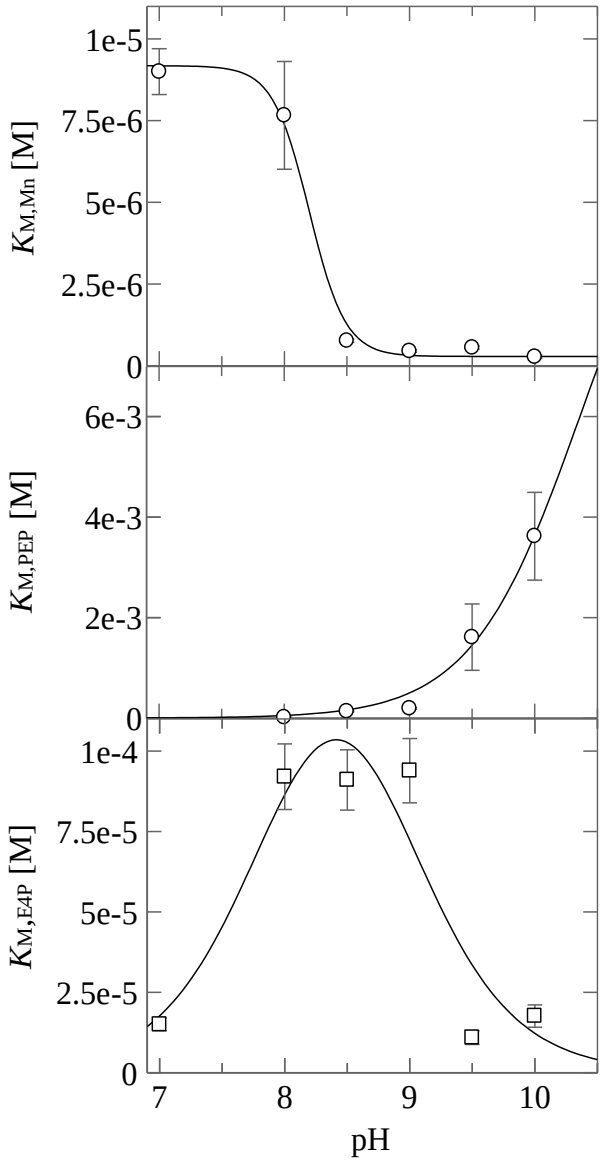

Figure 2.1 The pH profile of the Michaelis constants $K_{M,Mn}$, $K_{M,PEP}$ and $K_{M,E4P}$ as a function of pH.

The pH profile of the specificity constant $k_{cat}/(K_{M,Mn},K_{M,PEP},K_{M,E4P})$ was characterized by a bell-shaped curve with a basic limb located at a pK_a = 9.7 ± 0.2 (Figure 2.2). The acidic limb was located at pK_a = 7.0 ± 0.2. The catalytic efficiency reached its maximum at pH = 8.4.

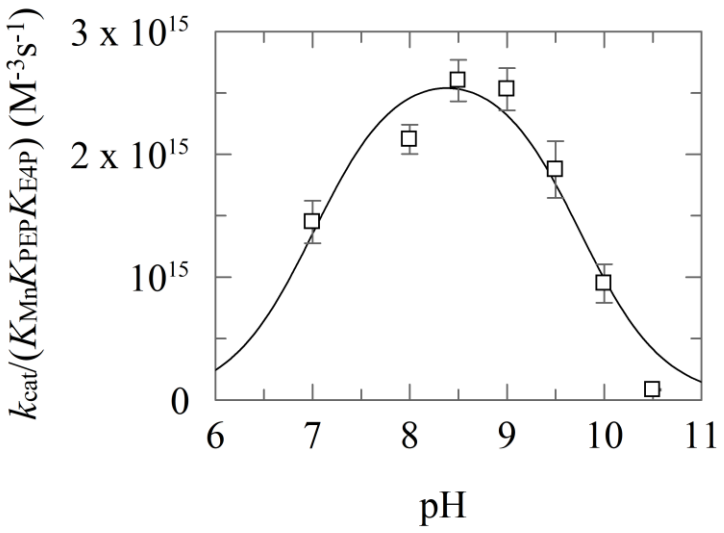

Figure 2.2 The pH profile of the specificity constant, $k_{cat}/(K_{M,Mn}K_{M,PEP}K_{M,E4P})$, of $DAHPS_{H6}$.

2.3.3. pH dependence of DAHP oxime inhibition

The apparent pH profile of DAHP oxime's K_i value was fitted to a purely competitive inhibition model (eq. **2.6**) and yielded a single pK_a (**eq. 2.7**) with a basic limb pK_a = 8.7 ± 0.1 (Figure 2.3). The acidic region could not be investigated due to enzyme denaturation during the rate assays at pH < 7. The apparent K_i value decreased significantly from neutral to basic pH, implying tighter binding at basic pH. As discussed below (Chapter 2.3.6), this change in apparent K_i was due to a change in the mode of inhibition.

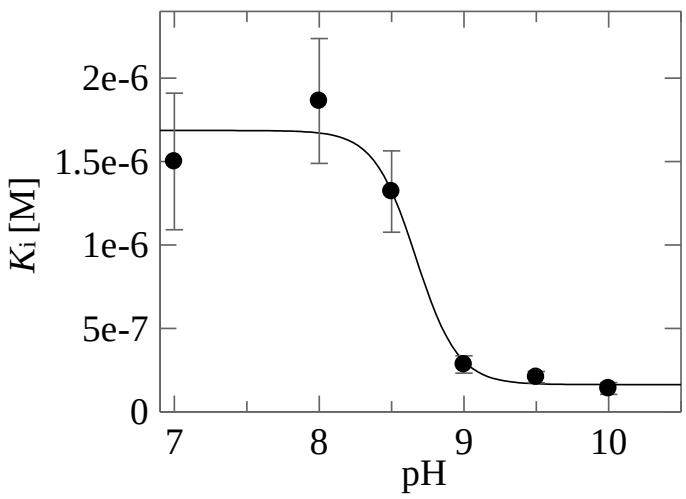

Figure 2.3 DAHP oxime pH profile assuming purely competitive inhibition.

K_i values at each pH were fitted using eq. **2.6**, then the pH-dependence of K_i was fitted to eq. **2.7**.

2.3.4. C61A's $K_{M,Mn}$ and K_i at pH 7 and pH 10

With $DAHPS_{H6,}$ the basic limbs for both $K_{M,Mn}$ and K_i were located at p$K_a \approx 8.2$, similar to the pK_a of an unperturbed Cys side chain. C61 is an active site residue and part of the metal binding site.[103] To examine if ionization of this residue was involved in the pH dependencies of $K_{M,Mn}$ and K_i, the C61A mutant was characterized (Figure 2.4). The decrease in $K_{M,Mn}$ from pH 7 to 10 in $DAHPS_{H6}$ was absent in C61A. Instead, there was a slight, 2.2-fold, increase in $K_{M,Mn}$ from pH 7 to 10 (Table 2.4). The 4-fold decrease in DAHP oxime's K_i value between pH 7 and pH 10 in C61A was less pronounced than the 11.5-fold decrease in $DAHPS_{H6}$ (Figure 2.4). K_i values were fitted based on the assumption that inhibitor binding was competitive with respect to all three substrates (eq. **2.6**).

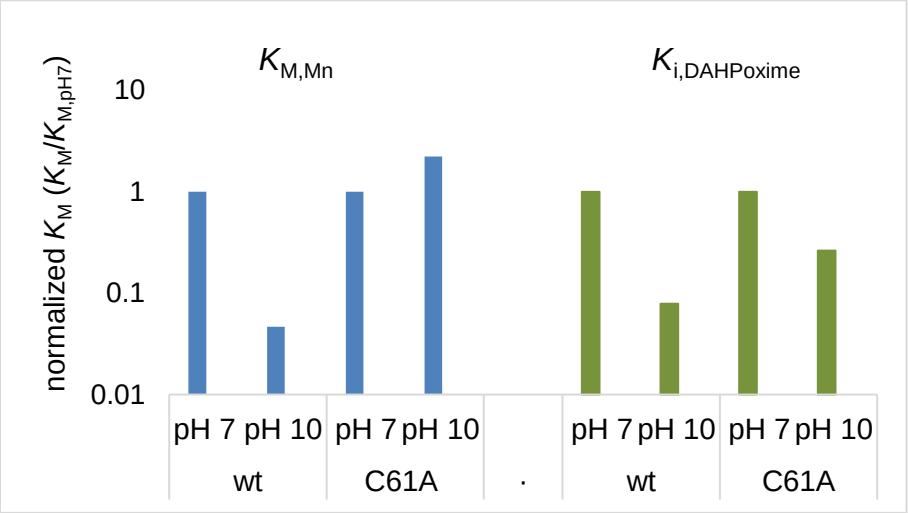

Figure 2.4 Normalized $K_{M,Mn}$ and K_i values at pH 7 and pH 10 for $DAHPS_{H6}$ wildtype (wt) and C61A mutant.

Table 2.4. $K_{M,Mn}$ and K_i values for $DAHPS_{H6}$ and C61A at pH 7 and 10.

	$DAHPS_{H6}$	C61A
	$K_{M,Mn}$ (M)	
pH 7	$(5.5 \pm 0.7) \times 10^{-6}$	$(9.0 \pm 1) \times 10^{-5}$
pH 10	$(2.6 \pm 1) \times 10^{-7}$	$(2.0 \pm 0.5) \times 10^{-4}$
$K_{M,Mn}$(pH 7)/$K_{M,Mn}$(pH 10)	21.2	0.45
	K_i (M)	
pH 7	$(1.5 \pm 0.4) \times 10^{-6}$	$(3.8 \pm 0.6) \times 10^{-4}$
pH 10	$(1.3 \pm 0.4) \times 10^{-7}$	$(1.0 \pm 0.3) \times 10^{-4}$
K_i(pH 7)/K_i(pH 10)	11.5	3.8

2.3.5. DAHP O-methyloxime inhibition at pH 7 and 10

$DAHPS_{H6}$ inhibition by DAHP *O*-methyloxime was tested under neutral and basic conditions. The K_i values were 7.9 ± 0.1 μM at pH 7 and 7.5 ± 0.2 μM at pH 10 (Figure 2.5). Therefore, there was no effect of pH on DAHP *O*-

methyloxime binding, in contrast to the apparent 12.7-fold decrease in DAHP oxime's K_i over the same pH range.

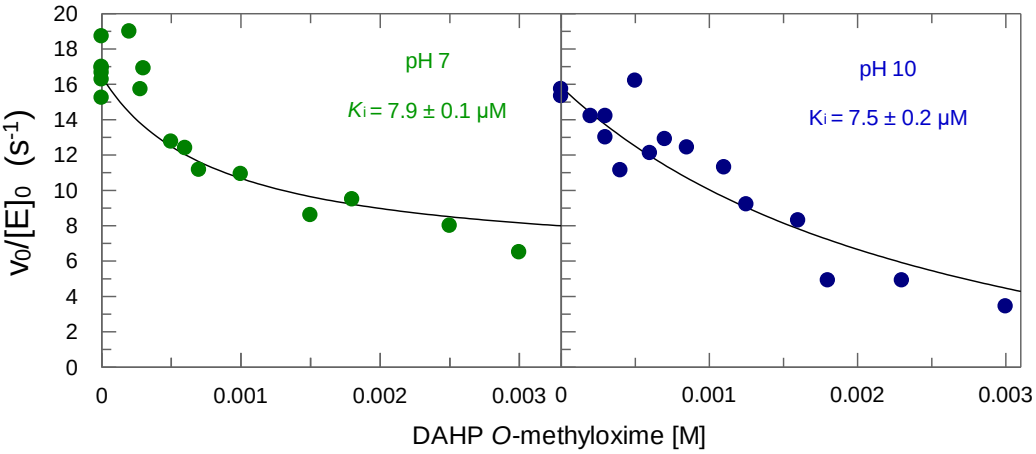

Figure 2.5 Inhibition of DAHP *O*-methyloxime at pH 7 (left) and pH 10 (right).

K_i values for DAHP *O*-methyloxime were found by fitting initial velocity data to eq. **2.6**, which assumed competitive inhibition with respect to all three substrates.

2.3.6. Mode of inhibition by DAHP oxime at pH 7 and pH 9

DAHP oxime's mode of inhibition with respect to the metal ion was further studied using ITC titrations. At a neutral pH, DAHP oxime bound to $DAHPS_{H6}$ with K_d = 3.1 µM, but it was not possible to detect binding to $DAHPS_{H6}{\cdot}Mn^{2+}$ in three independent trials. Binding of Mn^{2+} to $DAHPS_{H6}$, and therefore the formation of the $DAHPS_{H6}{\cdot}Mn^{2+}$ complex, was confirmed by a separate titration, and resulted in a K_d = 5.3 µM (Figure 2.6).

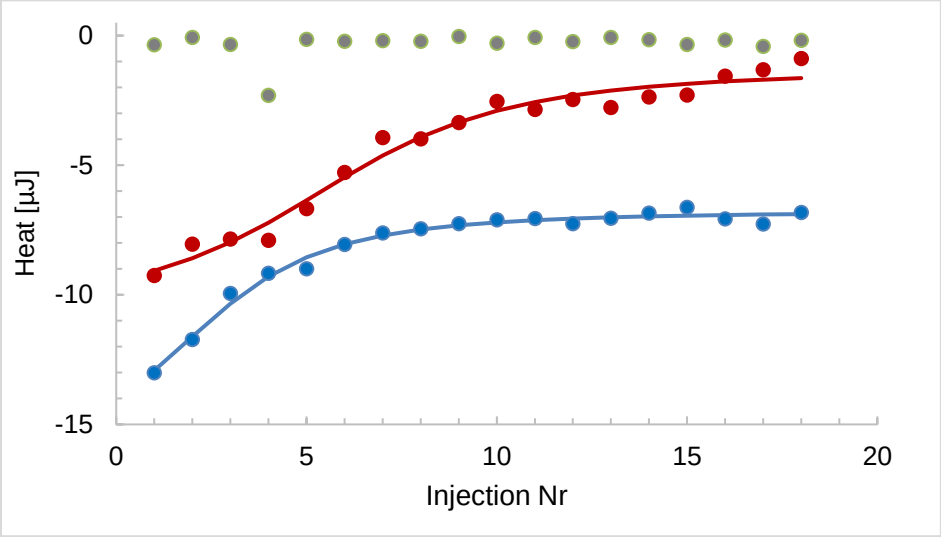

Figure 2.6 ITC titrations of DAHP oxime binding to $DAHPS_{H6}$ and $DAHPS_{H6}\cdot Mn^{2+}$.

Titrations were performed for Mn^{2+} binding to $DAHPS_{H6}$ (red), DAHP oxime binding to $DAHPS_{H6}$ (blue), and DAHP oxime binding to the $DAHPS_{H6}\cdot Mn^{2+}$ complex (grey). The data points for the $DAHPS_{H6}\cdot Mn^{2+}$ complex titration with DAHP oxime were shifted up by 4 µJ to improve visibility.

The mode of inhibition at pH 9 was investigated with both fast binding initial velocity experiments and ITC titrations. Both experiments demonstrated that inhibition was no longer competitive with respect to Mn^{2+} (Figure 2.7). Three independent ITC trials resulted in $K_d = 4.1 \pm 0.7$ µM for DAHP oxime binding to $DAHPS_{H6}\cdot Mn^{2+}$ at pH 9 (Figure 2.7B). The K_i did not differ significantly from the K_i at pH 7. At the same time, the competitive mode of inhibition of DAHPS by DAHP oxime and PEP was retained (Figure 2.7A).

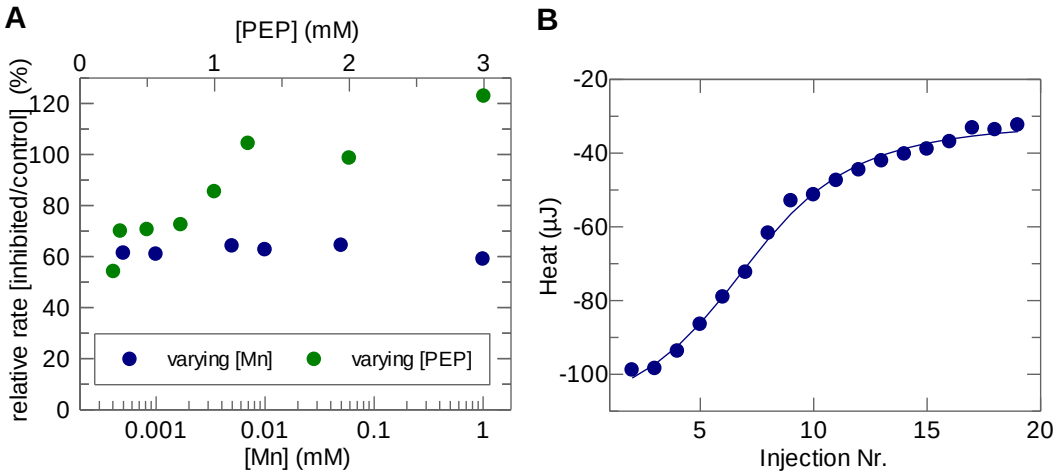

Figure 2.7 DAHP oxime's mode of $DAHPS_{H6}$ inhibition at pH 9.

(A) Relative initial velocities at pH 9 as a function of $[Mn^{2+}]$ and [PEP]. At fixed [DAHP oxime], increasing [PEP] increased the relative rate while increasing $[MnCl_2]$ did not. This indicated that Mn^{2+} did not compete with DAHP oxime. The fixed concentrations were 10 µM $MnCl_2$, 250 µM PEP, 50 µM DAHP oxime, with 25 nM $DAHPS_{H6}$. (B) ITC titrations showed DAHP oxime binding to $DAHPS_{H6}\cdot Mn^{2+}$ at pH 9, with K_d = 4.1 ± 0.7 µM.

2.3.7. Consequences of changing modes of inhibition on K_i determination

The initial velocity data for DAHP oxime inhibition of $DAHPS_{H6}$, which were previously fitted to a purely competitive model (eq. **2.6**) were re-fitted to a model that accommodated the change in mode inhibition with pH. In this model (eq. **2.17**) the mode of inhibition with respect to Mn^{2+} changed from competitive at low pH to noncompetitive at high pH. Based on this equation, the mode of inhibition changed with pK_a = 8.7 ± 0.1, while the change in dissociation constants was modest. For metal competitive inhibition, $K_{i,comp}$ = 3.7 ± 0.6 µM, while for metal noncompetitive inhibition, $K_{i,noncomp}$ = 6.6 ± 0.9 µM (Figure 2.8).

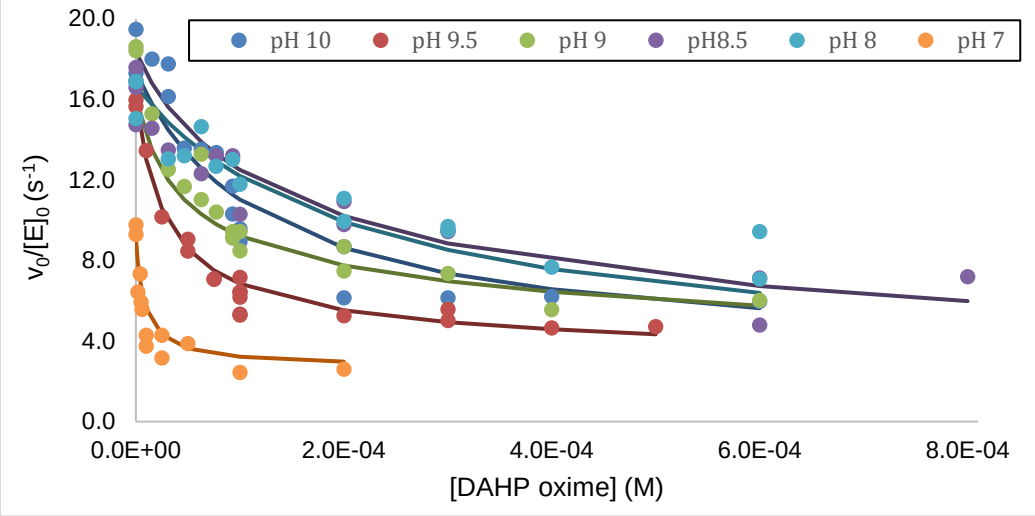

Figure 2.8 Fitting DAHP oxime's changing mode of inhibition at high pH.

$K_{i,comp}$ and $K_{i,noncomp}$ were fitted to a model (eq. **2.17**) that accounts for the change in mode of inhibition with respect to Mn^{2+} as a function of pH. The change in mode of inhibition occurred with pK_a = 8.7 ± 0.1. $K_{i,comp}$ = 3.7 ± 0.6 µM and $K_{i,noncomp}$ = 6.6 ± 0.9 µM, indicating that the inhibitor affinity was barely affected by pH.

2.3.8. DAHP O-methyloxime's mode of inhibition at basic pH

The mode of inhibition at pH 7 and 9 with respect to the metal ion was investigated for DAHP *O*-methyloxime by a fast binding initial velocity experiment. At constant DAHP *O*-methyloxime concentrations, increasing $MnCl_2$ concentrations reduced the extent of inhibition, indicating competitive binding behaviour at neutral and basic pH (Figure 2.9).

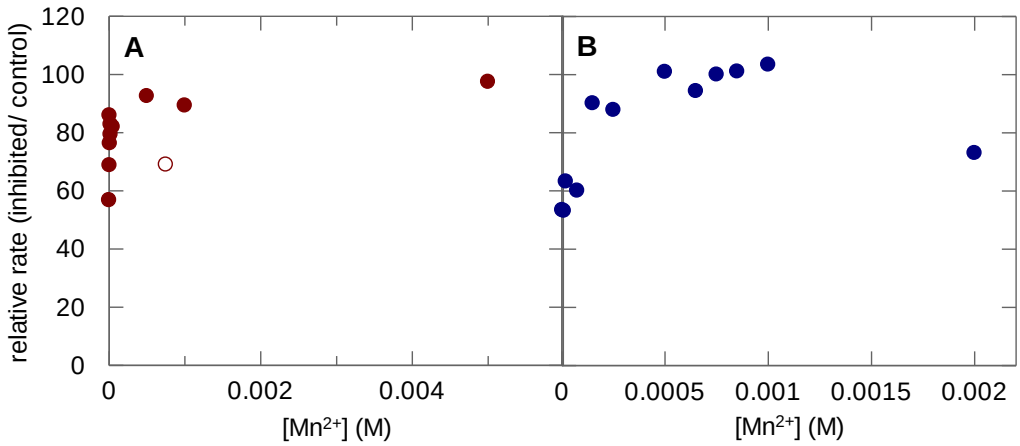

Figure 2.9 DAHP *O*-methyloxime's mode of $DAHPS_{H6}$ inhibition at pH 7 and 9.

Relative initial velocities at (A) pH 7 and (B) pH 9 as a function of $[Mn^{2+}]$ indicate competitive binding behaviour between DAHP *O*-methyloxime and Mn^{2+}. At constant [DAHP *O*-methyloxime], increasing $[Mn^{2+}]$ increased the relative rate.

2.3.9. Mutant enzymes' mode of inhibition

Given the extremely modest differences in $K_{i,comp}$ (predominating at pH < 8) and $K_{i,noncomp}$ (predominating at pH > 9), inhibitor ionization seemed unlikely to be responsible for the change in inhibition. The unperturbed pK_a value of an oxime hydroxyl group is ≈11.3 (see Chapter 3.3.1). Based on its location in the phosphate binding site in $DAHPS_{H6}$,[100] a lowered pK_a value in the active site is plausible, but the K_i value would be expected to decrease upon introducing a negative charge into a phosphate binding site. The essentially constant $K_{i,comp}$ versus $K_{i,noncomp}$ values argue against differences in the inhibitor, and prompted an investigation of ionizable active site residues. C61, D326 and H268 were identified as candidates based on their participation in metal ion binding and

proximity to the active site. D326 additionally coordinates DAHP oxime through O4 (Figure 2.10).

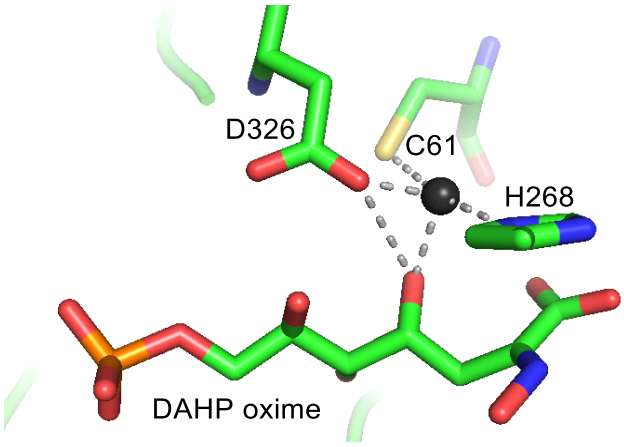

Figure 2.10 Model of the DAHPS·Mn^{2+}·DAHP oxime active site.

DAHP oxime and residues C61, H268 and D326 are from the $DAHPS_G$·DAHP oxime structure (pdb ID:5CKS)[100] and the Mn^{2+} ion is from the DAHPS·Mn^{2+}·PEP structure (pdb ID:1N8F).[109]

The mutant enzymes C61A, D326A and H268A were tested for their mode of inhibition by DAHP oxime using a variety of techniques. Fast binding inhibition experiments showed that DAHP oxime and Mn^{2+} binding was not competitive in the mutants C61A and D326A (Figure 2.11A). Specifically, increased [$MnCl_2$] could not reduce inhibition, indicating that the inhibition is not of a competitive nature. These results were further confirmed by an ITC titration for D326A (Figure 2.11B). DAHPS·Mn^{2+} was titrated with DAHP oxime and binding was observed with a K_d = 14.2 ± 5 μM from three independent trials, like the previously reported value.[106]

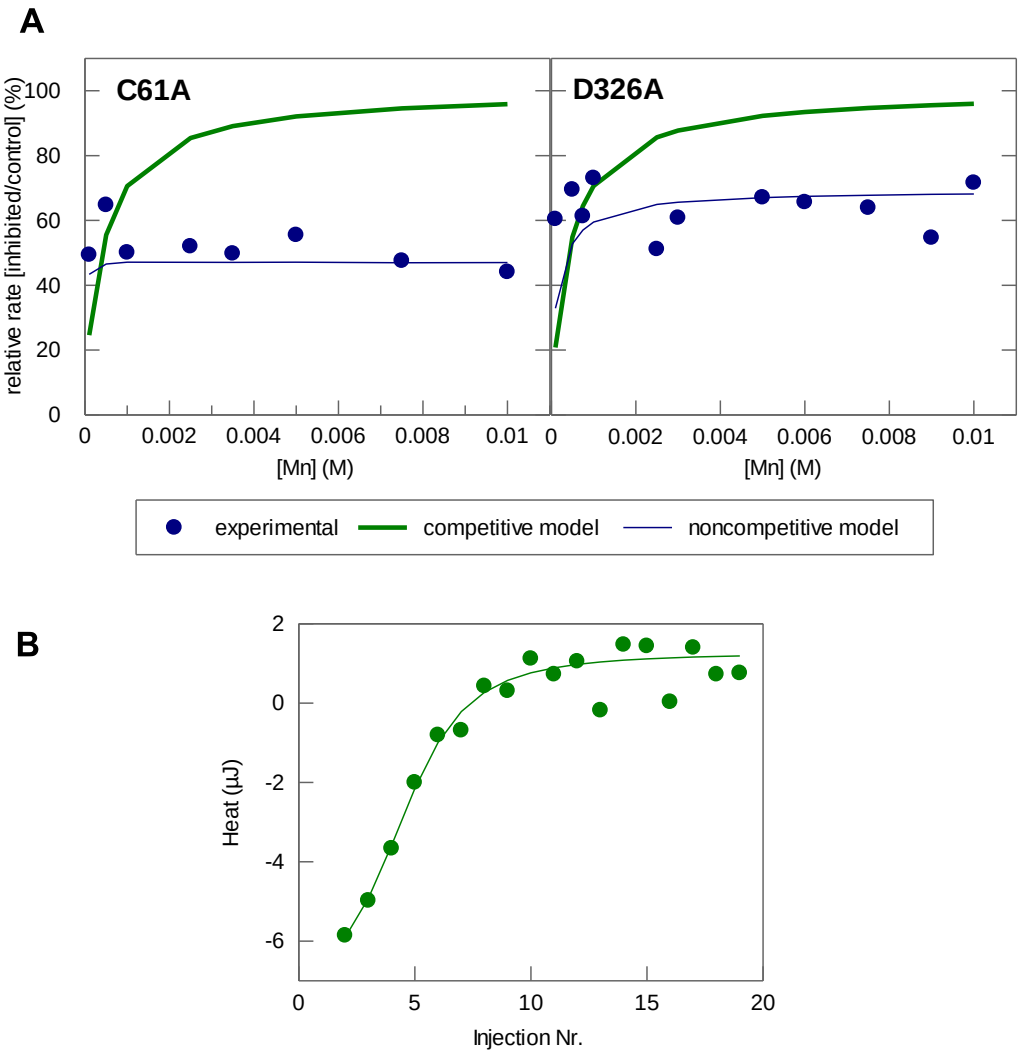

Figure 2.11 Mode of inhibition of DAHPS by DAHP oxime in the mutant enzymes D326A and C61.

(A) The inhibition of mutants C61A and D326A by DAHP oxime was not relieved by increasing Mn^{2+} concentrations. (B) ITC titration of D326A·Mn^{2+} with DAHP oxime indicated that Mn^{2+} and DAHP oxime were not competitive.

The low affinity of DAHP oxime for the C61A and H268A mutants prevented ITC titrations. For these mutants, the mode of inhibition was determined using Eadie-Hofstee plots (Figure 2.12). In an Eadie-Hofstee plot, plots of v_0 vs v_0/[S] are made at series of constant [I]. In this case, the varied

substrate was [Mn^{2+}]. Competitive inhibitors give lines that converge at the y-axis, while noncompetitive inhibitors give parallel lines and uncompetitive inhibitors give lines that converge at the x-axis. With C61A, the lines were parallel, indicating that DAHP oxime and Mn^{2+} binding was noncompetitive.

With H268A, the lines converged *toward*, but not *at* the y-axis (Figure 2.12B). This is because DAHP oxime shows partial inhibition due to its half-of-sites binding, which changes the Eadie-Hofstee plot. For a normal competitive inhibitor in a single substrate reaction, the Eadie-Hofstee plot (v_0 vs. v_0/[S]) rearranges to eq. **2.20**, where the slope is -$K_M(1+[I]/K_i)$ and the y-axis intercept is V_{max}.[147]

$$v_0 = -K_M\left(1+\frac{[I]}{K_i}\right)\frac{v_0}{[S]}+V_{max} \tag{2.19}$$

However, when there is an offset in the rate equation, as in eq. **2.6**, then the Eadie-Hofstee equation rearranges to eq. **2.21**, where the slope remains -$K_M(1+[I]/K_i)$, but the y-intercept now depends on [I], and is now $\{K_M \times (1+[I]/K_i) \times (offset/[S]) + V_{max} + offset\}$.

$$v_0 = -K_M\left(1+\frac{[I]}{K_i}\right)\left(\frac{v_0}{[S]}\right)+K_M\left(1+\frac{[I]}{K_i}\right)\left(\frac{offset}{[S]}\right)+V_{max}+offset \tag{2.20}$$

The fact that the Eadie-Hofstee plot of H268A converged toward the y-axis demonstrates that DAHP oxime binding was competitive with Mn^{2+}.

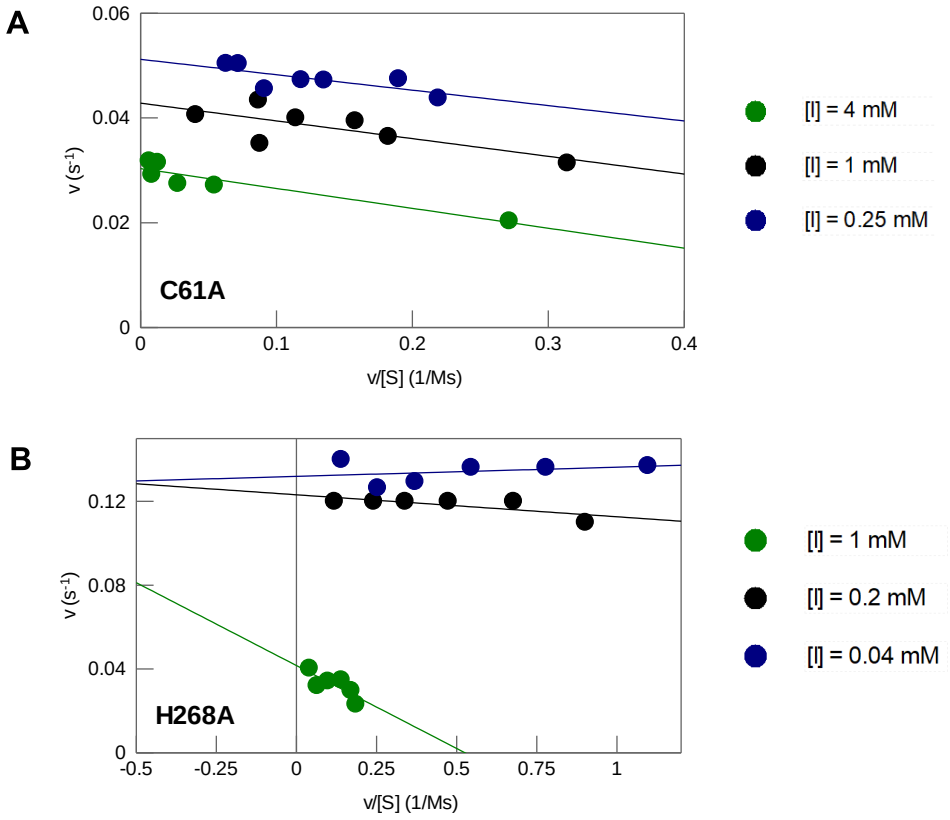

Figure 2.12 Eadie-Hofstee plot for the mutants C61A and H268A.

Parallel lines suggest a noncompetitive binding mode, as observed for the C61A mutant (A), while intercepting lines indicate competitive inhibition, as observed for the H268A mutant (B).

The pH dependence of K_i for C61A (Chapter 2.3.4) was re-fitted using the metal noncompetitive equation (eq. **2.16**). Now, treating DAHP oxime inhibition as competitive with respect to PEP and E4P only, the K_i stayed essentially constant at pH 7 and 10, with $K_i = 32 \pm 4$ µM and $K_i = 45 \pm 5$ µM, respectively. This consistency suggested that the C61A mutation eliminates the change in the mode of binding.

2.3.10. Fragment-based inhibitors' mode of inhibition

With D326A, DAHP oxime no longer exhibited competitive inhibition with respect to Mn^{2+}. Two independent crystal structures containing either DAHP oxime (pdb ID: 5CKS) or the Mn^{2+} (pdb ID: 1N8F) revealed that D326 is involved in coordinating both DAHP oxime and Mn^{2+}. There is no crystal structure that contains both a metal ion and DAHP oxime in the same binding pocket. Interaction with D326 could therefore be mutually exclusive. This raised the question of whether removing the inhibitor's interaction with D326 would render its binding noncompetitive with Mn^{2+}. D326 interacts with DAHP oxime's C4 hydroxyl group. Synthesizing 4-deoxy-DAHP oxime would have been extremely challenging. Its precursor, 4-deoxy-DAHP, is not a known compound. It could not be made using alternate substrates with DAHPS since 4-hydroxyl group is derived from E4P's carbonyl oxygen which is absolutely required for the DAHPS reaction.

As an alternate approach, two pairs of fragment-based inhibitors based on DAHP oxime were designed that were missing C4-O4, or C3. The combination of Gro3P and pyruvate oxime had no atoms equivalent to DAHP oxime's C4 hydroxyl group (Figure 2.13A). The combination of glyoxylate oxime and erythritol 4-phosphate (Ero4P) possesses a hydroxyl group equivalent to the C4 hydroxyl, but no equivalent to C3 (Figure 2.13B).

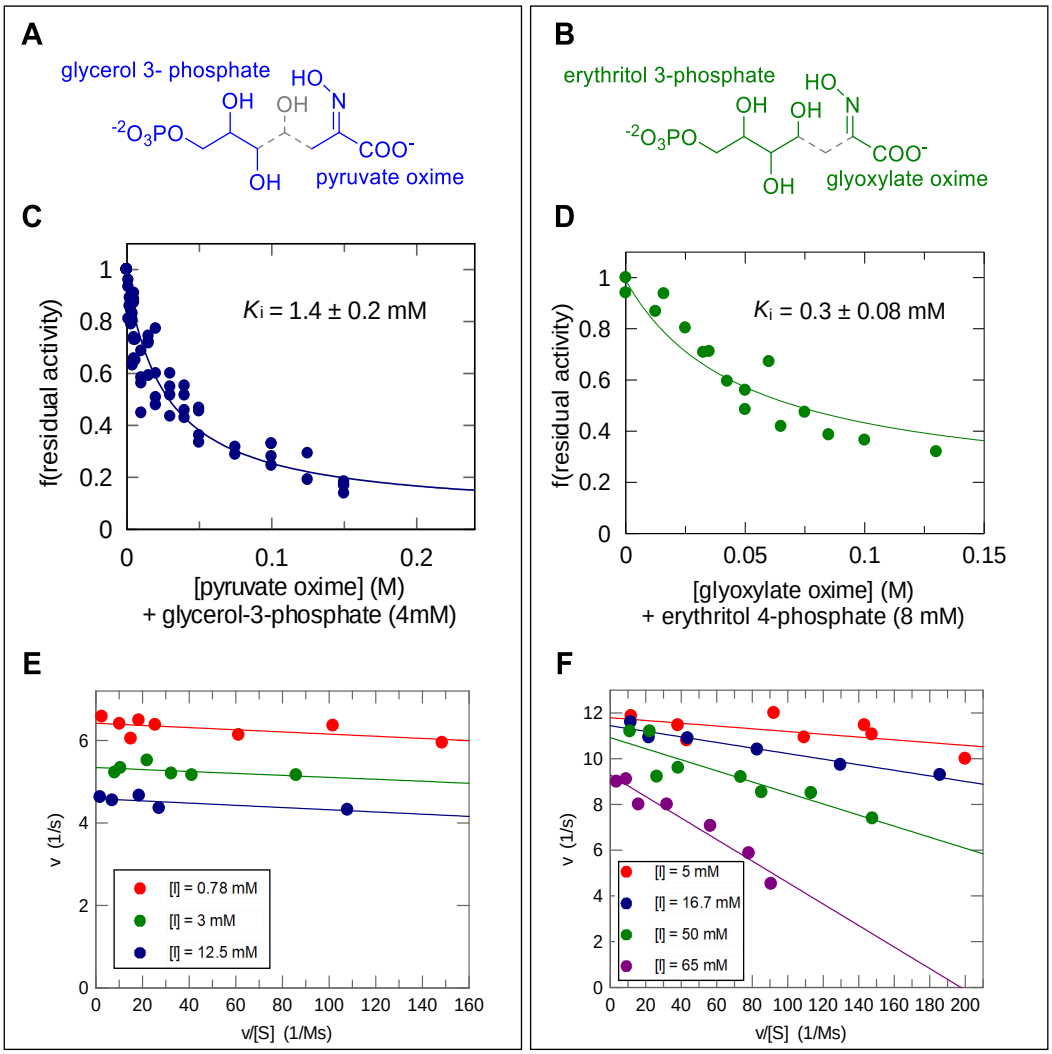

Figure 2.13 Fragment-based investigation of the origin of DAHP oxime/ Mn^{2+} competition.

(A, B) DAHP oxime was subdivided in fragments to examine the if the mode of inhibition is influenced by the inhibitor's C4 hydroxyl group. (C, D) Fast binding inhibition; the data for pyruvate oxime and Gro3P inhibition was obtained by S. Jiang.[146] (E, F) Eadie-Hofstee plot.to examine the mode of binding of the fragments. Parallel lines suggest a noncompetitive binding mode, while intercepting lines indicate competitive inhibition.

The two pairs of fragments were tested for $DAHPS_{H6}$ inhibition. None of the fragments inhibited $DAHPS_{H6}$ individually up to 25 mM; inhibition was only observed if both fragments were present (Figure 2.13C and D). In each pair, the

oxime-containing fragment was varied while the concentration of the phosphate-containing fragment was fixed. Thus, the reported K_i values were for the oxime-containing fragment in the presence of a high, though not necessarily saturating, concentration of the second fragment. The usable concentrations of the phosphate-containing fragments were limited by the concentration of contaminating P_i. The combination of pyruvate oxime and Gro3P had previously been tested,[146] but the data was re-fitted assuming noncompetitive binding with respect to Mn^{2+} (eq. **2.16**). The K_i for glyoxylate oxime and Ero4P was calculated based on a metal competitive mode of inhibition (eq. **2.6**). The choice for both equations used to calculate K_i was based on the result of an Eadie-Hofstee plot which helped determine the mode of inhibition for the fragments. The parallel lines for pyruvate oxime in combination with Gro3P suggest that the inhibition is noncompetitive with respect to the metal (Figure 2.13E). In contrast, the intercepting lines for glyoxylate oxime and Ero4P's inhibition indicate metal competitive binding properties (Figure 2.13F).

2.4. Discussion

2.4.1. The pH profiles of catalysis and inhibition

Investigating enzyme activity as a function of pH is a tool to deepen the understanding of catalysis. Changes in active site residue ionization can have crucial effects on substrate binding and catalysis. The analysis of these changes

can support the identification of the individual active site residues and their ionization states that are required for the success of the catalytic turnover.[148,149] Furthermore, a comparison of the pH profiles of catalysis and inhibition can reveal if an inhibitor acts a TS mimic. If the inhibitor's interactions in the active site are identical to the ones of the transition state, the bell-shaped curves of the pH profile of k_{cat}/K_M and $1/K_i$ should overlap.[150] In this project, we determined $DAHPS_{H6}$'s pH profile for the specificity constant $k_{cat}/(K_{M,Mn},K_{M,PEP},K_{M,E4P})$ and for the inhibitory constant K_i of DAHP oxime. It has previously been shown by a LFER analysis that the inhibitor is a TS mimic inhibitor of DAHPS (Chapter 1.11).[106] The pH profile was expected to yield additional evidence for this property. Instead, our results showed differing pH dependences for $k_{cat}/(K_{M,Mn},K_{M,PEP},K_{M,E4P})$ in comparison to K_i. Specifically, the pH profile for $k_{cat}/(K_{M,Mn},K_{M,PEP},K_{M,E4P})$ resulted in a bell-shaped curve with the optimal pH for enzyme activity at pH = 8.4 and a basic limb at $pK_a = 9.7$. In contrast, the inhibitor affinity seemingly increased at high pH, with a basic limb pK_a of 8.7. The pH profiles therefore showed opposing trends: While the specificity constant decreased towards the basic pH, inhibition appeared enhanced. This initially implied that either the ionization of enzymatic groups was affecting catalysis and inhibition in opposite directions, or that a functional group of the inhibitor, not present in the THI (e.g., the oxime group's OH), was ionized over the pH range and affecting inhibitor binding. These assumptions guided the initial investigation of the pH dependence of binding.

The individual substrate K_M values showed varying behaviour over the pH range. PEP's affinity decreased strongly at basic pH, while $K_{M,E4P}$'s pH dependence was bell-shaped. Most interestingly, Mn^{2+}'s affinity increased drastically at basic pH. The basic limb, with $pK_a = 8.3$, was close that of DAHP oxime's K_i, at $pK_a = 8.7$. This raised the possibility of a common cause for the basic limbs of $K_{M,Mn}$ and K_i. The observed pK_a value was close to the one of an unperturbed cysteine side chain, making the metal-binding residue C61 a candidate for causing tighter metal and inhibitor binding under basic conditions, even though it did not make direct contact with DAHP oxime in the crystal structure. As expected, the C61A mutant did not bind Mn^{2+} more tightly at pH 10 than pH 7, supporting a role for C61 in the pH dependence of $K_{M,Mn}$ (Figure 2.4A). However, its effect on DAHP oxime binding at high pH was ambiguous. DAHP oxime's apparent K_i with C61A decreased with pH (Figure 2.4B), but not as much as with $DAHPS_{H6}$ (4-fold vs. 12-fold), making it unclear whether the apparent change in K_i had a common cause with the change in $K_{M,Mn}$. This suggested that the ionization of C61 was not (solely) responsible for tighter inhibitor binding. At this point, inhibition was still assumed to be competitive with Mn^{2+} binding.

2.4.2. DAHP O-methyloxime as a tool to investigate inhibitor ionization

C61 ionization alone did not sufficiently explain why inhibition of DAHP oxime increased at basic pH. An alternative explanation involved ionization of the

inhibitor itself, specifically the oxime's OH group, with an expected pK_a of 11.3 (Figure 2.14A, Chapter 3.3.1). Even if this pK_a value is outside of the investigated pH range, it was possible that its pK_a value was altered by the active site environment, particularly in light of the fact that amino acids' sidechain pK_a values are commonly perturbed by > 5 pH units in enzyme active sites.[151] This is especially plausible given the fact that the oxime binding site binds the dianionic phosphate group of the THI and is surrounded by Arg and Lys residues. Introducing an ionizable group into an oppositely-charged surrounding can decrease its pK_a. A similar effect could apply to DAHP oxime inside the binding pocket. To prevent oxime ionization, DAHP *O*-methyloxime was synthesized (Figure 2.14B). The K_i was tested at neutral and basic pH. There was no decrease in K_i at basic pH (Figure 2.5), which suggested that ionization of DAHP oxime could indeed be the cause for tighter binding.

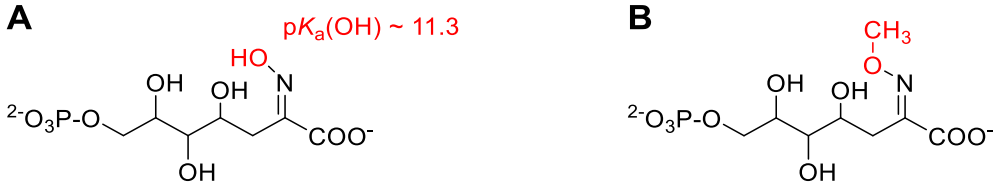

Figure 2.14 (A) DAHP oxime's ionizable group. (B) DAHP O-methyloxime.

2.4.3. Mode of DAHP oxime's inhibition at pH 7 and pH 9

A more detailed characterization of DAHP oxime binding to $DAHPS_{H6}$ was performed using ITC. Initially, mutually exclusive binding of DAHP oxime and Mn^{2+} to DAHPS under physiological conditions was confirmed (Figure 2.6).

However, at basic pH, the inhibitor was now able to interact with the DAHPS·Mn^{2+} complex, suggesting that the mode of binding was no longer competitive (Figure 2.7). Additionally, the K_d = 4.1 ± 0.7 μM did not suggest a decrease in the inhibitor's dissociation constant towards the basic pH. This indicated the requirement to re-examine the fitting of K_i values over the pH range. The model was changed from purely competitive inhibition (eq. **2.6**) to one where there was a pH-dependent change in the mode of DAHP oxime inhibition with respect to Mn^{2+} (eq. **2.17**). It was competitive at low pH, and noncompetitive at high pH. In this model there was a change in mode of inhibition, at pK_a = 8.7 (Figure 2.8). At pH < 8.7, DAHP oxime inhibition was primarily competitive with respect to Mn^{2+}, with $K_{i,comp}$ = 3.7 ± 0.6 μM. At pH > 8.7, inhibition was primarily noncompetitive with respect to Mn^{2+}, with $K_{i,noncomp}$ = 6.6 ± 0.9 μM. Now, based on evidence of a changing mode of inhibition, the K_i at various pH values was essentially constant, suggesting that inhibitor coordination itself in the active site is not, or barely, affected by the pH changes. Inhibitor ionization should alter the small molecule's ability to coordinate in the active site, so the lack of change in K_i implies there is no change in DAHP oxime's ionization state between pH 7 and 9.

The strong pH dependence of $K_{M,Mn}$ in $DAHPS_{H6}$ and its weak pH dependence in C61A (Figure 2.4) implicated C61 ionization resulted in increased Mn^{2+} binding at high pH. DAHP oxime's essentially constant K_i over this pH range suggests that C61 has little role in directly interacting with the inhibitor. However, the change in mode of inhibition with respect to Mn^{2+} is consistent with

C61 deprotonation causing a change in protein conformation that alleviates the competition between DAHP oxime and Mn^{2+}. This is consistent with the observation by electron paramagnetic spectroscopy of conformational changes in metal binding in DAHPS with pK_a ~ 8.5.[122] Therefore, the origin of the change in the mode of inhibition most likely lies in a conformation change due to the ionization of metal coordinating residues.

This finding initiated the investigation of DAHP oxime's mode of inhibition with respect to Mn^{2+} for C61A and other DAHPS mutant enzymes. The mutant enzymes C61A, H268A and D326A were selected, based on their location in the active site and their proximity to either metal ion and/or inhibitor (Figure 2.10). The mutant enzymes C61A and D326A showed noncompetitive inhibition (Figure 2.11, Figure 2.12). Binding of DAHP oxime to D326A·Mn^{2+} was observed by ITC, and an Eadie-Hofstee plot indicated noncompetitive inhibition for C61A. In contrast, inhibition remained competitive for H268A, as demonstrated by an Eadie-Hofstee plot. This suggests that the residues D326 and C61, based on their participation in metal binding and due to their spatial proximity to the inhibitor binding site, influence the binding mode. Both residues are located close to the inhibitor's C4 hydroxyl group, and D326 Oδ is located within hydrogen bonding distance, 3.1 Å, of the hydroxyl group. This C4 hydroxyl group originates from E4P's C1 carbonyl functional group. During catalysis, this residue is believed to coordinate to the metal ion, which leads to its activation for the nucleophilic attack by PEP's C3. It is likely that simultaneous

coordination of the metal ion and the inhibitor's C4 hydroxyl group by D326 is not possible, resulting in competitive binding. The mutation of either C61 or D326 could allow a shift in the position of the metal ion. From the perspective of catalysis, this shift could weaken the metal ion-E4P interaction and therefore negatively impact the activation of E4P's carbonyl group for catalysis. Ultimately, this would result in a decrease of $k_{cat}/K_{M,Mn}K_{M,PEP}K_{M,E4P}$. This hypothesis is supported by the unexpectedly large (440-fold) increase in $K_{M,E4P}$ for the C61A mutant.[106] The C61 is in close van der Waals contact with both DAHP oxime's O4 and the D326 sidechain (Figure 2.15A), so it would require only a small change in position due to deprotonation to open up sufficient space to accommodate the 4-hydroxyl group of DAHP oxime and the metal ion simultaneously, so that binding of the two ligands becomes noncompetitive (Figure 2.15B).

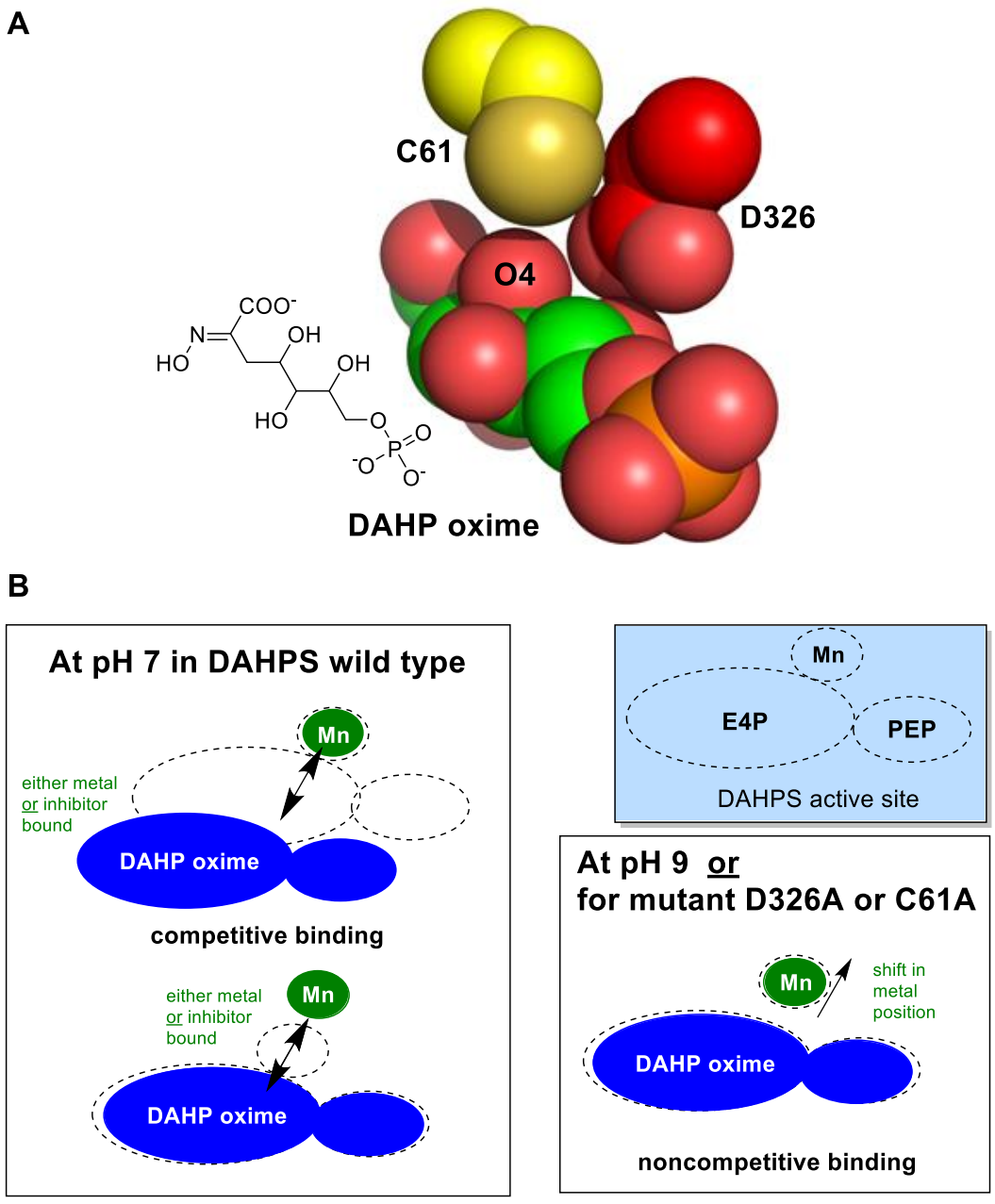

Figure 2.15 The mode of binding of DAHP oxime and the metal ion is influenced by pH and mutations of DAHPS.

(A) Interaction of the C61 sidechain (yellow carbon atoms) with D326 (red carbon atoms) and DAHP oxime (green carbon atoms). From pdb ID: 5CKS.[100] (B) Basic pH or mutations of the residue D326 or C61 are hypothesized to lead to a shift in metal coordination, allowing inhibitor and metal ion to bind simultaneously.

2.4.4. Fragment-based investigation of the binding mode

Based on our new understanding of the origin of metal competition, the next step was to find out if structural elements of the inhibitor could be altered to avoid it. The synthesis of a DAHP oxime derivative lacking the O4 group appeared challenging. An enzymatic synthetic pathway using DAHPS is impossible as the O4 group originates from E4P's aldehyde, which is essential for the catalytic mechanism. Extensive expertise in synthetic chemistry would be crucial to either chemically and stereocontrolled synthetize this compound, or to selectively remove the O4 group after DAHP has been enzymatically formed. To simplify the inhibitor design, DAHP oxime was subdivided in two pairs of fragments that excluded either the inhibitor's C4-O4 atoms (Gro3P + pyruvate oxime) or C3 atom (Ero4P + glyoxylate oxime) (Figure 2.13A and B). A crystal structure of Gro3P bound in the active site of DAHPS showed that Gro3P coordinates in the E4P binding site in the expected manner (Figure 1.11B).[70] This supports the fragment-based approach as a suitable technique for inhibitor optimization.

Both pairs of fragments inhibited $DAHPS_{H6}$. Inhibition by Gro3P + pyruvate oxime was noncompetitive with respect to Mn^{2+}, as demonstrated by an Eadie-Hofstee plot (Figure 2.13E). At the same time, Ero4P + glyoxylate oxime inhibited $DAHPS_{H6}$ competitively with respect to Mn^{2+} (Figure 2.13F). The two sets of inhibitor pairs lead to different modes of inhibition. Comparing their structures, Ero4P is extended by one additional hydroxymethyl group relative to

Gro3P, which implies that it possesses a group equivalent to DAHP oxime's C4-O4 (Figure 2.13B). Pyruvate oxime carries one additional carbon atom (C3) in comparison with glyoxylate oxime. The noncompetitive binding mode of Gro3P + pyruvate oxime implies that either the absence of a C4-O4 equivalent position or the presence of the C3 position makes inhibition noncompetitive. The latter does not seem likely, as DAHP oxime itself possesses C3 and shows competitive inhibition. Additionally, the ionization or mutation of residues in close proximity to O4 lead to a noncompetitive mode of inhibition (Chapter 2.3.9). These results combined with the fragments' mode of binding indicate that simultaneous presence of the DAHP oxime's C4 hydroxyl group and the C61 and D326 sidechains could be responsible for the metal competitive binding mode.

These results suggest that competitive binding with respect to the metal ion could be avoided by inhibitors lacking the O4 group. Removing the O4 group would presumably decrease its affinity for DAHPS, given the contacts observed in crystal structures. The presumed O4H$\cdots$Oδ D326 and O4$\cdots$Nϵ K97 hydrogen bonds would be lost. However, this loss would be offset by the lack of competition with intracellular metal ions, which would be likely to render O4-containing inhibitors ineffective in the cell.

2.5. Conclusion

In this study, we identified the pH-dependency of the mode of inhibition of DAHPS by DAHP oxime with respect to the metal cofactor. The identification of active site residues, as well as inhibitor functional groups which were at the origin of this competition enabled the proposal for an improved DAHPS inhibitor design to avoid metal competition and consequentially, to make DAHPS accessible as a reliable target for antibiotics.

Chapter 3. Fragment-based inhibitors and antibacterial properties

3.1. Introduction

While DAHP oxime is a potent DAHPS inhibitor *in vitro* (K_i = 1.5 μM), it does not significantly inhibit bacterial growth in cell culture.[141] Previously, concentration-dependent inhibition was only observed for *E. coli* strain XL-1 blue which is notable for its highly permeable cell membrane. No inhibition was observed for the strains MG1655 and AG1. Therefore, it is likely that DAHP oxime's negative charge hinders its cell membrane penetration. Similar problems have been observed with previously developed α-carboxyketose synthase inhibitors.[127,132] Furthermore, DAHP oxime's metal competitive mode of inhibition would hinder its effectiveness in cells (Chapter 2). To minimize the charge while conserving the key interactions and avoiding the metal competition, the size of DAHP oxime was reduced to a fragment, pyruvate oxime. This fragment in combination with glycerol 3-phosphate (Gro3P) showed weak DAHPS inhibition, and no more metal competition (Chapter 2). The technique of fragment-based drug discovery (FBDD) is an increasingly important tool in medicinal chemistry.[152] It is based on the screening of molecules with reduced size (typically 150−250 Da[153]) for their biological activity.[154] Despite relatively weak affinities of the fragments,[153] the advantage of FBDD is that it makes it possible to investigate a smaller chemical space more thoroughly.[155] This implies a reduced set of possible structures and therefore a higher likelihood for hits,[155] high-quality interactions of the fragments with their target,[153] and simplified

syntheses.[156] Once a hit is obtained, an optimization by growing, linking or merging the fragments follows, ideally resulting in a potent lead molecule.[157] In this study, fragment optimization was performed by introducing fluorine as an electron withdrawing group in the α-position relative to the oxime group of pyruvate oxime. The initial motivation for adding an electron withdrawing group was the observation that DAHP oxime's apparent K_i decreased with increasing pH, which could be explained by deprotonation of the oxime OH group. This led to the hypothesis that decreasing the OH group's pK_a with electron withdrawing groups would lead to more potent inhibitors. In the following, it became evident that the apparent pH dependence of DAHP oxime's K_i was the result of a change in the mode of inhibition (Chapter 2); however, pursuit of fluorinated inhibitor fragments turned out to be productive in its own right, and this line of investigation was continued.

Increasing the number of fluorine atoms in pyruvate oxime resulted in a decreased pK_a of the oxime's hydroxyl group, as well as a decreased K_i. $DAHPS_{H6}$ inhibition no longer required the addition of Gro3P. The 3,3,3-trifluoropyruvate (TFP) motif was then tested with other imine derivatives, including hydrazone and semicarbazone functional groups. Generally, the suitability of oxime derivatives for inhibitor design originates from the oxime's increased hydrolytic stability due to the ability of the oxime's oxygen to participate in the delocalization of charge.[158] Hydrazones and semicarbazones share this property (Figure 3.1). Pharmaceutically relevant small molecules with

oxime, hydrazone or semicarbazone functional groups are described in literature.[159–162] A widely known compound with a semicarbazone functional group is the antibiotic 5-nitro-2-furaldehyde semicarbazone (tradename Furacine).[159] Another example is morphinane-6-one which has been derivatized with all three imine derivatives.[160]

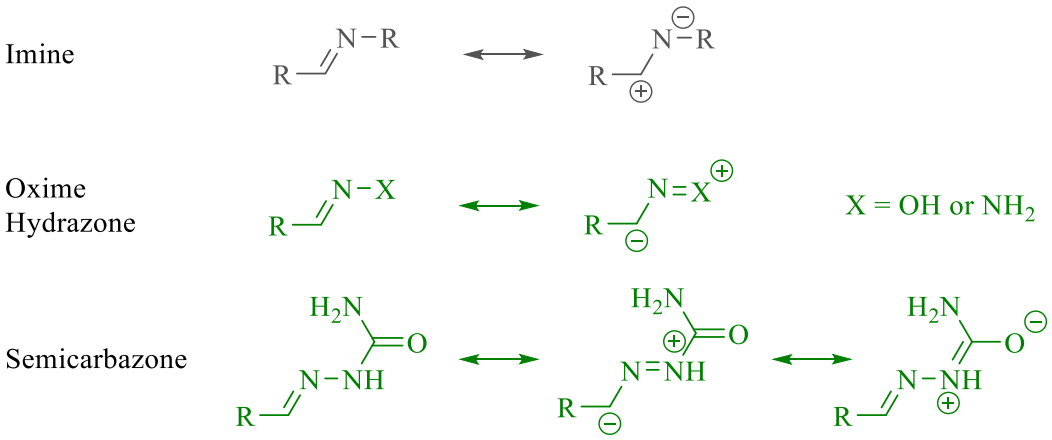

Figure 3.1 Resonance structures of imine derivatives.

The negative charge on the central carbon of oxime, hydrazone and semicarbazone functional groups in comparison to imines can be explained by resonance structures. Figure is based on Kalia and Raines.[158]

TFP hydrazone and TFP semicarbazone were tested as $DAHPS_{H6}$ inhibitors, and co-crystal structures of $DAHPS_G$ with TFP oxime and TFP semicarbazone were obtained to describe the inhibitors' active site interactions. By esterification of the inhibitor fragments, charge-free prodrugs were designed, and their efficacy was tested on bacterial cell culture. The high efficacy of the fragments suggested the synthesis of DAHP semicarbazone, as well as the introduction of a fluoro-group at the carbon α to the oxime functional group of DAHP oxime. Pathways for the synthesis of these compounds were explored.

3.2. Materials and Methods

3.2.1. Fragment synthesis

Several imine-based pyruvate and fluoropyruvate derivatives were synthesized. Purity and identity were confirmed using ^{1}H, ^{13}C, and ^{19}F NMR (if applicable), plus mass spectrometry (see Appendix).

3.2.1.1. Fluoropyruvate oxime

To a solution of 0.1 mmol β-fluoropyruvic acid sodium salt monohydrate in anhydrous ethanol, 0.4 mmol hydroxylamine (50 wt. % in H_2O) and 0.8 mmol formic acid were added. The reaction mix was stirred at 30 °C for 6 h. Excess hydroxylamine was removed with a SP-Sepharose (GE Healthcare) cation exchange column, using ddH_2O as the eluent.

3.2.1.2. TFP oxime

Ethyl 3,3,3-trifluoropyruvate (0.57 mmol) in 2.0 mL of water was stirred at room temperature. Following the addition of 0.66 mmol hydroxylamine (50 wt. % in H_2O), the pH was adjusted to pH 6. The mixture was subsequently heated under reflux for 6 h. A SP-Sepharose cation exchange column was used to remove the excess hydroxylamine. The reaction product was eluted with ddH_2O. Ester cleavage was performed by the addition of 0.86 mmol NaOH (aqueous solution) at room temperature. After 1.5 h, the product was dried down and

purified using a Q-Sepharose anion exchange column. A linear gradient of 0.3 M to 0.8 M ammonium bicarbonate (pH 9.2) over 30 min at a flow rate of 2 mL/min was used.

3.2.1.3. TFO oxime ethyl ester

The procedure for TFO oxime synthesis was followed as described above (Chapter 3.2.1.2), up to the point of the ester cleavage. The resulting TFP oxime ethyl ester was purified via silica column chromatography (85:15 ethyl acetate/ hexane) and dried with the rotary evaporator.

3.2.1.4. TFP hydrazone

The ester group's sensitivity to basic conditions necessitated its cleavage before the hydrazone synthesis. To 2 mL of 0.45 M NaOH, 0.3 mmol 3,3,3-trifluoropyruvate ethyl ester (97%, liquid) was added dropwise, then allowed to react for 1 h. The reaction mix was subsequently purified by SP-Sepharose cation exchange column, using ddH_2O as eluent. The recovered 3,3,3-trifluoropyruvic acid was resuspended in 2 mL anhydrous ethanol, with addition of sufficient formic acid to help dissolution. Slow addition of 5 mmol hydrazine hydrate (liquid) followed and the reaction was heated under reflux for 3 h. The mixture was dried under reduced pressure and purified by cation exchange on a SP-Sepharose column.

3.2.1.5. TFP hydrazone ethyl ester

A solution of 0.28 mmol of 3,3,3-trifluoropyruvate ethyl ester, 1.6 mmol hydrazine and 1.6 mmol acetic acid in 2mL of anhydrous EtOH was refluxed for 7 h. Removal of excess hydrazone was performed by SP-Sepharose cation exchange chromatography. The product was eluted with ddH_2O.

3.2.1.6. Pyruvate semicarbazone

A solution of 0.1 mmol semicarbazide hydrochloride and 0.1 mmol pyruvic acid sodium salt in 1 mL of ddH_2O was prepared and neutralized. An equal volume of anhydrous ethanol was added, and the reaction mix was refluxed for 4 h. The solvent was removed by rotary evaporator. The product was purified using a Q-Sepharose anion exchange column, with a linear gradient of 0.1 to 0.8 M ammonium formate in 10 mM ammonium bicarbonate, pH 6.2, over 30 min at a flow rate of 2 mL/min.

3.2.1.7. TFP semicarbazone ethyl ester

To a neutral aqueous solution of 1.25 mmol 3,3,3-trifluoropyruvate ethyl ester and 5 mmol semicarbazide hydrochloride in 5 mL of ddH_2O was added an equal volume of anhydrous ethanol. The solution was refluxed for 8 h. The solvent was removed by rotary evaporator and the product was purified by silica column in 60:40 ethyl acetate/hexane.

3.2.1.8. TFP semicarbazone

The ester cleavage of 1.25 mmol 3,3,3-trifluoropyruvate semicarbazone ethyl ester was performed by re-suspending the crude product in 5 mL of ddH_2O followed by the addition of 250 µL of 5 M NaOH. The solution was stirred for one hour at room temperature. A Q-Sepharose anion exchange column was used for purification, running a linear gradient of 0.3 M to 0.8 M ammonium bicarbonate (pH 9.2) over 30 min at a flow rate of 2 mL/min.

3.2.2. pK_a determination

All pK_a value measurements were performed with Varian Cary 100 Bio UV-Visible Spectrophotometer. A spectrum scan from 200 - 350 nm was performed against a buffer blank at varying pH using 200 µM compound to find the wavelength with the greatest change in absorbance (Table 3.1). The absorbance at this wavelength was then determined over the pH range. The pK_a was then fitted to equation **3.1**:

$$A_\lambda = \frac{\text{limit1} + \text{limit2} \times 10^{\text{pH-p}K_a}}{1 + 10^{\text{pH-p}K_a}} \quad (3.1),$$

where A_λ is the absorbance at wavelength λ, and limit1 and limit2 are the A_λ values at low and high pH, respectively.

Table 3.1 The fragments' absorbance maxima.

Fragment	λ_{max} (nm)	Fragment	λ_{max} (nm)
Pyruvate oxime	246	Pyruvate semicarbazone	289
3-fluoropyruvate oxime	250	3,3,3- TFP semicarbazone	289
3,3,3- TFP oxime	240		

3.2.3. K_i determination

Fast binding inhibition experiments were performed as described in Chapter 2.2.1, with initial rates determined using the Malachite Green/ammonium molybdate colorimetric assay for P_i production.[142] All inhibitors were tested in kinetics buffer. The substrate concentrations were 9 μM $MnCl_2$, 500 μM PEP and 250 μM E4P. The reaction was initiated by the addition of 100 nM $DAHPS_{H6}$. The K_i values were calculated assuming competitive inhibition with respect to PEP and E4P, and noncompetitive inhibition with respect to the metal ion (eq. **2.16**).

3.2.4. Protein crystallization

The His-tag cleavable $DAHPS_{H6\text{-}TEV}$ was designed by Naresh Balachandran.[141] The purification of $DAHPS_{H6\text{-}TEV}$ and TEV protease, and TEV cleavage were performed as described previously.[100] Post His_6-tag cleavage, the enzyme $DAHPS_G$ was obtained, which differs from the wild type DAHPS by an additional Gly residue at the *N*-terminus. A variety of crystallization conditions

were tried; the ones that produced crystals whose structures were solved were in 0.2 M trilithium citrate tetrahydrate and 20% (w/v) PEG 3350, with 12 mg/mL $DAHPS_G$ (in 20 mM Tris-HCl, pH 7.5, 0.1 mM TCEP, and inhibitor) and varying additives in a 1:1:0.2 drop ratio, using the hanging drop vapour diffusion method grown over 2 M ammonium sulfate at varying temperatures (Table 3.2).

Table 3.2 Crystallization conditions for the fragments.

crystal identity	Inhibitor identity	[Inhibitor]	Additive	Temp (°C)
TFPOX	TFP oxime	1.8 mM	40% (v/v) 1,3-propanediol	room temperature
TFPSC	TFP semicarbazone	2.0 mM	1.0 M $MnCl_2$	4 °C

The crystals were diffracted at the national user facility BioCARS in Chicago, Illinois by Dr. Murray Junop. Ryan Grainger performed the indexing, scaling and merging of the data with HKL 2000 software,[163] as well as molecular replacement using AutoMR in the Phenix software package,[164] with search model pdb ID: 5CKS.[100] The refinement was performed using Phenix refine[165] and WinCoot.[166] Ligand restraints and coordinates were calculated with Gaussian 09,[167] which was done by Dr. Berti, and finalized in elBOW.[168]

3.2.5. M9 preparation

M9 minimal salts were dissolved in ddH_2O (11.28 g/L) and autoclaved, followed by addition of a sterile-filtered mixture with final concentrations of 0.4 % (w/v) glycerol, 2 mM $MgSO_4$, 0.1 mM $CaCl_2$, 10 µg/mL thiamine-HCl, a 1/1000 dilution of trace metal mix and 10 µg/mL biotin. The trace metal mix was

prepared by adding 0.54 g $FeCl_3 \cdot 6HCl$, 0.026 g $ZnCl_2$, 0.2 g $(NH_4)_6Mo_7O_{24}$, 0.05 g $CaCl_2 \cdot 2H_2O$, 0.04 g $CoCl_2 \cdot 6H_2O$, 0.038 g $CuSO_4 \cdot 5H_2O$, 0.066 g $MnCl_2 \cdot 4H_2O$, 0.01 g H_3BO_3, and 2 mL concentrated HCl to 18 mL H_2O.

3.2.6. Inhibition of bacterial growth with TFP oxime ethyl ester and 3,3,3-TFP semicarbazone ethyl ester

E. coli BL21*(DE3) cells were grown overnight in M9 minimal medium containing 5% (v/v) lysogeny broth (LB). Cell growth was extremely slow when started in pure M9 minimal medium. The next day, the culture was diluted to OD_{600} = 0.1. A 96 well plate assay was then set up by the addition of 100 µl of M9 minimal medium to each well, followed by 2-fold serial dilutions of the inhibitor stock, starting at 26 mM for TFP oxime ethyl ester and 17 mM for TFP semicarbazone ethyl ester. Subsequently, 100 µL of the diluted cell culture was added to each well, and the solutions were mixed thoroughly. The plate was incubated with shaking (150 rpm) at 37 °C and the OD_{600} was measured after 0, 4 and 24 h.

3.2.7. Disk diffusion assay

A heat shock transformation of *E. coli* BL21*(DE3) competent cells with the vector aroG:pET300 was performed and the cells were plated on a LB/agar plate containing 100 µg/mL ampicillin. After overnight growth at 37 °C, a single colony was isolated to inoculate 50 mL of LB medium containing 100 µg/mL

ampicillin, followed by overnight growth at 37 °C. A 400 µL aliquot was then centrifuged at 1000 × g for 4 min. After discarding 250 µL, the remaining supernatant was used to re-suspend the cells, and the suspension was evenly spread onto LB/agar plates containing 100 µg/mL ampicillin. To initiate the overexpression of DAHPS, selected plates additionally contained 1 mM isopropyl β-D-1-thiogalactopyranoside (IPTG). After all liquid was absorbed into the agar, paper disks containing 260 µg of TFP oxime ethyl ester, 10 µg chloramphenicol (positive control) and ddH_2O (negative control) were added and the plate was cultured for 14 h. The result was documented by photography.

3.2.8. Synthesis of DAHP semicarbazone

DAHP was synthesized as described above (Chapter 2.2.6). To the crude 0.020 mmol DAHP, 0.04 mmol semicarbazide hydrochloride was added, as well as an equal volume of anhydrous ethanol. The mixture was heated to 60 °C for 3 h. Ethanol was removed by rotary evaporator and the purification was performed by HPLC, following the pyruvate semicarbazone purification procedure (Chapter 3.2.1.6). The identity was confirmed by ^{1}H NMR and mass spectrometry.

3.2.9. Attempted syntheses of 3-fluoro-DAHP oxime and 3-fluoro-NeuNAc oxime

To test the effect of fluorine in α-position to the oxime functional group in DAHP oxime, the synthesis of 3-fluoro DAHP-oxime was intended in a two-step

enzymatic synthesis, followed by the reaction of 3-fluoro-DAHP with hydroxylamine to form the oxime (Figure 3.2).

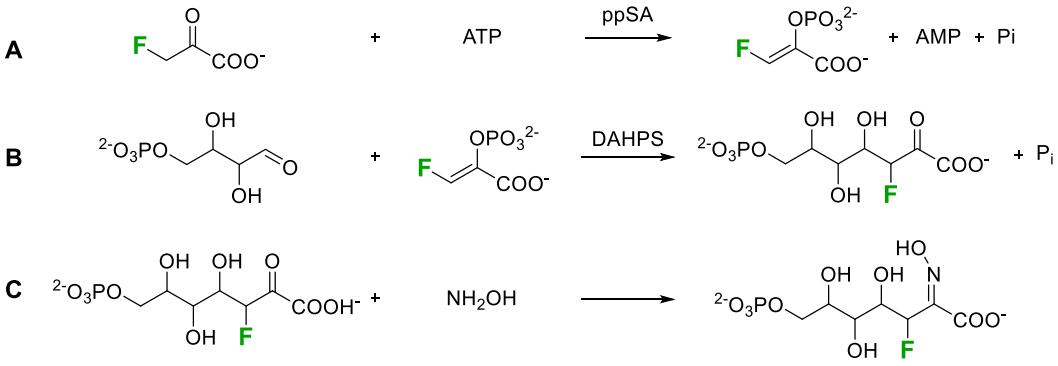

Figure 3.2 Strategy for synthesis of 3-fluoro-DAHP oxime.

(A) 3-Fluoropyruvate is reacted to (*Z*)-3-fluoro-PEP by ppsA. (B) (*Z*)-3-fluoro-PEP is reacted with E4P using DAHPS to yield in 3-fluoro-DAHP. (C) Planned reaction of 3-fluoro-DAHP and hydroxylamine to yield 3-fluoro-DAHP oxime.

3-Fluoro-NeuNAc was prepared in one enzymatic step from 3-fluoropyruvate and ManNAc (Figure 3.3). Due to this facile synthesis, the compound was suitable for wide range testing of various oxime reaction conditions.

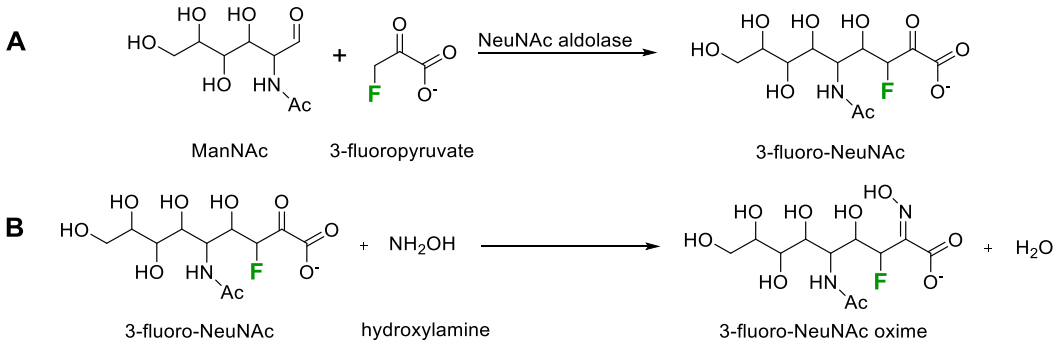

Figure 3.3 Strategy for the synthesis of 3-fluoro-NeuNAc oxime.

(A) NeuNAc aldolase accepted 3-fluoropyruvate as an alternate substrate. (B) The reaction of 3-fluoro-NeuNAc with hydroxylamine was hoped to yield in the oxime derivative.

3.2.9.1. Synthesis of 3-fluoro-PEP

The synthesis of 3-fluoro-PEP was carried out enzymatically with phosphoenolpyruvate synthetase (ppsA). A plasmid for the expression of ppsA, pET24b (DJ-104), was a gift from Dr. David Jakeman (Dalhousie University). Heat shock transformation of *E. coli* BL21(DE3) cells with pET24b (DJ-104) was performed and the cells were grown overnight at 37 °C on an agar plate containing 50 μg/mL kanamycin. A single colony was introduced into 50 mL of LB media with 50 μg/mL kanamycin and shaken at 37 °C for 16 h. This culture was added to 1 L of LB media with 50 μg/mL kanamycin and grown at 37 °C to a cell density of OD_{600} = 0.6. Expression of ppsA was induced by the addition of 0.3 mM IPTG. After 4 h at 37 °C, a cell pellet of 1.1 g was harvested by centrifugation for 20 min at 3800 × g. The pellet was resuspended in a lysis buffer of 5 mM Tris-HCl, pH 7.4, including protease inhibitor cocktail and homogenized by a cell disrupter at 20,000 psi. The homogenate was centrifuged for 20 min at 10,000 × g. The supernatant was stirred at 4 °C and ammonium sulphate was added slowly to a concentration of 242 g/L (40% saturation). The precipitate was removed by centrifugation for 20 min at 11,000 × g and a further 62 g/L of ammonium sulphate was added (50% saturation). The pellet was resuspended in 5 mL of storage buffer containing 50 mM Tris-OAc, pH 6.8, 0.2 mM EDTA, 1 mM phenylmethane sulfonyl fluoride (PMSF), 0.35 mM DL-dithiothreitol (DTT) and 10% glycerol. The partially purified protein was flash frozen and stored in aliquots at -80 °C.

Partially purified ppsA (100 μL) was added to 600 μL of a mixture of 30 mM ATP disodium salt, 12.5 mM β-fluoropyruvic acid sodium salt, 1 mM DTT and 20 mM $MgCl_2$ 400 mM Tris-OAc buffer, pH 8.4. The progress of the reaction was monitored by ^{31}P and ^{19}F NMR. The synthesis was complete after 4 h at room temperature.

3.2.9.2. Synthesis of 3-fluoro-DAHP

3-Fluoro-DAHP was synthesized directly in the 3-fluoro-PEP reaction mixture by adding 12.5 mM E4P, 20 μM $MnCl_2$, and 2.5 μM DAHP synthase and incubating overnight at room temperature. After the removal of the paramagnetic Mn^{2+} ions with Chelex-100, the success of the synthesis was confirmed by ^{31}P and ^{19}F NMR. 3-fluoro-DAHP was purified by HPLC via Mono-Q (1 mL column volume, GE Healthcare) anion exchange chromatography, using a gradient of 0.15 M to 0.65 M of ammonium formate in10 mM ammonium bicarbonate, pH 6.2, over 30 min at a flow rate of 0.5 mL/min.

3.2.9.3. Synthesis of 3-fluoro-NeuNAc

To a mixture of 50 mM β-fluoropyruvic acid sodium salt, 500 mM *N*-acetyl-D-mannosamine and 20 mM $MgCl_2$ in Tris-HCl buffer, pH 7.5, was added 0.004 U/μL *N*-acetylneuraminate aldolase. The reaction was incubated overnight at 37 °C. The progress of 3-fluoro-*N*-acetylneuraminic acid formation was followed by the consumption of β-fluoropyruvic acid using the lactate

dehydrogenase (LDH) assay.[169] In the LDH assay, β-fluoropyruvate is reduced to β-fluorolactate, with a concomitant oxidation of NADH to NAD^+ and a corresponding decrease in A_{340} ($\Delta\varepsilon_{340}$ = 6220 $M^{-1}s^{-1}$) as NADH is consumed. Furthermore, the success of the synthesis of 3-fluoro-*N*-acetylneuraminic acid was confirmed by ^1H NMR and mass spectrometry.

3.2.9.4. Synthesis attempts of the 3-fluoro analogues of DAHP oxime and NeuNAc oxime

Numerous conditions were tried to synthesize 3-fluoro-DAHP oxime and 3-fluoro-NeuNAc oxime (Table 3.3). Different molar equivalents of the fluorinated α-carboxyketose and hydroxylamine were set up at pH 1 to 9, at room temperature to reflux conditions, and in varying solvents. Catalysts of oxime synthesis, *m*-phenylenediamine (mPDA)[170] and *p*-phenylenediamine (pPDA)[171] were included in the reaction mixture, in concentrations up to 500 mM.

Table 3.3 Reaction conditions for attempted 3-fluoro-DAHP oxime and 3-fluoroNeuNAc oxime syntheses.

FDAHP [a]	hydroxylamine	other	Solvent	Temp	time
2 µmol	15.2 µmol	pH 3.5	H_2O	25 °C	3 d
2 µmol	15.2 µmol	formic acid 26.5 µmol	EtOH	25 °C	3 d
2 µmol	60.8 µmol	pH 3.5	H_2O	60 °C	2 h
2 µmol	45.6 µmol	formic acid 79.5 µmol.	EtOH	60 °C	4 h
FNeuNAc [b]					
2.5 µmol	1.5 mmol	500 mM pPDA, pH 4 and pH 8	H_2O	25 °C	overnight
2.5 µmol	1.5 mmol	500 mM mPDA, pH 4 and pH 8	H_2O	25 °C	overnight
2.5 µmol	1.5 mmol	500 mM pPDA, pH 4	H_2O	reflux	3h
1 µmol	0.3 mmol	500 mM pPDA, pH 7	H_2O	25 °C	overnight
1 µmol	5.0 mmol	50 mM each p/mPDA, pH 8	H_2O	25 °C	overnight
1 µmol	0.5 mmol	50 mM m-PDA, pH 7	H_2O	25 °C	2 weeks

[a] FDAHP – 3-fluoro-DAHP
[b] FNeuNAc – 3-fluoro-*N*-acetylneuraminic acid

3.3. Results

3.3.1. pK_a and K_i values of the fragments

The effect on pK_a and K_i of the introduction of fluorine in the imine's α-position on the pK_a and K_i was examined for all fragments. The mode of inhibition was assumed to be noncompetitive with respect to the metal ion (see below) and competitive with respect to PEP and E4P. The inhibitors occupied the PEP binding site in the crystal structures, which makes their binding necessarily competitive with respect to PEP. On the other hand, they did not appear to extend into the E4P binding site. At first glance, this raises the possibility of noncompetitive inhibition with respect to E4P; however, given $DAHPS_{H6}$'s ordered kinetic mechanism, an inhibitor that is competitive with PEP binding would also necessarily be competitive with the later binding substrate. In other words, since inhibitor forming the $DAHPS_{H6}$·I complex would block formation of the $DAHPS_{H6}$·Mn^{2+}·PEP complex, it would also necessarily block formation of the $DAHPS_{H6}$·Mn^{2+}·PEP·E4P complex, making inhibition competitive with respect to E4P. It is possible that $DAHPS_{H6}$·Mn^{2+}·E4P or $DAHPS_{H6}$·Mn^{2+}·I·E4P could form; however, since these species are not on a productive pathway in the kinetic mechanism, they are not relevant to the inhibitory mechanism.

The oxime-based derivatives showed a shift in the pK_a by -0.63 per fluorine atom, giving an overall pK_a shift from 11.3 for pyruvate oxime to 9.2 for

TFP oxime (Figure 3.4A). The inhibition constants for these fragments were examined, resulting in a K_i = 1.4 mM for the combination of pyruvate oxime with Gro3P (raw data obtained from S. Jiang (2011),[146] but with K_i recalculated based on metal noncompetitive inhibition), 900 μM for 3-fluoropyruvate oxime, and 76 μM for TFP oxime (Figure 3.4B). In case of the fluorinated pyruvate oxime derivatives, the combination with Gro3P did not improve inhibition. Overall, the introduction of fluorine resulted in a strong decrease of K_i.

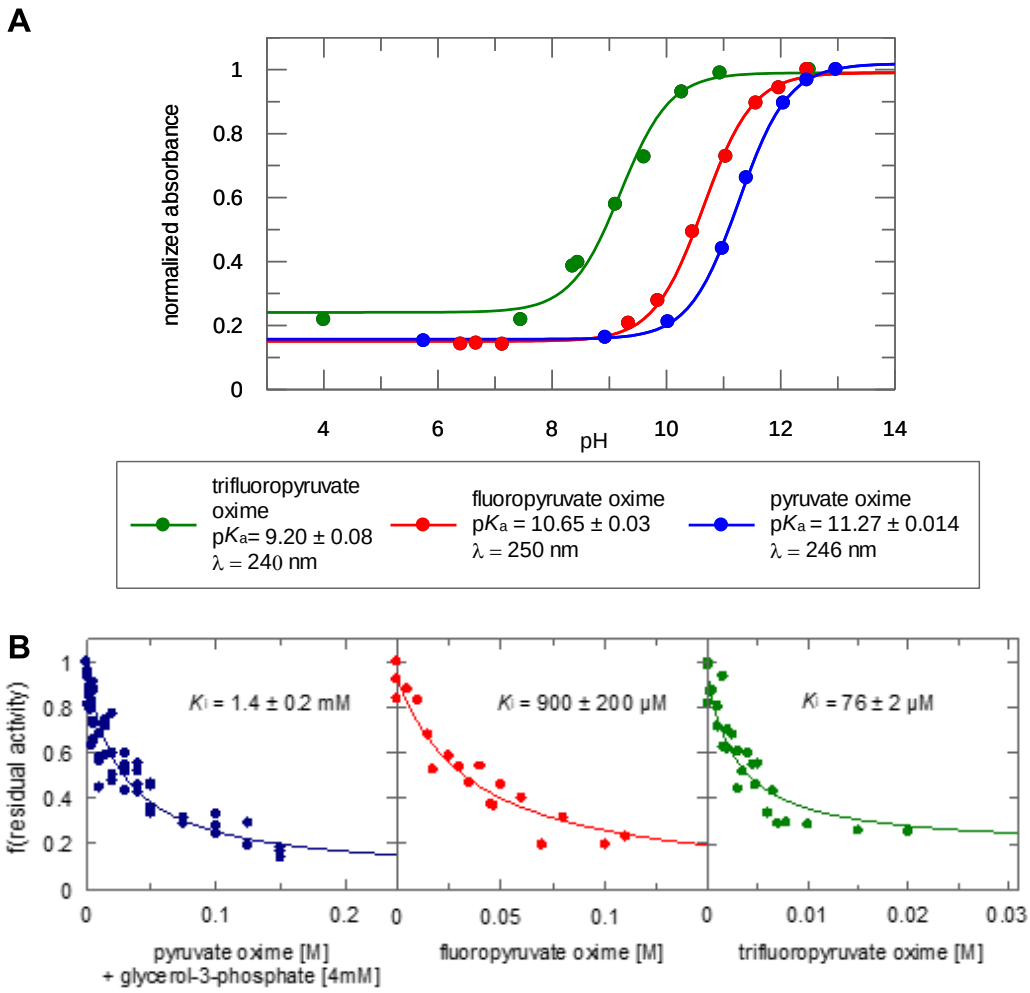

Figure 3.4 pK_a and K_i value determination for a series of pyruvate oxime-based fragments.

The introduction of fluorine leads to a decrease in (A) pK_a and (B) K_i.

The absorbance scan of the semicarbazone derivatives revealed pK_a values for pyruvate semicarbazone and TFP semicarbazone of 14.2 ± 0.3 and 10.9 ± 0.1, respectively (Figure 3.5A). Inhibition by pyruvate semicarbazone and TFP semicarbazone resulted in K_i = 694 µM and 8.3 µM, respectively (Figure 3.5B).

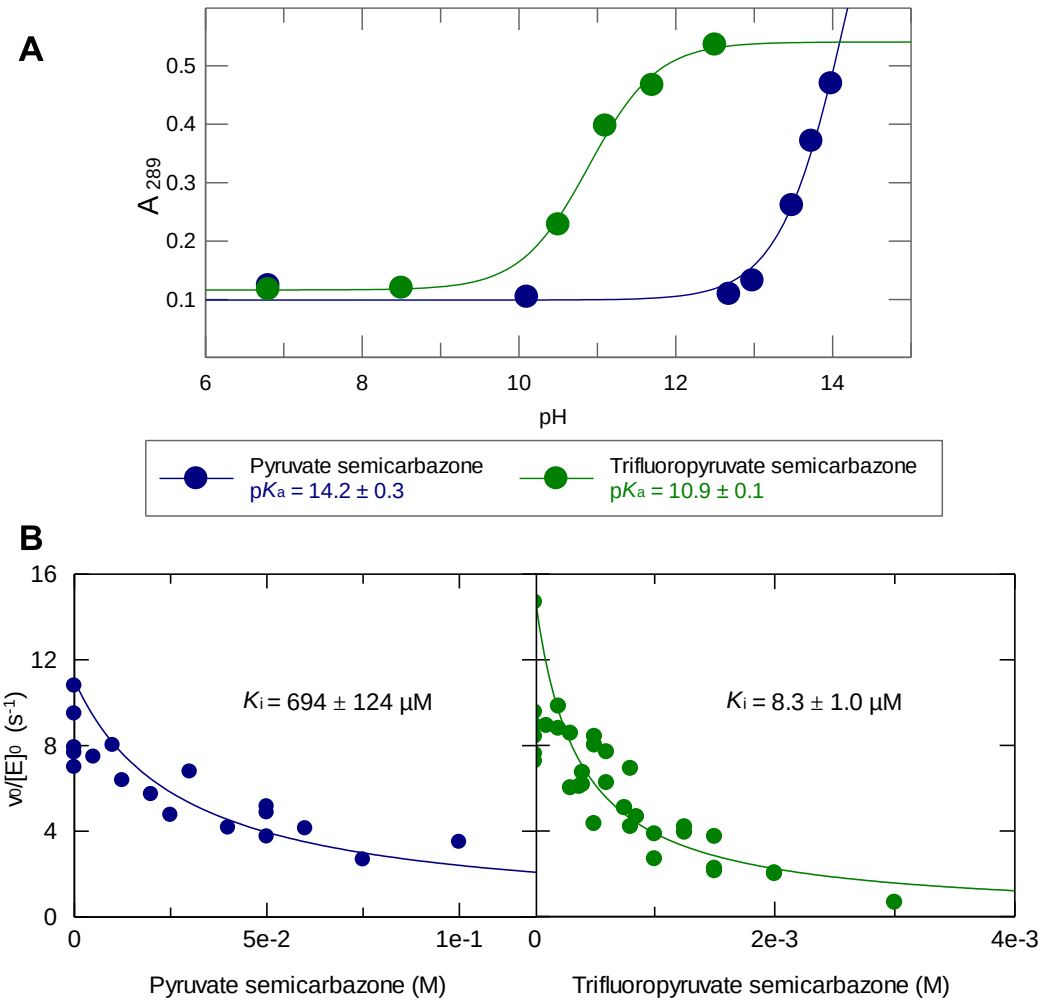

Figure 3.5 pK_a and K_i determination for pyruvate semicarbazone and its fluorinated derivative.

The introduction of fluorine in α-position to the semicarbazone functional group lowers the pK_a (A) and improves potency of inhibition (B).

The effect on the pK_a for the TFP hydrazone could not be determined as the fragment was not base stable. TFP hydrazone had K_i = 6 ±1 µM (Figure 3.6). Therefore, inhibition was 13-fold stronger than with TFP oxime.

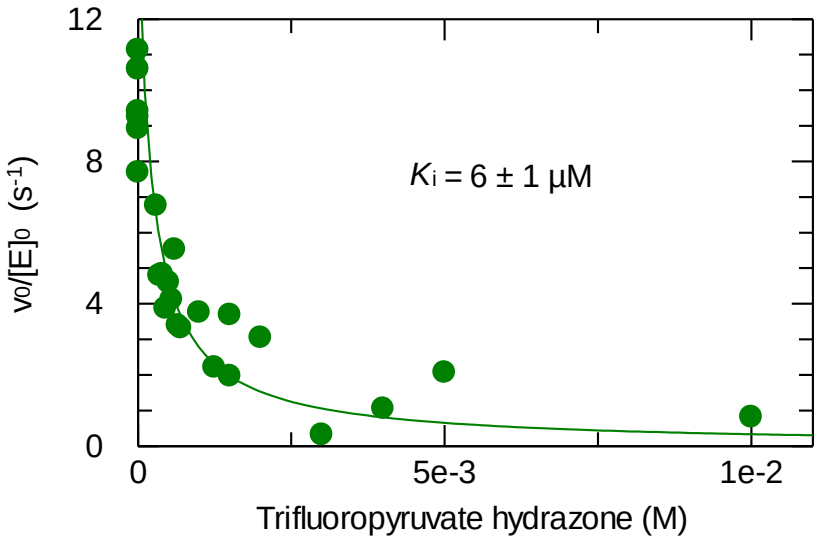

Figure 3.6 TFP hydrazone's inhibition of $DAHPS_{H6}$.

3.3.2. Crystal structures of DAHPS co-crystallized with fragments

$DAHPS_G$ was co-crystallized with TFP oxime (crystal ID: TFPOX, resolution = 2.8 Å) and TFP semicarbazone (crystal ID: TFPSC, 2.5 Å) (Table 3.4). These medium to low resolution structures allowed the protein structure and the location of the inhibitor in the active site to be determined, but the details of ligand coordination were ambiguous in some cases. Due to the low resolution, the localization of solvent molecules was difficult. The asymmetric unit consisted of one homotetrameric protein. In both structures, the first residues of the *N*-terminus could not be located, with the first visible residue being residues Asn5 to Asp7, depending on the structure and subunit. This is consistent with the $DAHPS_G$·DAHP oxime (5CKS), where the first visible residue as Asn5 or Asp6 in each subunit.[100]

Table 3.4 Data collection and model and refinement statistics for DAHPS structures co-crystallized with fragments

	TFPSC	TFPOX
	$DAHPS_G$·TFP semicarbazone$_4$	$DAHPS_G$·TFP oxime$_3$
Data collection		
wavelength	0.9794	0.9794
space group	C 1 2 1	C 1 2 1
unit cell parameters		
a, b, c, (Å)	210.28, 53.2, 150.79	209.789, 52.1899, 149.8
α, β, γ, (°)	90, 116.01, 90	90, 115.82, 90
no. of molecules per asymmetric unit	4	4
resolution range (Å)	72.02 – 2.50	71.55 - 2.80
no. of unique reflections	52544	31040
data redundancy	3.2	2.8
completeness (%)	99.9	98.38
I/σ(I)	6.8	5.5
R_{merge}	0.097	0.173
Model and Refinement		
resolution range (A)	50.22 - 2.5	71.55 - 2.80
R_{work}	0.1863	0.1894
R_{free}	0.2484	0.2611
no. of reflections	54185	30992
$F_{obs}/\sigma(F_{obs})$ cutoff	1.34	1.33
no. atoms		
protein	10131	10248
ligands	56	30
water	132	61
B-factor (Å^2)		
protein	51.3	36.3
ligands	60.0	55.2
water	39.9	28.6
rmsd for bond lengths (Å)	0.018	0.008
rmsd for bond angles (°)	1.07	0.99

A subunit alignment for the TFP semicarbazone structure suggested that all subunits were in a similar conformation, judged by the root-mean-square deviation (rmsd) of the Cα atom positions of the protein backbone in the individual subunits (Table 3.5). A comparison of the subunits' non-variable and variable regions led to a rmsd of 0.26 - 0.30 and 0.48 - 0.86 Å, respectively. The equal conformation of all subunits is in good accordance with the observation that all four chains are accommodating one inhibitor ligand equally bound in the subunits' active sites. Furthermore, the observed protein conformation resembled the one of PEP-bound DAHPS (pdb ID:1N8F was used for structure comparison). An alignment of the subunits B of both 1N8F and TFPSC resulted in a rmsd in the distances of the Cα atom positions in the non-variable region and the variable region of 0.21 and 0.63 Å. Overall, differences were minor.

Table 3.5 Subunit alignments within structures TFPSC and TFPOX.

Each subunit was structurally aligned using Pymol's alignment command, then the rmsd difference in Cα positions between the variable and non-variable regions were compared. The "non-variable" parts of the protein comprised 91% of the sequence: I13-Y94, G106-N187, I193-S311, and A319-G350. The variable region peptides (D6-E12, F95-K105, G188-T192, and L312-L318) were excluded from the structural alignment, and rmsd values were calculated based on the alignment of the non-variable regions. Areas of missing electron density were not included in the rmsd calculations. Differences between the subunits are minor for TFPSC. Subunit D in TFPOX seems to differ from the other subunits in the structure.

TFPSC		rmsd of Cα position (Å)			
		non-variable region			
	Subunit	A	B	C	D
variable region	A		0.28	0.30	0.30
	B	0.66		0.26	0.27
	C	0.87	0.48		0.30
	D	0.58	0.60	0.78	

TFPOX		rmsd of Cα position (Å)			
		non-variable region			
	Subunit	A	B	C	D
variable region	A		0.32	0.31	0.31
	B	0.68		0.31	0.36
	C	0.77	0.40		0.34
	D	1.21	1.62	1.42	

The subunit alignment in the case of TFPOX led to a less clear result (Table 3.5). While the three subunits A, B and C seem to align well to each other and show a similar conformation to the PEP-bound structure 1N8F (rmsd ~ 0.7 Å), subunit D shows greater differences in the alignment when compared to the other subunits (Table 3.5) and to 1N8F (rmsd ~ 2.1 Å) (Figure 3.7). This was surprising, as an inhibitor molecule was bound in subunits B, C and D, so binding of the fragment and structuring of the enzyme do not seem related in this specific structure. However, when aligning the TFP oxime molecules of all subunits, the fragment in subunit D was coordinating in a differing orientation. This could imply a non-specific binding in this subunit, which would explain the absence of active site structuring.

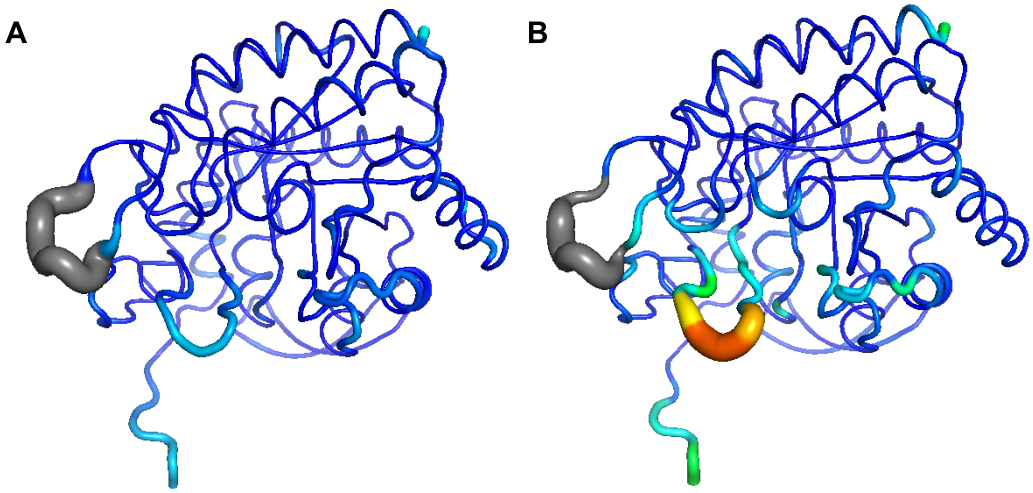

Figure 3.7 TFPOX subunit B (A) and D (B) aligned with subunit B of pdb ID: 1N8F.[109]

Differences in Cα positions are shown by both the ribbon thickness and colour, with the spectrum from blue (0 Å) to red (3.5 Å).

The loop L312-L318 was excluded from all alignments and rmsd calculations. This loop has been characterized as highly flexible and solvent exposed. In most of the subunits, the location of the loop residues could not be identified. Nonetheless, structuring of this loop occurred in some subunits (mainly subunit B), most likely due to intermolecular contacts in the crystal. An interaction of the L312-L318 loop with a neighboring subunit has been observed in this and in a previous study (Figure 3.8).[103] This structuring can therefore be considered a crystallographic artefact and is likely to have no biological relevance.

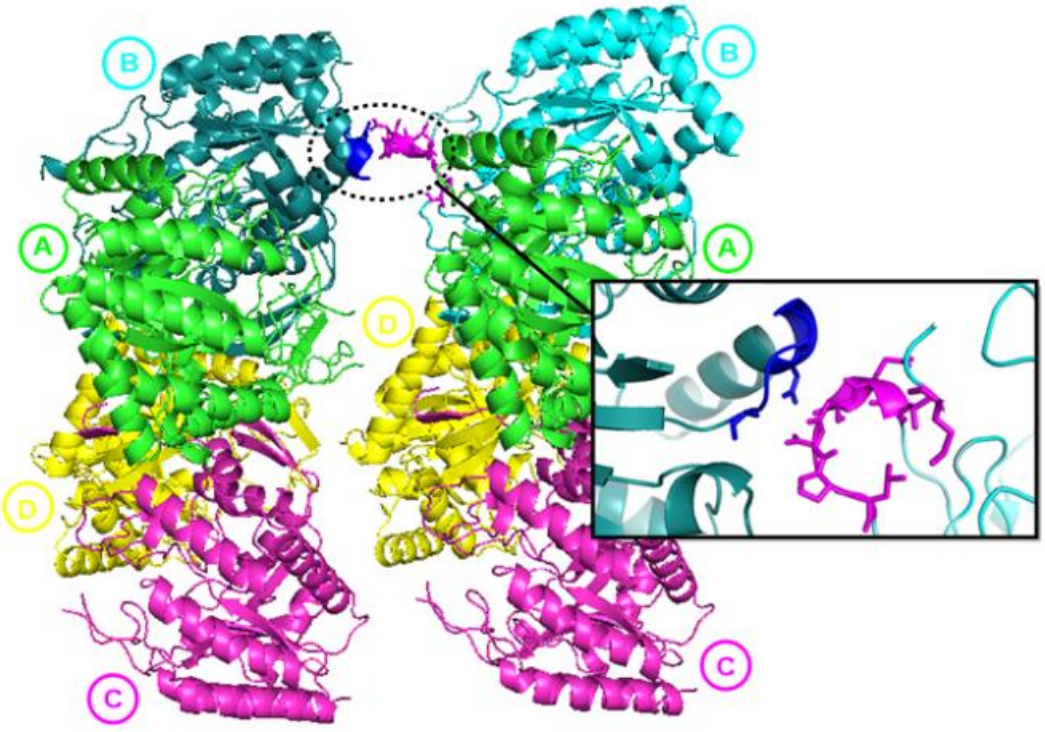

Figure 3.8 Intermolecular contacts lead to structuring of the loop 312-318 in some subunits.

3.3.2.1. TFP semicarbazone and Mn^{2+}coordination

$DAHPS_G$ was co-crystallized with the fragment TFP semicarbazone and Mn^{2+}. All four subunits contain an inhibitor molecule (Figure 3.9), as well as the divalent metal ion bound in the active site. The TFP semicarbazone molecules show differing occupancies depending on the subunit, with occupancy in subunits A – D of 0.93,0.85,0.88, and 0.73, respectively. The inhibitor coordinates in PEP's binding site (Figure 3.10), which demonstrates a competitive mode of binding with respect to PEP. The carbonyl oxygen of the semicarbazone group extends into the metal binding site, and is involved in metal coordination, with $O\cdots Mn^{2+}$ distances of 2.3 Å in subunits A and C, and 3.0 Å in subunit D. TFP semicarbazone captures interactions with five active site residues, namely Arg92, Lys97, Lys186, Arg234, and His268. Most of these residues are also involved in the coordination of PEP. Overall, the ligand binding aligns very well with the active site positioning of PEP. The inhibitor's carboxylate and trifluoromethyl group surround PEP's phosphate group and capture some of the phosphate's active site interactions. Additionally, the semicarbazone functional group replaces the interactions of PEP's carboxylate. The value of fluorine as hydrogen bond acceptors in biological systems has been a long-term topic of discussion.[172–175] Fluoromethyl groups have been observed to form hydrogen bonds with N-H donors.[173,175] The interaction of the inhibitor's trifluoromethyl group with Arg165 (distance 2.8 – 3.1 Å) therefore might add to the binding affinity of the fragment.

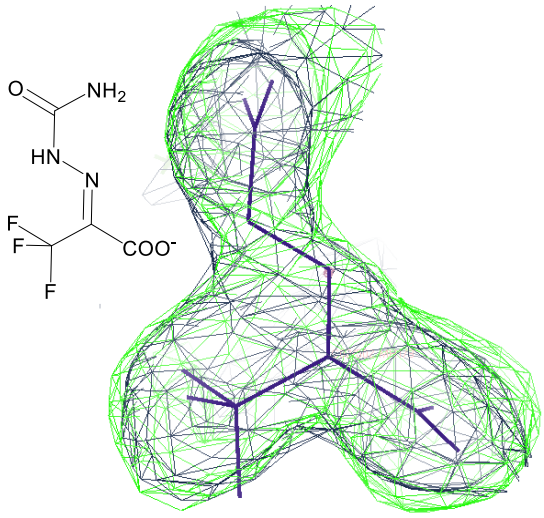

Figure 3.9 F_o-F_c omit map of TFP semicarbazone.

The $2mF_o$-DF_c map is represented in grey (contoured at 1.0 σ) and the mF_o-DF_c map colored in green (contoured at 3.0 σ).

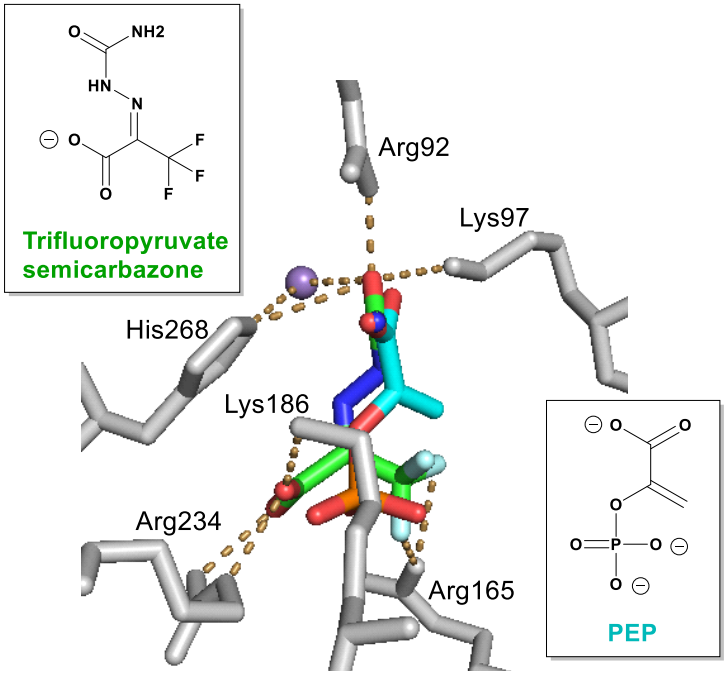

Figure 3.10 Binding of TFP semicarbazone in comparison to PEP from pdb ID: 1N8F.[109]

3.3.2.2. TFP oxime coordination

A crystal structure was obtained for DAHPS co-crystallized with TFP oxime. Subunits B, C and D were ligand-bound with the occupancies of 0.80, 0.87 and 0.89, respectively. In subunit A, no ligand could be located. In the active site, TFP oxime occupied the PEP binding site. Due to the small fragment size and low resolution (2.8 Å), the exact orientation of the fragment could not be defined with certainty. Two orientations seem likely, differing by swapping the positions of the carboxylate and trifluoromethyl groups (Figure 3.11). In both cases, the carboxylate and trifluoromethyl group of the inhibitor coordinate in place of PEP's phosphate group, taking advantage of the interactions with the active site residues Ala164, Arg165, K186 and Arg234 (Figure 3.11B). The electron density appears to be the better fit for option **1** (Figure 3.11A). Nonetheless, this orientation implies accepting a 3 Å distance between the carboxylate and Glu143, which seems rather unfavorable. In option **2**, the orientation of the groups would be identical to the one of TFP semicarbazone and the position of the oxime functional group is in agreement with the one of DAHP oxime (Figure 3.11C). Regardless of whether option **1** or **2** is correct, the overall position of the fragment is inverse to the one of DAHP oxime's pyruvate moiety. This is beneficial for fragment coordination as the carboxylate and the trifluoromethyl group occupy the space of the two crystallographic waters that were described in the DAHP oxime structure as replacements of the non-bridging oxygens of the phosphate group (Figure 1.16).

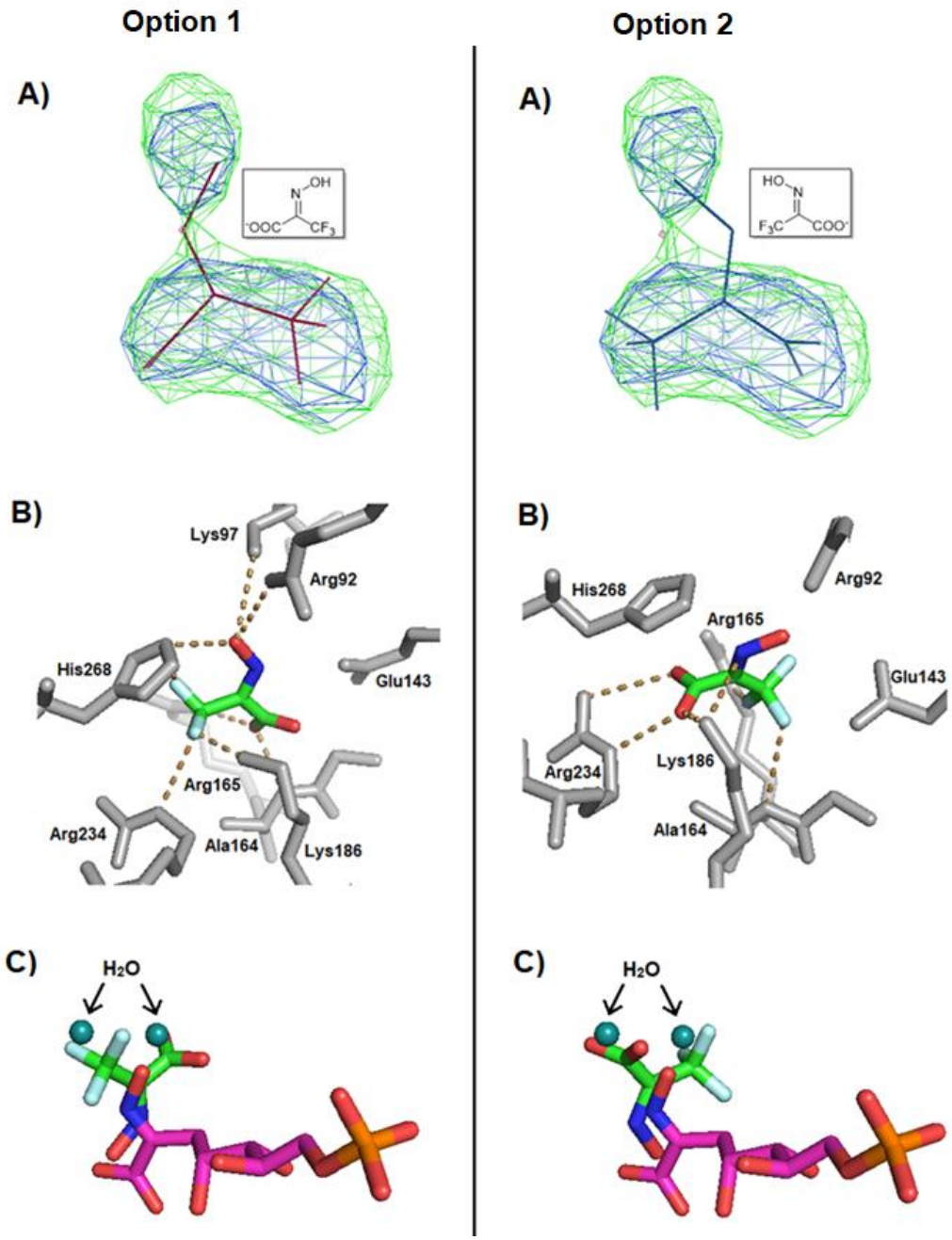

Figure 3.11 Two possible orientations of TFP oxime in the active site.

(A) The $2mF_o$-DF_c map (blue, contoured at 1.0 σ) and the mFo-DFc map (green, contoured at 3.0 σ) show the fit of two plausible orientations of the ligand to the electron density. (B) Active site coordination of the ligand and interaction with active site residues. (C) Alignment with DAHP oxime and the two coordinated crystallographic water from pdb ID: 5CKS.[100]

3.3.3. Bacterial growth inhibition with the esterified fragments

TFP oxime ethyl ester inhibited growth of *E. coli* strain BL21*(DE3) in culture. At t = 4 h after adding the compound to culture, IC_{50} = 0.21 ± 0.01 mg/mL was measured, while at t = 24 h IC_{50} = 0.73 ± 0.03 mg/mL (Figure 3.12, A and B).

TFP semicarbazone ethyl ester also inhibited *E. coli* growth, with IC_{50} = 0.77 ± 0.07 mg/mL after 4 h. Over 24 h, the IC_{50} increased to 1.13 ± 0.03 mg/mL (Figure 3.12, C and D).

No growth inhibition was obtained with TFP hydrazone ethyl ester. This was presumably because of its extremely limited solubility under the assay conditions.

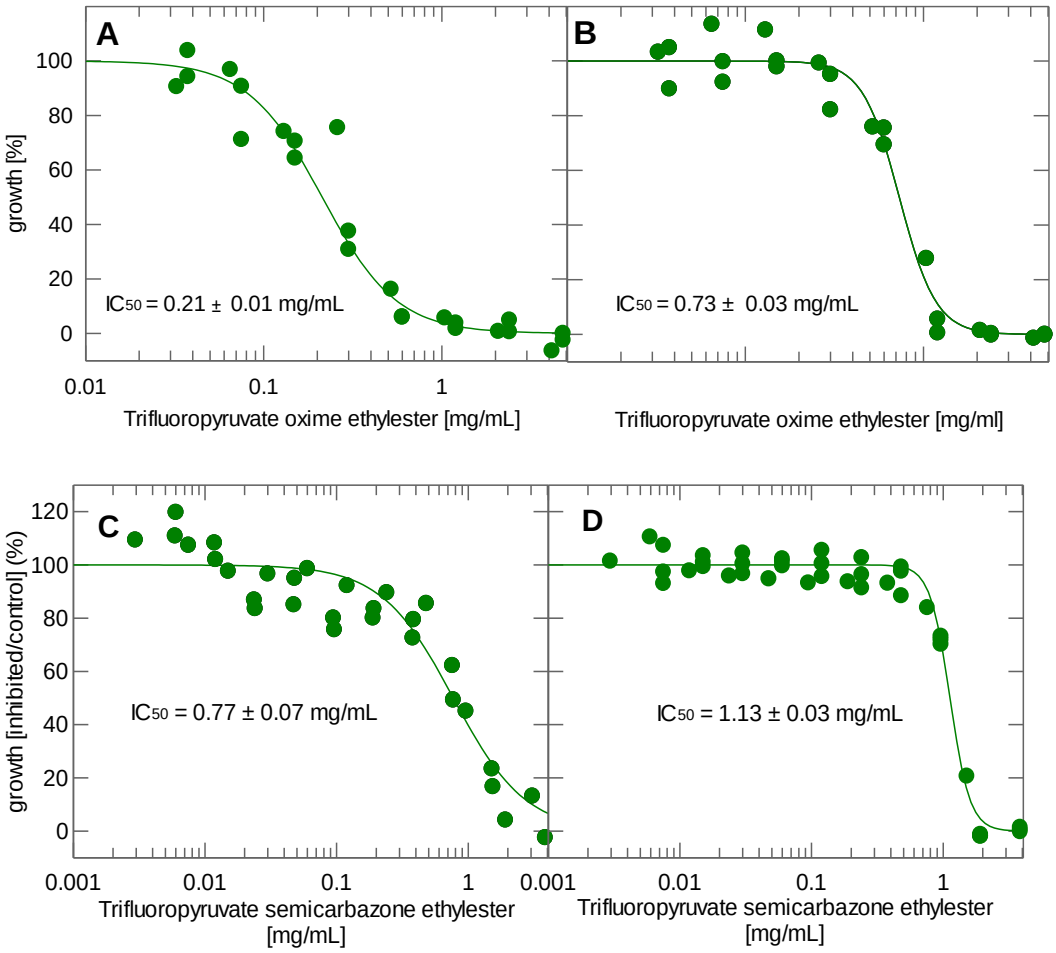

Figure 3.12 Bacterial growth inhibition of the *E. coli* strain BL21*(DE3) by the fragments.

Inhibition by TFP oxime ethyl ester (A) after 4 h and (B) after 24 h, and TFP semicarbazone ethyl ester (C) after 4 h and (D) after 24 h.

3.3.4. Disk diffusion assay with TFP oxime ethyl ester

Cultures of *E. coli* BL21*(DE3) competent cells containing the vector aroG:pET300 were grown on LB/agar plates with and without IPTG. The effect of inhibition by TFP oxime ethyl ester (Figure 3.13A, "O") was clearly reduced for cells overexpressing $DAHPS_{H6}$ (Figure 3.13B, "O") in comparison to the non-

induced *E. coli* cells (Figure 3.13A). A clear zone of inhibition could no longer be identified for the DAHPS overexpressing cells.

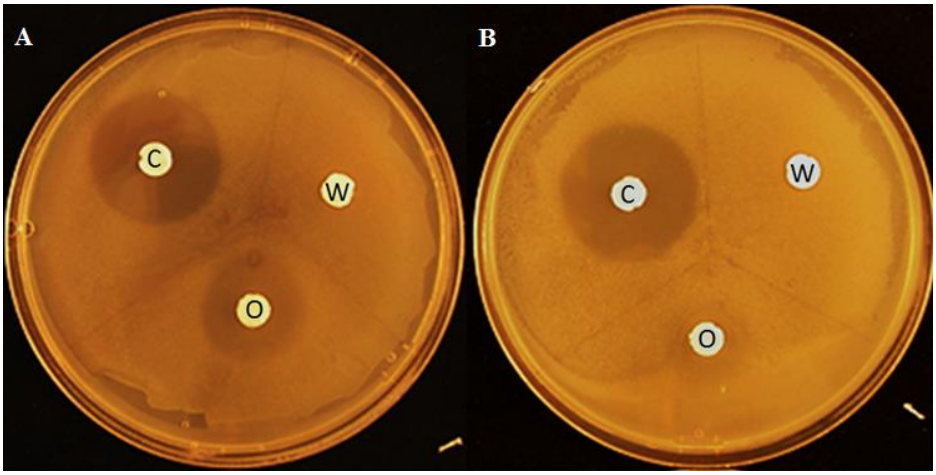

Figure 3.13 Disk diffusion assay with TFPOEE.

E. coli BL21*(DE3) cells containing the aroG:pET300 vector ($DAHPS_{H6}$) were grown in the (A) absence and (B) presence of 1 mM IPTG. **O** – 260 µg TFPOEE, **C** – 10 µg chloramphenicol, **W** - water.

3.3.5. Inhibition testing with DAHP semicarbazone

DAHP semicarbazone synthesis was successful, but resulted in a low yield. For this reason, only preliminary data for the inhibition of DAHPS could be obtained (Figure 3.14). The K_i was calculated based on eq. **2.6** and resulted in $K_i = 2.4 \pm 0.1$ µM.

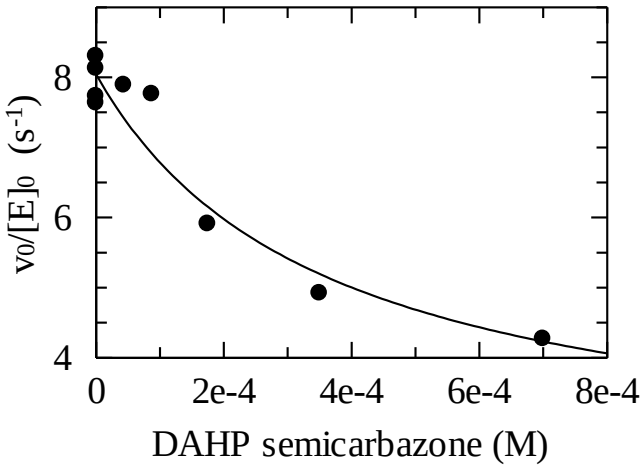

Figure 3.14 Inhibition of DAHPS with DAHP semicarbazone.

3.3.6. Synthesis of 3-fluoro-DAHP oxime and 3-fluoro-NeuNAc oxime

The synthesis of the 3-fluoro analogue of DAHP was performed using two enzymatic reactions. The PEP synthetase ppsA exclusively produces (*Z*)-3-fluoro-PEP when using 3-fluoropyruvate as a substrate.[176] As expected, one single peak was observed in 3-fluoro-DAHP's ^{19}F NMR spectrum with a chemical shift of -144 ppm, which was in accordance to the literature and supported the proposed stereoselectivity of synthesis (Figure 3.15B).[176] The stereoselective mechanism of DAHPS's catalysis has widely been discussed.[103,109,177] The *si*-face attack of (*Z*)-3-fluoro-PEP's C3 on the C1 *re*-face of E4P is expected to lead to stereochemically pure (*S*)-3-fluoro-DAHP (Figure 3.15A).

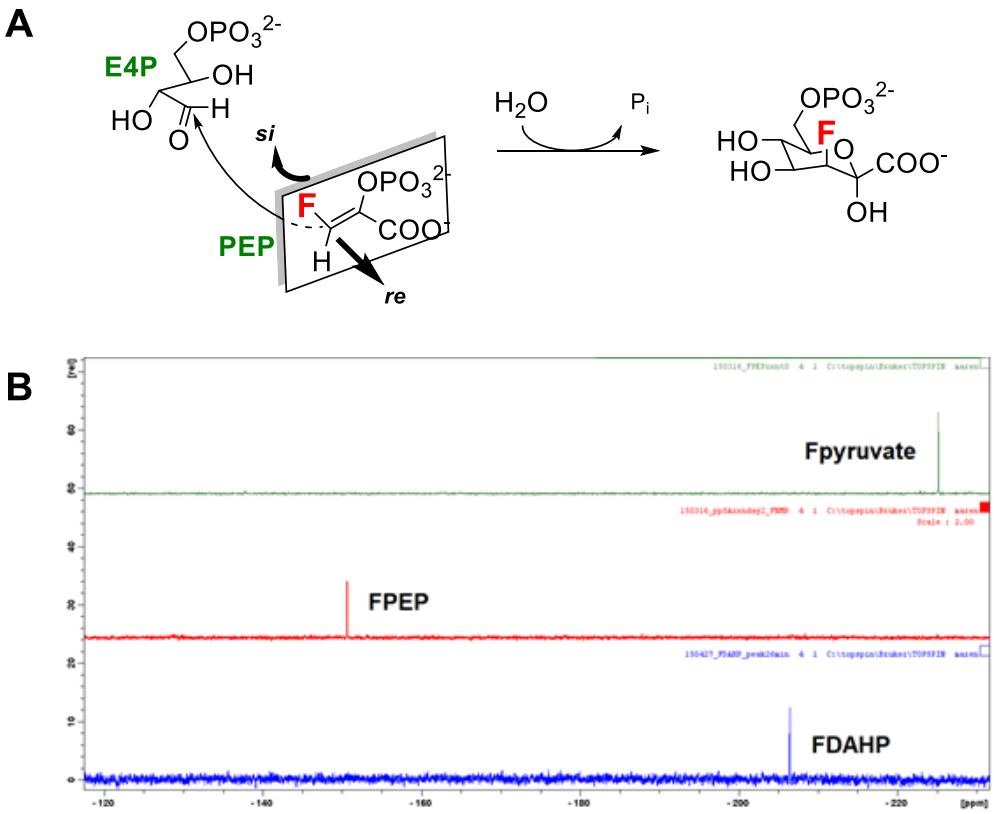

Figure 3.15 Stereoselective synthesis of (S)-3-fluoro-DAHP.

(A)The *si*-face of (*Z*)-3-fluoro-PEP attacking the *re*-face of E4P results in (*S*)-3-fluoro-DAHP. (B) The reaction was followed by proton decoupled ^{19}F NMR. The presence of one single signal confirms the stereoselectivity of the reaction.

All attempts to synthetize oxime derivatives of 3-fluoro-DAHP failed.

3.4. Discussion

3.4.1. Fragment-based inhibitors as DAHPS inhibitors

DAHP oxime did not significantly inhibit bacterial growth, except for one *E. coli* strain which is notable for its leaky cell membranes.[141] This points to cell permeability being the problem, presumably due to its high hydrophilicity and

negative charges. To increase lipophilicity and at the same time to eliminate metal competition, DAHP oxime's size was reduced to a fragment. This fragment-based design helped to limit the molecule to those structural elements that form the key interactions for inhibition of DAHPS. Starting from pyruvate oxime + Gro3P (Chapter 2, Figure 2.13A), a variety of pyruvate derivatives with the common structural element of an imine functional group and an increasing number of electron withdrawing fluorine atoms were designed and tested for $DAHPS_{H6}$ inhibition. The decrease in the pK_a values due to the introduction of the fluorine in the position α to the imine functional group went along with a decrease in K_i. Furthermore, introducing fluorine improved the binding of the small molecule, such that inhibition was achieved by the pyruvate-based fragments alone, and without the need for the second fragment (Gro3P), which was needed for pyruvate oxime to be an inhibitor. The K_i value of TFP oxime improved to 76 µM, compared to 1.4 mM for pyruvate oxime and Gro3P in combination. The TFP hydrazone and semicarbazone even showed K_i values below 10 µM (Figure 3.16). Overall, the small molecule inhibitors with a MW = 120 - 180 g/mol showed excellent potency relative to their size: the calculation of the free energy of fragment binding per non-hydrogen atom (N) enables a quantification of the ligand efficiency (LE) relative to size (eq. **3.2**).[178]

$$\mathrm{LE} = \frac{-RT\ln(K_i)}{N} \qquad (3.2)$$

The LE calculation for the fragments resulted in 0.56 kcal/mol for TFP oxime, 0.53 kcal/mol for TFP semicarbazone and 0.71 kcal/mol for TFP hydrazone. For comparison, an examination of ~150 ligands showed previously that for ligands with < 15 non-hydrogen atoms, each atom contributes to the binding affinity with a maximum of -1.5 kcal/mol.[179] Most compounds range notably below this maximum, with LE of around 0.2 - 0.3 kcal/mol per non-hydrogen atom being common for fragment-based inhibitor design.[178]

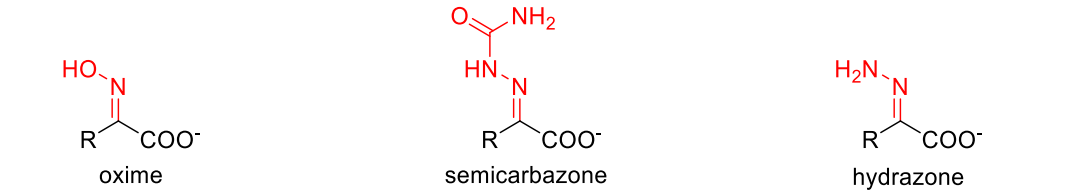

oxime		semicarbazone		hydrazone	
R = CH_3	K_i = 1.4 ± 0.2 mM [a,b]	R = CH_3	K_i = 700 ± 100 µM	R = CH_3	K_i = 53 ± 1 µM[c]
R = CH_2F	K_i = 900 ± 200 µM	R = CF_3	K_i = 8.3 ± 1.0 µM	R = CF_3	K_i = 6 ± 1 µM
R = CF_3	K_i = 76 ± 2 µM				

[a] in combination with Gro3P
[b] data collected by S. Jiang
[c] data collected by M. Peng

Figure 3.16 Pyruvate-based inhibitors of the purified DAHPS.

The co-crystal structures of TFP oxime and TFP semicarbazone with $DAHPS_G$ were solved. Both were localized in PEP's binding site, which implies competitive binding with respect to PEP and E4P (Chapter 3.3.2). For both ligands, properly oriented inhibitor molecules in the active site introduced an enzyme conformation which resembled PEP-bound protein. The co-crystallization of $DAHPS_G$ and TFP semicarbazone was successful when Mn^{2+} was present in the crystallization medium. Indeed, the inhibitor and Mn^{2+} were simultaneously

bound to the crystallized enzyme. In addition, the metal ion was coordinated by the semicarbazone functional group which demonstrated conclusively that binding of this fragment and the metal ion were no longer mutually exclusive. The previously observed competitive binding between the metal ion and inhibitor for DAHP oxime was avoided with this inhibitor fragment. TFP semicarbazone was observed in all four subunits, consistent with the observation of complete inhibition, as all active sites were blocked. Therefore, this fragment possesses improved inhibitory properties over DAHP oxime, as the latter showed half-of-site binding accompanied by a residual enzyme activity even at high inhibitor concentrations.

3.4.2. Bacterial growth inhibition with fragment-based inhibitors

The low K_i values encouraged the testing of the TFP-based fragments on bacterial cell culture. To enable cell membrane penetration, the fragments were esterified to neutralize the carboxylate groups' negative charges (Figure 3.17). These ethyl ester derivatives are expected to serve as prodrugs. Once the compound is taken up, the cell's esterases will hydrolyse the ester functional group. Therefore, the active form of the inhibitor in the biological system is likely the carboxylate. The oxime and the semicarbazone derivative showed bacterial growth inhibition. TFP hydrazone ethyl ester possessed low solubility and precipitated out during the 4 h incubation period. No IC_{50} value could be determined.

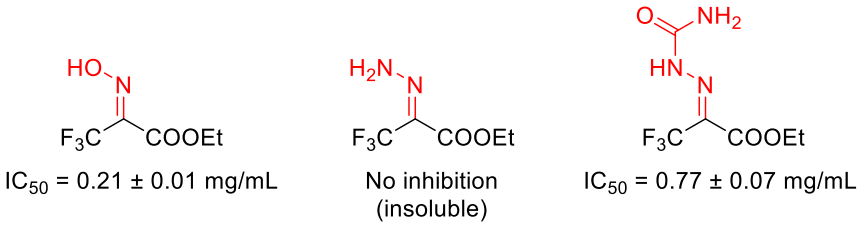

Figure 3.17 Esterified fragments for bacterial growth inhibition.

The IC_{50} value after 4h is presented.

TFP oxime ethyl ester showed the lowest IC_{50} and was examined in more detail. By a disk diffusion assay, the specificity of inhibition was tested. Overexpression of $DAHPS_{H6}$ in *E. coli* led to a decline in inhibition, confirming DAHPS as a target for the inhibition. This finding validated for the first time that DAHPS is a suitable target for bacterial growth inhibition by small molecules. It is also worth noting that the disk diffusion assay was conducted on a complex medium, LB/agar, which would contain aromatic amino acids. The observed bacterial growth inhibition argued that uptake of exogenous amino acids could not compensate for the lack of an operative shikimate pathway, at least for this strain of *E. coli*. Previously designed inhibitors of DAHPS did either not show inhibition of bacterial growth or the target of the inhibition was not confirmed.[127,132] Therefore, this project first demonstrates that bacterial growth inhibition can be achieved by selectively targeting DAHPS with a rationally designed small molecule inhibitor.

3.4.3. Suggestions for structural improvement of DAHPS inhibitors from the experience with pyruvate-based fragments

The fragment-based inhibitor study was conducted to identify the key interactions of the inhibitor with the enzyme and to install novel functional groups with simplified syntheses. The fragments were then intended to serve as starting blocks for the following growing of these small molecules to higher molecular weight inhibitors. It has previously been observed with α-carboxyketose synthase inhibitors that extension of the molecules to dual site inhibitors (this means binding in the PEP and E4P binding pocket) increased the potency.[123,126] An identical approach for our fragments was intended, including the syntheses of 3-fluoro-DAHP oxime and 3-fluoro-NeuNAc oxime based on 3-fluoropyruvate oxime, as well as of DAHP semicarbazone, based on the fragment pyruvate semicarbazone (Figure 3.18). The synthesis of DAHP semicarbazone yielded product, but the quantity was low. Inhibition testing resulted in the preliminary K_i = 2.4 µM, which indicates a comparable potency to DAHP oxime. The inhibitor has not been characterized in more detail, so to date it is unknown if this small molecule inhibits DAHPS to completion or if its binding is competitive with respect to the metal ion. The synthesis of 3-fluoro-DAHP oxime and 3-fluoro-NeuNAc oxime remained unsuccessful. One of the main synthetic challenges seemed to be the fact that, unlike the fragments, DAHP and NeuNAc exist mainly in the cyclic hemiketal forms. Since only the ring-opened form will react with hydroxylamine, we suspect that reduced mutarotation (as a proxy for the rate of

ring opening) could be responsible for the lack of success of the oxime synthesis. Similar problems have been observed with 2-deoxy-2-fluoroglucose (FDG), a well-studied molecule used in radiochemistry.[180] A reduced mutarotation in comparison to the fluorine-free derivative has been described,[181] with increased ring-opening only at high temperatures (80 - 120 °C) and acidic conditions (pH 1.5 − 2.5).[182] New strategies for 3-fluoro-DAHP oxime synthesis need to be developed in the future which may allow the oxime synthesis prior to the introduction of the fluorine in its α-position.

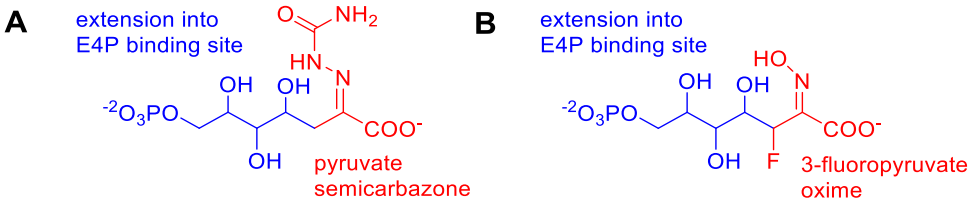

Figure 3.18 Suggested extension of inhibitor fragments to dual site inhibitors.

(A) DAHP semicarbazone and (B) 3-fluoro-DAHP oxime.

The analysis of the TFP oxime and semicarbazone bound crystal structures revealed that the TFP derivatives do not bind in the same orientation as the corresponding structural moiety of DAHP oxime (Figure 3.11C). Instead, both fragments showed inverse binding in comparison with DAHP oxime. This leads to the fragments occupying the same physical space as the two crystallographic waters that assist DAHP oxime's binding (Figure 1.16C). These two crystallographic waters have previously been described to coordinate together with the oxime functional group in the phosphate binding site and mimic phosphate binding. In fact, the same crystallographic waters were identified in the

DAHP hydrazone structure (Chapter 4), being placed almost identically to the ones of the DAHP oxime structure. This points out the importance of those solvent molecules to ligand coordination. The fragment inhibitors are able to occupy the binding sites of these two water molecules. Capturing this binding energy and creating entropic advantages by extending the DAHP-based inhibitors could lead to significant gains in inhibitory efficacy, as many literature examples have shown.[183–185] *O*-alkyl oxime and *O*-(fluoroalkyl) oxime inhibitors have been previously synthetized in our lab. Therefore, a feasible optimization would be the synthesis of DAHP *O*-(3-trifluoromethyl) oxime (Figure 3.19A). Based on the alignment of DAHP oxime with TFP semicarbazone, a second reasonable modification could be the replacement of the carboxylic acid of DAHP oxime by an amide (Figure 3.19B). Both inhibitors interact with Lys97 and Arg97. The semicarbazone group offers the advantage of being uncharged which should help cell membrane penetration.

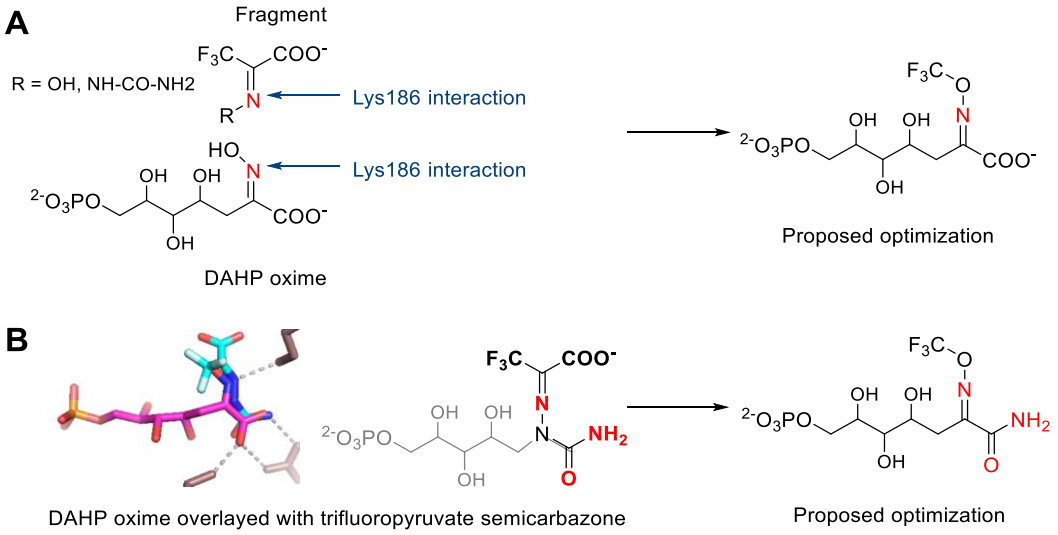

Figure 3.19 Proposals for future DAHPS inhibitors.

(A) The carboxylate and trifluoromethyl groups of TFP oxime and TFP semicarbazone extend into the space occupied by two crystallographic waters in the $DAHPS_G$·DAHP oxime structure which, together with the oxime functional group, mimic the interaction of the THI's phosphate group with the enzyme. Merging the fragments with DAHP oxime at the oxime's nitrogen extends the inhibitor into the waters' binding space. (B) The semicarbazone functional group is positioned in the same space as the carboxylate of DAHP oxime. Replacing the carboxylate with an amide reduces charge in the inhibitor.

3.5. Conclusion

The fluorinated imine-based fragments show excellent properties as DAHPS inhibitors. TFP semicarbazone overcomes the metal competition and the residual activity exhibited by DAHP oxime, and the esterified TFP oxime derivative showed DAHPS-specific inhibition of bacterial growth in cell culture. The next steps for this project will be the growth of these fragments and their extension to molecules that can capture additional binding energy from interactions with DAHPS's active site.

Chapter 4. Structural analysis of DAHPS' complete inhibition

4.1. Introduction

X-ray crystallography enables the visualization of protein-ligand interactions, and can therefore guide rational ligand optimization.[186] DAHPS is a potential target for antibiotics, but its inhibition by the TS mimic inhibitor DAHP oxime was incomplete.[106] There was 15% residual activity even at high inhibitor concentrations, a consequence of half-of-sites inhibitor binding.[100] This residual activity could be sufficient for bacterial survival, so any inhibitor showing half-of-sites binding would be disqualified as an antimicrobial. It is therefore crucial to understand the causes and possible ways to circumvent half-of-sites binding. The $DAHPS_G \cdot$DAHP $oxime_2$ co-crystal structure showed that inhibitor binding occurs exclusively in two of the four subunits of the enzyme (Figure 4.1).[100] The unbound subunits are therefore responsible for the reported residual activity.

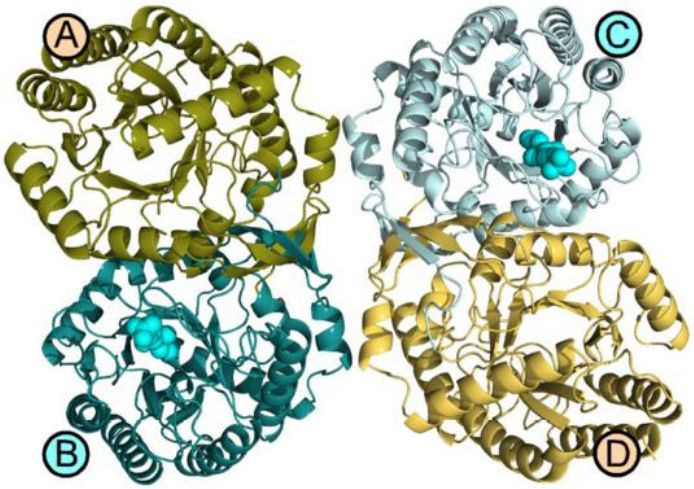

Figure 4.1 DAHP oxime binds in two subunits of the homotetrameric $DAHPS_G$.

Inhibitor binding occurs in the subunits B and C, which show a closed conformation, while subunits A and D are unbound, and show an open conformation. Figure taken from reference.[100]

An alignment of the Cα atoms of the protein backbone revealed conformational differences between the inhibitor-bound subunits (B and C) and free (A and D) subunits, with structural discrepancies predominantly in individual loops (Figure 4.2). Great structural divergence was observed in the amino acid sequence F95-K105, a loop that forms part of the active site. In contrast, an alignment of the two ligand-bound subunits B and C revealed very few differences in the positioning of the individual chains (Figure 4.2). The most notable mismatch was the flexible, solvent exposed loop L312- L318. The electron density was visible throughout the loop in subunit B, but not subunits A, C, or D. Subunit B was the only one where the loop made contact with residues from another asymmetric unit. This could imply that the loop structure was a

crystallographic artefact (Chapter 3.3.2). However, the electron density is visible and the structure is largely the same for the L312 – L318 loop of subunit A of the DAHPS·Mn^{2+}·PEP·SO_4^{2-} structure (pdb ID: 1N8F), which does not make contact with any other subunits.[109] Thus, the L312 – L318 loop appears to be variable, with its structure being determined by a combination of factors.

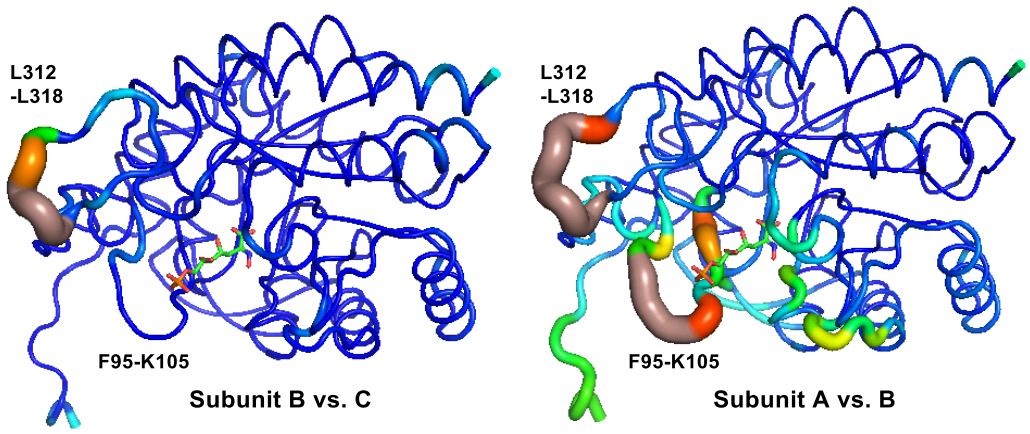

Figure 4.2 Subunit alignment of DAHPS·DAHP oxime$_2$.

A structural alignment of the Cα positions in subunits B and C of DAHPS$_G$· DAHP oxime$_2$ revealed few differences between the inhibitor-bound subunits. A comparison between subunit A (free) versus B (inhibitor bound) shows significant differences in several loop regions. Differences in Cα positions are shown by both the ribbon thickness and colour, with the spectrum from blue (0 Å) to red (3.5 Å). The inhibitor is shown as a stick model with light green carbon atoms. Loops colored in dark salmon show missing residues. Figure generated from pdb ID: 5CKS.[100]

The subunit alignments therefore revealed a structural asymmetry between inhibitor-bound and unbound subunits. Additionally, the observation of 15% residual activity when half the subunits were inhibitor-bound indicated that the unbound subunits experienced a 3-fold decrease in k_{cat} despite the absence of inhibitor in those subunits. This suggested that information was being transmitted from the bound to the unbound subunits. Our lab has proposed that this subunit

communication could be mediated by protein dynamics: Spatially resolved H/D exchange data show that substrate binding initiates an extensive stabilization of loops along the tight dimer interface, some far removed from the active site.[113,141] DAHPS is an oligomeric enzyme, like other α-carboxyketose synthases of the NeuB superfamily. To date, it is not known why these enzymes are oligomeric. DAHP oxime binding shows signs of subunit communication, resulting in reduced k_{cat} in unbound subunits. Therefore, regulation could be a reason for the oligomericity. DAHP hydrazone and DAHP *O*-(2-fluoroethyl) oxime were previously characterized in our lab, and both showed complete inhibition at high concentrations (Figure 4.3).[141] These molecules now serve as important mechanistic tools to explore the residual activity's origin and to identify inhibitor features that are essential for full inhibition.

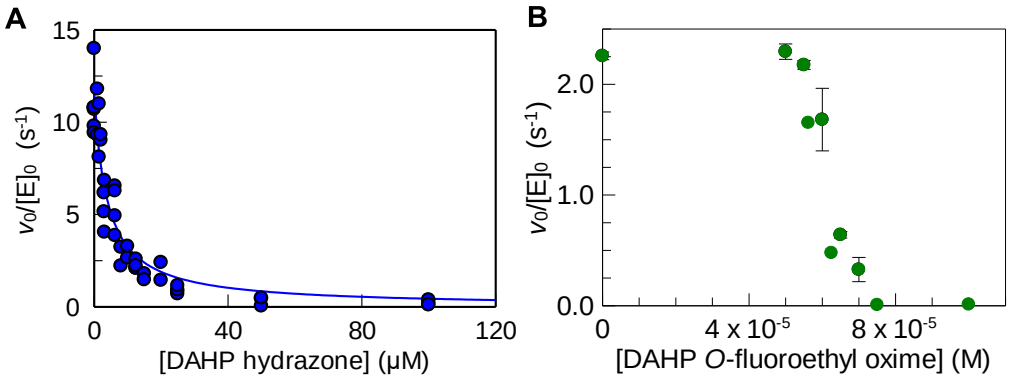

Figure 4.3 Complete DAPHS$_{H6}$ inhibition by DAHP hydrazone and DAHP *O*-(2-fluoroethyl) oxime.

(A) DAHP hydrazone inhibition. The K_i was determined 200 μM E4P and PEP, 100 μM $MnCl_2$, and 50 nM DAHPS$_{H6}$ (B) DAHP *O*-(2-fluoroethyl) oxime. Inhibition was measured in the presence of 125 μM E4P and PEP, 10 μM $MnCl_2$ and 50 nM DAHPS$_{H6}$. Data were collected by (A) J. Wild (undergraduate thesis work) and (B) N. Balachandran.[141]

Despite the structural similarities of DAHP hydrazone and DAHP oxime as imine-based derivatives of DAHP, the hydrazone showed improved inhibitory properties (J. Zheng, J. Wild, undergraduate thesis work). The K_i was 100-fold lower, resulting in a 10 ± 1 nM inhibitor. DAHP *O*-(2-fluoroethyl) oxime also showed no residual activity and a strong positive cooperativity of inhibitor binding (Figure 4.3B).[141] The apparent IC_{50} for DAHP *O*-(2-fluoroethyl)oxime was 62 ± 1 μM. However, the Hill coefficient, *n*, was 19 ± 4. This would conventionally be interpreted as indicating that ~19 inhibitor molecules bind per $DAHPS_{H6}$ tetramer.[187] This seems unlikely, and we do not yet have a good interpretation of the apparently strong cooperativity of DAHP *O*-(2-fluoroethyl)oxime binding.

To characterize the structural differences in binding between DAHP oxime and its derivatives, DAHP hydrazone and DAHP *O*-(2-fluoroethyl) oxime were co-crystallized with DAHPS. Of special interest was the question of whether full inhibition was due to the inhibitors' binding in all four $DAHPS_G$ subunits, or if binding in two subunits diminished the residual activity of the unbound subunits to effectively zero.

4.2. Materials and Methods

4.2.1. Protein crystallization

Protein purification, His_6-tag cleavage, and the setting up of drops by the hanging drop vapour diffusion method was performed as described above (Chapter 3.2.4). Several successful crystallization conditions were found (Table 4.1).

Table 4.1 Crystallization conditions for DAHP hydrazone and DAHP *O*-(2-fluoroethyl) oxime.

crystal identity	Inhibitor identity	[Inhibitor]	Additive	Temperature (°C)
MJ6341	DAHP hydrazone	1.9 mM	40% (v/v) n-propanol	4°C
MJ6212	DAHP hydrazone	2 mM	1.0 M NDSB-256	4°C
MJ6338	DAHP hydrazone	1.9 mM	30% (v/v) ethylene glycol	4°C
MJ6216	DAHP O-(2-(fluoroethyl) oxime	2 mM	1.0 M NDSB-256, 0.05 mM PEP	4°C
MJ6201	DAHP O-(2-fluoroethyl) oxime	2 mM	40% v/v 1,4 butanediol	room temperature

The diffraction and data analysis were performed as described above (Chapter 3.2.4). The structures were refined by the author, Dr. Berti, and Ryan Grainger.

4.2.2. Synthesis of DAHP hydrazone

The DAHP hydrazone synthetic method was previously established in our lab by Jenny Zheng and Jennifer Wild, undergraduate thesis students.

DAHP was synthesized as described above (Chapter 2.2.6), and purified by HPLC using the Q-Sepharose anion exchange column with a linear gradient of 0.1 M to 0.8 M ammonium formate in 10 mM ammonium bicarbonate, pH 6.2 over 30 min at a 2 mL/min flow rate. Repeated lyophilization followed for the removal of ammonium formate. Purified DAHP (0.02 mmol) was dissolved in 1 mL of ddH_2O, then 0.2 mmol hydrazine hydrate was added and the pH was adjusted to pH 8. The reaction was left to react at room temperature for 5 days. Excess hydrazine was removed by lyophilisation.

4.2.3. Synthesis of DAHP O-(2-fluoroethyl) oxime

O-(2-fluoroethyl) hydroxylamine was synthesized following a procedure for the preparation of *O*-substituted hydroxylamines from alcohols.[188] A solution of 6 mmol 2-fluoroethanol in 10 mL dry dichloromethane and 13.6 mmol triethylamine was prepared and kept under argon. After dropwise addition of 7.3 mmol methanesulfonyl chloride, the reaction mixture was stirred at 0°C for 1 h. Then, 10 mL of an aqueous 2 M ammonium chloride solution was added, and the reaction mixture was extracted with 3 × 20 mL dichloromethane. The organic layer was then washed with 2 × 10 mL of an aqueous 20% (w/v) NaCl solution, dried with $MgSO_4$, and concentrated by vacuum evaporation. The resulting 2-fluoroethanol mesylate was resuspended in 3 mL anhydrous ethyl ether and added dropwise into an ice-cooled solution of 9.0 mmol DBU and 8.4 mmol *N*-Boc-hydroxylamine in 3 mL of anhydrous ethyl ether under argon. The reaction

mixture was incubated for one day at room temperature, then concentrated by lyophilization and left under stirring for two additional days. The product was extracted by adding 20 mL ethyl ether, and the organic layer was washed with 10 mL of an aqueous 2 M ammonium chloride solution and 2 × 10 mL of 20% (w/v) aqueous NaCl. The organic layer was then dried with $MgSO_4$ and the solvent was removed by vacuum evaporation. *N*-Boc-*O*-(2-fluoroethyl) hydroxylamine was purified by flash chromatography with a solvent system of 80:20 ethyl acetate and cyclohexane. The deprotection of the hydroxylamine derivative was then performed by dissolving the purified product in 5 mL anhydrous ethyl ether under addition of 5 mL of 2.2 M HCl in anhydrous ethyl ether. The reaction was stirred overnight, and a precipitate was collected.

DAHP was synthesized as described above (Chapter 2.2.6). To a 10 mL reaction mixture containing 0.045 mmol DAHP was added 0.3 mmol *O*-(2-fluoroethyl) hydroxylamine. The pH was adjusted to 5.5 and the reaction was left overnight. The purification was performed by HPLC using the Q-Sepharose anion exchange column under the conditions described above (Chapter 4.2.2).

4.3. Results

4.3.1. Diffraction results

$DAHPS_G$·DAHP $hydrazone_4$ crystals diffracted to a resolution of 2.15 Å for structures MJ6212 and MJ6338, and 1.8 Å for structure MJ6341. The inhibitor

was visible in all the structures. Crystals from the co-crystallization of $DAHPS_G$ and DAHP *O*-(2-fluoroethyl) oxime were obtained (crystal ID: MJ6202, resolution = 2.1 Å; crystal ID: MJ6216, resolution = 2.8 Å), but none of them had inhibitor bound, and the structures were therefore not refined further. The asymmetric unit of structures MJ6212, MJ6338, and MJ6341 all contained one $DAHPS_G$ tetramer. As observed in 5CKS[100] and in TFPOX and TFPSC (Chapter 3.3.2), the first residue with visible electron density was Asn5 to Asp7, depending on the subunit. As all $DAHPS_G$·DAHP $hydrazone_4$ structures showed comparable properties, the most in-depth refinement was performed for MJ6341, the structure with the highest resolution (Table 4.2). All data discussed in the following is obtained from the analysis of MJ6341.

Table 4.2 Data collection and refinement results.

	MJ6341
	$DAHPS_G$·DAHP $hydrazone_4$
Data collection	
wavelength	0.9794
space group	I 1 2 1
unit cell parameters	
a, b, c, (Å)	150.180, 53.550, 198.413
α, β, γ, (°)	90.00, 107.48, 90.00
no. of molecules per asymmetric unit	4
resolution range (Å)	94.63 - 1.80
no. of unique reflections	102385
data redundancy	4.7
completeness (%)	100.0
I/σ(I)	10.5
R_{merge}	0.070
Model and Refinement	
resolution range (A)	37.42-1.8
R_{work}	0.2013
R_{free}	0.2314
no. of reflections	102319
$F_{obs}/\sigma(F_{obs})$ cutoff	1.34
no. atoms	
protein	10151
ligands	76
water	351
B-factor (Å^2)	
protein	49.0
ligands	55.9
water	41.2
rmsd for bond lengths (Å)	0.007
rmsd for bond angles (°)	0.805

4.3.2. DAHP hydrazone binding

DAHP hydrazone coordinated in all four binding pockets, with occupancies in subunits A to D of 0.76, 0.79, 0.81, and 0.67. The electron density in subunits A to C was clearly visible (Figure 4.4). The density in subunit D was weaker, and the calculated occupancy for the inhibitor was low. On its own, the amount of electron density might not constitute prima facie evidence for inhibitor binding. The scattered density could potentially originate from bound P_i and solvent molecules. However, it is noteworthy that when the contour level in the omit map was decreased, the shape of the electron density was as expected for DAHP hydrazone. That is, strongest density was visible around the phosphate group, the hydroxyl oxygens and around the carboxylate and hydrazone groups. The weakest density was around C3, the same position where it was weakest with DAHP oxime binding.[100] The fact that DAHP hydrazone demonstrated complete DAHPS inhibition would tend to support inhibitor binding to all four subunits. Thus, in the context of the weak but correctly positioned and shaped electron density, and the complete inhibition by DAHP hydrazone, the balance of probabilities favoured the inhibitor being bound to subunit D. If this conclusion is incorrect, then the following discussion regarding conformational differences between subunit D and the bound subunits, and the energetic consequences of breaking subunits' conformational symmetry are equally valid.

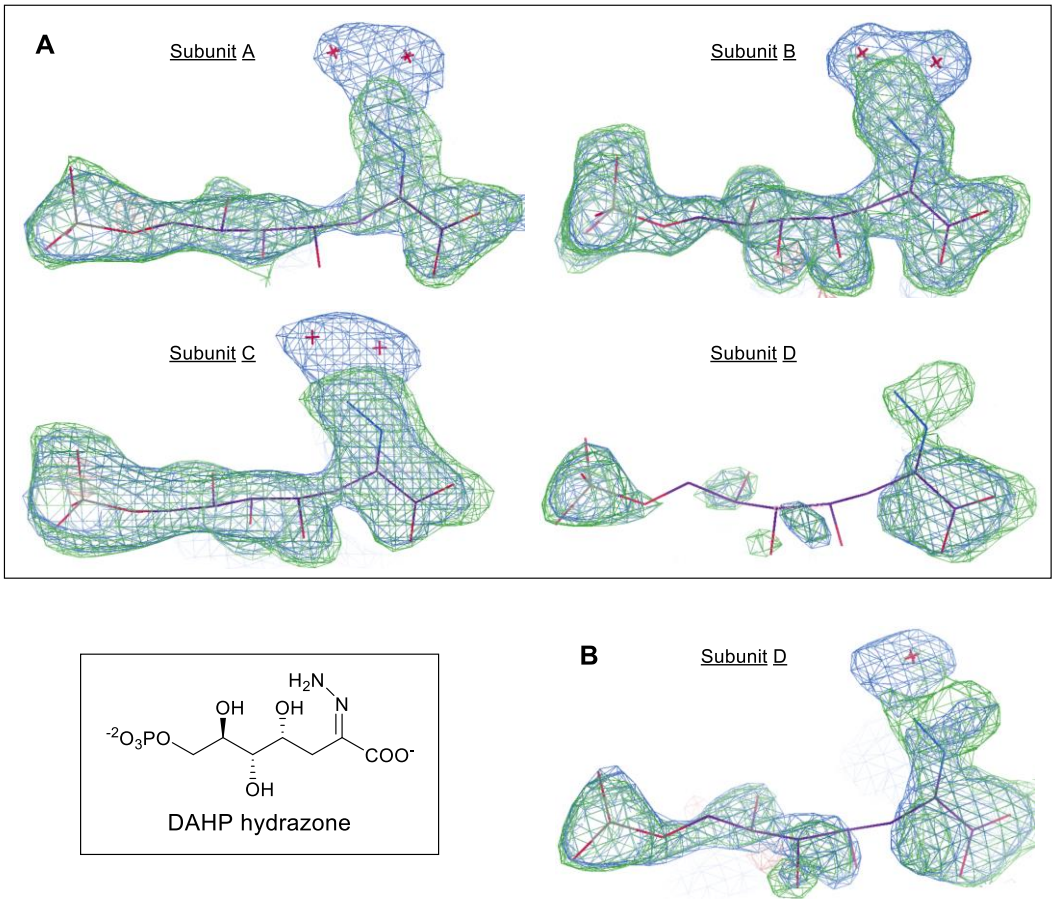

Figure 4.4 F_o-F_c omit map for DAHP hydrazone in all subunits.

(A) The 2mF_o-DF_c map (blue, contoured at 1.0 σ) and the mFo-DFc map (green, contoured at 3.0 σ) is shown for DAHP hydrazone in each subunit. (B) The 2mF_o-DF_c map (blue, contoured at 0.7 σ) and the mFo-DFc map (green, contoured at 2.5 σ) is shown for DAHP hydrazone in subunit D.

Overall, binding of DAHP hydrazone in the active sites of subunits A to C was structurally almost identical to DAHP oxime (structure ID: 5CKS[100]) (Figure 4.6A). The most striking difference was the presence of an additional water molecule that coordinated with the hydrazone functional group and assisted ligand binding in the active site, as well as a shift in the water-coordinating residue Glu143 (Figure 4.5).

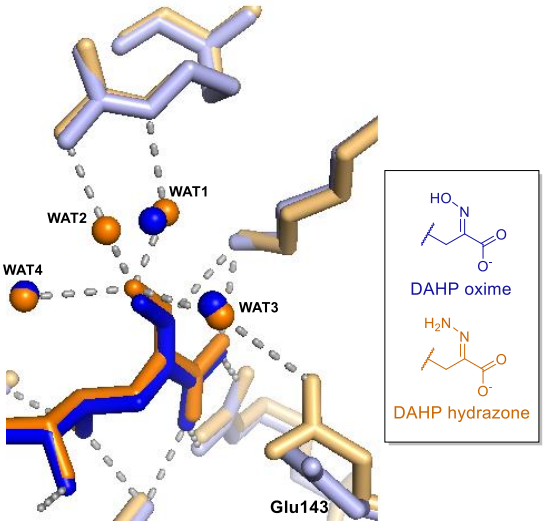

Figure 4.5 Water coordination of the hydrazone functional group.

WAT1, 3 and 4 are located at similar positions as observed for DAHP oxime (pdb ID: 5CKS[100], blue). Wat2 is an additional water molecule aiding the hydrazone's coordination. Glu143 is shifted to coordinate WAT3. The $DAHPS_G$·DAHP $hydrazone_4$ structure MJ6341 is presented in orange.

Inhibitor binding in subunit D's active site differed (Figure 4.6B). Residues Arg99 and Thr100, which coordinated with the phosphate group of DAHP hydrazone in the other three subunits (Figure 4.6A), were disconnected from this interaction. There was a 1.1 Å shift in the position of Asp326's Cγ atom, a residue that usually coordinates DAHP hydrazone's O4 and O6 position. Additionally, the electron density for the Lys97 sidechain was not visible. This residue typically coordinates the carboxylate group as well as the O4 position. Four crucial active site residues were therefore not positioned to form effective interactions with the inhibitor molecule. Moreover, compared to the closed conformation of the inhibitor-bound subunit B in 5CKS, the backbone trace of active site loop F95 -K105 was significantly different (Figure 4.6B).

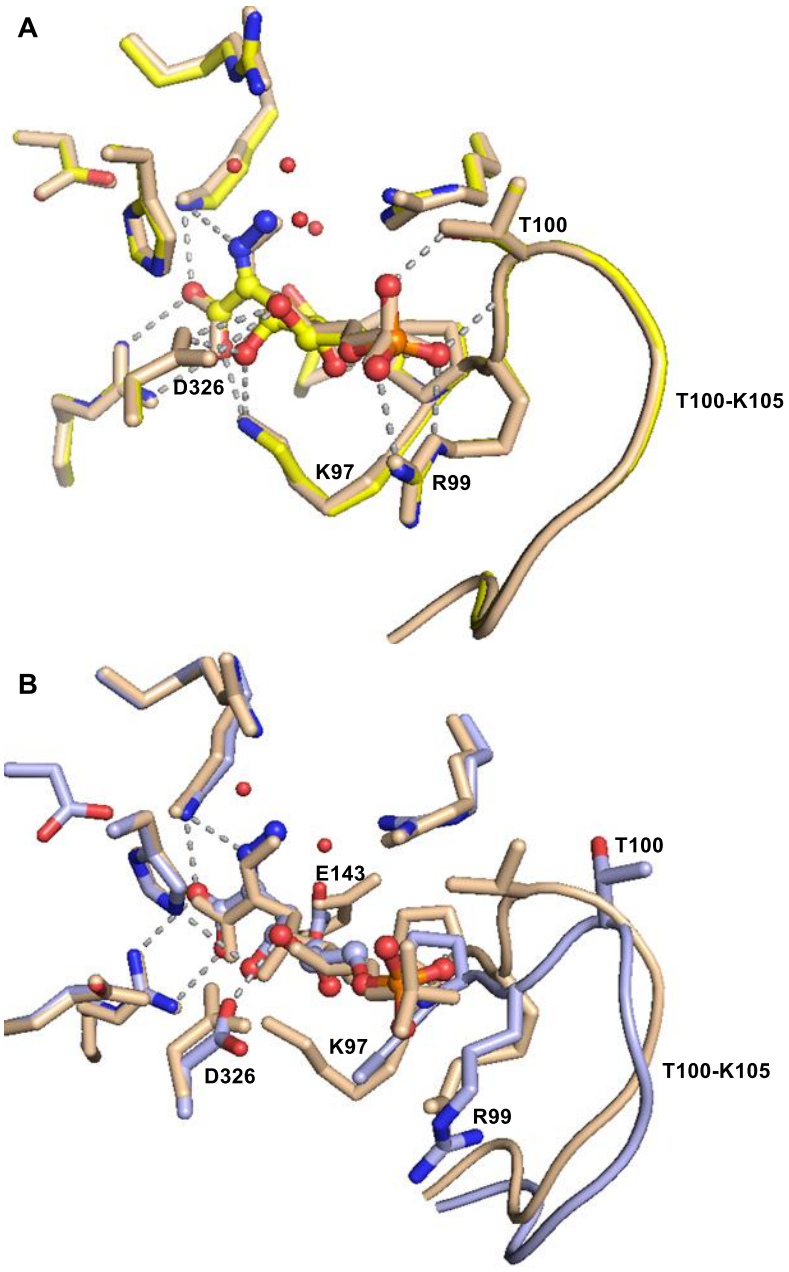

Figure 4.6 Comparison of DAHP hydrazone versus DAHP oxime binding.

Active site structures of different inhibitor-bound and -unbound $DAHPS_G$ structures. (A) Subunits B of MJ6341 (DAHP hydrazone, yellow carbon atoms, closed conformation) and 5CKS (DAHP oxime, beige, closed). B) Subunit D of MJ6341 (DAHP hydrazone, light blue carbon atoms, open conformation) and subunit B of 5CKS (DAHP oxime, beige, closed).

4.3.3. Subunit structure

Variable and non-variable regions of the DAHPS structure were previously defined based on the $DAHPS_G \cdot$DAHP oxime structure, 5CKS.[141] The non-variable region consisted of 91% of the amino acids in the structure, and, upon structural alignment, had rmsd values in the Cα atom positions of 0.23 to 0.43 Å. The variable regions, consisting of residues D6 - E12, F95 - K105, G188 - T192, and L312 - L318, made up 9% of each subunit's amino acid residues and had rmsd differences of 0.30 Å between the closed conformation subunits, B and C, 0.45 Å between the open conformation subunits, A and D, and 1.8 Å to 2.0 Å when comparing open versus closed conformations in 5CKS.

Comparing the Cα positions in the MJ6341 structure revealed that the four subunits were not all in identical conformations. The non-variable regions of subunits A to C were essentially identical within the resolution of the structure. The rmsd values for Cα positions were of 0.19 Å to 0.23 Å, compared with estimated coordinate errors of 0.19 Å.[165] The values were slightly larger when comparing subunit D to subunits A to C, 0.30 Å to 0.36 Å, but still very small. In the variable regions, subunits A to C still aligned well with each other, with rmsd ≤ 0.62 Å, while subunit D differed more, with rmsd ~ 2 Å. (Table 4.3).

Table 4.3 Subunit alignment for DAHPS$_G$·DAHP hydrazone (MJ6341).

The structural alignment was performed using the "superimpose" command in Pymol. The non-variable regions of the protein were aligned, while the variable loops D6 - E12, F95 - K105, G188 - T192, and L312 - L318 did not contribute to the structural alignment. Regions with missing residues were excluded from the rmsd calculation. Overall, subunit D showed larger structural differences in comparison to the other three subunits.

MJ6341		rmsd difference in Cα position (Å)			
		non-variable region			
	Subunit	A	B	C	D
variable region	A		0.23	0.23	0.36
	B	0.55		0.19	0.30
	C	0.62	0.27		0.33
	D	1.89	1.97	1.97	

Differences in the subunits were located mainly in variable loops. The vast majority of the protein aligned well in the non-variable region (Figure 4.7). Subunits A to C barely differed over the entire structure. Likewise, the comparison of subunits A to C to subunit D showed a well-aligned non-variable region, but revealed strong variability around the active site and at the *N*-terminus.

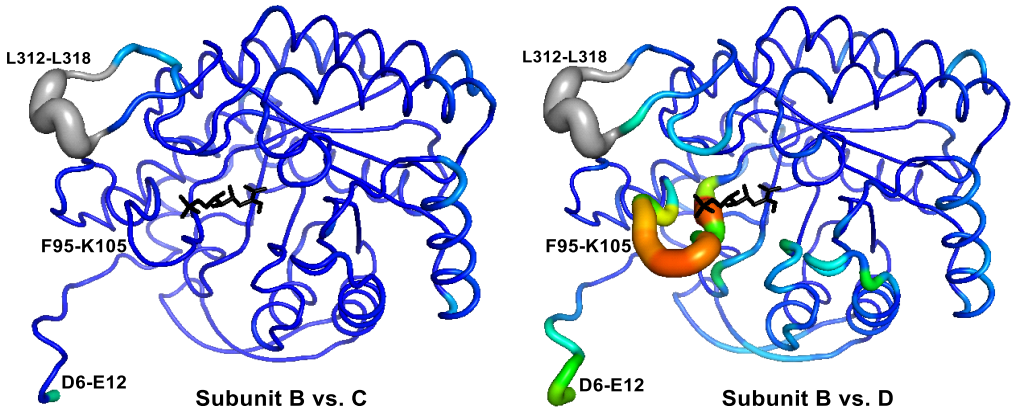

Figure 4.7 Subunit structural alignment of MJ6341.

Individual subunits in the $DAHPS_G$·DAHP hydrazone structure MJ6341 were structurally aligned. (A) Alignment of subunits B and C showed minor differences. (B) Alignment of subunits B and D showed greater divergence, especially around the ligand binding site. Differences in Cα positions are shown by both the ribbon thickness and colour, with the spectrum from blue (0 Å) to red (3.5 Å). The inhibitor is shown in black. The loop L312-L318 is colored in grey as missing residues in subunit C and D made an alignment impossible.

The individual MJ6341 subunits were further compared to stereotypical open (5CKS, subunit D) and closed (5CKS, subunit B) conformations (Table 4.4). The non-variable regions were too similar to distinguish between conformations, but the differences were visible in the rmsd values of the variable regions. Subunits A – C had typical closed conformations, and were as similar to 5CKS's subunit B as 5CKS subunits B and C were to each other. This suggests that the nature of the inhibitor's functional group, oxime vs. hydrazone, had no measurable effect on the subunit structure when it was tightly bound. Subunit D of MJ6341 had an almost typical open conformation (Figure 4.8). The biggest difference between subunits D of 5CKS and MJ6341 was in residues T189-D190, a surface-exposed loop that is not part of active site or inter-subunit interactions, and so does not appear to be functionally important (Figure 4.8). Most importantly, the active site loop, F95 – K105, was very similar to the open conformation of 5CKS's subunit D, and clearly different to the closed conformation of 5CKS's subunit B (Figure 4.9).

Table 4.4 Structural alignment of DAHP oxime versus DAHP hydrazone structures.

Structural alignments were made between the open and closed conformations, subunits A and B, respectively of the $DAHPS_G$·DAHP oxime (5CKS) with individual subunits of $DAHPS_G$·DAHP hydrazone (MJ6341) as in Table 4.3.

		rmsd difference in Cα positions (Å)			
		5CKS			
	Subunit →	D (open)		B (closed)	
	↓	non-variable	variable	non-variable	variable
MJ6341	A	0.42	2.0	0.26	0.44
	B	0.44	2.2	0.14	0.40
	C	0.46	2.0	0.22	0.36
	D	0.28	0.77	0.26	1.6

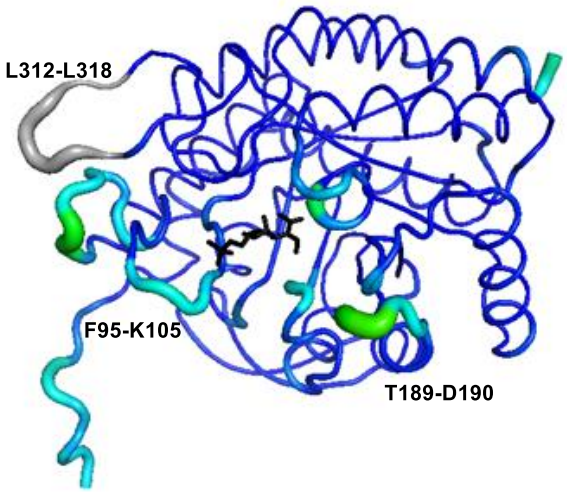

Figure 4.8 Structural alignment of open conformation subunits.

Structural alignment of subunits D of 5CKS[100] and MJ6341. The ribbon thickness and colour indicate the difference in Cα position, with the spectrum from blue (0 Å) to red (3.5 Å). The structural differences were small, demonstrating that both subunits were in an open conformation. The loop L312 – L318 is grey, as residues for subunit D of MJ6341 were missing.

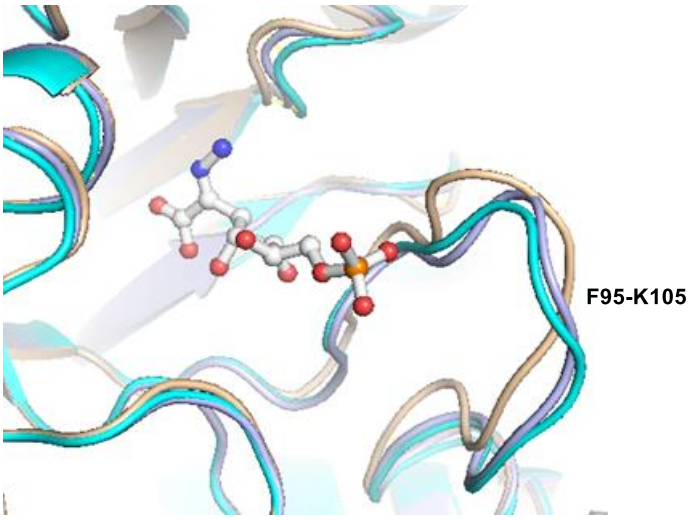

Figure 4.9 Comparison of loop F95 – K105 in the open and closed conformation.

The active site for subunits D MJ6341 (DAHP hydrazone, blue ribbon, open), subunit D of 5CKS (unbound, cyan, open), and subunit of B of 5CKS (bound, beige, closed). DAHP hydrazone is shown in a ball and stick representation.

4.4. Discussion

DAHP oxime inhibits DAHPS with a 15% residual rate, most likely due to the inhibitor's half-of-sites binding, leaving two subunits empty and available for enzymatic turnover. DAHP *O*-(2-fluoroethyl) oxime and DAHP hydrazone lead to full inhibition of the enzyme. The reason for this complete inhibition was unknown. To find out whether they bound to all four subunits or inhibited the unbound subunits allosterically, the co-crystallization of both inhibitors with $DAHPS_G$ was attempted. All co-crystallization attempts for DAHP *O*-(2-fluoroethyl) oxime were unsuccessful. Crystals that diffracted were obtained, but the inhibitor was not present in the structure. For $DAHPS_G$·DAHP $hydrazone_4$, several crystals were obtained under saturating ligand conditions. Binding of

DAHP hydrazone was observed in all four binding sites, which explained the complete inhibition by this ligand. Nonetheless, the enzyme was not fully symmetrical, with subunits A – C having closed conformations, while D was in the open conformation. Subunits A - C were essentially identical to each other and to (inhibitor-bound) subunit B in the $DAHPS_G \cdot$DAHP oxime structure, 5CKS[100] (Table 4.4). Thus, in spite of the 100-fold tighter binding by DAHP hydrazone with K_i = 10 nM, than DAHP oxime with K_i = 1.5 μM,[100] the inhibitor did not detectably affect the protein's active site structure (Figure 4.6A). The only visible difference between DAHP hydrazone and oxime binding in the active site of subunits A – C was a change in the Glu143 sidechain position, which reflected the arrangement of water molecules around the hydrazone versus oxime groups (Figure 4.5). Though the protein structure did not change, there was an additional water molecule that was coordinated to the hydrazone functionality. Active site-bound waters have been frequently described in literature as mediators between ligands and enzymes that assist in ligand binding, and in some cases improve potency and selectivity of binding.[163,189–195] An example for the importance of active site waters is the L-arabinose binding protein which has an excellent affinity to L-arabinose due to two active site waters that help its binding, but a low affinity to D-fructose as the active site water interactions are unfavourable for this molecule.[191] Substrate specificity is therefore determined by the ability to accommodate active site water. Another example is a cyclosporine A derivative

which was designed to capture additional binding interactions in the active site due to a structure extension, but the replacement of tightly bound active site waters resulted in an 8 - 9 fold decrease in overall binding affinity.[194] DAHP hydrazone's ability to capture additional binding energy by accommodating an extra water molecule could explain some of its increased potency over DAHP oxime. The water molecules WAT1 and WAT2 each form a hydrogen bond of 2.4 Å with the hydrazone functional group (Figure 4.5). This distance is short for a hydrogen bond. Standard hydrogen bonds typically range around 2.8 Å. Nevertheless, interactions < 2.55 Å, identified as low-barrier hydrogen bonds, have previously been described in enzymatic systems.[196–198] They occur when the pK_a of the two participating groups are similar.[196] Predicting pK_a values inside an enzymatic binding pocket is difficult, as the active site's microenvironment has a great influence on the apparent pK_a values (Chapter 2.4.2). This is especially true of active site water molecules, for which pK_a values as low as 7.5 have been reported.[199,200] Therefore, similarities in pK_a values are difficult to predict. To exclude other possibilities, the structure MJ6341 has been refined replacing WAT1 and WAT2 with other negatively charged ions which were contained in the crystallization condition. Negatively charged ions were selected based on the prevalence of the positively charged active site residues in the phosphate group binding pocket. Possible candidates were Cl^- and formate (crystallization conditions Chapter 3.2.4 and 4.2.1). The latter anion originated from the DAHP hydrazone purification by anion exchange. The refinement indicated that these

ligands did not fit the density. Furthermore, the possibility that DAHP hydrazone was formylated at the hydrazone's NH_2 group (H-(C=O)NH-N=C) was examined. This molecule fit the density well, but there was no chemical precedent for a reaction between hydrazone and a carboxylate group. In addition, a mass spectrogram of the DAHP hydrazone sample used for crystallization, collected after the diffraction data were collected, confirmed the presence of DAHP hydrazone and absence of formylated DAHP hydrazone. The water molecules were therefore the most plausible fit for the observed density.

The open conformation adopted by subunit D involved conformational changes, most notably in the active site loop, F95 – K105, along the E4P binding site (Figure 4.9). Many of the inhibitor interactions at the hydrazone end of the inhibitor were maintained, though with fewer water molecules around the hydrazone group (Figure 4.6). One exception was the 1.1 Å shift in the D326 sidechain, which reduced its hydrogen bonds to the inhibitor from three (two to O4, one to O5) to one (to O5) (Figure 4.6B). Another exception was the K97 sidechain, which formed an ion pair with the inhibitor's O1 (carboxylate) and O4 (hydroxyl) groups in subunit B. In subunit D there was no electron density visible beyond Cβ, meaning those interactions were likely lost. Disruptions at the phosphate end of DAHP hydrazone were more dramatic. Movement of the R99 sidechain broke a bidentate ion pair with the phosphate oxygens, while movement of T100 broke its hydrogen bond with a phosphate oxygen. The energetic penalties to DAHP hydrazone binding of these structural changes can be

estimated based on their effects on DAHP oxime binding.[106] Since these interactions are distant from the oxime/hydrazone groups, they are likely to be similar between both inhibitors. The K_i values for the R99A and T100A mutants increased 380-fold and 3-fold, respectively, for an overall 1140-fold, or 4 kcal/mol, effect. The D326A mutation increased K_i 11-fold, though the energetic penalty in subunit D could be less since one of its three hydrogen bonds was retained. The energetic contribution of the K97 sidechain is not known. Based on just the R99 and T100 interactions, the loss of inhibitor binding energy experienced by subunit D is likely at least 4 kcal/mol. The fact that subunit D had an open rather than closed conformation implies that the energetic penalty for an all-closed conformation is very large, at least 4 kcal/mol. This is also consistent with the observation that the $DAHPS_G \cdot$DAHP $oxime_2$ crystal exhibited half-of-sites inhibitor binding even though the DAHP oxime concentration in the crystallization medium, 2.5 mM, was over 1000-fold greater than K_i, 1.5 μM.[100] Overall, the differences in subunit conformation, along with the implied differences in interaction energies raises the question of whether DAHP hydrazone's K_i value is identical for all active sites. As proposed for DAHP oxime, cooperative effects between the subunits in this oligomeric enzyme that control ligand binding are likely. Regardless, the inhibition profile fitted well to a single K_i value (Figure 4.3A), meaning that if the K_i values are different for

different subunits, the differences are too small to be observed experimentally, meaning less than a factor of 100.

4.5. Conclusion

DAHP hydrazone leads to full inhibition of DAHPS because binding is observed in all subunits. Nonetheless, binding in the individual subunits is not equivalent. The inhibitor molecule in subunit D captures fewer active site interactions and the protein remains in an open conformation. Cooperative effects between the DAHPS' subunits, as previously proposed, can therefore not be excluded. The increased potency of DAHP hydrazone vs. DAHP oxime might originate from the coordination of an additional active site water molecule to the hydrazone functional group, as well as DAHP hydrazone's ability to coordinate in all four active sites.

Chapter 5. Concluding Remarks

5.1. Conclusions

Overall, this project deepened the understanding of DAHPS's function and inhibition, as well as confirmed its suitability as an antimicrobial target.

Characterizing DAHPS's inhibition by DAHP oxime as a function of pH revealed that the inhibitor's mode of binding changed from metal competitive to noncompetitive at high pH. The competitiveness of inhibition with respect to the metal ion was surprising because the inhibitor and metal ion did not occupy the same space in the enzyme active site. It was a potential problem because the high intracellular concentrations of metal ions in bacterial cells could render DAHP oxime ineffective *in vivo*. Ionization of metal coordinating residues was suspected to be the underlying cause. A kinetic model was developed that was able to model the shift from metal-competitive to metal-noncompetitive inhibition and accurately fit the K_i versus pH data. Mutant enzymes and inhibitor fragments helped to identify inhibitor-enzyme interactions that triggered the competitiveness of inhibition. In detail, competitive inhibition with respect to the metal ion depended on interactions involving O4 hydroxyl group of DAHP oxime and the sidechains for residues Asp326 and Cys61. The shift to noncompetitive inhibition at high pH was attributed to the deprotonation of Cys61. Recommendations for future inhibitor design were outlined, specifically removing the O4 hydroxyl group from inhibitors.

The lack of effect of DAHP oxime on bacterial growth in cell culture was addressed with a fragment-based experiment. The inhibitor structure was reduced to those functional groups that formed the key interactions with the enzyme. This re-sizing simultaneously reduced the inhibitor's charge, while an addition of fluorine in Cα position to the oxime functional group increased potency. DAHPS-specific inhibition of bacterial growth was now observed, which was confirmed by an overexpression of the target enzyme, since the inhibitor's effect was diminished in DAHPS overexpressing cells.

DAHP oxime inhibits DAHPS with a residual activity of 15%. This incomplete inhibition of enzyme function poses the risk for bacterial survival. Previously, two DAHP-based inhibitors in our lab showed no residual activity. In this project, the co-crystallization of DAHPS·DAHP hydrazone$_4$ was successful. Inhibition was complete as DAHP hydrazone was localized in all four subunits. Regardless, asymmetry in the DAHPS structure left open the question of cooperativity of inhibitor binding, and by implication, in catalysis as well.

Overall, this project successfully implemented and outlined ideas for improved DAHPS inhibitors. Critical properties such as metal competition of inhibition, as well as low effectiveness *in vivo* and the residual activity were analyzed in depth and their origin was examined. Concepts were presented for the future design of improved DAHPS inhibitors.

5.2. Future work

The origin of DAHP oxime's metal competition has been investigated, and a structure for an improved inhibitor has been suggested. Nonetheless, the synthesis of a DAHP oxime derivative lacking the O4 group remains a major challenge. An enzymatic synthetic pathway using DAHPS is impossible, as the O4 group originates from E4P's aldehyde, which is essential for the catalytic mechanism. Extensive expertise in synthetic chemistry would be crucial to either build up a 4-deoxy-DAHP backbone in a stereocontrolled manner, or to selectively remove the O4 group after DAHP has been enzymatically formed.

Besides metal competition, the low cell permeability of DAHP oxime due to high charge has been of previous concern. Charge-free fragments showed inhibition in culture. Extending these fragments by growing and or linking them with a second ligand will help to receive inhibitors with additional potency (Chapter 3.4.3).

The crystal structure of DAHPS·DAHP hydrazone$_4$ revealed that DAHP hydrazone can bind in all four subunits of DAHPS and leads to full inhibition of the enzyme. Nonetheless, the structural differences between the subunits leave the question of cooperativity in DAHPS. An investigation of the inhibitor's effect on protein dynamics would be of interest. Spatially-resolved HDX experiments with PEP showed that substrate binding caused changes in protein dynamics that were concentrated at the tight dimer interface, remote from the active site. This suggests that the inter-domain communication observed kinetically and

structurally in inhibitor binding as a basis in protein dynamic changes. An investigation of the effects on protein dynamics of binding by DAHP hydrazone and DAHP *O*-(2-fluoroethyl) oxime, in comparison with DAHP oxime, might help to elucidate the difference in binding between these DAHP derivatives.

DAHP *O*-(2-fluoroethyl) oxime showed complete inhibition of DAHPS. The synthesis of DAHP *O*-(2,2,2-trifluoroethyl) oxime could be of interest. The reactant 2,2,2-trifluoroethoxyamine hydrochloride is now commercially available (Sigma Aldrich). The preparation of DAHP *O*-(2,2,2-trifluoroethyl) oxime should therefore be straightforward. Similarly, based on the location of the trifluoromethyl groups of the TFP oxime and TFP semicarbazone molecules in the crystal structures, DAHP *O*-(1,1,1-trifluoromethyl) oxime could also be of interest. The inhibitory properties, as well as the structural aspects of binding could then be characterized by fast and slow binding experiments as well as by protein X-ray crystallography.

Our crystallization conditions have been proven to be highly reproducible. The co-crystallization of four different inhibitors as well as substrates and the metal ion was tolerated and successful under these conditions. To date, no DAHPS crystal structure has been obtained that contained the substrate E4P. All knowledge of E4P's position in the active site is based on E4P analogues or DAHP inhibitors. Therefore, the co-crystallization of Mn^{2+}, 2-phosphoglycolic acid with E4P is suggested under the above specified conditions. Based on the pdb structures 1GG1[103] and 1N8F[109], phosphoglycolic acid binding should be

essentially the same as PEP, but with the lack of C3 preventing enzymatic turnover.

The co-crystallization of DAHP hydrazone and DAHPS revealed that similar to DAHP oxime, conserved crystallographic waters assist the coordination of the inhibitor in the active site and help the phosphate mimicking property. To take advantage of this additional space in the active site and to potentially benefit from capturing additional binding energy, a covalently bound functional group as an extension of the hydrazone could increase potency. Formic hydrazide can be purchased from Sigma Aldrich, and the reaction of acetone with formic hydrazide has been previously described in literature, resulting in formylhydrazone.[201] Similar reaction conditions could be successful to form DAHP formylhydrazone.

References

(1) Fleming, A. (1926) On the antibacterial action of cultures of a penicillium, with special reference to their use in the isolation of B. influenzae. *Br J Exp Pathol. 10*, 226–236.

(2) Abraham, E. P., Chain, E., Fletcher, C. M., Gardner, A. D., Heatley, N. G., Jennings, M. A., and Florey, H. W. (1941) Further observations on penicillin. *Lancet 238*, 177–189.

(3) Gerhard Domagk. (1935) Ein Beitrag zur Chemotherapie der bakteriellen Infektionen. *Dtsch. Medizinische Wochenschrift 61*, 250–253.

(4) Saga, T., and Yamaguchi, K. (2009) History of antimicrobial agents and resistant bacteria. *Japan Med. Assoc. J. 52*, 103–108.

(5) Best, W. R. (1963) Drug-Associated Blood Dyscrasias. *Japan Med. Assoc. J. 185*, 286–290.

(6) Mohr, K. I. (2016) History of Antibiotics Research, in *How to Overcome the Antibiotic Crisis : Facts, Challenges, Technologies and Future Perspectives* (Stadler, M., and Dersch, P., Eds.), pp 237–272. Springer International Publishing, Cham.

(7) Ehrlich, J., Bartz, Q. R., Smith, R. M., Joslyn, D. A., and Burkholder, P. R. (1947) Chloromycetin, a New Antibiotic From a Soil Actinomycete. *Science (80-.). 106*, 417.

(8) Waksman, S. A., and Woodruff, H. B. (1942) Streptothricin, a New Selective Bacteriostatic and Bactericidal Agent, Particularly Active Against Gram-Negative Bacteria. *Proc. Soc. Exp. Biol. Med. 49*, 207–210.

(9) Westerman, E. L. (1984) Antibiotic prophylaxis in surgery: Historical background, rationa1e, and relationship to prospective payment. *Am. J. Infect. Control 12*, 339–343.

(10) Barber, M., and Rozwadowska-Dowzenko, M. (1948) Infection by penicillin-resistant staphylococci. *Lancet 252*, 641–644.

(11) Watanabe, T. (1963) Infective heredity of multiple drug resistance in bacteria. *Bacteriol. Rev. 27*, 87.

(12) Rice, L. B. (2008) Federal Funding for the Study of Antimicrobial

Resistance in Nosocomial Pathogens: No ESKAPE. *J. Infect. Dis. 197*, 1079–1081.

(13) Levy, S. B., and Marshall, B. (2004) Antibacterial resistance worldwide: causes, challenges and responses. *Nat. Med. 10*, 122–129.

(14) Kolář, M., Urbánek, K., and Látal, T. (2001) Antibiotic selective pressure and development of bacterial resistance. *Int. J. Antimicrob. Agents 17*, 357–363.

(15) Aminov, R. I., and Mackie, R. I. (2007) Evolution and ecology of antibiotic resistance genes. *FEMS Microbiol. Lett. 271*, 147–161.

(16) Goossens, H., Ferech, M., Vander Stichele, R., and Elseviers, M. (2005) Outpatient antibiotic use in Europe and association with resistance: A cross-national database study. *Lancet 365*, 579–587.

(17) WHO. (2011) Step-by-step approach for development and implementation of hospital antibiotic policy and standard treatment guidelines. World Health Organization, Regional Office for South-East Asia.

(18) Landers, T. F., Cohen, B., Wittum, T. E., and Larson, E. L. (2012) A review of antibiotic use in food animals: perspective, policy, and potential. *Public Health Rep. 127*, 4–22.

(19) Garau, J., Nicolau, D. P., Wullt, B., and Bassetti, M. (2014) Antibiotic stewardship challenges in the management of community-acquired infections for prevention of escalating antibiotic resistance. *J. Glob. Antimicrob. Resist. 2*, 245–253.

(20) Aminov, R. I. (2010) A brief history of the antibiotic era: Lessons learned and challenges for the future. *Front. Microbiol. 1*, 1–7.

(21) Lewis, K. (2013) Platforms for antibiotic discovery. *Nat. Rev. Drug Discov. 12*, 371–387.

(22) Boucher, H. W., Talbot, G. H., Bradley, J. S., Edwards, J. E., Gilbert, D., Rice, L. B., Scheld, M., Spellberg, B., and Bartlett, J. (2009) Bad Bugs, No Drugs: No ESKAPE! An Update from the Infectious Diseases Society of America. *Clin. Infect. Dis. 48*, 1–12.

(23) Ventola, C. L. (2015) The antibiotic resistance crisis: part 1: causes and threats. *P T A peer-reviewed J. Formul. Manag. 40*, 277–83.

(24) Projan, S. J. (2003) Why is big Pharma getting out of antibacterial drug discovery? *Curr. Opin. Microbiol. 6*, 427–430.

(25) Tommasi, R., Brown, D. G., Walkup, G. K., Manchester, J. I., and Miller, A. A. (2015) ESKAPEing the labyrinth of antibacterial discovery. *Nat. Rev. Drug Discov. 14*, 662–662.

(26) Coggins, J. R., Abell, C., Evans, L. B., Frederickson, M., Robinson, D. a, Roszak, a W., and Lapthorn, a P. (2003) Experiences with the shikimate-pathway enzymes as targets for rational drug design. *Biochem. Soc. Trans. 31*, 548–552.

(27) Herrmann, K. M. (1995) The shikimate pathway as an entry to aromatic secondary metabolism. *Plant Physiol. 107*, 7–12.

(28) Floss, H. G. (1979) The Shikimate Pathway, in *Biochemistry of Plant Phenolics* (Swain, T., Harbone, J. B., and Van Sumere, C. F., Eds.), pp 59–89. Springer US, Boston, MA.

(29) Bentley, R. (1990) Metabolic Tree with Many Branches. *Methods 25*, 307–383.

(30) Knaggs, A. R. (1999) The biosynthesis of shikimate metabolites. *Nat. Prod. Rep. 16*, 525–560.

(31) Herrmann, K. M. (1995) The Shikimate Pathway: Early Steps in the Biosynthesis of Aromatic Compounds. *Plant Cell Online 7*, 907–919.

(32) Light, S. H., and Anderson, W. F. (2013) The diversity of allosteric controls at the gateway to aromatic amino acid biosynthesis. *Protein Sci. 22*, 395–404.

(33) Gibson, F., and Pittard, J. (1968) Pathways of biosynthesis of aromatic amino acids and vitamins and their control in microorganisms. *Bacteriol. Rev. 32*, 465–92.

(34) McArthur, J. D., West, N. P., Cole, J. N., Jungnitz, H., Guzmán, C. A., Chin, J., Lehrbach, P. R., Djordjevic, S. P., and Walker, M. J. (2003) An aromatic amino acid auxotrophic mutant of Bordetella bronchiseptica is attenuated and immunogenic in a mouse model of infection. *FEMS Microbiol. Lett. 221*, 7–16.

(35) Parish, T., and Stoker, N. G. (2002) The common aromatic amino acid biosynthesis pathway is essential in Mycobacterium tuberculosis.

Microbiology 148, 3069–77.

(36) Priebe, G. P., Meluleni, G. J., Coleman, F. T., Goldberg, J. B., and Pier, G. B. (2003) Protection against fatal Pseudomonas aeruginosa pneumonia in mice after nasal immunization with a live, attenuated aroA deletion mutant. *Infect. Immun. 71*, 1453–1461.

(37) Mutunga, M., Graham, S., De Hormaeche, R. D., Musson, J. A., Robinson, J. H., Mastroeni, P., Khan, C. M. A., and Hormaeche, C. E. (2004) Attenuated Salmonella typhimurium htrA mutants cause fatal infections in mice deficient in NADPH oxidase and destroy NADPH oxidase-deficient macrophage monolayers. *Vaccine 22*, 4124—4131.

(38) Stritzker, J., Janda, J., Schoen, C., Pilgrim, S., Gentschev, I., Schreier, P., Geginat, G., Goebel, W., Stritzker, J., Janda, J., Schoen, C., Taupp, M., Pilgrim, S., Gentschev, I., Schreier, P., Geginat, G., and Goebel, W. (2004) Growth , Virulence , and Immunogenicity of Listeria monocytogenes aro Mutants Growth , Virulence , and Immunogenicity of Listeria monocytogenes aro Mutants *72*, 5622–5629.

(39) Kärnell, A., Cam, P. D., Verma, N., and Lindberg, A. A. (1993) AroD deletion attenuates Shigella flexneri strain 2457T and makes it a safe and efficacious oral vaccine in monkeys. *Vaccine 11*, 830–836.

(40) Li, A., Pál, T., Forsum, U., and Lindberg, A. A. (1993) Safety and immunogenicity of the live oral auxotrophic Shigella flexneri SFL124 in adult Vietnamese volunteers. *Vaccine 11*, 180–189.

(41) Baird, D. D., Upchurch, R. P., Homesley, W. B., Franz, J. E., and editors. (1971) Introduction of a new broad spectrum post emergence herbicide of a new broad spectrum post emergence herbicide class with utility for herbaceous perennial weed control., in *26th North Central Weed Control Conf.*, pp 64–68.

(42) Amrhein, N., Deus, B., Gehrke, P., and Steinrucken, H. C. (1980) The site of the inhibition of the shikimate pathway by Glyphosate - Interference of glyphosate with chorismate formation in vivo and in vitro. *Plant Physiol 66*, 830–834.

(43) Steinrücken, H. C., and Amrhein, N. (1980) The herbizide glyphosate is a potent inhibitor of 5-enolpyruvyl-shikimic acid-3-phosphate synthase. *Biochem. Biophys. Res. Commun. 94*, 1207–1212.

(44) Schönbrunn, E., Eschenburg, S., Shuttleworth, W. A., Schloss, J. V, Amrhein, N., Evans, J. N., and Kabsch, W. (2001) Interaction of the herbicide

glyphosate with its target enzyme 5-enolpyruvylshikimate 3-phosphate synthase in atomic detail. *Proc. Natl. Acad. Sci. U. S. A. 98*, 1376–80.

(45) Gordon, S., Simithy, J., Goodwin, D. C., and Calderón, A. I. (2015) Selective mycobacterium tuberculosis shikimate kinase inhibitors as potential antibacterials. *Perspect. Medicin. Chem. 7*, 9–20.

(46) Cheung, V. W. N., Xue, B., Hernandez-Valladares, M., Go, M. K., Tung, A., Aguda, A. H., Robinson, R. C., and Yew, W. S. (2014) Identification of polyketide inhibitors targeting 3-dehydroquinate dehydratase in the shikimate pathway of Enterococcus faecalis. *PLoS One 9*, 1–9.

(47) Kapnick, S. M., and Zhang, Y. (2008) New tuberculosis drug development: targeting the shikimate pathway. *Expert Opin. Drug Discov. 3*, 565–77.

(48) Srinivasan, P. R., and Sprinson, D. B. (1959) 2-Keto-3-deoxy-d-arabo -heptonic Acid 7-Phosphate Synthetase. *J. Biol. Chem. 234*, 716–722.

(49) Light, S. H., Halavaty, A. S., Minasov, G., Shuvalova, L., and Anderson, W. F. (2012) Structural analysis of a 3-deoxy-D-arabino-heptulosonate 7-phosphate synthase with an N-terminal chorismate mutase-like regulatory domain. *Protein Sci. 21*, 887–895.

(50) Wu, J., and Woodard, R. W. (2006) New insights into the evolutionary links relating to the 3-deoxy-D-arabino-heptulosonate 7-phosphate synthase subfamilies. *J. Biol. Chem. 281*, 4042–4048.

(51) Nimmo, H. G., and Coggins, J. R. (1996) Evidence for a novel class of microbial 3-deoxy- heptulosonate-7-phosphate synthase rimosus and Neurospora crassa. *Pharmacia 142*, 1973–1982.

(52) Gosset, G., Bonner, C. A., and Jensen, R. A. (2001) Microbial Origin of Plant-Type 2-Keto-3-Deoxy-D-arabino-Heptulosate 7-Phosphate Synthases, Exemplified by the Chorismate- and Tryptophan-Reguated Enzyme from Xathomonas campestris. *J. Bacteriol. 183*, 4061–4070.

(53) Subramaniam, P. S., Xie, G., Xia, T., and Jensen, R. A. (1998) Substrate Ambiguity of 3-Deoxy-D-manno-Octulosonate 8-Phosphate Synthase from Neisseria gonorrhoeae in the Context of Its Membership in a Protein Family Containing a Subset of 3-Deoxy-D-arabino -Heptulosonate 7-Phosphate Synthases. *Microbiology 180*, 119–127.

(54) Ahmad, S., and Jensen, R. A. (1989) The stable phylogenetic

distribution of the recently evolved 1-phenylalanine-inhibited isozyme of 3-deoxy-d-arabino-heptulosonate 7-phosphate synthase in enteric bacteria. *Curr. Microbiol. 18*, 341–349.

(55) Brown, K. D., and Doy, C. H. (1963) End-product regulation of the general aromatic pathway in Escherichia coli W. *Biochem. Biophys. Res. Commun. 77*, 170–172.

(56) Wallace, B. J., and Pittard, J. (1967) Genetic and biochemical analysis of the isoenzymes concerned in the first reaction of aromatic biosynthesis in Escherichia coli. *J. Bacteriol. 93*, 237–244.

(57) Pittard, J., and Yang, J. (2008) Biosynthesis of the aromatic amino acids. *EcoSal Plus 3*, 1–75.

(58) Shumilin, I. A., Kretsinger, R. H., and Bauerle, R. H. (1999) Crystal structure of phenylalanine-regulated 3-deoxy-D-arabino-heptulosonate-7-phosphate synthase from Escherichia coli. *Structure 7*, 865–875.

(59) Bravo, I. G., García-Vallvé, S., Romeu, A., and Reglero, Á. (2004) Prokaryotic origin of cytidylyltransferases and α-ketoacid synthases. *Trends Microbiol. 12*, 120–128.

(60) Comb, D. G., and Roseman, S. (1960) The Sialic Acids. Structure and enzymatic synthesis of N-Acetylneuraminic acid. *J. Biol. Chem. 235*, 2529–2537.

(61) LEVIN, D. H., and RACKER, E. (1959) Condensation of arabinose 5-phosphate and phosphorylenol pyruvate by 2-keto-3-deoxy-8-phosphooctonic acid synthetase. *J. Biol. Chem. 234*, 2532–2539.

(62) Gunawan, J., Simard, D., Gilbert, M., Lovering, A. L., Wakarchuk, W. W., Tanner, M. E., and Strynadka, N. C. J. (2005) Structural and mechanistic analysis of sialic acid synthase NeuB from Neisseria meningitidis in complex with Mn2+, phosphoenolpyruvate, and N-acetylmannosaminitol. *J. Biol. Chem. 280*, 3555–3563.

(63) DeLeo, A. B., and Sprinson, D. B. (1968) Mechanism of 3-Deoxy-D-arabino-heptulosonate 7-phosphate (DAHP) synthetase. *Biochem. Biophys. Res. Commun. 32*, 873–877.

(64) Hedstrom, L., and Abeles, R. (1988) 3-Deoxy-D-manno-octulosonate-8-phosphate synthase catalyzes the C-O bond cleavage of phosphoenolpyruvate. *Biochem. Biophys. Res. Commun. 157*, 816–820.

(65) Radaev, S., Dastidar, P., Patel, M., Woodard, R. W., and Gatti, D. L. (2000) Structure and Mechanism of 3-Deoxy-D-manno-octulosonate 8-Phosphate Synthase*. *J. Biol. Chem. 275*, 9476–9484.

(66) Hartmann, M., Schneider, T. R., Pfeil, A., Heinrich, G., Lipscomb, W. N., and Braus, G. H. (2003) Evolution of feedback-inhibited beta /alpha barrel isoenzymes by gene duplication and a single mutation. *Proc. Natl. Acad. Sci. U. S. A. 100*, 862–7.

(67) Duewel, H. S., and Woodard, R. W. (2000) A metal bridge between two enzyme families: 3-deoxy-D-manno-octulosonate-8-phosphate synthase from Aquifex aeolicus requires a divalent metal for activity. *J. Biol. Chem. 275*, 22824–22831.

(68) Hao, J., Balagurumoorthy, P., Sarilla, S., and Sundaramoorthy, M. (2005) Cloning, expression, and characterization of sialic acid synthases. *Biochem. Biophys. Res. Commun. 338*, 1507–1514.

(69) Shulami, S., Furdui, C., Adir, N., Shoham, Y., Anderson, K. S., and Baasov, T. (2004) A reciprocal single mutation affects the metal requirement of 3-deoxy-D-manno-2-octulosonate-8-phosphate (KDO8P) synthases from aquifex pyrophilus and Escherichia coli. *J. Biol. Chem. 279*, 45110–45120.

(70) König, V., Pfeil, A., Braus, G. H., and Schneider, T. R. (2004) Substrate and metal complexes of 3-deoxy-D-arabino-heptulosonate-7-phosphate synthase from Saccharomyces cerevisiae provide new insights into the catalytic mechanism. *J. Mol. Biol. 337*, 675–690.

(71) Ghalambor, M. A., and Heath, E. C. (1965) The Biosynthesis of Cell Wall Lipopolysaccharide in Escherichia Coli. (IV) Purification and Properties of Cytidine monophosphate 3-Deoxy-D-Manno-octulosonate synthase. *J. Biol. Chem. 241*, 32216–3221.

(72) Varki, A., and Gagneux, P. (2012) Multifarious roles of sialic acids in immunity. *Ann. N. Y. Acad. Sci. 1253*, 16–36.

(73) Vimr, E., and Lichtensteiger, C. (2002) To sialylate, or not to sialylate: That is the question. *Trends Microbiol. 10*, 254–257.

(74) Vimr, E. R., Kalivoda, K. A., Deszo, E. L., and Steenbergen, S. M. (2004) Diversity of microbial sialic acid metabolism. *Microbiol. Mol. Biol. Rev. 68*, 132–53.

(75) Roseman, S., Jourdian, G. W., Watson, D., and Rood, R. (1961)

Enzymatic synthesis of sialic acid 9-phosphates. *Proc. Natl. Acad. Sci. U. S. A. 47*, 958–961.

(76) Liu, F., Lee, H. J., Strynadka, N. C. J., and Tanner, M. E. (2009) Inhibition of Neisseria meningitidis sialic acid synthase by a tetrahedral intermediate analogue. *Biochemistry 48*, 9194–9201.

(77) Baardsnes, J., and Davies, P. L. (2001) Sialic acid synthase: The origin of fish type III antifreeze protein? *Trends Biochem. Sci. 26*, 468–469.

(78) Ghalambor, M. A., and Heath, E. C. (1966) the Biosynthesis of Cell Wall Lipopolysaccharide in Escherichia Coli. III. The Isolation and Characterization of 3-Deoxyoctulosonic acid. *J. Biol. Chem. 241*, 3207–3215.

(79) Raetz, C. R. H. (1990) Biochemistry of Endotoxins. *Annu. Rev. Bioehem 59*, 129–70.

(80) Dröge, W., Lehmann, V., Lüderitz, O., and Westphal, O. (1970) Structural Investigations on the 2-Keto-Deoxyoctonate Region of Lipopolysaccharides. *Eur. J. Biochem. 14*, 175–184.

(81) Osborn, M. J. (1963) Studies on the Gram-Negative Cell Wall, I. Evidence for the Role of 2-Keto-3-Deoxyoctonate in the Lipopolysaccharide of Salmonella Typhimurium. *Proc. Natl. Acad. Sci. U. S. A. 50*, 499.

(82) Rick, P. D., and Young, D. A. (1982) Isolation and Characterization of a Temperature-Sensitive Lethal Mutant of Samonella typhimurium That Is Conditionally Defective in 3-Deoxy-D-Manno-Octulosonate-8-Phosphate Synthesis. *J. Bacteriol. 150*, 447–455.

(83) Rick, P. D., and Osborn, M. J. (1977) Lipid A Mutants of Salmonella typhimurium. *J. Biol. Chem. 252*, 4895–4903.

(84) Wang, C., Bendle, J., Yang, Y., Yang, H., Sun, H., Huang, J., and Xie, S. (2016) Impacts of pH and temperature on soil bacterial 3-hydroxy fatty acids: Development of novel terrestrial proxies. *Org. Geochem. 94*, 21–31.

(85) Ahn, M., Pietersma, A. L., Schofield, L. R., and Parker, E. J. (2005) Mechanistic divergence of two closely related aldol-like enzyme-catalysed reactions. *Org. Biomol. Chem. 3*, 4046–9.

(86) Ray, P. H. (1980) Purification and Characterization of 3-Deoxy-D-manno- Octulosonate 8-Phosphate Synthetase from Escherichia coli. *J. Bacteriol. 141*, 635–644.

(87) Birck, M. R., and Woodard, R. W. (2001) Aquifex aeolicus 3-deoxy-D-manno-2-octulosonic acid 8-phosphate synthase: a new class of KDO 8-P synthase? *J. Mol. Evol. 52*, 205–214.

(88) Cochrane, F. C., Cookson, T. V. M., Jameson, G. B., and Parker, E. J. (2009) Reversing Evolution: Re-establishing Obligate Metal Ion Dependence in a Metal-independent KDO8P Synthase. *J. Mol. Biol. 390*, 646–661.

(89) Oliynyk, Z., Briseño-Roa, L., Janowitz, T., Sondergeld, P., and Fersht, A. R. (2004) Designing a metal-binding site in the scaffold of Escherichia coli KDO8PS. *Protein Eng. Des. Sel. 17*, 383–390.

(90) Li, J., Wu, J., Fleischhacker, A. S., and Woodard, R. W. (2004) Conversion of Aquifex aeolicus 3-deoxy-D-manno-octulosonate 8-phosphate synthase, a metalloenzyme, into a nonmetalloenzyme. *J. Am. Chem. Soc. 126*, 7448–7449.

(91) Shumilin, I. a, Bauerle, R., Wu, J., Woodard, R. W., and Kretsinger, R. H. (2004) Crystal structure of the reaction complex of 3-deoxy-D-arabino-heptulosonate-7-phosphate synthase from Thermotoga maritima refines the catalytic mechanism and indicates a new mechanism of allosteric regulation. *J. Mol. Biol. 341*, 455–66.

(92) Howe, D. L., Sundaram, A. K., Wu, J., Gatti, D. L., and Woodard, R. W. (2003) Mechanistic insight into 3-deoxy-D-manno-octulosonate-8-phosphate synthase and 3-deoxy-D-arabino-heptulosonate-7-phosphate synthase utilizing phosphorylated monosaccharide analogues. *Biochemistry 42*, 4843–4854.

(93) Li, Z., Sau, A. K., Shen, S., Whitehouse, C., Baasov, T., and Anderson, K. S. (2003) A snapshot of enzyme catalysis using electrospray ionization mass spectrometry. *J. Am. Chem. Soc. 125*, 9938–9939.

(94) Onderka, D. K., and Floss, H. G. (1969) Steric Course of the Chorismate Synthetase Reaction and the 3-Deoxy-D-arabino-heptulosonate 7-Phosphate (DAHP) Synthetase Reaction. *J. Am. Chem. Soc. 91*, 5894–5896.

(95) Kohen, A., Berkovich, R., Belakhov, V., and Baasov, T. (1993) Stereochemistry of the KDO8P synthase. An efficient synthesis of the 3-fluoro analogues of KDO8P. *Bioorganic Med. Chem. Lett. 3*, 1577–1582.

(96) Asojo, O., Friedman, J., Adir, N., Belakhov, V., Shoham, Y., and Baasov, T. (2001) Crystal structures of KDOP synthase in its binary complexes with the substrate phosphoenolpyruvate and with a mechanism-based inhibitor. *Biochemistry 40*, 6326–6334.

(97) Kohen, A., Jakob, A., and Baasov, T. (1992) Mechanistic studies of 3-deoxy-D-manno-2-octulosonate-8-phosphate synthase from Escherichia coli. *Eur. J. Biochem. 208*, 443–449.

(98) Schoner, R., and Herrmann, K. M. (1976) 3-Deoxy-D-arabino-heptulosonate 7-Phosphate Synthase. Purification, Properties, and Kinetics of the Tyrosine-Sensitive Isoenzyme from Escherichia coli. *J. Biol. Chem. 251*, 5440–5447.

(99) Nimmo, G. A., and Coggins, J. R. (1981) Some kinetic properties of the tryptophan-sensitive 3-deoxy-D-arabino-heptulosonate 7-phosphate synthase from Neurospora crassa. *Biochem. J. 199*, 657–665.

(100) Balachandran, N., Heimhalt, M., Liuni, P., To, F., Wilson, D. J., Junop, M. S., and Berti, P. J. (2016) Potent Inhibition of 3-Deoxy- D - arabino heptulosonate-7-phosphate (DAHP) Synthase by DAHP Oxime , a Phosphate Group Mimic. *Biochemistry 48*, 6617–6629.

(101) Gama, S. (2017) Characterization of the Metal-Dependent KDO8P Synthase from Campylobacter Jejuni and Inhibition by KDO8P Oxime, A Novel Slow-Binding Inhibitor.

(102) Furdui, C., Zhou, L., Woodard, R. W., and Anderson, K. S. (2004) Insights into the mechanism of 3-deoxy-D-arabino-heptulosonate 7-phosphate synthase (Phe) from Escherichia coli using a transient kinetic analysis. *J. Biol. Chem. 279*, 45618–45625.

(103) Wagner, T., Shumilin, I. A., Bauerle, R., and Kretsinger, R. H. (2000) Structure of 3-deoxy-d-arabino-heptulosonate-7-phosphate synthase from Escherichia coli: comparison of the Mn(2+)*2-phosphoglycolate and the Pb(2+)*2-phosphoenolpyruvate complexes and implications for catalysis. *J. Mol. Biol. 301*, 389–99.

(104) Clark, M. E., and Berti, P. J. (2007) Enolpyruvyl activation by enolpyruvylshikimate-3-phosphate synthase. *Biochemistry 46*, 1933–1940.

(105) Loncke, P. G., and Berti, P. J. (2006) Implications of protonation and substituent effects for C-O and O-P bond cleavage in phosphate monoesters. *J. Am. Chem. Soc. 128*, 6132–6140.

(106) Balachandran, N., To, F., and Berti, P. J. (2017) Linear Free Energy Relationship Analysis of Transition State Mimicry by 3-Deoxy- D - arabino heptulosonate-7-phosphate (DAHP) Oxime , a DAHP Synthase Inhibitor and Phosphate Mimic. *Biochemistry 56*, 592–601.

(107) McCandliss, R., Poling, M., and Herrmann, K. (1978) 3-Deoxy-D-arabino-heptulosonate 7-phosphate synthase. Purification and molecular characterization of the phenylalanine-sensitive isoenzyme from Escherichia coli. *J. Biol. Chem. 253*, 4259–4265.

(108) Shumilin, I. A., Zhao, C., Bauerle, R., and Kretsinger, R. H. (2002) Allosteric inhibition of 3-deoxy-D-arabino-heptulosonate-7-phosphate synthase alters the coordination of both substrates. *J. Mol. Biol. 320*, 1147–1156.

(109) Shumilin, I. A., Bauerle, R., and Kretsinger, R. H. (2003) The high-resolution structure of 3-Deoxy-D-arabino-heptulosonate-7-phosphate synthase reveals a twist in the plane of bound phosphoenolpyruvate. *Biochemistry 42*, 3766–3776.

(110) Ray, J. M., and Bauerle, R. (1991) Purification and Properties of Tryptophan-Sensitive 3-Deoxy-D- arabino-Heptulosonate-7-Phosphate Synthase from Escherichia coli. *J. Bacteriol. 173*, 1894–1901.

(111) Lindqvist, Y. (1985) Structure of glycolate oxidase from spinach *82*, 6855–6859.

(112) Ochoa-Leyva, A., Soberón, X., Sánchez, F., Argüello, M., Montero-Morán, G., and Saab-Rincón, G. (2009) Protein Design through Systematic Catalytic Loop Exchange in the (β/α)8 Fold. *J. Mol. Biol. 387*, 949–964.

(113) Rob, T., Liuni, P., Gill, P. K., Zhu, S., Balachandran, N., Berti, P. J., and Wilson, D. J. (2012) Measuring dynamics in weakly structured regions of proteins using microfluidics-enabled subsecond H/D exchange mass spectrometry. *Anal. Chem. 84*, 3771–3779.

(114) Stephens, C. M., and Bauerle, R. (1991) Analysis of the Metal Requirement of 3-Deoxy-D-arabino-heptulosonate-7-phosphate synthase from Escherichia coli. *J. Biol. Chem. 266*, 20810–20817.

(115) McCandliss, R. J., and Herrmann, K. M. (1978) Iron, an essential element for biosynthesis of aromatic compounds. *Proc. Natl. Acad. Sci. U. S. A. 75*, 4810–3.

(116) Staub, M., and Dénes, G. (1968) Purification and properties of the 3-Deoxy-D-Arabino-Heptulosonate-7-Phosphate Synthase (Phenylalanine sensitive) of Escherichia coli K12. *Biochim. Biophys. Acta 178*, 588–598.

(117) Ganson, R. J., and Jensen, R. A. (1988) The Essential Role of Cobalt in the Inhibition of the Cytosolic lsozyme of 3-Deoxy-D-arabino-heptulosonate-7-

phosphate Synthase from Nicotiana silvestris by Glyphosate. *Arch. Biochem. Biophys. 260*, 85–93.

(118) Baasov, T., and Knowles, J. R. (1989) Is the First Enzyme of the Shikimate Pathway , 3-Deoxy-D-arabino-Heptulosonate-7-Phosphate Synthase (Tyrosine Sensitive), a Copper Metalloenzyme ? *J. Bacteriol. 171*, 6155–6160.

(119) Stephens, C. M., and Bauerle, R. (1992) Essential Cysteines in 3-Deoxy-D-arabino-heptulosonate-7-phosphate Synthase from Escherichia coli. *J. Biol. Chem. 267*, 5762–5767.

(120) Sundaram, A. K., Howe, D. L., Sheflyan, G. Y., and Woodardj, R. W. (1998) Probing the potential metal binding site in Escherichia coli 3-deoxy- -arabino-heptulosonate 7-phosphate synthase (phenylalanine-sensitive). *FEBS Lett. 441*, 195–199.

(121) Pearson, R. G. (1968) Hard and Soft Acids and Bases. *J. Chem. Educ. 45*, 581–587.

(122) Jordan, P. A., Bohle, D. S., Ramilo, C. A., and Evans, J. N. S. (2001) New insights into the metal center of 3-deoxy-D-arabino-heptulosonate 7-phosphate synthase. *Biochemistry 40*, 8387–8396.

(123) Reichau, S., Jiao, W., Walker, S. R., Hutton, R. D., Baker, E. N., and Parker, E. J. (2011) Potent inhibitors of a shikimate pathway enzyme from Mycobacterium tuberculosis: Combining mechanism- and modeling-based design. *J. Biol. Chem. 286*, 16197–16207.

(124) Walker, S., Cumming, H., and Parker, E. (2009) Substrate and reaction intermediate mimics as inhibitors of 3-deoxy-D-*arabino*-heptulosonate 7-phosphate synthase. *J. Org. Biomol. Chem. 7*, 3031–3035.

(125) Walker, S. R., and Parker, E. J. (2006) Synthesis and evaluation of a mechanism-based inhibitor of a 3-deoxy-d-arabino heptulosonate 7-phosphate synthase. *Bioorganic Med. Chem. Lett. 16*, 2951–2954.

(126) Walker, S. R., Jiao, W., and Parker, E. J. (2011) Synthesis and evaluation of dual site inhibitors of 3-deoxy-d-arabino- heptulosonate 7-phosphate synthase. *Bioorganic Med. Chem. Lett. 21*, 5092–5097.

(127) Grison, C., Petek, S., Finance, C., and Coutrot, P. (2005) Synthesis and antibacterial activity of mechanism-based inhibitors of KDO8P synthase and DAH7P synthase. *Carbohydr. Res. 340*, 529–537.

(128) Du, S., Faiger, H., Belakhov, V., and Baasov, T. (1999) Towards the development of novel antibiotics: Synthesis and evaluation of a mechanism-based inhibitor of Kdo8P synthase. *Bioorganic Med. Chem. 7*, 2671–2682.

(129) García-Alles, L. F., and Erni, B. (2002) Synthesis of phosphoenolpyruvate (PEP) analogues and evaluation as inhibitors of PEP-utilizing enzymes. *Eur. J. Biochem. 269*, 3226–3236.

(130) Nowak, T., and Mildvan, A. S. (1970) Stereoselective interactions of phosphoenolpyruvate analogues with phosphoenolpyruvate-utilizing enzymes. *J. Biol. Chem. 245*, 6057–6064.

(131) Bearne, S. L., and Kluger, R. (1992) Phosphoenol acetylphosphonates: Substrate analogues as inhibitors of phosphoenolpyruvate enzymes. *Bioorg. Chem. 20*, 135–147.

(132) Belakhov, V., Dovgolevsky, E., Rabkin, E., Shulami, S., Shoham, Y., and Baasov, T. (2004) Synthesis and evaluation of a mechanism-based inhibitor of KDO8P synthase. *Carbohydr. Res. 339*, 385–392.

(133) Ray, P. H., Kelsey, J. E., Bigham, E. C., Benedict, C. D., and Miller, T. A. (1983) Synthesis and Use of 3-Deoxy-D-manno-2-octulosonate (KDO) in Escherichia coli Potential Sites of Inhibition, in *ACS Symp. Ser.*, p 231:141-169.

(134) Popovic, V. (2012) Inhibition of the bacterial sialic acid synthase, NeuB. *Master thesis, McMaster Univ.* 62p.

(135) Morrison, E. (2009) NeuNac oxime: a potent inhibitor of the sialic acid synthase, NeuB. *Master thesis, McMaster Univ.* 79p.

(136) Westheimer, F. H. (1987) Why nature chose phosphates. *Science (80-.). 235*, 1173–1178.

(137) Elliott, T. S., Slowey, A., Ye, Y., and Conway, S. J. (2012) The use of phosphate bioisosteres in medicinal chemistry and chemical biology. *Medchemcomm 3*, 735.

(138) Meanwell, N. A. (2011) Synopsis of some recent tactical application of bioisosteres in drug design. *J. Med. Chem. 54*, 2529–2591.

(139) Pauling, L. (1948) Nature of forces between large molecules of biological interest. *Nature 161*, 707–709.

(140) Schramm, V. L. (1998) Enzymatic Transition States and Transition

State Analog Design. *Annu. Rev. Biochem. 67*, 693–720.

(141) Balachandran, N. (2014) DAHP Oxime : A Transition State Mimic Inhibitor Of DAHP Synthase. *Ph.D. Thesis, McMaster Univ.* 200p.

(142) Lanzetta, P. A., Alvarez, L. J., Reinach, P. S., and Candia, O. A. (1979) An improved assay for nanomole amounts of inorganic phosphate. *Anal. Biochem. 100*, 95–97.

(143) Sieben, A. S., Perlin, A. S., and Simpson, F. J. (1966) An improved preparative method for D-Erythrose 4-phosphate. *Can. J. Biochem. 44*, 663–669.

(144) Segel, I. H. (1975) Enzyme Kinetics-Behavior and Analysis of Rapid Equilibrium and Steady-State Enzyme Systems. John Wiley and Sons, New York.

(145) Microcal. (2004) ITC Data Analysis in Origin®: Tutorial Guide. *Northampton, MA.*

(146) Jiang, S. (2011) Characterization of Fosfomycin-Resistant MurA from Borrelia burgdorferi, Fragment-based Inhibitor Design for AroA and DAHP Synthase.

(147) Hofstee, B. J. H. (1959) Non-Inverted Versus Inverted Plots in Enzyme Kinetics. *Nature 184*, 1296–1298.

(148) Nielsen, J. E. (2009) Chapter 9. Analyzing enzymatic pH activity profiles and protein titration curves using structure-based pKa calculations and titration. curve fitting. *Methods Enzymol. 454*, 233–258.

(149) Copeland, R. A. (2005) Evaluation of Enzyme Inhibitors in Drug Discovery: A Guide for Medicinal Chemists and Pharmacologists. John Wiley & Sons, Inc., Hoboken, NJ.

(150) Gloster, T. M., and Davies, G. J. (2010) Glycosidase inhibition: assessing mimicry of the transition state. *Org. Biomol. Chem. 8*, 305–20.

(151) Harris, T. K., and Turner, G. J. (2002) Structural Basis of Perturbed pKa Values of Catalytic Groups in Enzyme Active Sites. *IUBMB Life 53*, 85–98.

(152) Scott, D. E., Coyne, A. G., Hudson, S. A., and Abell, C. (2012) Fragment-Based Approaches in Drug Discovery and Chemical Biology. *Biochemistry 51*, 4990–5003.

(153) Murray, C. W., and Rees, D. C. (2009) The rise of fragment-based drug discovery. *Nat. Chem. 1*, 187–192.

(154) Murray, C. W., Verdonk, M. L., and Rees, D. C. (2012) Experiences in fragment-based drug discovery. *Trends Pharmacol. Sci. 33*, 224–232.

(155) Davies, T. G., and Hyvönen, M. (2012) Fragment-Based Drug Discovery and X-Ray Crystallography. *Top. Curr. Chem. 317*, 2–3.

(156) Davies, T. G., and Tickle, I. J. (2012) Fragment screening using X-ray crystallography. *Top. Curr. Chem. 317*, 33–59.

(157) Joseph-McCarthy, D., Campbell, A. J., Kern, G., and Moustakas, D. (2014) Fragment-Based Lead Discovery and Design. *J. Chem. Inf. Model. 54*, 693–704.

(158) Kalia, J., and Raines, R. T. (2008) Hydrolytic Stability of Hydrazones and Oximes. *Angew Chem Int Ed Engl. 47*, 7523–7526.

(159) Dodd, M. C. (1946) The Chemotherapeutic Properties of 5-Nitro-2-Furaldehyde semicarbazone (Furazin). *J. Pharmacol. Exp. Ther. 8*, 311–323.

(160) Melorose, J., Perroy, R., and Careas, S. (1990) Irreversible Blockade of the high and low affinity (3H)Naloxone binding site by C-6 Derivatives of Morphinane-6-ones. *Life Sci. 48*, 439–451.

(161) O'Callaghan, C. H., Sykes, R. B., Griffiths, A., and Thornton, J. E. (1976) Cefuroxime, a New Cephalosporin Antibiotic : Activity In Vitro. *Antimicrob Agents Chemother 9*, 511–519.

(162) Dawson, R. M. (1994) Review of oximes available for treatment of nerve agent poisoning. *J. Appl. Toxicol. 14*, 317–331.

(163) Otwinowski, Z., and Minor, W. (1997) Processing of X-ray diffraction data collected in oscillation mode. *Methods Enzymol. 276*, 307–326.

(164) Adams, P. D., Grosse-Kunstleve, R. W., Hung, L. W., Ioerger, T. R., McCoy, A. J., Moriarty, N. W., Read, R. J., Sacchettini, J. C., Sauter, N. K., and Terwilliger, T. C. (2002) PHENIX: building new software for automated crystallographic structure determination. *Acta Crystallogr. D. Biol. Crystallogr. 58*, 1948–1954.

(165) Afonine, P. V., Grosse-Kunstleve, R. W., Echols, N., Headd, J. J., Moriarty, N. W., Mustyakimov, M., Terwilliger, T. C., Urzhumtsev, A., Zwart, P.

H., and Adams, P. D. (2012) Towards automated crystallographic structure refinement with phenix.refine. *Acta Crystallogr. Sect. D Biol. Crystallogr. 68*, 352–367.

(166) Emsley, P., Lohkamp, B., Scott, W. G., and Cowtan, K. (2010) Features and development of Coot. *Acta Crystallogr. Sect. D 66*, 486–501.

(167) Frisch, M. J., Trucks, G. W., Schlegel, H. B., Scuseria, G. E., Robb, M. A., Cheeseman, J. R., Montgomery, J., J. A. Vreven, T., Kudin, K. N., Burant, J. C., Millam, J. M., Iyengar, S. S., Tomasi, J., Barone, V., Mennucci, B., Cossi, M., Scalmani, G., Rega, N., Petersson, G. A., Nakatsuji, H., Hada, M., Ehara, M., Toyota, K., Fukuda, R., Hasegawa, J., Ishida, M., Nakajima, T., Honda, Y., Kitao, O., Nakai, H., Klene, M., Li, X., Knox, J. E., Hratchian, H. P., Cross, J. B., Bakken, V., Adamo, C., Jaramillo, J., Gomperts, R., Stratmann, R. E., Yazyev, O., Austin, A. J., Cammi, R., Pomelli, C., Ochterski, J. W., Ayala, P. Y., Morokuma, K., Voth, G. A., Salvador, P., and Dannenberg, J. J. Zakrzewski, V. G., Dapprich, S., Daniels, A. D., Strain, M. C., Farkas, O., Malick, D. K., Rabuck, A. D., Raghavachari, K., Foresman, J. B., Ortiz, J. V., Cui, Q., Baboul, A. G., Clifford, S., Cioslowski, J., Stefanov, B. B., Liu, G., Li, J. A. (2009) Gaussian 09, Gaussian, Inc., Wallingford CT.

(168) Moriarty, N. W., Grosse-Kunstleve, R. W., and Adams, P. D. (2009) Electronic ligand builder and optimization workbench (eLBOW): A tool for ligand coordinate and restraint generation. *Acta Crystallogr. Sect. D Biol. Crystallogr. 65*, 1074–1080.

(169) Hadjivassiliou, A. G., and Rieder, S. V. (1968) The enzymatic assay of pyruvic and lactic acids. A definitive procedure. *Clin. Chim. Acta 19*, 357–361.

(170) Rashidian, M., Mahmoodi, M. M., Shah, R., Dozier, J. K., Wagner, C. R., and Distefano, M. D. (2013) A highly efficient catalyst for oxime ligation and hydrazone-oxime exchange suitable for bioconjugation. *Bioconjug. Chem. 24*, 333–342.

(171) Mahmoodi, M. M., Rashidian, M., Zhang, Y., and Distefano, M. D. (2015) Application of meta- and para-Phenylenediamine as Enhanced Oxime Ligation Catalysts for Protein Labeling, PEGylation, Immobilization, and Release. *Curr. Protoc. protein Sci. 79*, 15.4.1-28.

(172) Zhou, P., Zou, J., Tian, F., and Shang, Z. (2009) Fluorine Bonding - How Does It Work In Protein - Ligand Interactions ? *J. Chem. Inf. Model 49*, 2344–2355.

(173) Bissantz, C., Kuhn, B., and Stahl, M. (2010) A medicinal chemist's

guide to molecular interactions. *J. Med. Chem. 53*, 5061–5084.

(174) Dunitz, J. D., and Taylor, R. (1997) Organic Fluorine Hardly Ever Accepts Hydrogen Bonds. *Chem. - A Eur. J. 3*, 89–98.

(175) Dalvit, C., and Vulpetti, A. (2016) Weak Intermolecular Hydrogen Bonds with Fluorine: Detection and Implications for Enzymatic/Chemical Reactions, Chemical Properties, and Ligand/Protein Fluorine NMR Screening. *Chem. - A Eur. J. 22*, 7592–7601.

(176) Jakeman, D. L., and Evans, J. N. S. (1998) Overexpression, Purification, and Use of Phosphoenol Pyruvate Synthetase in the Synthesis of PEP Analogues. *Bioorg. Chem. 26*, 245–253.

(177) Furdui, C. M., Sau, A. K., Yaniv, O., Belakhov, V., Woodard, R. W., Baasov, T., and Anderson, K. S. (2005) The use of (E)- and (Z)-phosphoenol-3-fluoropyruvate as mechanistic probes reveals significant differences between the active sites of KDO8P and DAHP synthases. *Biochemistry 44*, 7326–7335.

(178) Hopkins, A. L., Groom, C. R., and Alex, A. (2004) Ligand efficiency: a useful metric for lead selection. *Drug Discov. Today 9*, 430–431.

(179) Kuntz, I. D., Chen, K., Sharp, K. A., and Kollman, P. A. (1999) The maximal affinity of ligands. *Proc. Natl. Acad. Sci. 96*, 9997–10002.

(180) Maschauer, S., and Prante, O. (2014) Sweetening Pharmaceutical Radiochemistry by 18 F-Fluoroglycosylation: A Short Review. *Biomed Res. Int. 2014*, 1–16.

(181) O'Haagan, D. (Fife), and Li, X.-G. (TurunYliopisto). (2014) Method of labelling a biologically active molecule with 5-fluoro-5deoxypetose or a 3-fluoro-3-deoxypentose. US patent no. 2014/0227181 A1, United States.

(182) Namavari, M., Cheng, Z., Zhang, R., De, A., Levi, J., Hoerner, J. K., Yaghoubi, S. S., Syud, F. A., and Gambhir, S. S. (2009) A Novel Method for Direct Site-Specific Radiolabeling of Peptides Using [18 F]FDG. *Bioconjugate Chem. 20*, 432–436.

(183) Chen, J. M., Xu, S. L., Wawrzak, Z., Basarab, G. S., and Jordan, D. B. (1998) Structure-based design of potent inhibitors of scytalone dehydratase: Displacement of a water molecule from the active site. *Biochemistry 37*, 17735–17744.

(184) Lam, P. Y. S., Ru, Y., Jadhav, P. K., Aldrich, P. E., DeLucca, G. V,

Eyermann, C. J., Chang, C. H., Emmett, G., Holler, E. R., Daneker, W. F., Li, L. Z., Confalone, P. N., McHugh, R. J., Han, Q., Li, R. H., Markwalder, J. A., Seitz, S. P., Sharpe, T. R., Bacheler, L. T., Rayner, M. M., Klabe, R. M., Shum, L. Y., Winslow, D. L., Kornhauser, D. M., Jackson, D. A., EricksonViitanen, S., and Hodge, C. N. (1996) Cyclic HIV protease inhibitors: Synthesis, conformational analysis, P2/P2' structure-activity relationship, and molecular recognition of cyclic ureas. *J. Med. Chem. 39*, 3514–3525.

(185) Campiani, G., Kozikowski, A. P., Wang, S., Ming, L., Nacci, V., Saxena, A., and Doctor, B. P. (1998) Synthesis and anticholinesterase activity of huperzine a analogues containing phenol and catechol replacements for the pyridone ring. *Bioorganic Med. Chem. Lett. 8*, 1413–1418.

(186) Tickle, I., Sharff, A., Vinkovic, M., Yon, J., and Jhoti, H. (2004) High-throughput protein crystallography and drug discovery. *Chem. Soc. Rev. 33*, 558–565.

(187) Stefan, M. I., and Le Novère, N. (2013) Cooperative Binding. *PLoS Comput. Biol. 9*, 1–6.

(188) Albrecht, S., Defoin, A., and Tarnus, C. (2006) Simple preparation of O-substituted hydroxylamines from alcohols. *Synthesis (Stuttg). 10*, 1635–1638.

(189) García-Sosa, A. T., Firth-Clark, S., and Mancera, R. L. (2005) Including tightly-bound water molecules in de novo drug design. exemplification through the in silico generation of poly(ADP-ribose)polymerase ligands. *J. Chem. Inf. Model. 45*, 624–633.

(190) Adler, M., Davey, D. D., Phillips, G. B., Kim, S. H., Jancarik, J., Rumennik, G., Light, D. R., and Whitlow, M. (2000) Preparation, characterization, and the crystal structure of the inhibitor ZK-807834 (CI-1031) complexed with factor Xa. *Biochemistry 39*, 12534–12542.

(191) Quiocho, F. A., Wilson, D. K., and Vyas, N. K. (1989) Substrate specificity and affinity of a protein modulated by bound water molecules. *Nature 340*, 404–407.

(192) Narayana Bhat, T., Bentley, G. A., Boulot, G., Greene, M. I., Tello, D., Dall 'acqua, W., Souchon, H., Schwarz, F. P., Mariuzza, R. A., and Poljak, R. J. (1994) Bound water molecules and conformational stabilization help mediate an antigen-antibody association (antigen-andbody complex/three-dimensional structure/enthalpy and entropy of association/hydration). *Immunology 91*, 1089–1093.

(193) Chung, E., Henriques, D., Renzoni, D., Zvelebil, M., Bradshaw, J. M., Waksman, G., Robinson, C. V., and Ladbury, J. E. (1998) Mass spectrometric and thermodynamic studies reveal the role of water molecules in complexes formed between SH2 domains and tyrosyl phosphopeptides. *Structure 6*, 1141–1151.

(194) Mikol, V., Papageorgiou, C., and Borer, X. (1995) The Role of Water Molecules in the Structure-Based Design of (5-Hydroxynorvaline)-2-cyclosporin: Synthesis, Biological Activity, and Crystallographic Analysis with Cyclophilin A. *J. Med. Chem. 38*, 3361–3367.

(195) Lam, P. Y. S., Jadhav, P. K., Eyermann, C. J., Hodge, C. nicholas, Ru, Y., Bacheler, L. T., Meek, J. L., Otto, M. J., Rayner, M. M., Wong, Y. N., Chang, C.-H., Weber, P. C., Jackson, D. A., Sharpe, T. R., and Erickson-Viitanen, S. (1994) Rational design of potent, bioavailable, nonpeptide cyclic ureas as HIV protease inhibitors. *Science (80-.). 263*, 380+.

(196) Cleland, W. W. (1992) Low-Barrier Hydrogen Bonds and Low Fractionation Factor Bases in Enzymatic Reactions. *Biochemistry 31*, 317–319.

(197) Schiøtt, B., Iversen, B. B., Madsen, G. K. H., Larsen, F. K., and Bruice, T. C. (1998) On the electronic nature of low-barrier hydrogen bonds in enzymatic reactions. *Proc. Natl. Acad. Sci. 95*, 12799–12802.

(198) Frey, P., Whitt, S., and Tobin, J. (1994) A Low-Barrier Hydrogen Bond in the Catalytic Triad of Serine Proteases. *Science (80-.). 264*, 1927–1930.

(199) Sakurai, M., Furuki, T., and Inoue, Y. (1995) The pKa of the zinc-bound water in carbonic anhydrase and its model compounds as studied by the AM1 calculation coupled with a reaction field theory. *J. Phys. Chem. 99*, 17789–17794.

(200) Aubert, S. D., Li, Y., and Raushel, F. M. (2004) Mechanism for the Hydrolysis of Organophosphates by the Bacterial Phosphotriesterase. *Biochemistry 43*, 5707–5715.

(201) Miró Sabaté, C., and Delalu, H. (2012) Synthesis and characterization of acetone hydrazones. *Zeitschrift fur Anorg. und Allg. Chemie 638*, 57–63.

(202) Schmidt, H., and Friebolin, H. (1983) H-NMR-untersuchungen an sialinsauren, IV kinetik und mechanismus des austauschs von protonen an c-3 der n-acetyl-q-neuraminsaure gegen deuterium oder tritium. *J. Carbohydr. Chem. 2*, 405–413.

(203) Dorland, L., Haverkamp, J., Schauer, R., Veldink, G. A., and Vliegenthart, J. F. G. (1982) The preparation of specifically deuterium- or tritium-labeled N-acetylneuraminic acid as precursors for glycoconjugate synthesis. *Biochem. Biophys. Res. Commun. 104*, 1114–1119.

(204) Horenstein, B. A., and Bruner, M. (1996) Acid-catalyzed solvolysis of CMP-N-acetyl neuraminate: Evidence for a sialyl cation with a finite lifetime. *J. Am. Chem. Soc. 118*, 10371–10379.

Chapter 6. Appendix

DAHP O-methyloxime

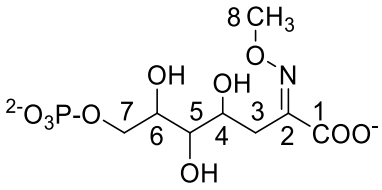

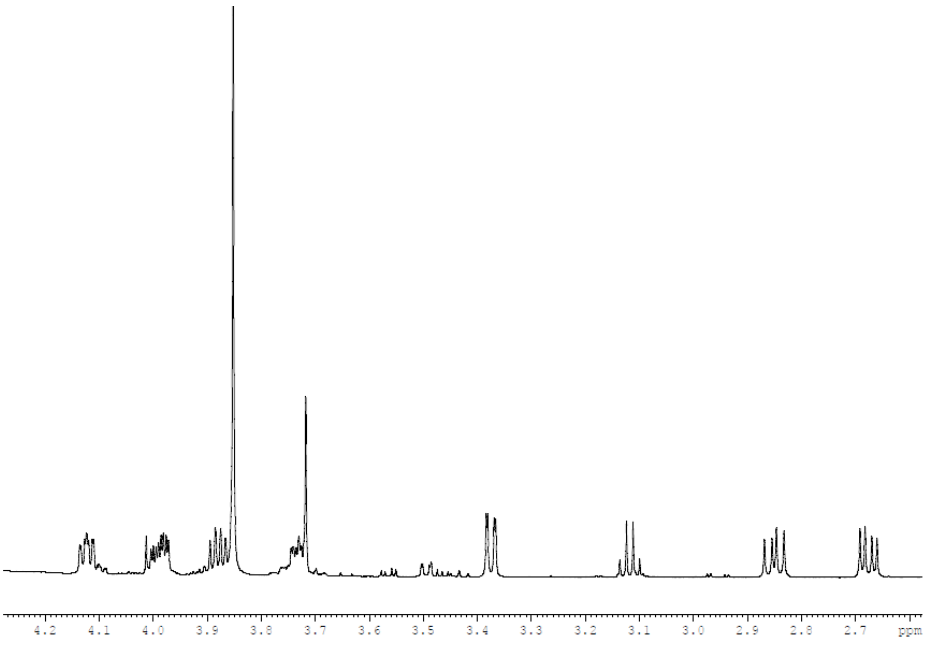

Table A.6.1 ^{1}H NMR spectrum of DAHP *O*-methyloxime.

The spectrum was acquired on a 600 MHz NMR spectrometer in D_2O.

Proton	^{1}H δ (ppm)	J_{H-H} (Hz)
H3	2.67	(dd) 13.3, 5.7
H3’	2.85	(dd) 13.3, 8.4
H4	4.12	(m)
H5	3.37	(dd) 8.8, 1.6,
H6	3.88	(m) 5.8
H7	3.98	(m)
H8	3.85	(s)

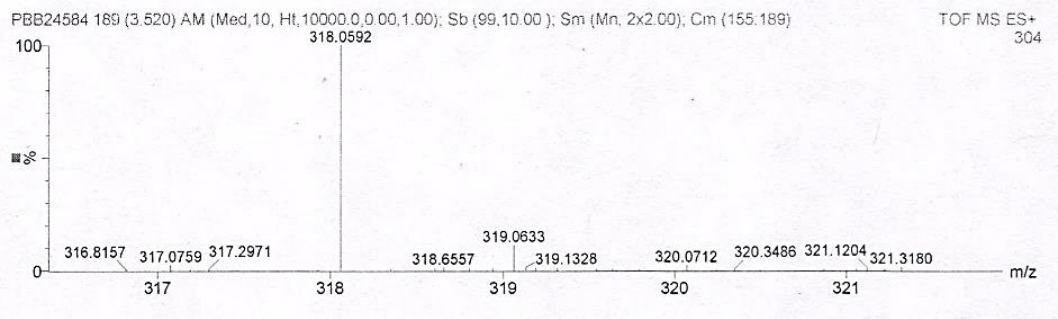

Figure A.6.1 High resolution mass spectrum of DAHP *O*-methyloxime.

Calculated mass of the M+1 peak is 318.0590 Da.

3-Fluoropyruvate oxime

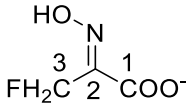

a)

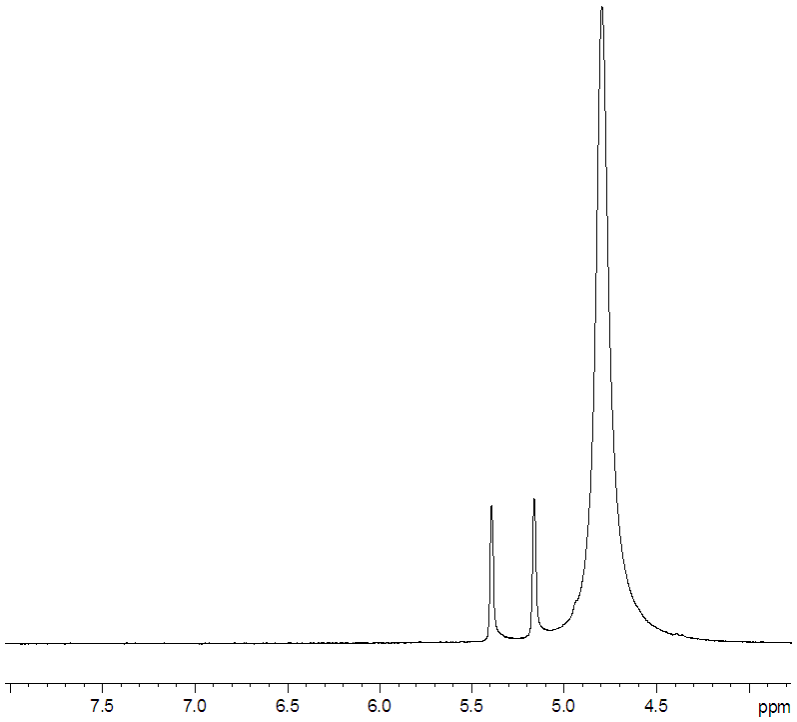

b)

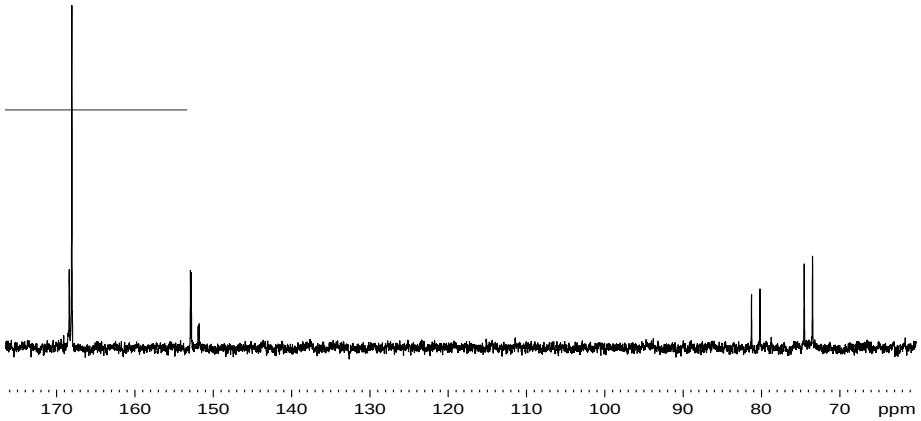

c)

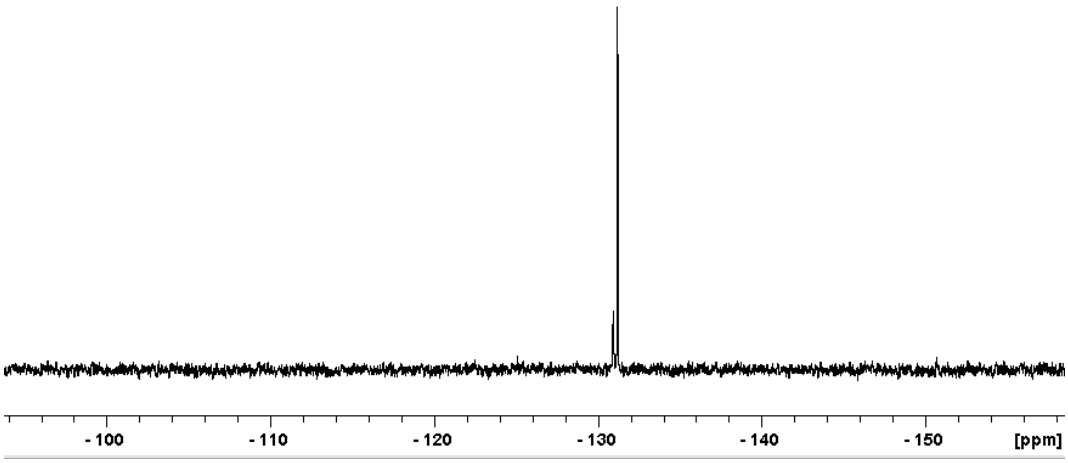

Table A.6.2 NMR spectra of 3-fluoropyruvate oxime.

The ^{1}H and ^{19}F spectra were acquired on a 200 MHz NMR spectrometer in D_2O. The ^{13}C spectrum was acquired on a 600 MHz NMR spectrometer in D_2O. (a) ^{1}H, (b) ^{13}C, (c) ^{19}F.

Proton	^{1}H δ (ppm)	J_{H-F} (Hz)	Carbon	^{13}C δ (ppm)	J_{C-F} (Hz)
H3	5.28	(d) 46	C1	168.39, 168.07	(s)
Fluorine	^{19}F δ (ppm)	J_{F-F} (Hz)	C2	152.86, 151.86	(d) 17.4
F3	-131.22, -130.97	(s)	C3	74.01, 80.73	(dd) 160.2

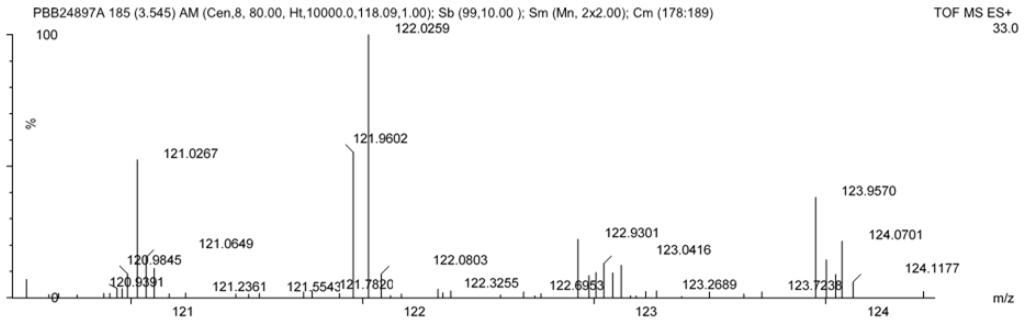

Figure A.6.2 High resolution mass spectrum of 3-fluoropyruvate oxime.

Calculated mass of the M+1 peak is 122.0253 Da.

3,3,3- Trifluoropyruvate oxime

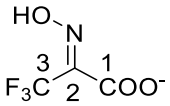

a)

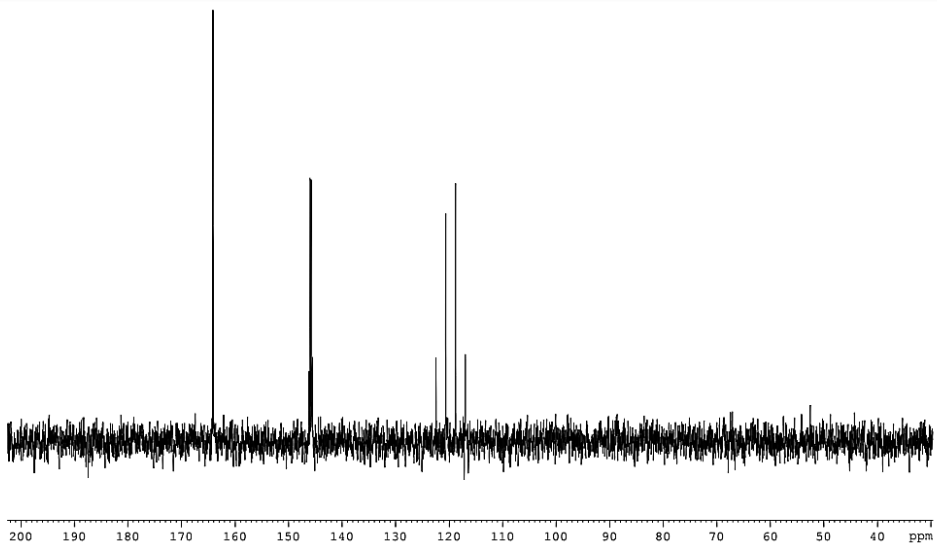

b)

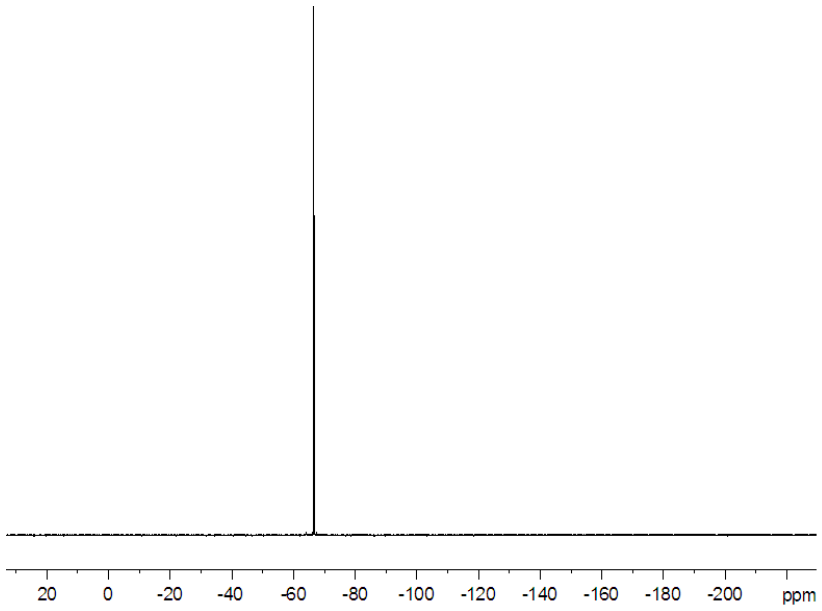

Table A.6.3 NMR spectra of 3,3,3-trifluoropyruvate oxime.

The ^{13}C spectrum was acquired on a 600 MHz NMR spectrometer in D_2O. The ^{19}F spectrum was acquired on a 200 MHz NMR spectrometer in D_2O. (a) ^{13}C, (b) ^{19}F.

Fluorine	^{19}F δ (ppm)	J_{F-F} (Hz)	Carbon	^{13}C δ (ppm)	J_{C-F} (Hz)
F3	-66.58	(s)	C1	164.15	(s)
			C2	145.9	(q) 32.76
			C3	119.73	(q) 272.8

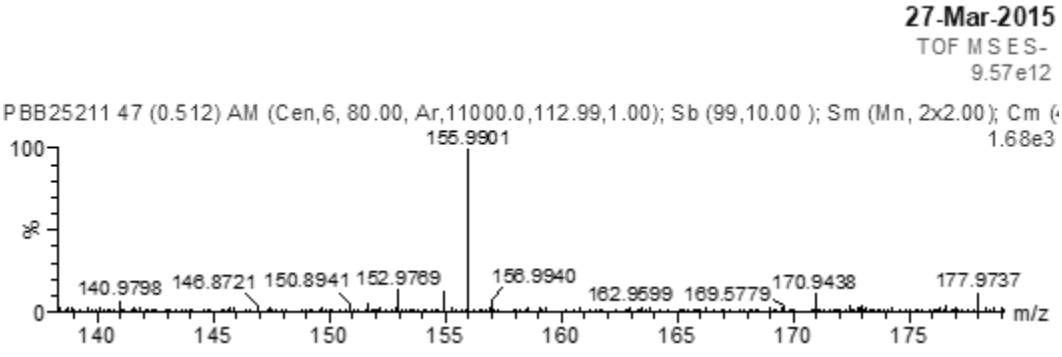

Figure A.6.3 High resolution mass spectrum of 3,3,3-trifluoropyruvate oxime.

Calculated mass of the M-1 peak is 155.9909 Da.

3,3,3-Trifluoropyruvate oxime ethyl ester

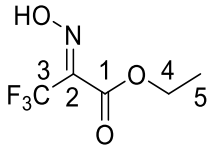

a)

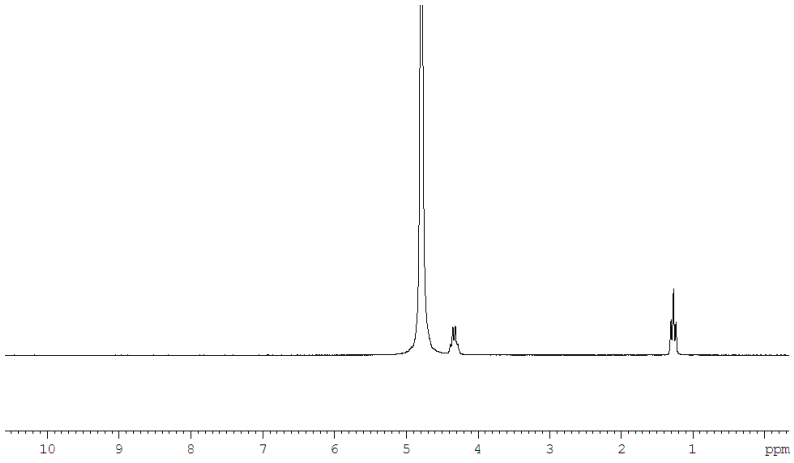

b)

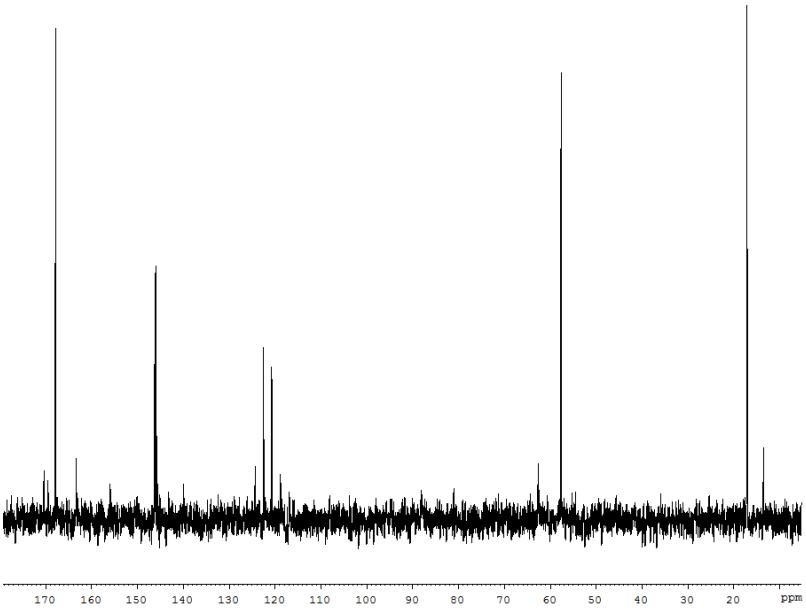

c)

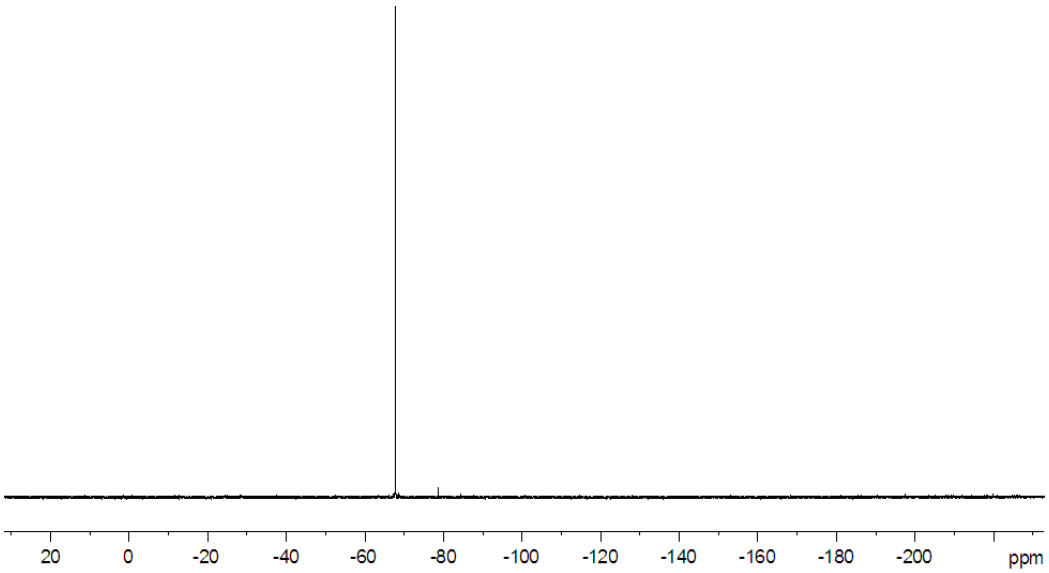

Table A.6.4 NMR spectra of 3,3,3-trifluoropyruvate oxime ethyl ester.

The ^{1}H and ^{19}F spectrum were acquired on a 200 MHz NMR spectrometer in D_2O. The ^{13}C spectrum was acquired on a 600 MHz NMR spectrometer in D_2O. (a) 1H, (b) ^{13}C, (c) ^{19}F.

Proton	^{1}H δ (ppm)	J_{H-H} (Hz)	Carbon	^{13}C δ (ppm)	J_{C-F} (Hz)
H4	4.33	(q) 7.18	C1	167.87	(s)
H5	1.27	(t) 7.18	C2	146.11	(q) 33.9
Fluorine	^{19}F δ (ppm)	J_{F-F} (Hz)	C3	121.68	(q) 273.5
F3	-67.78	(s)	C4	57.71	(s)
			C5	17.15	(s)

Note: A high resolution mass spectrum of 3,3,3-trifluoropyruvate oxime ethyl ester could not be received. In negative ion mode, 3,3,3-trifluoropyruvate oxime was the predominant peak, indicating a loss of the ester functional group. 3,3,3-trifluoropyruvate oxime was synthetized from 3,3,3-trifluoropyruvate oxime ethyl ester. A high resolution mass spectrum for this compound is reported (Figure A.6.3).

3,3,3-Trifluoropyruvate hydrazone

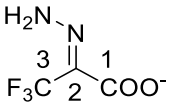

a)

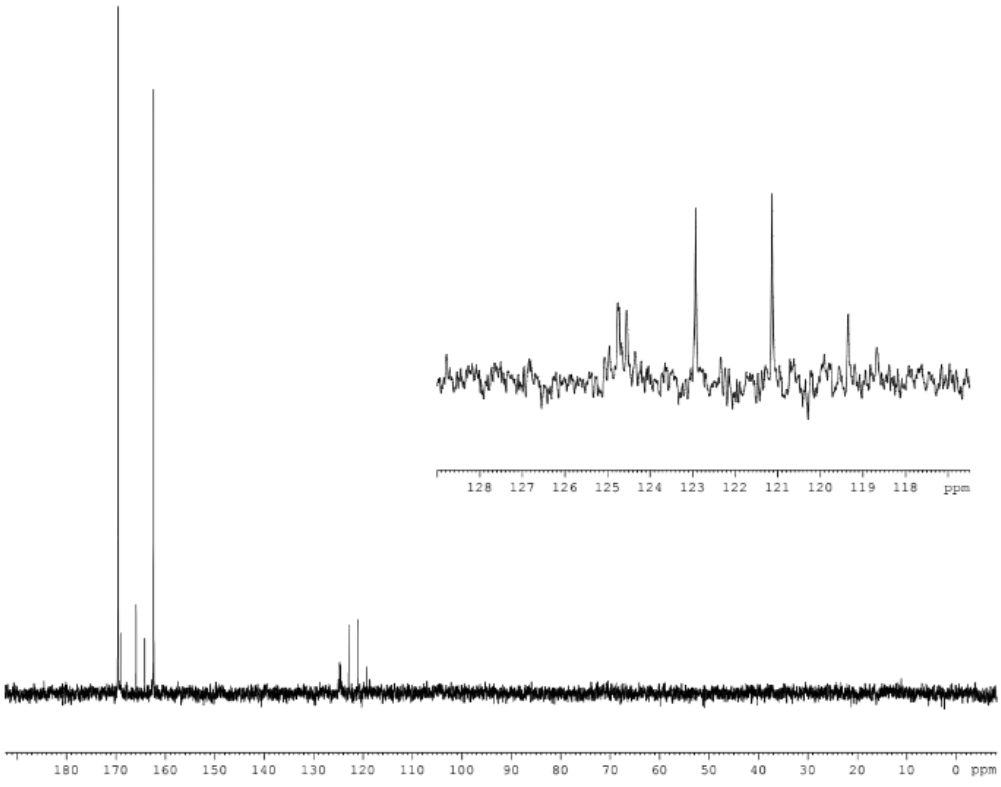

b)

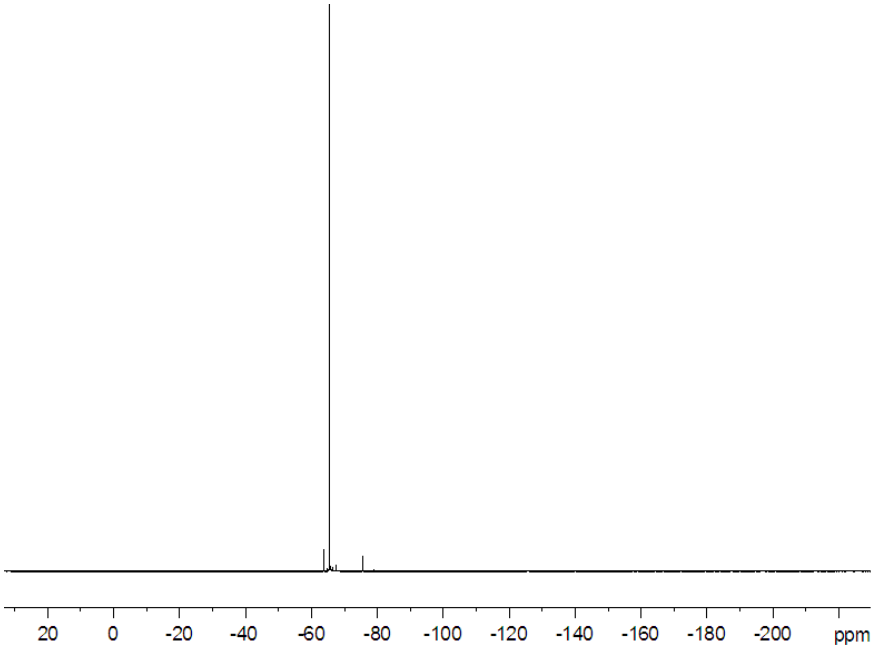
20
0
-20
-40
-60
-80
-100
-120
-140
-160
-180
-200
ppm

c)

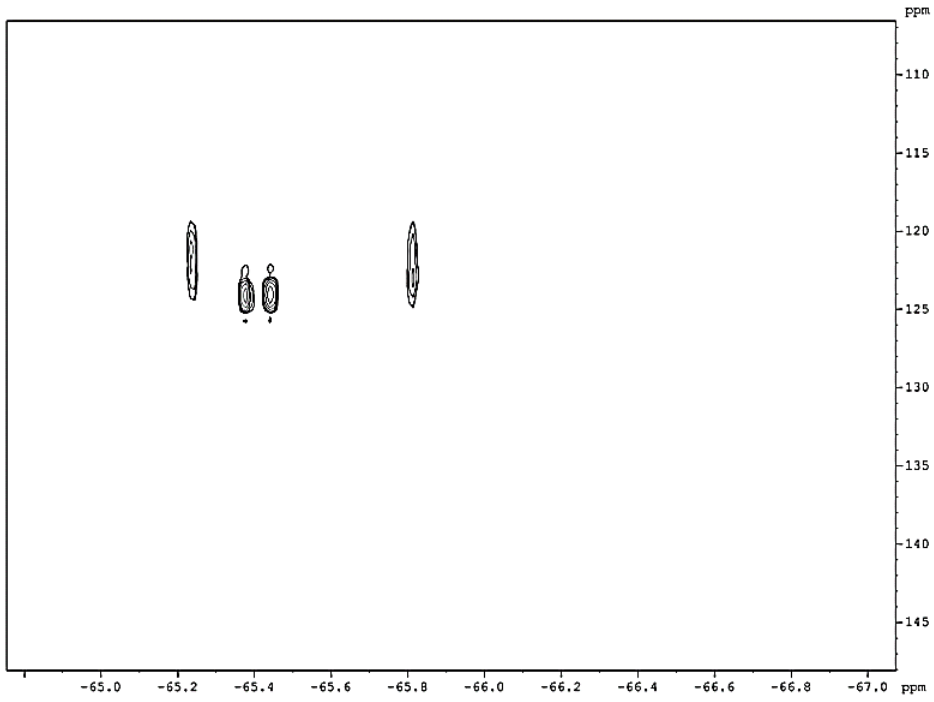
ppm
110
115
120
125
130
135
140
145
-65.0
-65.2
-65.4
-65.6
-65.8
-66.0
-66.2
-66.4
-66.6
-66.8
-67.0
ppm

Table A.6.5 NMR spectra of 3,3,3-trifluoropyruvate hydrazone.

The ^{19}F spectrum was acquired on a 200 MHz NMR spectrometer in D_2O. The ^{13}C and ^{13}C-^{19}F HMBC.spectra were acquired on a 500 MHz NMR spectrometer in D_2O. (a) ^{13}C, (b) ^{19}F, (c) ^{13}C-^{19}F HMBC.

Fluorine	^{19}F δ (ppm)	J_{F-F} (Hz)	Carbon	^{13}C δ (ppm)	J_{C-F} (Hz)
F3	-65.51	(s)	C1	*169.58*	(s)
			C2	*124.65*	*31.6*
			C3	*122.03*	*270.6*

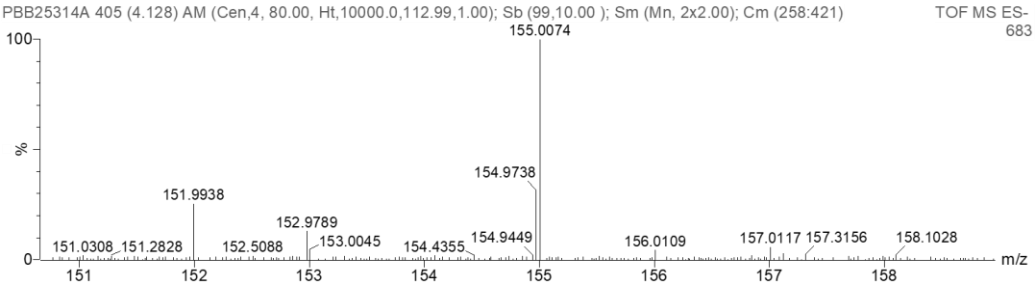

Figure A.6.4: High resolution mass spectrum of 3,3,3-trifluoropyruvate hydrazone.

Calculated mass of the M-1 peak is 155.0068 Da.

3,3,3-trifluoropyruvate hydrazone ethyl ester

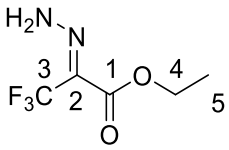

a)

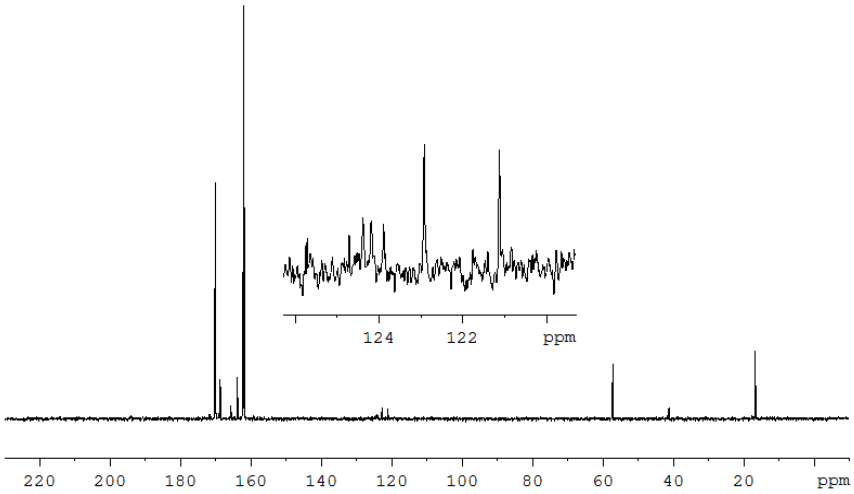

b)

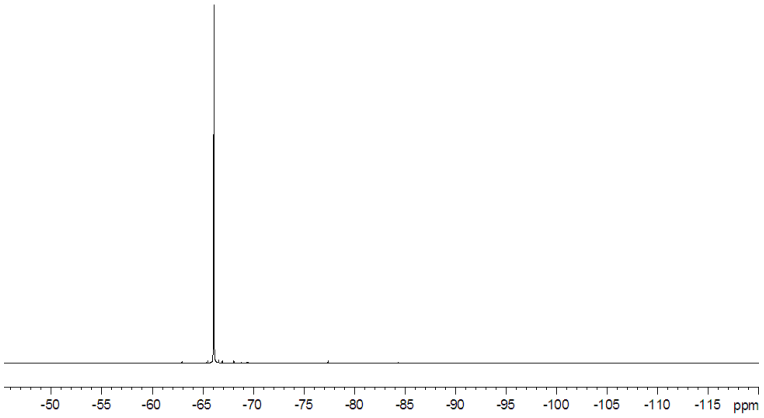

Table A.6.6 NMR spectra of 3,3,3-trifluoropyruvate hydrazone ethyl ester.

The ^{19}F spectrum was acquired on a 200 MHz NMR spectrometer in D_2O. The ^{13}C spectrum was acquired on a 600 MHz NMR spectrometer in D_2O. (a) ^{13}C, (b) ^{19}F.

Fluorine	^{19}F δ (ppm)	J_{F-F} (Hz)	Carbon	^{13}C δ (ppm)	J_{C-F} (Hz)
F3	-66.09	(s)	C1	170.31	(s)
			C2	124.29	(q) 30.2
			C3	122.02	(q) 270.6
			C4	57.27	(s)
			C5	16.78	(s)

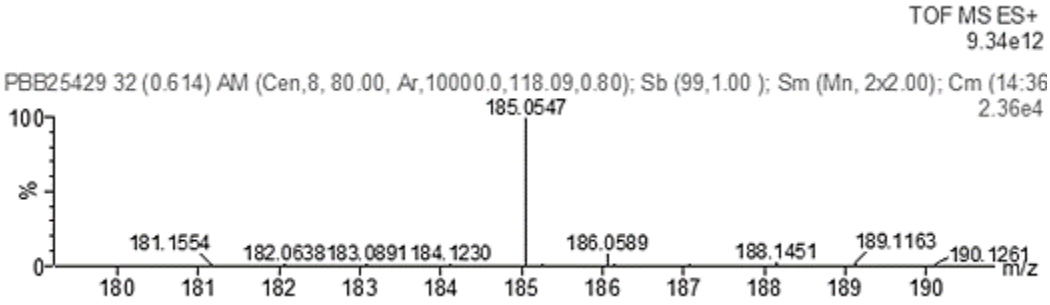

Figure A.6.5 High resolution mass spectrum of 3,3,3-trifluoropyruvate hydrazone ethyl ester.

Calculated mass of the M+1 peak is 185.0538 Da.

Pyruvate semicarbazone

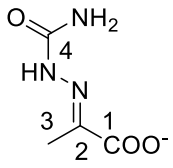

a)

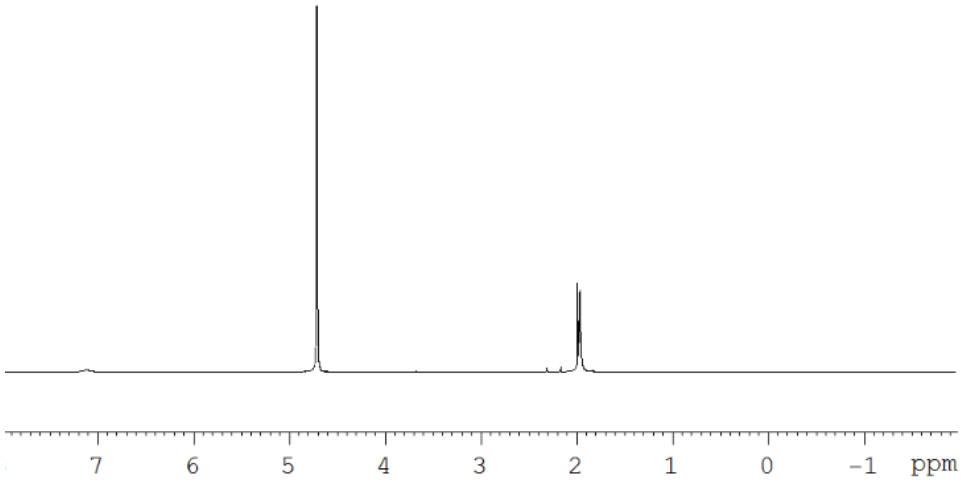

b)

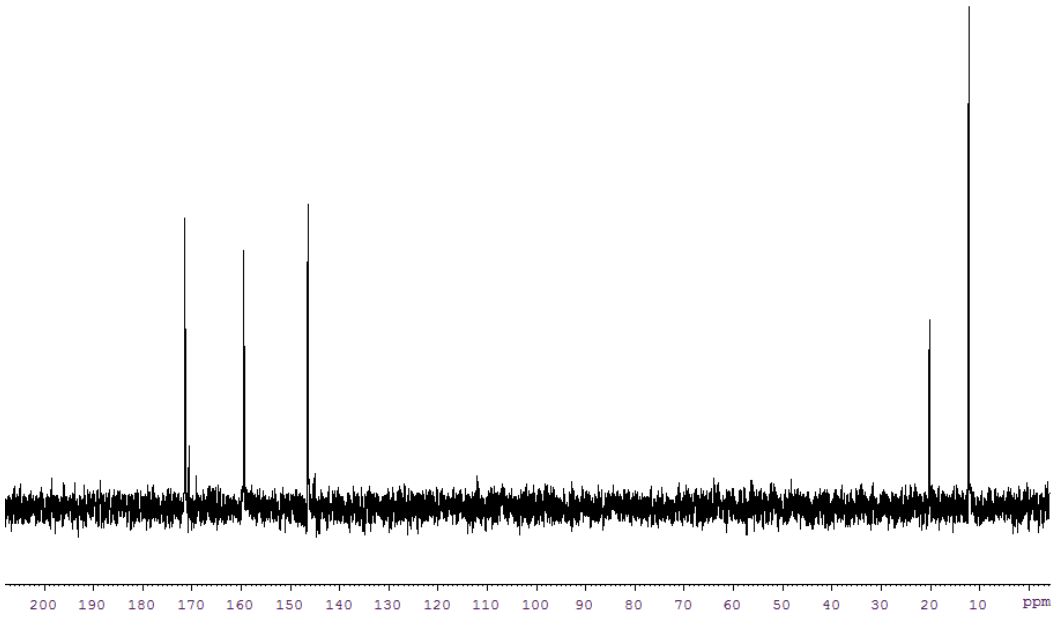

Table A.6.7 NMR spectra of pyruvate semicarbazone.

The ^{1}H spectrum was acquired on a 200 MHz NMR spectrometer in D_2O. The ^{13}C spectrum was acquired on a 600 MHz NMR spectrometer in D_2O. (a) ^{1}H, (b) ^{13}C.

Proton	^{1}H δ (ppm)	J_{H-H} (Hz)	Carbon	^{13}C δ (ppm)
H3	*1.98*	(s)	C1	*171.50, 170.50*
H3’	*1.96*	(s)	C2	*146.50*
			C3	*20.22, 12.23*
			C4	*159.56*

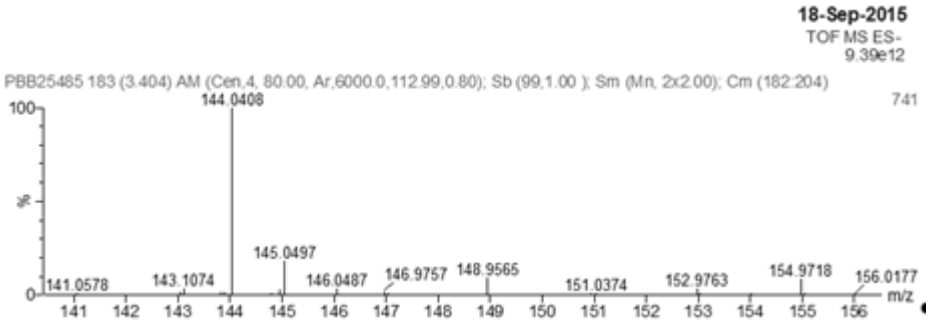

Figure A.6.6 High resolution mass spectrum of pyruvate semicarbazone.

Calculated mass of the M-1 peak is 144.0409 Da.

3,3,3-trifluoropyruvate semicarbazone

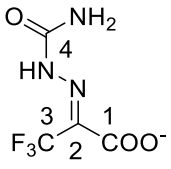

a)

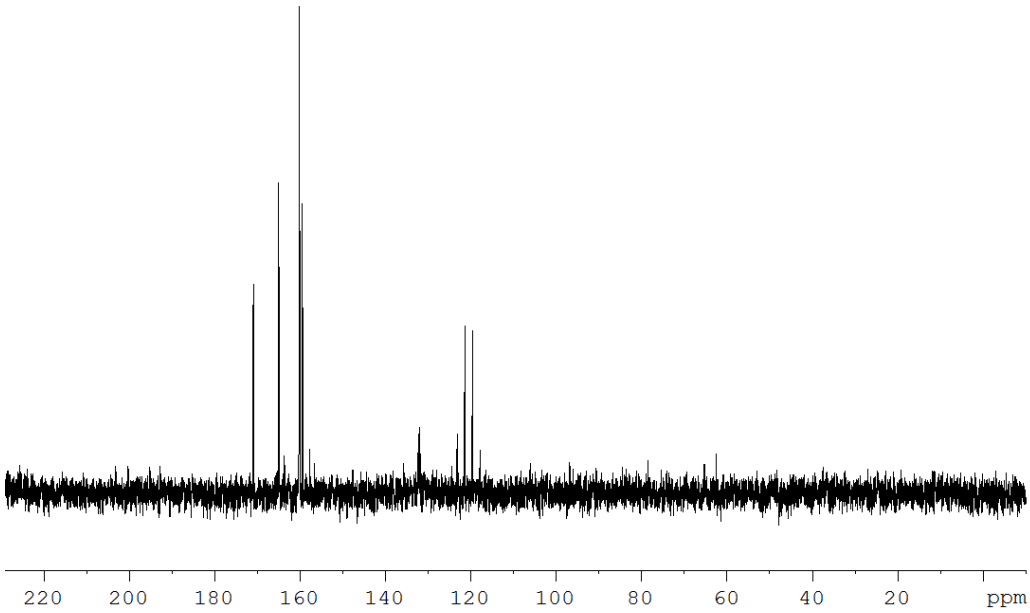

b)

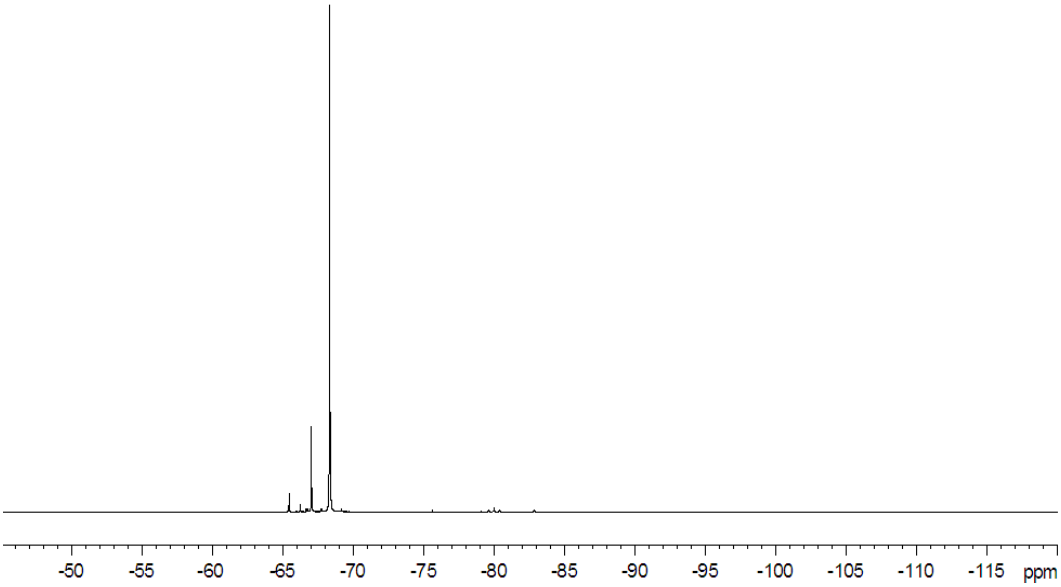

Table A.6.8 NMR spectra of 3,3,3-trifluoropyruvate semicarbazone.

The ^{19}F spectrum was acquired on a 200 MHz NMR spectrometer in D_2O. The ^{13}C spectrum was acquired on a 600 MHz NMR spectrometer in D_2O. (a) ^{13}C, (b) ^{19}F.

Fluorine	^{19}F δ (ppm)	J_{F-F} (Hz)	Carbon	^{13}C δ (ppm)	J_{C-F} (Hz)
F3	-68.36	(s)	C1	171.02	(s)
			C2	132.09	(q) 34.3
			C3	120.56	(q) 271.6
			C4	159.52	(s)

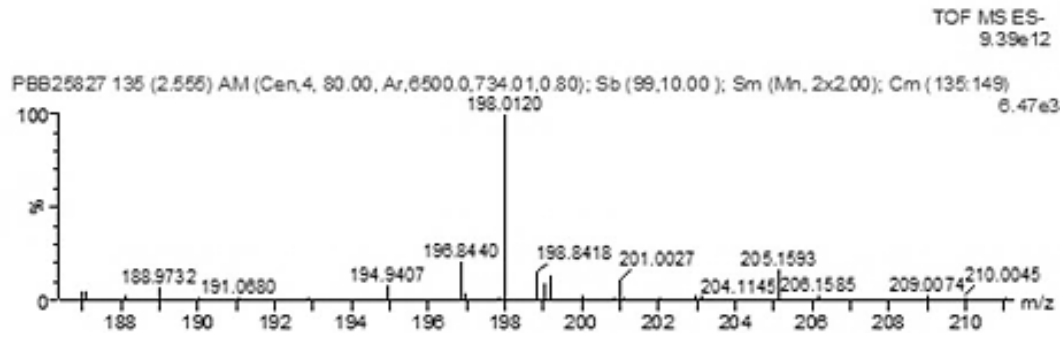

Figure A.6.7 High resolution mass spectrum of 3,3,3-trifluoropyruvate semicarbazone.

Calculated mass of the M-1 peak is 198.0126 Da.

3,3,3-Trifluoropyruvate semicarbazone ethyl ester

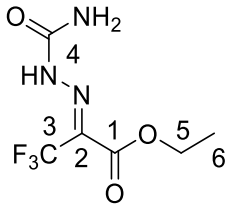

a)

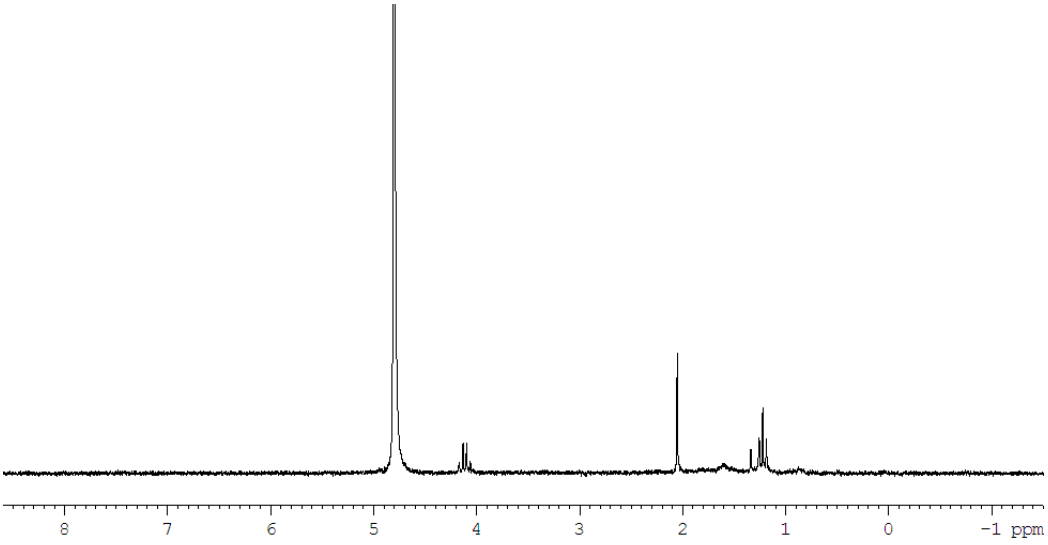

b)

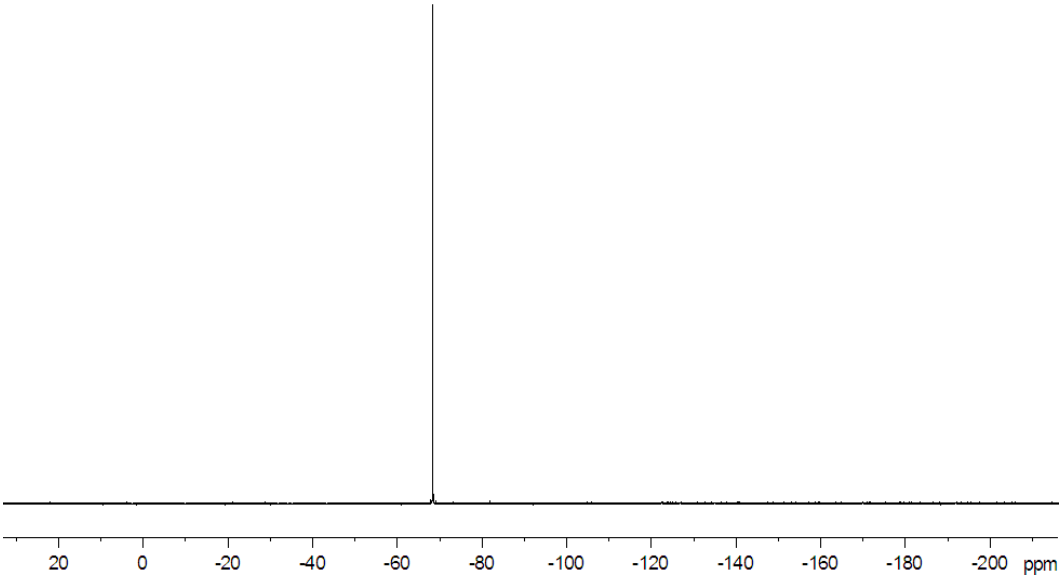

Table A.6.9 NMR spectra of 3,3,3-trifluoropyruvate semicarbazone ethyl ester.

The ^{1}H and ^{19}F spectra were acquired on a 200 MHz NMR spectrometer in D_2O. (a) ^{1}H, (b) ^{19}F.

Proton	^{1}H δ (ppm)	J_{H-H} (Hz)	Fluorine	^{19}F δ (ppm)
H5	4.11	(q) 7.2	F3	-68.39
H6	1.22	(t) 7.2		

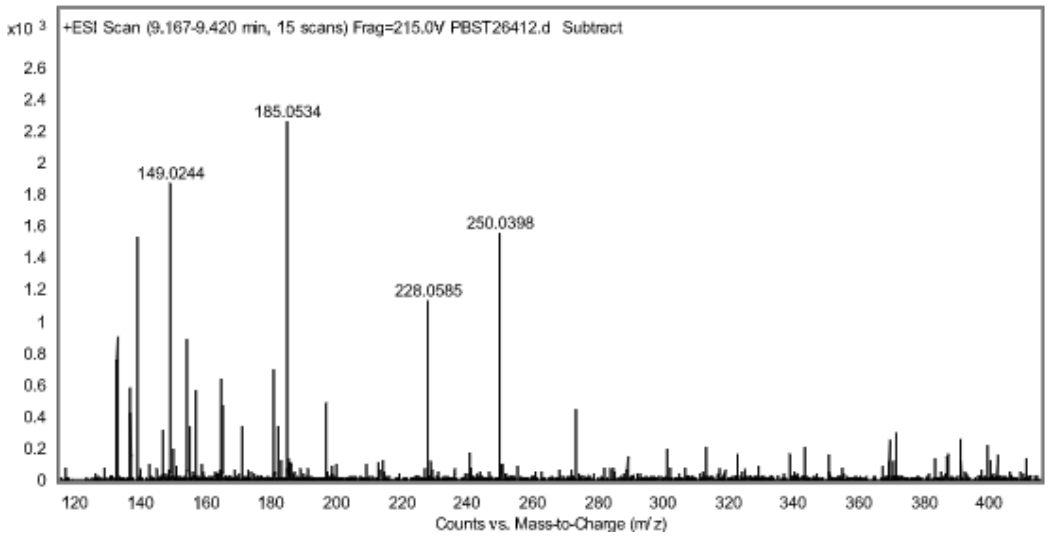

Figure A.6.8 High resolution mass spectrum of 3,3,3-trifluoropyruvate semicarbazone ethyl ester.

Calculated mass of the M+1 peak is 228.0591 Da.

DAHP semicarbazone

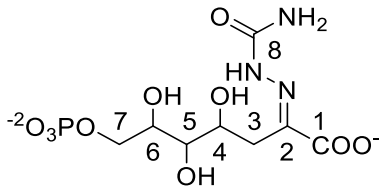

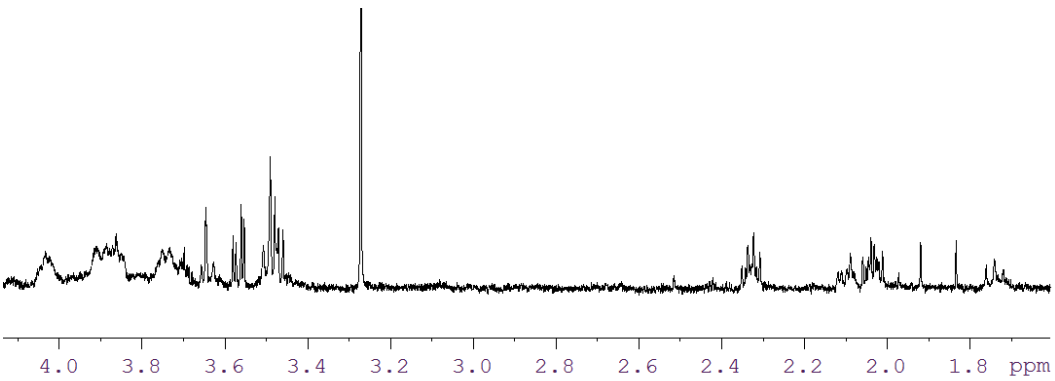

Table A.6.10 NMR spectrum of DAHP semicarbazone.

The ^{1}H spectrum was acquired on a 600 MHz NMR spectrometer in D_2O.

Proton	^{1}H δ (ppm)
H3	2.04
H3’	2.33
H4	4.02
H5	3.48
H6	3.74
H7	3.87

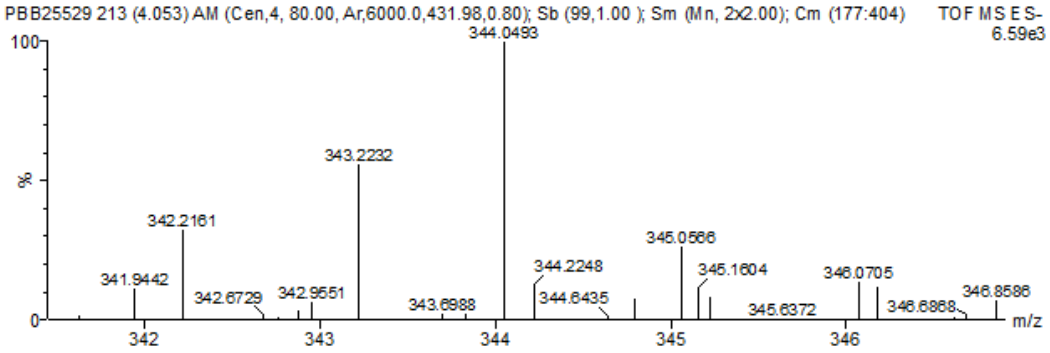

Figure A.6.9 High resolution mass spectrum of DAHP semicarbazone.

Calculated mass of the M-1 peak is 344.0495 Da.

.

3-Fluoro-PEP

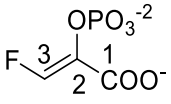

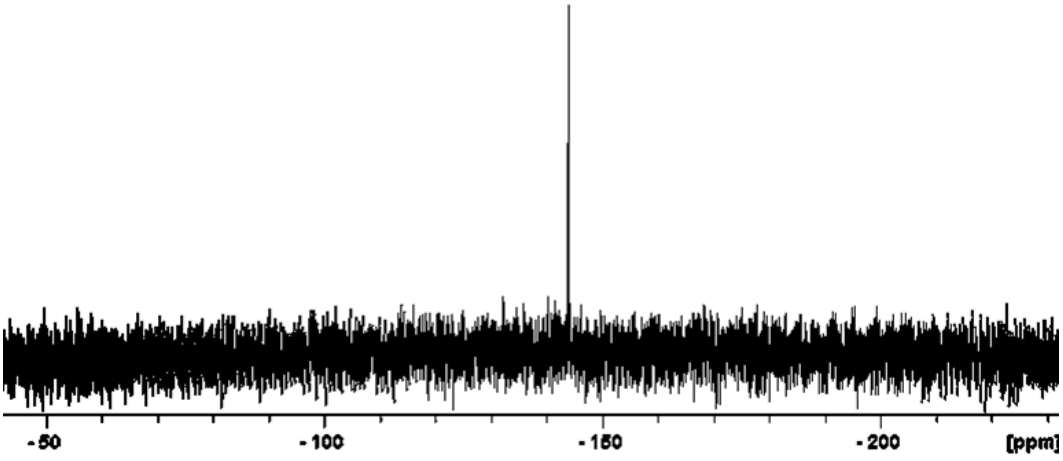

Table A.6.11 NMR spectra of 3-fluoro-PEP.

The ^{19}F spectrum was acquired on a 200 MHz NMR spectrometer in D_2O.

Fluorine	^{19}F δ (ppm)
F3	-142.97

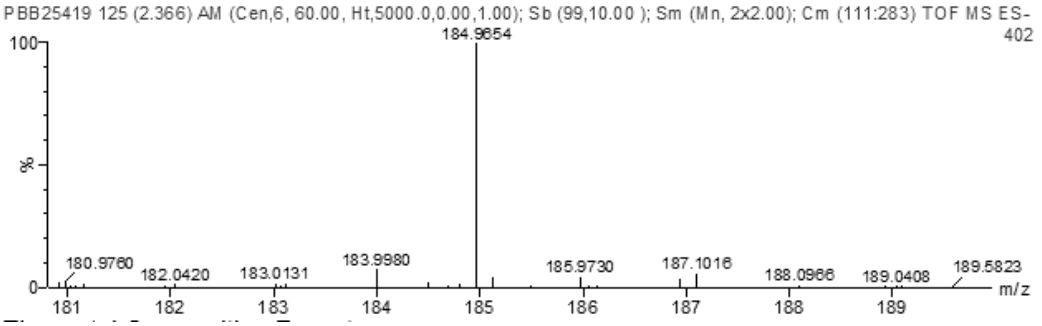

Figure A.6.10 High resolution mass spectrum of 3-fluoro-PEP.

Calculated mass of the M-1 peak is 184.9651 Da.

3-Fluoro-DAHP

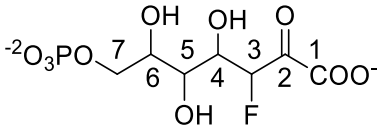

a)

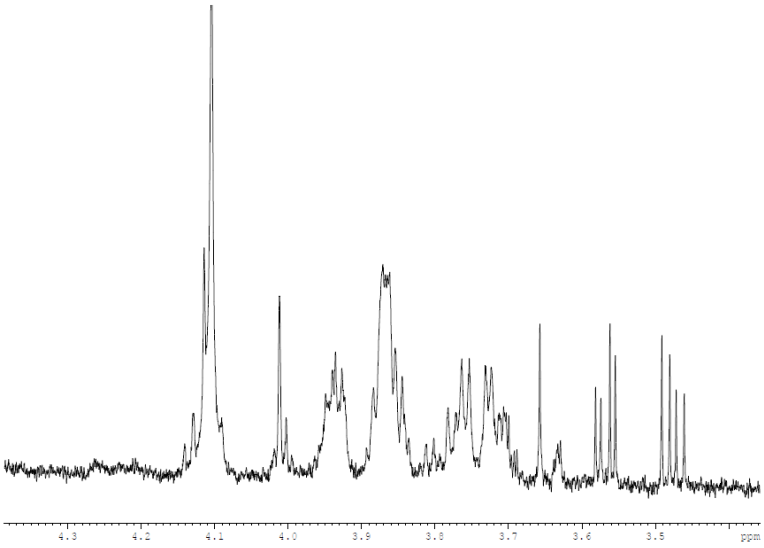

b)

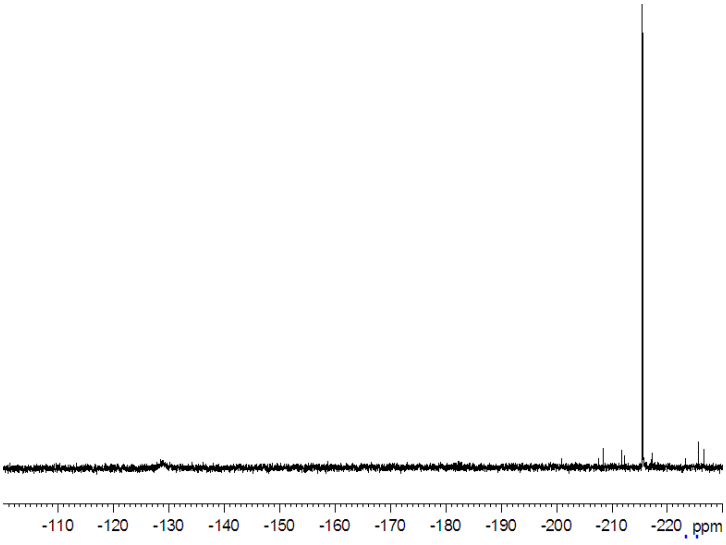

Table A.6.12 NMR spectra of 3- fluoro-DAHP.

The ^{1}H spectrum was acquired on a 600 MHz NMR spectrometer in D_2O. The ^{19}F spectra was acquired on a 200 MHz NMR spectrometer in D_2O. (a) ^{1}H, (b) ^{19}F.

Proton	^{1}H δ (ppm)	Fluorine	^{19}F δ (ppm)
H4	*4.01*	F3	*-215.51*
H3	4.11		
H5	*3.52*		
H6	*3.74*		
H7	*3.87*		
H7’	*3.93*		

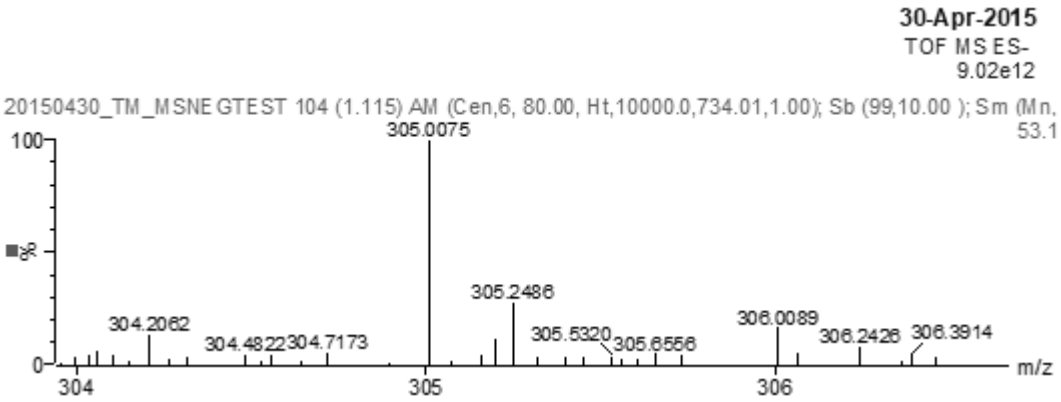

Figure A.6.11 High resolution mass spectrum of 3-fluoro-DAHP.

Calculated mass of the M-1 peak is 305.0074 Da.

3-Fluoro-NeuNAc

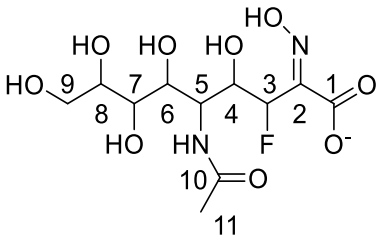

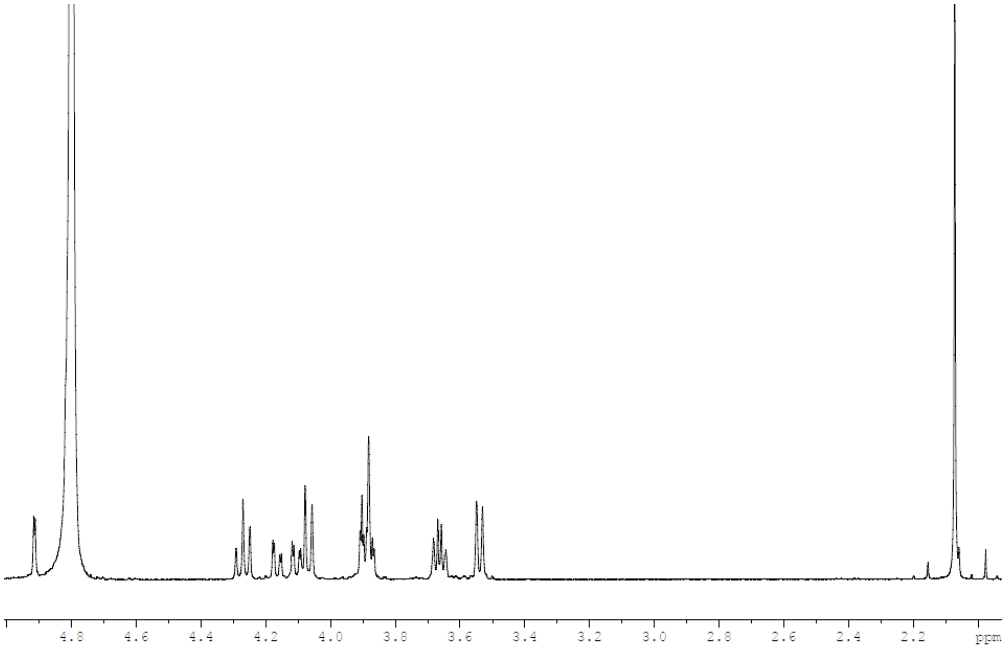

Table A.6.13 NMR spectra of 3-fluoro-NeuNAc.

The ^{1}H spectrum was acquired on a 600 MHz NMR spectrometer in D_2O.

Proton	^{1}H δ (ppm)	J_{H-H} / J_{F-H} (Hz)
H3	4.82	(d) 2.41
H4	4.17	(ddd) 29.92, 10.69, 2.37
H5	4.04	(t) 10.71
H6	3.97	(d) 10.49
H7	3.44	(d) 9.39
H8	3.57	(q) 5.51
H9	3.78	(m)
H11	1.97	(s)

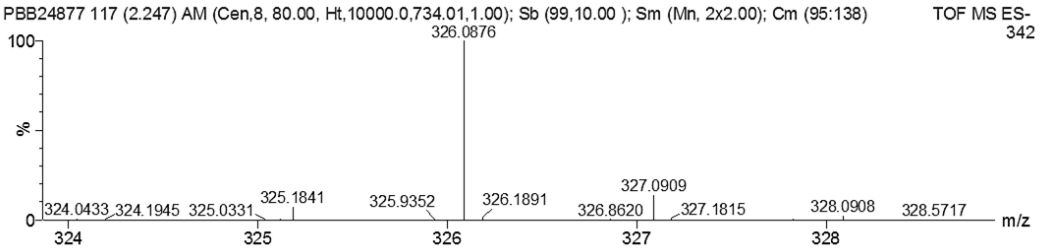

Figure A.6.12 High resolution mass spectrum of 3-fluoro-NeuNAc.

Calculated mass of the M-1 peak is 326.0887 Da.

O-(2-fluoroethyl) hydroxylamine

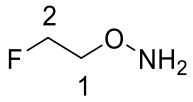

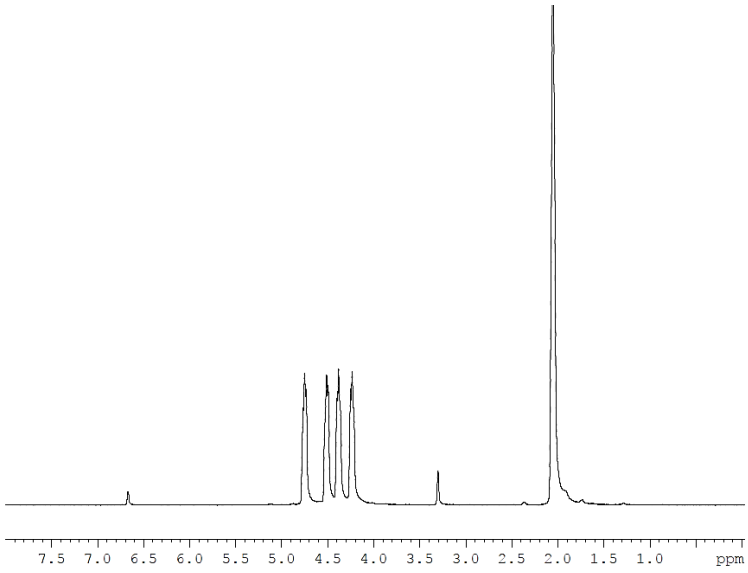

Table A.6.14 NMR spectra of *O*-(2-fluoroethyl) hydroxylamine.

The ^{1}H spectrum was acquired on a 200 MHz NMR spectrometer in acetone- d_6.

Proton	^{1}H δ (ppm)	J_{H-H} (Hz)	J_{F-H} (Hz)
H1	4.30	(t) 2.6	(d) 47
H2	4.63	(t) 2.6	(d) 29.3

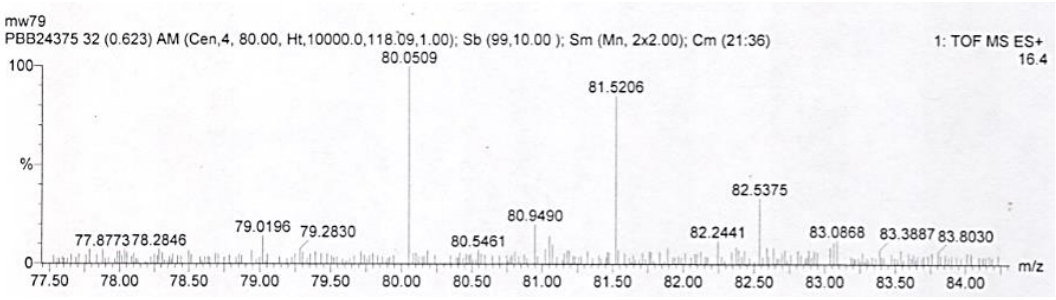

Figure A.6.13 High resolution mass spectrum of *O*-(2-fluoroethyl) hydroxylamine.

Calculated mass of the M+1 peak is 80.0512 Da.

DAHP O-(2-fluoroethyl) oxime

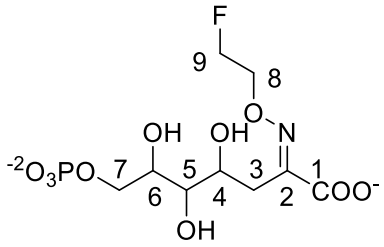

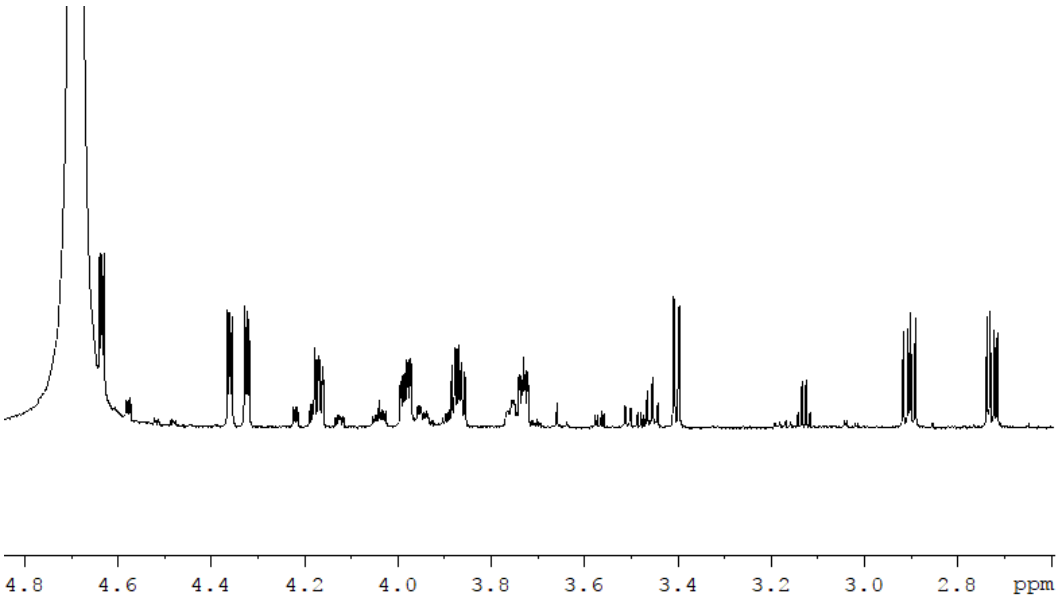

Table A.6.15 NMR spectra of DAHP *O*-(2-fluoroethyl) oxime.

The ^{1}H spectrum was acquired on a 600 MHz NMR spectrometer in D_2O.

Proton	^{1}H δ (ppm)	J_{H-H} (Hz)
H3	2.74	(dd) 13.27, 5.50
H3’	2.92	(dd) 13.28, 8.68
H4	4.19	(m)
H5	3.42	(dd) 8.88, 1.64
H6	3.75	(m)
H7	3.89	(m)
H7’	3.99	(m)
H8	4.33	(t) 3.98
H8’	4.39	(t) 3.98
H9	4.64	(t) 3.98

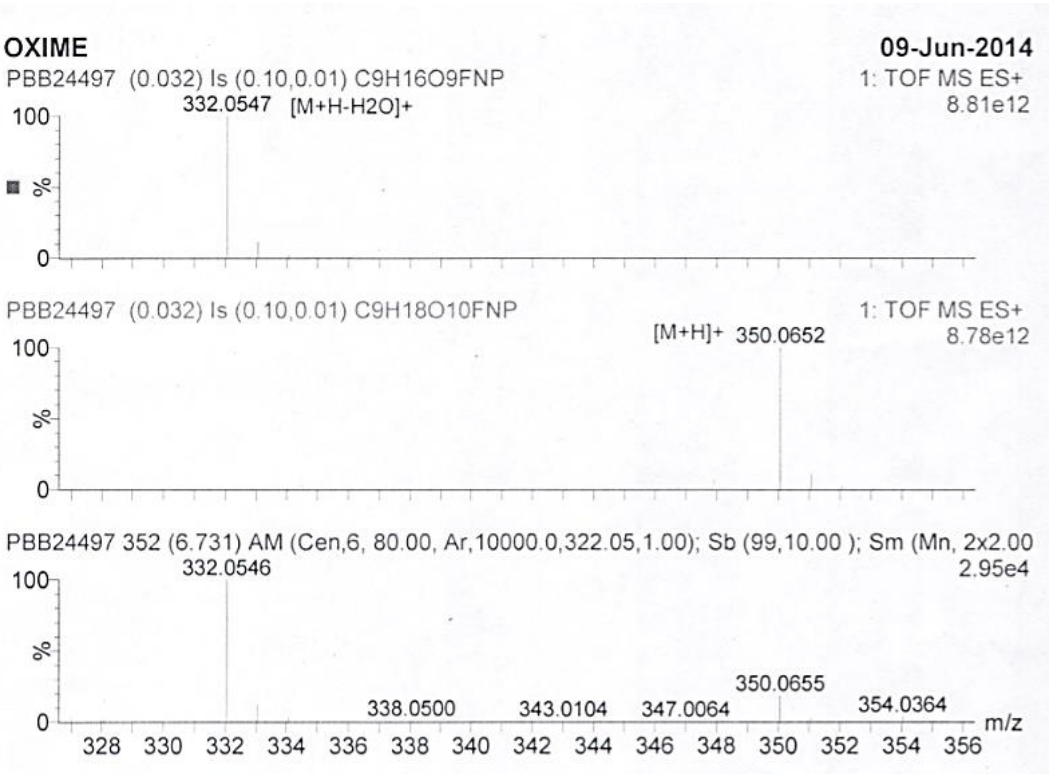

Figure A.6.14 High resolution mass spectrum of DAHP *O*-(2-fluoroethyl) oxime.

Calculated mass of the M+1 peak is 350.0652 Da.

DAHP hydrazone

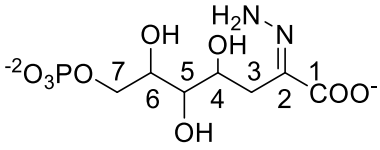

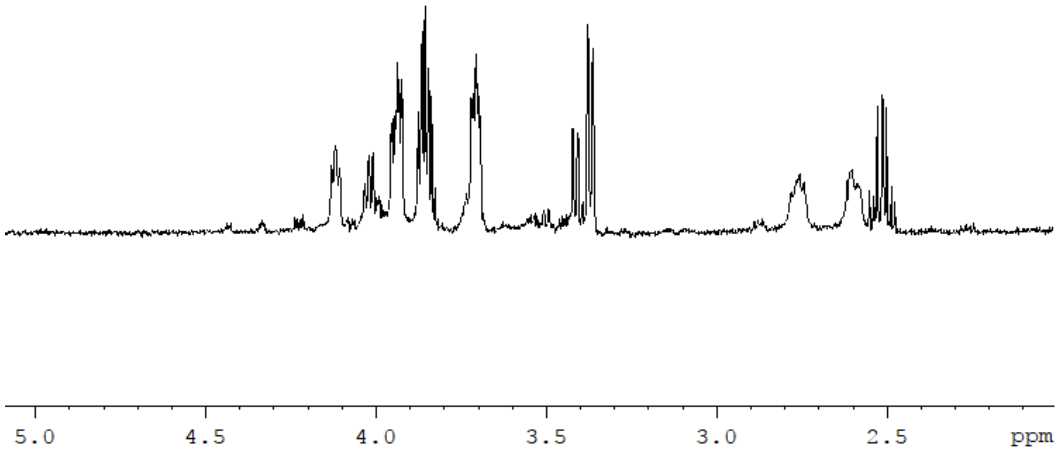

Table A.6.16 NMR spectra of DAHP hydrazone.

The ^{1}H spectrum was acquired on a 600 MHz NMR spectrometer in D_2O.

Proton	^{1}H δ (ppm)
H3	2.59
H3’	2.74
H4	3.92
H5	3.39
H6	3.7
H7	3.86

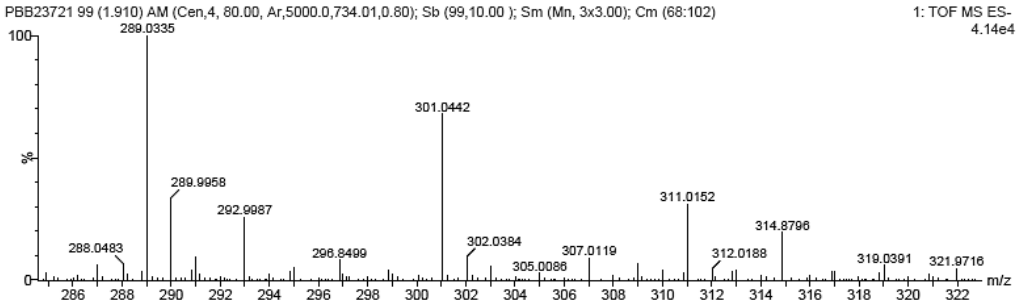

Figure A.6.15 High resolution mass spectrum of DAHP hydrazone.

Calculated mass of the M-1 peak is 301.0447 Da.

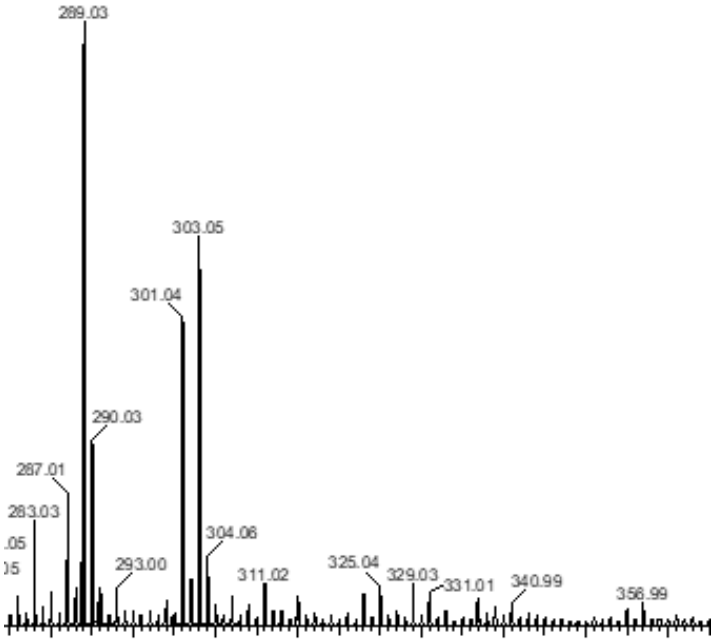

Figure A.6.16 Low resolution mass spectrum of DAHP hydrazone.

Calculated mass of the M-1 peak is 301.04 Da. Expected mass for DAHP formylhydrazone 329.17 Da. Expected mass for DAHP is 287.01 Da. The peaks at 273 and 303 Da originate from deuterium exchange at C3 due to the sample being used for NMR and being dissolved in D_2O. Similar reactions were previously observed.[202–204]